

Doctorate Dissertation

博士論文

Performance of Si/CdTe Semiconductor Compton Telescope

for detecting polarization of gamma-rays

(ガンマ線偏光の検出を目的とした

Si/CdTe 半導体コンプトン望遠鏡の性能評価)

A Dissertation Submitted for Degree of Doctor of Philosophy

平成 30 年 12 月博士 (理学) 申請

December 2018

Department of Physics, Graduate School of Science,
The University of Tokyo

東京大学大学院理学系研究科物理学専攻

Yuusuke Uchida

内田 悠介

Abstract

Polarimetry investigations in the X-ray and gamma-ray bands are showing to be promising at providing information of high-energy phenomena in the Universe. In particular, X-ray and gamma-ray polarimetry provides us with crucial information about the radiation mechanisms, the magnetic field in the emitting region, and also the structure of the emitting regions. However, detecting the state of polarization of radiation in the X-ray and gamma-ray energy range is still in the development phase, because measuring polarization in these energy range is more challenging compared to performing polarization measurements in the optical, infrared, or radio frequency bands.

In this thesis, we investigate the performance of Soft Gamma-ray Detector (SGD) on board the sixth Japanese X-ray astronomy Satellite, *Hitomi*, that measures in the energy range of 60–600 keV with a sensitivity at 300 keV, which is 10 times better than the performance of the *Suzaku* Hard Xray Detector. By measuring Compton scattering in the detector system, the SGD had the ability to perform both spectroscopic and high-precision polarimetry measurements. The response of the spectrum was performed through a detailed study of the energy calibration. A detection system that can observe the polarization state of gamma-ray was developed at SPring-8, which is a synchrotron radiation factory in Japan that produces a monochromatic fully linearly polarized synchrotron radiation. We describe the performances of the spectroscopy and the polarimetry, as well as in the orbit performances including background. This data is highly useful for future gamma-ray missions. Additionally, we discuss the numerical model of the pulsar wind nebula based on the observation of the Crab Nebula.

During the start-up period of the spacecraft, the system of the SGD turned on for only a short amount of time to observe celestial object such as Crab Nebula. In total, the SGD was able to observe the Crab Nebula for about 5000 seconds. After careful analysis, we derived the polarization amplitude of the Crab to be $Q = 0.1425$ ($-0.0682/ + 0.0681$) in 60 – 160 keV, at a 99.3% confidence level. An ability to derive information of the polarization in such a short observing time demonstrates the effectiveness of the SGD design thanks to the high modulation factor of the azimuthal angle dependence, and the dependence of the high modulation factor of the azimuthal angle.

The investigation found that the degree of polarization in the gamma-ray energy range is lower than predicted by theory. To understand this result, we developed a model that allows us to account for a number of effects, which are expected to be important in the pulsar wind nebula. This includes a realistic distribution of the magnetic field strength, particle transport and cooling, relativistic transformation of emission, and relativistic de-polarization. Our analysis shows that the effect is very weak.

Contents

| | | |
|----------|--|-----------|
| 1 | Introduction | 1 |
| 2 | Polarization mechanisms and Polarimeters | 3 |
| 2.1 | Polarization | 3 |
| 2.1.1 | Stokes parameters | 4 |
| 2.2 | Polarized Emission | 7 |
| 2.2.1 | Synchrotron radiation | 8 |
| 2.2.2 | Compton scattering | 13 |
| 2.3 | Astrophysical Objects with Polarized Radiation | 16 |
| 2.3.1 | Pulsar wind nebulae – the Crab Nebula | 16 |
| 2.3.2 | Black hole binaries – Cygnus X-1 | 17 |
| 2.4 | X-ray and Gamma-ray Polarimetry | 17 |
| 2.4.1 | Polarization measurements | 18 |
| 2.4.2 | Interactions sensitive to X-ray and gamma-ray polarization | 20 |
| 2.4.3 | Polarimeters using different interactions | 21 |
| 3 | Compton Camera | 27 |
| 3.1 | Principle of Compton Camera | 27 |
| 3.1.1 | Compton Kinematics | 27 |
| 3.1.2 | Angular resolution of a Compton camera | 29 |
| 3.1.3 | The effect of energy resolution | 29 |
| 3.1.4 | The effect of position resolution | 30 |
| 3.1.5 | Doppler broadening | 31 |
| 3.2 | Si/CdTe Compton camera | 33 |
| 3.2.1 | Concept | 33 |
| 3.2.2 | Si semiconductor detectors | 36 |
| 3.2.3 | CdTe semiconductor detectors | 36 |
| 3.2.4 | Prototypes of Si/CdTe Compton camera | 37 |
| 4 | The Soft Gamma-ray Detector on board <i>Hitomi</i> | 41 |
| 4.1 | The <i>Hitomi</i> Mission | 41 |
| 4.2 | Overview of the Soft Gamma-ray Detector | 42 |
| 4.3 | Components and Structure | 45 |
| 4.3.1 | Si/CdTe Compton camera | 45 |
| 4.3.2 | Si pad and CdTe pad detectors | 49 |

| | | |
|----------|--|------------|
| 4.3.3 | Front end electronics | 52 |
| 4.3.4 | Active BGO shield | 54 |
| 4.3.5 | Fine collimator | 54 |
| 5 | Calibration and Performance Study of the SGD | 57 |
| 5.1 | Experiments on Ground and in Orbit | 57 |
| 5.1.1 | On ground | 57 |
| 5.1.2 | In orbit | 58 |
| 5.2 | Energy Calibration | 60 |
| 5.2.1 | Contents of test pulse experiments | 60 |
| 5.2.2 | Calibration status | 63 |
| 5.2.3 | Software thresholds | 70 |
| 5.3 | Data analysis method | 71 |
| 5.3.1 | Event reconstruction | 71 |
| 5.3.2 | Data reductions by using flags | 74 |
| 5.3.3 | Dead time corrections | 76 |
| 5.4 | Performance of Ground-based Compton camera | 76 |
| 5.5 | Performance in orbit | 84 |
| 6 | Polarized Photon Experiments at Spring-8 | 93 |
| 6.1 | Monte Carlo Simulator | 93 |
| 6.2 | Experiment at SPring-8 | 94 |
| 6.3 | Compare to simulation | 96 |
| 6.3.1 | Si detector response | 96 |
| 6.3.2 | CdTe detector response | 99 |
| 6.3.3 | Implementation of triggering efficiency | 99 |
| 6.4 | Comparison of Compton reconstruction data | 100 |
| 6.5 | Performance as Polarimetry | 103 |
| 6.5.1 | The polarization by various rotation angles of the detector | 107 |
| 6.6 | Response of the spectrum | 107 |
| 7 | Crab Observation | 113 |
| 7.1 | Crab pulsar wind nebula | 113 |
| 7.2 | Observations | 115 |
| 7.2.1 | Crab observation | 115 |
| 7.3 | Polarization Analysis | 116 |
| 7.3.1 | parameter search method | 116 |
| 7.3.2 | Fitting Results | 117 |
| 7.4 | Discussions | 118 |
| 8 | Polarization degree of torus modeled on Crab Wind Nebula | 125 |
| 8.1 | Model of the electron flow and magnetic field of the Crab Nebula | 125 |
| 8.1.1 | Broadband spectrum | 126 |
| 8.1.2 | Simple calculation of the degree of polarization | 127 |
| 8.1.3 | MHD model by Kennel & Coroniti | 131 |

| | | |
|----------|--|------------|
| 8.1.4 | Condition at the inner boundary of the nebula | 131 |
| 8.1.5 | Propagation of the flow in the downstream | 133 |
| 8.1.6 | Particle cooling | 135 |
| 8.1.7 | Synchrotron radiation | 137 |
| 8.1.8 | Lorentz transformation of electromagnetic fields | 139 |
| 8.2 | Torus geometry | 140 |
| 8.3 | Calculation of polarization | 142 |
| 8.4 | Conclusion | 148 |
| 9 | Conclusion | 149 |

Chapter 1

Introduction

Understanding the non-thermal phenomena in the Universe is one of the key goals of modern astrophysics. The understanding extreme cosmic accelerators that can accelerate galactic and extragalactic cosmic rays up to and above 10^{12} eV energies still remain premature.

Polarimetry investigations in the X-ray and gamma-ray bands is showing to be promising at probing high-energy phenomena in the Universe. In general, polarimetry provides us with crucial information about the radiation mechanisms, as well as providing information on the structure and content of the emitting regions (Coppi et al., 2014). The only satellite instrument with significant polarization capability were the OSO-8, which was launched in 1975 and detected the Crab nebula in X-rays (Weisskopf et al., 1976), and the INTEGRAL SPI and IBIS which detected the gamma-ray polarization signal emitted by the Crab pulsar and nebulae (Dean et al., 2008, Forot et al., 2008), as well as studying other objects. However, these measurements are still in the development phase because measuring X-ray and gamma-ray polarization is more challenging compared to performing polarization measurements in the optical, infrared, or radio frequency bands.

Tremendous efforts have been made to improve the performance of highly sensitive instruments that can detect gamma-ray polarization such as the Si/CdTe Compton Camera (Takahashi et al., 2001, Takeda et al., 2009, Watanabe et al., 2006). Various prototypes of these devices that combine layers of Si and CdTe double sided detectors have been developed.

The Soft Gamma-ray Detector (SGD), which was onboard the sixth Japanese X-ray Observatory ASTRO-H (Hitomi), is based on the concept of a Si/CdTe Compton camera with a narrow FOV active collimator in order to reduce the background noise coming from both the outside of FOV and from the activation of gamma-rays inside the detector itself (Tajima et al., 2010, Watanabe et al., 2014). Extensive tests were performed using a prototype detector (Uchida, 2015). The SGD was designed not only for spectroscopy but also for high-precision polarimetry by measuring Compton scattering in the detector system. A beam test of the final-prototype of an SGD Compton camera was developed to demonstrate its polarimetric capability and to verify and calibrate the Monte Carlo simulation of the instrument. The modulation factor of the SGD prototype camera was measured to be 0.5–0.75 (at 194.5 keV) at varying polarization angles with respect to the detector. The relative systematic uncertainty of the modulation factor was as small as $\sim 3\%$ (Katsuta et al., 2016).

SGD covered an energy range of 60–600 keV with a sensitivity at 300 keV. Unfortunately, after a successfully start-up operation, the satellite lost contact with the mission control. During

the start-up operation of the SGD, we pointed the detector at the Crab Nebula and succeeded to detect signals. In this thesis, we utilize the data obtained from this observation. In spite of a very short exposure time, we have succeeded in observing the Crab Nebula and extracted polarization information of the emitted radiation (Hitomi Collaboration et al., 2018).

The star that exploded which created the Crab nebula was observed by ancient astronomers in 1054. In the center of the Crab nebula lies a neutron star, which rotates with a high angular velocity. The neutron star in the Crab Nebula is classified as a pulsar, and its pulsation is observed in multi wavelength. Like all isolated pulsars, observations show that the rotation of the Crab pulsar is slowing down over time. It is also observed that due to the pulsar winds, electrons are accelerated and interact with the magnetic field and emit synchrotron photons.

Polarimetric observations of synchrotron photons in X-ray and gamma-ray are particularly important as these high energy photons carry information regarding the high energy end of the electron velocity distribution. Because of the energy-dependent electron-cooling time, high energy electrons that are responsible for the emission of X-rays and gamma-rays cool down more rapidly. Therefore, X-ray and gamma-ray polarization gives us a very important clues to an understanding of the geometry of the acceleration sites.

The emission intensity depends on the magnetic field and the electron energy distribution, and the degree of polarization depends on the geometry of the magnetic field and spatial distribution of high-energy electrons. To study the polarimetric properties of the observational data, a detailed model for the synchrotron radiation using a magnetohydrodynamic (MHD) model to describe the structure of the nebula and by accounting for relativistic transformation of emission and polarization has to be developed.

In this thesis, we study the performance of the SGD as a spectrometer and a polarimeter in hard X-ray and gamma-ray range. Chapter 2 reviews the polarization mechanism in astrophysical radiation and detection techniques of polarization. In Chapter 3, we introduce Compton cameras and the Si/CdTe Compton Camera which is the base concept of the SGD. In Chapter 4, we describe the system of the SGD. In Chapter 5 and 6, we study the performance of the Compton camera modules in the SGD based on the data we obtained in the laboratory and also at the SPring-8 synchrotron facility. In Chapter 7, we report the polarization detection from the radiation of the Crab Nebula. In Chapter 8, we introduce a new analytical calculation to study polarization degrees in pulsar wind nebulae. The observational results of X-ray and gamma-ray polarization in the Crab Nebula at different energies are compared with results from the calculation.

Chapter 2

Polarization mechanisms and Polarimeters

Polarization is one of the most important phenomena in astrophysics. Light emitted from astrophysical objects is sometimes polarized, and the effect is detected by polarimeters. In this Chapter, we review mechanisms of polarized radiation in astrophysical objects including synchrotron radiation and Compton scattering. We also review astrophysical objects emitting polarized X-rays/gamma-rays, and typical polarimetry used in their observations.

2.1 Polarization

Polarization is one of fundamental nature of light. When we consider light as electromagnetic waves, the electric and magnetic field vectors are perpendicular to each other, and to the direction of light propagation. The state of polarization can be specified by oscillations of these vectors. In this section, we describe the nature of polarization based on Landau and Lifshitz (1975), and Rybicki and Lightman (1979) as references.

In classical electrodynamics, light propagation is described by a wave equation. From Maxwell equations, the electric field vector of monochromatic plane-wave light can be written by

$$\mathbf{E} = \text{Re} \{ \mathbf{E}_0 e^{i(\mathbf{k} \cdot \mathbf{r} - \omega t)} \}, \quad (2.1)$$

where \mathbf{E}_0 is a complex vector, \mathbf{k} is a wave number vector, \mathbf{r} is the position vector, ω is the angular frequency and t is time. Let us choose z -axis as the direction of wave propagation, and examine the electric vector at $\mathbf{r} = 0$. Then, denoting the unit vectors along x -axis and y -axis as $\hat{\mathbf{x}}$ and $\hat{\mathbf{y}}$, respectively, the oscillation in the (x, y) plane is described as

$$\mathbf{E} = \text{Re} \{ (E_{0x} \hat{\mathbf{x}} + E_{0y} \hat{\mathbf{y}}) e^{-i\omega t} \}, \quad (2.2)$$

where E_{0x} and E_{0y} are complex amplitudes because \mathbf{E}_0 is a complex vector. These amplitudes can be expressed with phases φ_x and φ_y , respectively, as

$$E_{0x} = |E_{0x}| e^{i\varphi_x}, \quad E_{0y} = |E_{0y}| e^{i\varphi_y}. \quad (2.3)$$

Equation (2.2) is rewritten as

$$\begin{aligned} \mathbf{E} &= \text{Re} \{ (|E_{0x}|e^{i\varphi_x}\hat{\mathbf{x}} + |E_{0y}|e^{i\varphi_y}\hat{\mathbf{y}})e^{-i\omega t} \} \\ &= |E_{0x}|(\cos \omega t \cos \varphi_x + \sin \omega t \sin \varphi_x)\hat{\mathbf{x}} + |E_{0y}|(\cos \omega t \cos \varphi_y + \sin \omega t \sin \varphi_y)\hat{\mathbf{y}} \\ &= E_x\hat{\mathbf{x}} + E_y\hat{\mathbf{y}}, \end{aligned} \quad (2.4)$$

where

$$\begin{aligned} E_x &= |E_{0x}|(\cos \omega t \cos \varphi_x + \sin \omega t \sin \varphi_x), \\ E_y &= |E_{0y}|(\cos \omega t \cos \varphi_y + \sin \omega t \sin \varphi_y). \end{aligned} \quad (2.5)$$

By eliminating the time dependent factors in these equations, we obtain

$$\frac{E_x^2}{|E_{0x}|^2} + \frac{E_y^2}{|E_{0y}|^2} - 2\frac{E_x}{|E_{0x}|}\frac{E_y}{|E_{0y}|}\cos \varphi = \sin^2 \varphi, \quad (2.6)$$

where $\varphi = \varphi_y - \varphi_x$ is a phase difference. The shape of the trajectory of Equation (2.6), depending on φ , $|E_{0x}|$, and $|E_{0y}|$, can be classified into the following three cases.

CASE 1 : Elliptical Polarization

The light is generally said to be elliptically polarized, because Equation (2.6) describes an ellipse on the (x, y) plane, as illustrated in Figure 2.1. The sign of φ specifies the sense of motion of \mathbf{E} around the z -axis. When $\varphi > 0$, it is counterclockwise, and, when $\varphi < 0$, it is clockwise.

CASE 2 : Linear Polarization

If the phase difference is $\varphi = 0$, the light is said to be linearly polarized, because the trajectory becomes a line segment, which makes an angle of χ to the x -axis (Figure 2.1).

CASE 3 : Circular Polarization

When the phase difference is $\varphi = \pm\pi/2$ and $|E_{0x}| = |E_{0y}| \neq 0$, the light is said to be circularly polarized, because Equation (2.6) becomes a circle in this case. When $\varphi = \pi/2$, the light is left hand circularly polarized. On the other hand, when $\varphi = -\pi/2$, the light is right hand circularly polarized.

2.1.1 Stokes parameters

As in Equation (2.6), the polarization of a monochromatic plane wave can be specified by three free parameters; $|E_{0x}|$, $|E_{0y}|$ and φ . Alternatively, we may use four characteristic parameters introduced by Sir George Stokes in 1852, called Stokes parameters, which provide a very convenient representation of polarized light. Although the Stokes parameters can describe incoherent superposition of waves of different polarizations, we first describe them for monochromatic plane waves, referring to Chandrasekhar (1960) and Rybicki and Lightman (1979).

We think of the ellipse described in Figure 2.1 whose principal axes are tilted at an angle χ to the x - and y -axes. Let us denote the major and minor axes of the ellipse as x' and y' , respectively. Then, the trajectory along the ellipse can be readily expressed as

$$E_{x'} = E_0 \cos \beta \cos \omega t, \quad E_{y'} = -E_0 \sin \beta \sin \omega t, \quad (2.7)$$

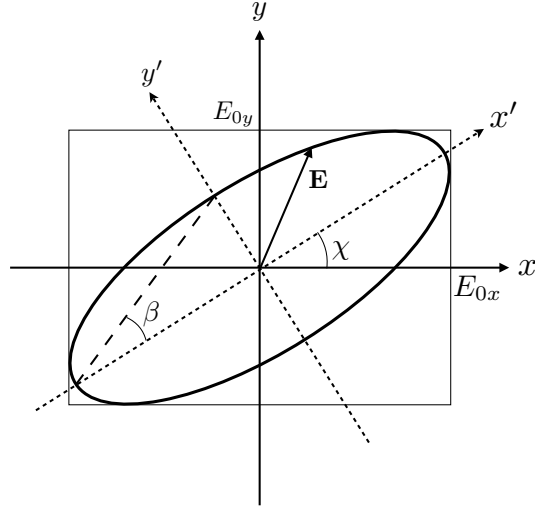


Figure 2.1: The ellipse of polarization at $z = 0$, where β is the ellipticity.

where $E_0 = \sqrt{|E_{0x}|^2 + |E_{0y}|^2}$, and β is ellipticity given by the ratio between the major and minor axes of the ellipse.

We attempt to make connections between Equations (2.5) and (2.7). If we rotate the principal axes of the ellipse to x - and y -axes with an angle χ , E_x and E_y can be given by

$$\begin{aligned} E_x &= E_0(\cos \beta \cos \chi \cos \omega t + \sin \beta \sin \chi \sin \omega t), \\ E_y &= E_0(\cos \beta \sin \chi \cos \omega t - \sin \beta \cos \chi \sin \omega t). \end{aligned} \quad (2.8)$$

A comparison of these equations with Equation (2.5) yields

$$\begin{aligned} |E_{0x}| \cos \varphi_x &= E_0 \cos \beta \cos \chi, & |E_{0x}| \sin \varphi_x &= E_0 \sin \beta \sin \chi, \\ |E_{0y}| \cos \varphi_y &= E_0 \cos \beta \sin \chi, & |E_{0y}| \sin \varphi_y &= -E_0 \sin \beta \cos \chi. \end{aligned} \quad (2.9)$$

As a result, E_{0x} , E_{0y} and φ can be expressed by E_0 , χ and β as

$$\begin{aligned} |E_{0x}|^2 &= E_0^2 (\cos^2 \beta \cos^2 \chi + \sin^2 \beta \sin^2 \chi), \\ |E_{0y}|^2 &= E_0^2 (\cos^2 \beta \sin^2 \chi + \sin^2 \beta \cos^2 \chi), \\ 2|E_{0x}||E_{0y}| \cos \varphi &= E_0^2 \cos 2\beta \sin 2\chi, \\ 2|E_{0x}||E_{0y}| \sin \varphi &= E_0^2 \sin 2\beta. \end{aligned} \quad (2.10)$$

Using equations (2.10), the four Stokes parameters are defined as

$$I \equiv |E_{0x}|^2 + |E_{0y}|^2 = E_0^2, \quad (2.11)$$

$$Q \equiv |E_{0x}|^2 - |E_{0y}|^2 = E_0^2 \cos 2\beta \cos 2\chi, \quad (2.12)$$

$$U \equiv 2|E_{0x}||E_{0y}| \cos \varphi = E_0^2 \cos 2\beta \sin 2\chi, \quad (2.13)$$

$$V \equiv 2|E_{0x}||E_{0y}| \sin \varphi = E_0^2 \sin 2\beta. \quad (2.14)$$

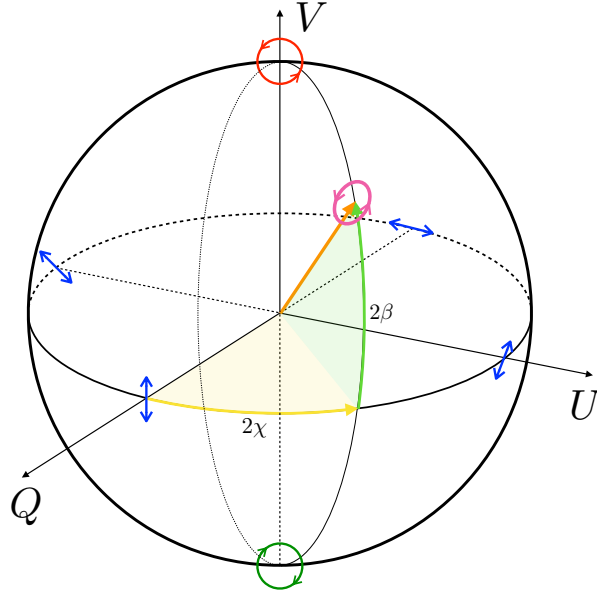


Figure 2.2: A Poincaré sphere expressed by three Stokes parameters, Q , U , and V . The radius equals to the first Stokes parameter, I . Thus, the Poincaré sphere can visualize the Stokes parameters.

These equations can be reversed to express E_0 , β and χ by the Stokes parameters as

$$E_0 = \sqrt{I}, \quad \sin 2\beta = \frac{V}{I}, \quad \tan 2\chi = \frac{U}{Q}. \quad (2.15)$$

Thus, for a monochromatic plane wave, the four Stokes parameters are not independent, because they satisfy a relation

$$I^2 = Q^2 + U^2 + V^2. \quad (2.16)$$

According to Equation (2.15), the state of the polarization can be described as a point on the 3-dimensional sphere, known as the Poincaré sphere shown in Figure 2.2. The sphere is expressed by axes of three Stokes parameters, Q , U , and V , and the radius equal to the first Stokes parameter I of Equation (2.16). On the equatorial circle on the Q - U plane, the light is linearly polarized, at the north or the south pole it is left- or right-hand circular polarized, and on the other positions on the surface it is elliptically polarized. Thus, the polarization status of monochromatic plane wave is specified by the position on this spherical surface. More specifically, if we obtain the ellipticity β , the angle of the polarization χ and the intensity of the radiation, then we can determine the specific polarization state.

Natural light is an incoherent mixture of electromagnetic waves of different elliptically polarizations. Then, the Stokes parameters are sum of these of each electromagnetic wave, and

are given by

$$\begin{aligned}
 I &= \sum_m I^{(m)}, \\
 Q &= \sum_m Q^{(m)} = \sum_m I^{(m)} \cos 2\beta_m \cos 2\chi_m, \\
 U &= \sum_m U^{(m)} = \sum_m I^{(m)} \cos 2\beta_m \sin 2\chi_m, \\
 V &= \sum_m V^{(m)} = \sum_m I^{(m)} \sin 2\beta_m,
 \end{aligned}
 \tag{2.17}$$

where an integer m indicates the component waves. Then, Equation (2.16) becomes

$$I^2 \geq Q^2 + U^2 + V^2 \tag{2.18}$$

as described, e.g., in Chandrasekhar (1960) and Rybicki and Lightman (1979).

Compared to the triplet (E_{0x}, E_{0y}, ϕ) or (E_0, β, χ) , the clear advantage of the Stokes parameters is that they can describe incoherent mixtures of polarized plane waves, as clearly shown by Equations (2.17) and (2.18). Therefore, in terms of them, we can decompose any radiations into polarized and unpolarized parts as

$$\begin{bmatrix} I \\ Q \\ U \\ V \end{bmatrix} = \begin{bmatrix} I - \sqrt{Q^2 + U^2 + V^2} \\ 0 \\ 0 \\ 0 \end{bmatrix} + \begin{bmatrix} \sqrt{Q^2 + U^2 + V^2} \\ Q \\ U \\ V \end{bmatrix}. \tag{2.19}$$

Then the degree of polarization is defined by the ratio of total intensity to the polarized intensity as

$$\Pi = \frac{I_{\text{pol}}}{I} = \frac{\sqrt{Q^2 + U^2 + V^2}}{I}. \tag{2.20}$$

Similarly, the Poincaré sphere (Figure 2.2) can express both the perfectly polarized light ($\Pi = 1$) and partially polarized one ($\Pi < 1$). The former falls on the surface of the sphere, whereas the latter occupies its interior.

2.2 Polarized Emission

In astrophysics, the information of polarized radiation reflects some anisotropy, or deviations from spherical symmetry, that resides in the emission mechanism, the source geometry, or the process of radiation transfer. These include, e.g., magnetic fields, beaming of electrons, and non-spherical (particularly disk-like) shape of scattering media. Because these anisotropic effects are usually stronger in non-thermal processes than in thermal radiation, the study of polarized radiation is considered to provide an important tool in high energy astrophysics. In X-ray and gamma-ray bands, synchrotron radiation and Compton scattering are important processes which involve photon polarization. Below, we review polarization mechanisms in these two processes.

2.2.1 Synchrotron radiation

Charged particles emit radiation if acceleration is not zero. Thus, when charged particles move in magnetic fields, and the motion is not parallel to the fields, they have non-zero acceleration and must emit radiation. If the particles are relativistic, the radiation is known as synchrotron radiation or magnetobremstrahlung. The theory of synchrotron radiation is presented in several articles and books, e.g., Ginzburg and Syrovatskii (1965), Rybicki and Lightman (1979) and Longair (2011). We follow the description mainly of Rybicki and Lightman (1979).

A motion of a single electron in a magnetic field

Let us consider a particle of mass m , charge q , and Lorentz factor γ , moving in a uniform magnetic field B . When the motion is not parallel to the fields, the particle gyrates around the fields by Lorentz force. Then, the particle velocity is $v = c\sqrt{1 - 1/\gamma^2}$, the angular frequency of gyration is

$$\omega_B = \frac{qB}{\gamma mc}, \quad (2.21)$$

where c is the speed of light, so that the acceleration is $\mathbf{a} = \mathbf{v}_\perp \omega_B$, where v_\perp is the velocity normal to the field.

The synchrotron radiation is emitted in the direction of particle motion. If the particle is non-relativistic, the radiation, known as cyclotron radiation, is dipole radiation. Although synchrotron radiation is dipole radiation in the particle's instantaneous rest frame, the radiation, when is transformed into the laboratory frame, is beamed because of a Doppler effect in the direction of electron's motion within an angle $2/\gamma$. In other words, synchrotron radiation makes a radiation cone with an angle $2/\gamma$. An observer will see electromagnetic field which vary periodically with an angle frequency ω_B . If $\gamma \sim 1$, this variation is approximately sinusoidal, so the emitted spectrum peaks at an angular frequency $\omega \sim \omega_B$. However, if $\gamma \gg 1$, the variation is no longer sinusoidal, and the observed fields consist of a train of sharp pulses with an interval of $2\pi/\omega_B$. As a result, the radiation spectrum becomes dominated by higher harmonics of ω_B . The most dominant harmonics appear at a characteristic angular frequency ω_c , given as

$$\omega_c = \frac{3}{2}\gamma^3\omega_B \sin \alpha \propto \gamma^2 B \sin \alpha, \quad (2.22)$$

where α is a pitch angle between the magnetic field vector and the velocity vector of the particle.

Synchrotron spectrum of an accelerated particle

Radiation from an accelerated particle can be given by calculation of Liénard-Wiechert potential. According to Rybicki and Lightman (1979), the emitted by unit frequency per unit solid angle is expressed as

$$\frac{dW}{d\omega d\Omega} = \frac{q^2 \omega^2}{4\pi^2 c} \left| \int \mathbf{n} \times (\mathbf{n} \times \boldsymbol{\beta}) \exp [i\omega (t - \mathbf{n} \cdot \mathbf{r}(t)/c)] dt \right|^2, \quad (2.23)$$

where ω is the observed angular frequency, \mathbf{n} is the observer direction, $\boldsymbol{\beta} = \mathbf{v}/c$ is velocity of the particle, and $\mathbf{r}(t)$ is a particle position at an arbitrary time t .

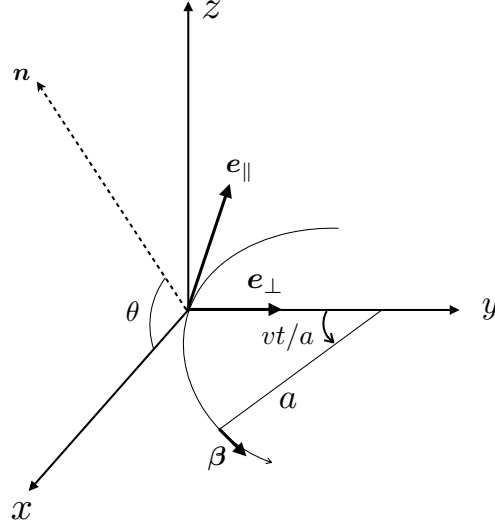


Figure 2.3: A trajectory of a particle moving in uniform magnetic field in the z direction. The particle is at the coordinate origin at $t = 0$. The observer is in the x - z plane, and its direction \vec{n} makes an angle θ to the x -axis. The unit vector \mathbf{e}_\perp is along the y -axis, and parallel to $\mathbf{n} \times \boldsymbol{\beta}$ at $t = 0$. The other unit vector \mathbf{e}_\parallel is perpendicular to the y -axis and \mathbf{n} . a is the curvature of helical motion of the particle.

We consider a particle trajectory as shown in Figure 2.3. Equation (2.23) can be divided into two components. One is along y -axis which is the same direction as the acceleration vector, and the other is perpendicular to the observer direction and y -axis. We express unit vectors parallel to y -axis as \mathbf{e}_\parallel ($\parallel \mathbf{n} \times \boldsymbol{\beta}$) and that perpendicular to the y -axis and the observer direction \mathbf{e}_\perp ($\parallel \mathbf{n} \times \mathbf{e}_\parallel$). After complex calculations in Rybicki and Lightman (1979), Equation (2.23) is expanded to

$$\frac{dW}{d\omega d\Omega} \equiv \frac{dW_\parallel}{d\omega d\Omega} + \frac{dW_\perp}{d\omega d\Omega}, \quad (2.24a)$$

$$\frac{dW_\parallel}{d\omega d\Omega} = \frac{q^2 \omega^2}{4\pi^2 c} \left| \int \frac{ct}{a} \exp \left[\frac{i\omega}{2\gamma^2} \left(\theta_\gamma^2 t + \frac{c^2 \gamma^2 t^3}{3a^2} \right) \right] dt \right|^2, \quad (2.24b)$$

$$\frac{dW_\perp}{d\omega d\Omega} = \frac{q^2 \omega^2 \theta^2}{4\pi^2 c} \left| \int \exp \left[\frac{i\omega}{2\gamma^2} \left(\theta_\gamma^2 t + \frac{c^2 \gamma^2 t^3}{3a^2} \right) \right] dt \right|^2, \quad (2.24c)$$

where a is the radius of curvature of the trajectory and $\theta_\gamma^2 \equiv 1 + \gamma^2 \theta^2$. Since the radiation cone is limited to $|\theta| \leq \gamma^{-1}$, the element of solid angle is

$$d\Omega = 2\pi \sin \alpha d\theta. \quad (2.25)$$

As a result of integration, we obtain the radiation emissivities as

$$\frac{dW_{\parallel}}{d\omega} = \frac{\sqrt{3}q^2\gamma \sin \alpha}{2c} [F(x) - G(x)], \quad (2.26a)$$

$$\frac{dW_{\perp}}{d\omega} = \frac{\sqrt{3}q^2\gamma \sin \alpha}{2c} [F(x) + G(x)], \quad (2.26b)$$

where

$$F(x) \equiv x \int_x^{\infty} K_{\frac{5}{3}}(\xi) d\xi, \quad G(x) \equiv x K_{\frac{2}{3}}(x). \quad (2.27)$$

Here, $x \equiv \omega/\omega_c$ is normalized frequency, and $K_{\frac{5}{3}}(\xi)$ is a modified Bessel function.

The radiation power emitted per unit frequency is obtained when we divide Equation (2.26) by the orbital period of the particle, $T = 2\pi/\omega_B$, as

$$P_{\parallel}(\omega) = \frac{\sqrt{3}q^3 B \sin \alpha}{4\pi mc^2} [F(x) - G(x)], \quad (2.28a)$$

$$P_{\perp}(\omega) = \frac{\sqrt{3}q^3 B \sin \alpha}{4\pi mc^2} [F(x) + G(x)]. \quad (2.28b)$$

Therefore, the total emitted power per frequency is expressed as

$$P(\omega) = P_{\perp}(\omega) + P_{\parallel}(\omega) = \frac{\sqrt{3}q^3 B \sin \alpha}{2\pi mc^2} F(x). \quad (2.29)$$

As shown in Figure 2.4, the shape of the spectrum of synchrotron radiation is determined by the function $F(x)$. Thus, the spectrum from a particle has a broad distribution peaked at $\omega \lesssim \omega_c$ of Equation (2.22), or $x \lesssim 1$, because a large number of higher harmonics of ω_B can no longer be separated individually. As clear from Equation (2.22), the frequency of the spectrum peak scaled as $\propto \gamma^2 B$.

For an ensemble of electrons, the total synchrotron radiation power is a super-position of the radiation of each electron. When the electron energy distribution is $N(E)dE$, where $N(E)$ is the number of electrons within $E \sim E + dE$, we convolve Equation (2.29) with $N(E)$ and integrate over the electron energy, to obtain

$$P_{\text{tot}}(\omega) = \int P(\omega) N(E) dE, \quad (2.30)$$

which can be regarded as the intensity of the radiation, I .

Charged particles with a power-law energy distribution

An important case for various practical applications is realized when the particles obey a power-law energy distribution expressed as

$$N(E)dE = K E^{-p} dE, \quad (2.31)$$

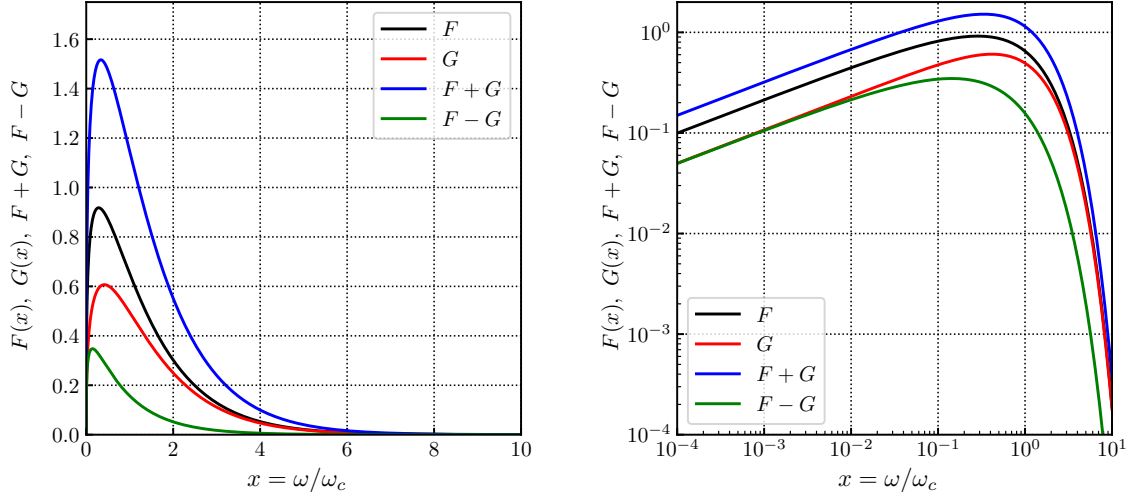


Figure 2.4: Functional shapes of $F(x)$ (black solid line), $G(x)$ (red solid line), $F + G$ (blue solid line) and $F - G$ (green solid line). Left panel is a linear plot, and right panel is logarithmic.

where p is a positive constant. Then, the total power per unit frequency of synchrotron radiation is obtained as

$$P_{\text{tot}}(\omega) = K \int_{E_1}^{E_2} P(\omega) E^{-p} dE \propto \int_{E_1}^{E_2} F(x) E^{-p} dE. \quad (2.32)$$

Using Equation (2.22) which means $x \propto \gamma^{-2} \propto E^{-2}$, Equation (2.32) can be rewritten as

$$P_{\text{tot}}(\omega) \propto \omega^{-(p-1)/2} \int_{x_1}^{x_2} F(x) x^{(p-3)/2} dx. \quad (2.33)$$

In the case of $x_1 \approx 0$ and $x_2 \approx \infty$, the integration become approximately constant. Therefore, the total power per unit frequency becomes proportional to $\omega^{-(p-1)/2}$. Thus, the emitted synchrotron photons also obey a power-law distribution. The power-law index of ω , called spectral index, can be expressed as

$$s = \frac{p-1}{2}. \quad (2.34)$$

The total radiation power can be written as

$$P_{\text{tot}} = \frac{\sqrt{3}q^3 B \sin \alpha}{2\pi m c^2 (p+1)} \Gamma\left(\frac{p}{4} + \frac{19}{12}\right) \Gamma\left(\frac{p}{4} - \frac{1}{12}\right) \left(\frac{m c \omega}{3qB \sin \alpha}\right)^{-(p-1)/2}, \quad (2.35)$$

where Γ is a gamma function.

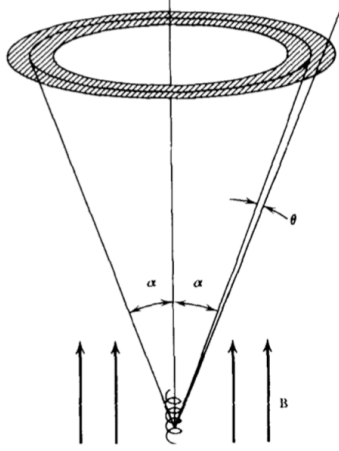


Figure 2.5: A schematics of synchrotron radiation, with pitch angle α . The radiation is only within minute angle θ (adopted from Rybicki and Lightman, 1979).

Polarization

Synchrotron radiation from a single charged particle is elliptically polarized. The electric field of the radiation is oscillating along a direction parallel to \mathbf{e}_{\parallel} . The direction corresponds to the particles' acceleration vector \mathbf{a} , which is parallel to $\mathbf{v} \times \mathbf{B}$. In the plane normal to the wave vector \mathbf{k} , the projected magnetic field \mathbf{B}_{proj} is parallel to \mathbf{e}_{\perp} . Then, the major axis of the ellipse of polarization lies on \mathbf{e}_{\parallel} . We recall that radiation of a single relativistic electron is beaming in the angle $\theta \sim \gamma^{-1}$. In addition, Equation (2.24) show that the polarization depends on θ . Then the radiation towards the inner and outer regions (the shadow area shown in Figure 2.5) of radiation cone are left- and right-elliptically polarized, respectively, and that towards $\theta = 0$ is linearly polarized (Ginzburg and Syrovatskii, 1965, Rybicki and Lightman, 1979).

In practice, the particles must have a certain distribution in α . Then, for an observer, the radiation from particles with $\alpha + \delta$ and $\theta - \delta$ (with δ being a small angle) and from these with $\alpha - \delta$ and $\theta + \delta$ would have the 4th Stokes parameter V with the opposite signs. As a result, the elliptical components are canceled. Therefore, the radiation become partially linear polarized. The polarization degree is written, in terms of the powers of the parallel and perpendicular components, as

$$\Pi(\omega) = \frac{P_{\perp}(\omega) - P_{\parallel}(\omega)}{P_{\perp}(\omega) + P_{\parallel}(\omega)} = \frac{G(x)}{F(x)}. \quad (2.36)$$

When the electrons are power-law distributed, this Π can be expressed by only p of Equation (2.31) as

$$\Pi = \frac{p + 1}{p + \frac{7}{3}}. \quad (2.37)$$

This relation can be interpreted in a simple physical way. When p is high (i.e., the electron spectrum is steep), the radiation spectrum observed at a particular frequency ω would be

dominated by contributions from those electrons which have slightly lower γ but slightly higher x . Such radiation has a higher value of $\Pi = G(x)/F(x)$, because this ratio approaches unity towards $x \gg 1$ as seen from Figure 2.3. For typical cases of $p = 2.0$ ($s = 0.5$) and $p = 3$ ($s = 1$), we expect $\Pi = 0.69$ and $\Pi = 0.75$, respectively.

Assuming the configuration of Figure 2.3, the Stokes parameters for synchrotron radiation are given as

$$I \equiv P_{\perp} + P_{\parallel}, \quad (2.38)$$

$$Q \equiv (P_{\perp} - P_{\parallel}) \cos 2\chi, \quad (2.39)$$

$$U \equiv (P_{\perp} - P_{\parallel}) \sin 2\chi, \quad (2.40)$$

$$V \equiv 0, \quad (2.41)$$

where the first equation implicates the total intensity. Then, the polarization degree is given by

$$\Pi = \frac{\sqrt{Q^2 + U^2 + V^2}}{I} = \frac{P_{\perp} - P_{\parallel}}{P_{\perp} + P_{\parallel}}. \quad (2.42)$$

which is equal to Equation (2.36).

For an ensemble of electrons, the Stokes parameters can be written by using electron energy distribution $N(E)$, as

$$I_{\text{tot}} = \int (P_{\perp} + P_{\parallel}) N(E) dE, \quad (2.43)$$

$$Q_{\text{tot}} = \int (P_{\perp} - P_{\parallel}) N(E) dE \times \cos 2\chi, \quad (2.44)$$

$$U_{\text{tot}} = \int (P_{\perp} - P_{\parallel}) N(E) dE \times \sin 2\chi, \quad (2.45)$$

$$V_{\text{tot}} = 0. \quad (2.46)$$

Then, the expression of the degree of polarization is the same as Equation (2.42). Note that the angle of polarization χ does not depend on the electron energy.

2.2.2 Compton scattering

Compton scattering is one of the most basic interactions between a photon and a free electron. When a photon collides with a free electron at rest, the photon transfers a portion of its energy to the electron, and is scattered into a new direction. Even when the electron is bound to a nucleus, it can be regarded as a free electron if the incident photon energy is much higher than the electron's binding energy.

Cross section of Compton scattering

Unlike synchrotron radiation, we detect secondary photons in Compton scattering. The cross section of this process depends on the polarization of the primary photon (Lei et al., 1997).

The differential cross section of Compton scattering is described by the Klein-Nishina formula, which is derived from quantum electrodynamics as explained in many books and articles. Below, we review the Klein-Nishina formula after Heitler (1954). If the incident radiation is linearly polarized, the differential cross section of Compton scattering is given by

$$\frac{d\sigma}{d\Omega} = \frac{r_0^2}{4} \left(\frac{E'_\gamma}{E_\gamma} \right)^2 \left(\frac{E'_\gamma}{E_\gamma} + \frac{E_\gamma}{E'_\gamma} - 2 + 4 \cos^2 \Theta \right), \quad (2.47)$$

where Θ is the angle between the electric vectors of the incident and scattered photons.

Equation (2.47) can be decomposed into components for which the electric vector of the scattered radiation is parallel and perpendicular to the electric field \mathbf{e}_0 of the incident radiation, as

$$\left(\frac{d\sigma}{d\Omega} \right)_\parallel = \frac{r_0^2}{4} \left(\frac{E'_\gamma}{E_\gamma} \right)^2 \left(\frac{E'_\gamma}{E_\gamma} + \frac{E_\gamma}{E'_\gamma} + 2 - 4 \sin^2 \theta \cos^2 \varphi \right), \quad (2.48)$$

$$\left(\frac{d\sigma}{d\Omega} \right)_\perp = \frac{r_0^2}{4} \left(\frac{E'_\gamma}{E_\gamma} \right)^2 \left(\frac{E'_\gamma}{E_\gamma} + \frac{E_\gamma}{E'_\gamma} - 2 \right), \quad (2.49)$$

where θ is the scattering angle between the incident and scattered photons, and φ is azimuthal angle of scattering. Then, Equation (2.47) can be rewritten as

$$\frac{d\sigma}{d\Omega} = \left(\frac{d\sigma}{d\Omega} \right)_\parallel + \left(\frac{d\sigma}{d\Omega} \right)_\perp = \frac{r_0^2}{4} \left(\frac{E'_\gamma}{E_\gamma} \right)^2 \left(\frac{E'_\gamma}{E_\gamma} + \frac{E_\gamma}{E'_\gamma} - 2 \sin^2 \theta \cos^2 \varphi \right). \quad (2.50)$$

For incident unpolarized radiation, it should be averaged over φ , to become

$$\frac{d\sigma}{d\Omega} = \frac{r_0^2}{2} \left(\frac{E'_\gamma}{E_\gamma} \right)^2 \left(\frac{E'_\gamma}{E_\gamma} + \frac{E_\gamma}{E'_\gamma} - \sin^2 \theta \right). \quad (2.51)$$

The differential cross section of Equation (2.51) is depicted in Figure 2.6, which shows that forward scattering ($\theta \sim 0$) dominates the Compton scattering when the incident photon energy becomes higher than $m_e c^2$.

Thomson scattering

In the low energy limit, $E_\gamma/m_e c^2 \ll 1$, the Compton scattering process reduces to Thomson scattering. Since Thomson scattering is non-relativistic, the photon conserves its energy through the scattering. Therefore, the differential cross section (2.51) is rewritten, with $E_\gamma \simeq E'_\gamma$, as

$$\frac{d\sigma}{d\Omega} = \frac{r_0^2}{2} (1 + \cos^2 \theta). \quad (2.52)$$

The total cross section, called Thomson cross section, is expressed as

$$\sigma_T = \frac{8\pi}{3} r_0^2. \quad (2.53)$$

It does not depend on the incident photon energy.

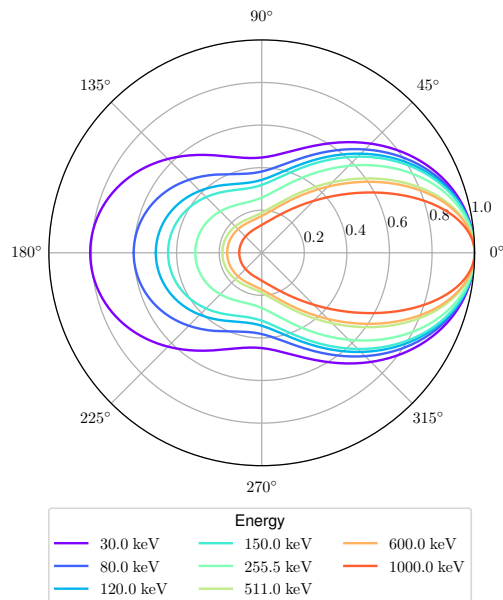


Figure 2.6: The Klein-Nishina differential cross section of Equation (2.51), assuming $\varphi = 0$, shown as a function of θ , for a range of incident photon energies.

Polarization

Since the differential cross section of Equation (2.48) depends on φ , the polarization properties of radiation changes through Compton scattering. In particular, the scattered radiation generally becomes polarized to some extent, even when the incident radiation is unpolarized. In evaluating the polarization by Compton scattering, we only need to consider unpolarized and polarized situations.

When the incident radiation is unpolarized, the degree of polarization of Compton scattered radiation is given by

$$\Pi = \frac{I_{\perp} - I_{\parallel}}{I_{\perp} + I_{\parallel}}, \quad (2.54)$$

where I_0 is the incident radiation intensity, while I_{\perp} and I_{\parallel} are given as

$$I_{\perp} = I_0 \left(\frac{d\sigma}{d\Omega} \right)_{\perp}, \quad I_{\parallel} = I_0 \left(\frac{d\sigma}{d\Omega} \right)_{\parallel}. \quad (2.55)$$

Substituting Equation (2.48) and (2.49), we obtain

$$\Pi = \frac{\sin^2 \theta}{\frac{E'_{\gamma}}{E_{\gamma}} + \frac{E_{\gamma}}{E'_{\gamma}} - \sin^2 \theta}. \quad (2.56)$$

In the Thomson limit, this equation reduces to

$$\Pi = \frac{\sin^2 \theta}{(1 + \cos^2 \theta)}. \quad (2.57)$$

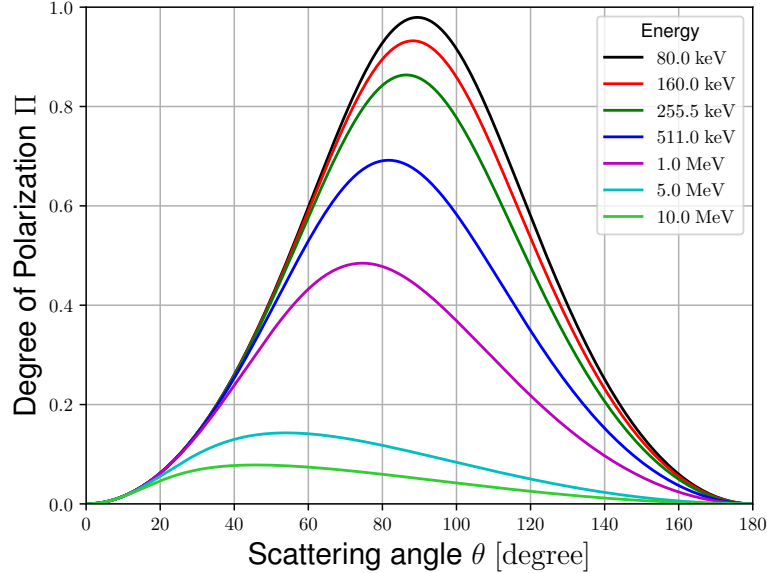


Figure 2.7: The degree of linear polarization of Compton scattered photons as a function of the scattering angle θ .

Equation (2.56) is shown in Figure 2.7 as a function of θ for several photon energies. Thus, in the Thomson limit, a strong polarization can be produced by $\theta \sim 90^\circ$ scattering of unpolarized radiation. In these cases, the scattering occurs mainly in the azimuths of $\phi \sim 0$ or $\phi \sim \pi$, and the outgoing photons are polarized nearly in the same direction as the incident ones.

2.3 Astrophysical Objects with Polarized Radiation

In high energy astrophysics, polarization provides important information to understand the emission mechanisms and the emitting objects. For example, if strong X-ray/gamma-ray polarization is detected from a non-thermal emitter, we can confirm that the emission is due to synchrotron process, and can estimate the magnetic field configure. In addition, detection of non-zero polarization in Compton scattered radiation can tell us the geometry of the source, including in particular its deviation from a spherical symmetry.

2.3.1 Pulsar wind nebulae – the Crab Nebula

A pulsar is a fast rotating neutron star with strong magnetic fields. A pulsar produces outflows consisting of relativistic particles (electrons and positrons) and magnetic fields, which are called pulsar winds. Pulsar wind nebulae radiate synchrotron radiation by the relativistic electrons in the wind. By observing polarization of these X-rays, we can estimate the magnetic field structure of the nebula.

The Crab Nebula, known to have been born in 1054 through a supernova explosion, is a textbook-case object of pulsar wind nebula (see a review of e.g. Zanin, 2017). The nebula emits

in extremely broad frequency, ranging from radio to gamma-ray frequencies. X-ray imaging observations (e.g. Brinkmann et al., 1985, Pelling et al., 1987, Weisskopf et al., 2000a) revealed that the synchrotron emission has a toroidal-shaped morphology around the central pulsar. The Crab Nebula is the first celestial object polarization measurement. In X-ray band, the Graphite Crystal X-ray Spectrometer (see §2.4.3) on board OSO-8 succeeded to detect the polarization at 2.6 keV and 5.2 keV, with a polarization degree of $19.2 \pm 1.0\%$ and $19.5 \pm 2.8\%$, respectively (Weisskopf et al., 1976). The position angle of polarization was $156^\circ \pm 1.4^\circ$ at 2.6 keV, whereas $152.6^\circ \pm 4.0^\circ$ at 5.2 keV. In the gamma-ray band, INTEGRAL SPI and IBIS observed and derived the polarization degree as $128 \pm 6\%$ at 130–440 keV, and 47% at 200–800 keV (Chauvin et al., 2013, Forot et al., 2008).

2.3.2 Black hole binaries – Cygnus X-1

When a black hole is in a binary system with a stellar companion, matter flows from the companion star and accretes onto the black hole, forming an accretion disk. X-ray and gamma-ray photons are radiated from the accretion disk. Cygnus X-1 is the best studied black-hole binaries and one of the brightest X-ray sources in the sky. It is known that such black holes typically take different states depending on the rate of accretion, and the spectrum takes two states, the hard state and the soft state (see e.g. Zdziarski and Gierliński, 2004).

The X-ray properties of an accounting black hole, including polarization, depend on the spectral state (Kamae et al., 2008). In the hard state, an inner part of the accretion disk turns into a geometrically-thick and optically-thin flow, and hot electrons in this flow inverse-Compton scatters soft X-rays from the outer accretion disk. As a result, the spectrum becomes very hard, and extends to ~ 100 keV. In the soft state, which is realized at high accretion rates, the hot-flow region seen in the hard state diminishes, and the accretion disk continues down to the “last stable orbit” inside which the Kepler motion becomes unstable due to general relativity. As a result, the spectrum becomes much softer, peaking at \lesssim several keV. Furthermore, these photons are Compton scattered on the accretion disk to partially polarized the X-rays (§2.2.2). When the Compton scattering occurs close to last stable orbit, the polarization parameters become energy dependent (Kamae et al., 2008). Measuring this effect will provide valuable information on general relativistic effects around a black hole.

The INTEGRAL/IBIS detected polarization from Cygnus X-1 (Laurent et al., 2011), degree of polarization is $67 \pm 30\%$ between 400 keV and 2 MeV. In the energy band from 250 to 400 keV, the degree of polarization was only 20%. A tight upper-limit on polarization from Cygnus X-1 obtained with the PoGO+ balloon experiment (§2.4.3), ruled out such general relativistic effects, and suggested that the Compton scattering is taking place at a large distance from the black hole (Chauvin et al., 2018).

2.4 X-ray and Gamma-ray Polarimetry

Although the polarization of synchrotron radiation from the Crab Nebula was detected in radio and optical bands in 1950s, the detection of its polarization in X-ray had to wait till 1976 (Weisskopf et al., 1976, §2.3.1). Since then, the research made little progress, until various new attempts started in early 2000s in the X-ray and gamma-ray polarimetry. In these high energy

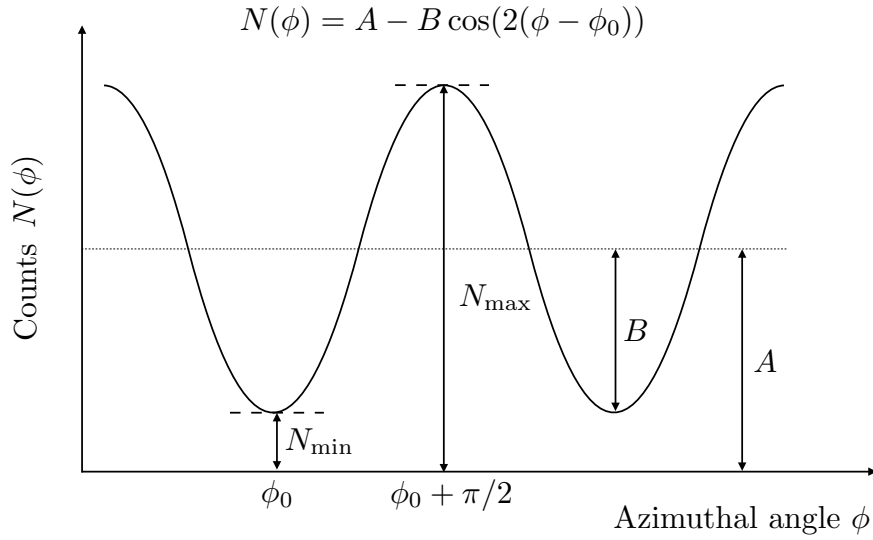


Figure 2.8: Azimuthal distribution of polarized X-rays when detected with a polarization-sensitive detector.

photons, the polarization is measured, photon-by-photon basis, by detecting anisotropy of traveling directions of the secondary photons or electrons generated by some interactions between the incident radiation and materials of some detectors, instead of directly measuring the electric field of the incident radiation as in radio and optical bands. The utilized polarization-sensitive interactions include Bragg reflection, photoelectric effect, and Compton scattering. We need to choose an interaction which is suitable for the energy range of observation.

2.4.1 Polarization measurements

Modulation factor

In order to quantify the degree of polarization, we use a quantity called modulation factor. If the incident radiation is polarized, the azimuthal distribution of the photon counts, detected with a polarization-sensitive method, becomes dependent on the azimuth angle ϕ as shown in Figure 2.8. The distribution is called a modulation curve, and expressed as

$$N(\phi) = A - B \cos(2(\phi - \phi_0)), \quad (2.58)$$

where ϕ_0 is the angle of polarization of the incoming radiation, A is the average of the maximum count N_{\max} and the minimum count N_{\min} , and B is the amplitude of the cosine curve.

To extract the polarization information from a modulation curve, a useful parameter is the modulation factor, which is defined as

$$Q = \frac{N_{\max} - N_{\min}}{N_{\max} + N_{\min}} = \frac{B}{A}. \quad (2.59)$$

We can rewrite Equation (2.58) as

$$N(\phi) = N_0 [1 - Q \cos(2(\phi - \phi_0))], \quad (2.60)$$

where N_0 ($= A$) is the offset of the modulation curve.

When the incident radiation is fully polarized, i.e., $\Pi = 1$ in Equation (2.20), we express the observed modulation factor as Q_{100} , which take a value of $0 \leq Q_{100} \leq 1$ depending on the polarization sensitivity of the detector. If the detector has a high ability to measure polarization, Q_{100} becomes high, until it reaches unity as the detector becomes ideal. Therefore, Q_{100} is useful to compare different detectors and/or different detection techniques. Then, the degree of polarization of the incident radiation is expressed as

$$\Pi = \frac{Q}{Q_{100}}. \quad (2.61)$$

Minimum detectable polarization

Even when the incident X-rays are unpolarized, Q would fluctuate due to photon statistics, and would give a false detection ($Q > 0$) of polarization. Therefore, when the detector performance Q_{100} and the detected photon number N are specified, we may define a quantity called minimum detectable polarization (MDP), above which the detection of polarization is regarded as significant. According to Weisskopf et al. (2009), the MDP is calculated thorough the following procedure. The probability of measuring a particular modulation factor Q and polarization angle ϕ_0 is given by

$$P(Q, Q_0, \phi, \phi_0) = \frac{NQ}{4\pi} \exp \left[-\frac{N}{4} (Q^2 + Q_0^2 - 2QQ_0 \cos(2(\phi - \phi_0))) \right], \quad (2.62)$$

where Q and ϕ are the measured modulation factor and polarization angle, respectively, while Q_0 and ϕ_0 are the true modulation factor and polarization angle, respectively. When $Q_0 = 0$, or the case of non-polarization, the probability becomes

$$P(Q) = \frac{NQ}{4\pi} \exp \left[-\frac{NQ^2}{4} \right]. \quad (2.63)$$

Then, the maximum value of Q that arises due to fluctuation at the 99% confidence level, to be denoted as Q_c is obtained by requiring

$$\int_{Q_c}^{\infty} P(Q) dQ = 0.01, \quad (2.64)$$

which gives

$$Q_c = \frac{4.29}{\sqrt{N}}. \quad (2.65)$$

Finally, the MDP is given as $\text{MDP} = Q_c/Q_{100}$.

The value of N is a mixture of source counts and background counts. When the observation time is T , we can write as $N = (R_S + R_B)T$, where R_S and R_B are the source and background

counts rates, respectively. Further expressing Equation (2.65) as a function of the source count, the threshold becomes

$$Q_S = Q_c \times \frac{R_S + R_B}{R_S} = \frac{4.29}{R_S} \left[\frac{R_S + R_B}{T} \right]^{1/2}. \quad (2.66)$$

Thus, the MDP is given as

$$\text{MDP}_c = \frac{Q_S}{Q_{100}} = \frac{4.29}{Q_{100} R_S} \left[\frac{R_S + R_B}{T} \right]^{1/2}. \quad (2.67)$$

When the MDP_c is small, it can be said that the polarization sensitivity of the observation is high.

2.4.2 Interactions sensitive to X-ray and gamma-ray polarization

Bragg reflection

Considering X-rays of wavelength λ incident on a crystal of lattice constant d , with an incident angle θ_B . Then, the wave interference occurs constructively, when the condition

$$n\lambda = 2d \sin \theta_B \quad (2.68)$$

is satisfied, where n is an integer. The condition is called Bragg's law.

A polarimeter of Bragg reflection type uses a difference of reflectance between the two polarizations; so-called σ and π polarizations, which have electric vector perpendicular and parallel, respectively, to the plane defined by the incident and reflected rays. The former and the latter components are called σ polarization and π polarization, respectively, which are fully linearly polarization. When $\theta_B = 45^\circ$, called Brewster's angle, the π polarization is not reflected. Then, the reflected X-rays are σ polarized, implying $Q = 1.0$ (Weisskopf et al., 1972).

Photoelectric effect

The angular distribution of photo-electrons due to K-shell photoionization is expressed (e.g. Costa et al., 2001) by the differential cross section as

$$\frac{d\sigma}{d\Omega} \propto Z^5 \frac{\sin^2 \theta \cos^2 \phi}{(1 - \beta \cos \theta)^4}, \quad (2.69)$$

where β is the photo-electron velocity, while θ and ϕ are the scattering and azimuthal angles of the electron, respectively. The equation indicates that the photo-electron is emitted preferentially along the electric vector of the incident photon ($\phi \sim 0$ or π). Therefore, by tracking the photoelectrons, we can measure the polarization of incident photons individually.

Compton scattering

As reviewed in §2.2.2 Compton scattering is yet another elementary process with polarization sensitivity. In the rest frame of the electron, the conservation of energy is expressed as

$$E'_\gamma = E_\gamma - E'_e, \quad (2.70)$$

where E_γ is the energy of the incident photon, E'_γ is that of the scattered photon, and E'_e is that of the recoil electron. Furthermore, as a function of the scattering angle θ between the directions of incident and scattered photons, E'_γ is given as

$$E'_\gamma = \frac{E_\gamma}{1 + \frac{E_\gamma}{m_e c^2} (1 - \cos \theta)}, \quad (2.71)$$

where $m_e c^2$ is electron rest-mass energy. This relation can be rewritten as

$$\cos \theta = 1 - m_e c^2 \left(\frac{1}{E'_\gamma} - \frac{1}{E_\gamma} \right). \quad (2.72)$$

The directional distribution of scattered photons is described by the differential cross section of Compton scattering, namely, the Klein-Nishina formula, Equation (2.50). When $\theta \sim \pi/2$, $d\sigma/d\Omega$ becomes dependent on φ , in such a way that the photons are preferentially scattered into $\varphi \sim \pm\pi/2$, namely, in directions perpendicular to the electric vector of the incident photon.

2.4.3 Polarimeters using different interactions

In § 2.4.2, we described three techniques to detect X-ray and gamma-ray polarization. In this subsection, their applications are reviewed.

Bragg reflection type

This has become the first successful method to detect X-ray polarization. Historically, the most well known instrument of this type is the Graphite Crystal X-ray Spectrometer on board OSO-8 (Kestenbaum et al., 1976, Weisskopf et al., 1976), which is shown in Figure 2.9. X-rays reflected by a graphite panel are detected with a proportional counter. The detector can detect the polarization in energies which are 2.4 – 2.8 and 4.8 – 5.6 keV, corresponding to $n = 1$ and $n = 2$ of Equation (2.68), respectively. The method of the polarization measurement was to rotate the detector to scan the azimuth ϕ in Figure 2.8.

As inherent properties of polarimeters of this type, the OSO-8 instrument had a large modulation factor Q , but worked only on two narrow energy ranges which satisfy the Bragg condition of Equation (2.68). As represented by the name of OSO (Orbiting Solar Observatory), the instrument was primarily meant for the X-ray polarimetry of solar flares. However, it was employed in observations of the Crab Nebula, and yield the first successful detection of cosmic X-ray polarization (§2.3.1).

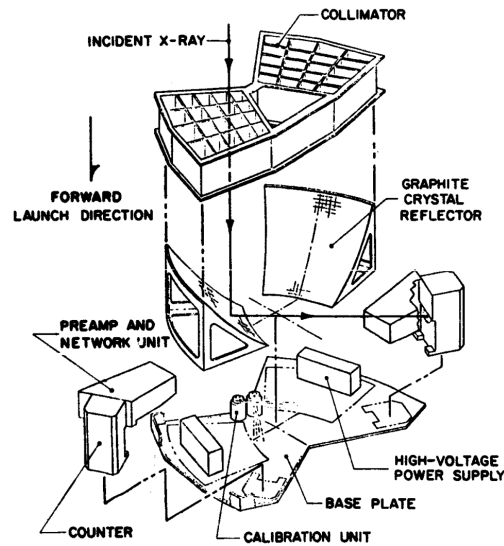


Figure 2.9: A schematic of the Graphite Crystal X-ray Spectrometer on board *OSO-8*. X-rays that are Bragg-reflected by a graphite panel are detected with a proportional counter (adopted from Weisskopf et al., 1976).

Photoelectric effect type

This is a method to detect the anisotropy of photo-electrons ejected by photoelectric absorption (§2.4.2). Generally, photo-electrons have typical ranges of a few micrometers in solid, and a few mm in gas. Therefore, the key technology here is how to detect, with a high position resolution, ionized tracks of photo-electrons. In energies below ~ 10 keV, gas trackers are generally suited, because the electron ranges are relatively long in gases even at low X-ray energies. In ≥ 10 keV where gas stopping power decreases, solid-state trackers become more suitable. One of the first demonstrations of this technique used X-ray CCDs (Tsunemi et al., 1992).

Figure 2.10 shows a typical gas based photoelectric polarimeter, which has been developed at RIKEN, Japan (Tamagawa et al., 2006). An incident X-ray is detected in a gas chamber via photoelectric effect (left), and the emitted photoelectron runs inside the gas to produce an ionization track which is elongated in the direction of initial electric field. Using a micro-pixel foil electrode called Gas Electron Multiplier (GEM), combined with pixel anode readouts, the photoelectron track is detected as shown in the right panel. As a future mission using this technique, the NASA's Imaging X-ray Polarimetry Explore (IXPE) which involves Japan's contribution, is scheduled for launch in the 2020s. Using the GEM technique developed in Japan (Tamagawa et al., 2006), this polarimetry is able to detect polarization of X-rays below about 10 keV.

Compton scattering type

As represented by Equation (2.50), this method utilizes the anisotropy of direction of Compton scattered photons. As shown in Figure 2.12, a polarimeter of this type generally consists of a

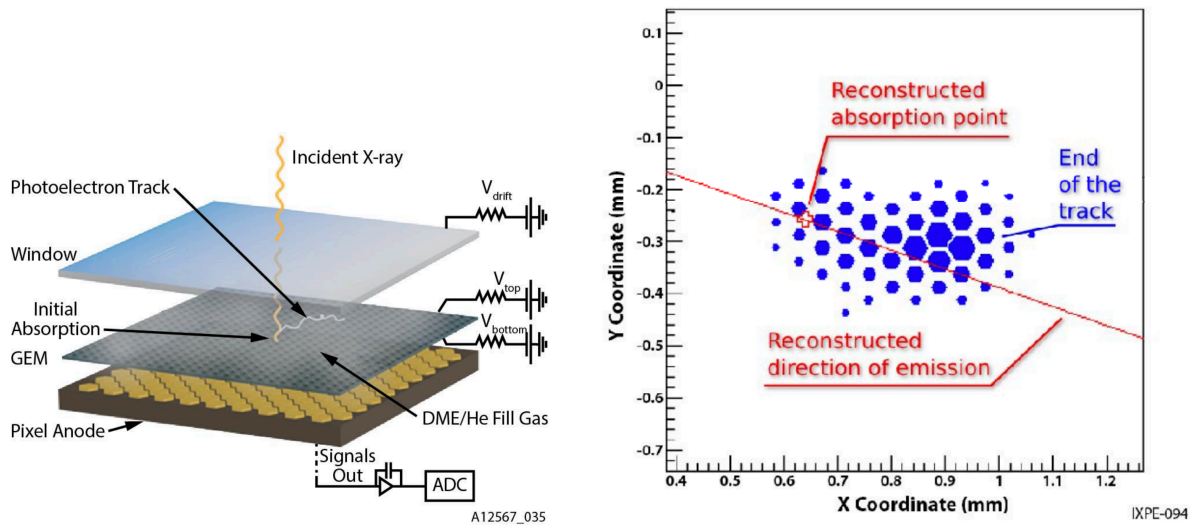


Figure 2.10: (Left) Schematic of gas type X-ray polarimeter on board IXPE. (Right) An electron cloud of a photo-electron detected by a pixel detector (adopted from Weisskopf et al., 2016).

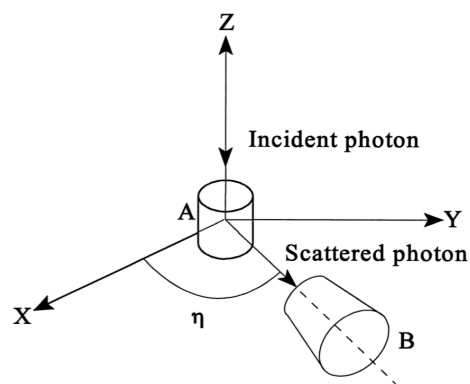


Figure 2.11: A schematic configuration Compton polarimetry (adopted from Lei et al., 1997).

scatterer which causes Compton scattering, and a position-sensitive absorber which captures scattered photons. This type of polarimeters are suitable to photons with energies above ~ 20 keV, where the photoelectric technique no longer works due to the reduced cross section. As described below, this technique has been utilized in several space projects.

The COMPTEL onboard the Compton Gamma-Ray Observatory (CGRO) is a Compton telescope (Schoenfelder et al., 1993) MeV gamma-rays. The scatterer is an array of liquid scintillator NE213A, and the absorber is an array of NaI(Tl) crystal scintillators located 1.5 m below. Each detector is surrounded by thin plastic scintillator which provides anti-coincidence shield to reject charged particles. The COMPTEL was primarily meant to detect positions of 0.8-30 MeV gamma-rays, using the coarse positional information in the top and bottom layers, and the time-of-flight information between them. Although Compton scattering is a polarization-sensitive process (§2.4.2) However, gamma-ray polarization was not detected from any celestial objects, because the COMPTEL used nearly-forward scattering [$\theta \sim 0$ in Equation (2.50)], where the polarization sensitivity (dependence on φ) is very small.

PoGO+ (Polarized Gamma-ray Observer) is a balloon mission, which aimed at detections of X-ray polarization in energies in ~ 20 -180 keV (Chauvin et al., 2016, Weisskopf, 2018). The scatterer is 61 units of plastic scintillators arranged in a honeycomb shape. Each unit is wrapped by a metal collimator to limit the field of view, and the entire 61 units are surrounded by segmented BGO scintillators on the bottom and sides. An incident photon through the passive collimator is scattered at a plastic scintillator, and the scattered photon is detected by one of the BGO scintillators. In order to remove systematic errors of the instrument, the whole balloon gondola was rotated slowly. The balloon flight was performed in 2016 July, and the polarization of the Crab Nebula was successfully detected in 18-160 keV Chauvin et al. (2017). Furthermore, a PoGO+ observation of the black-hole binary Cygnus X-1 (§2.3.2) has provided a rather tight upper limit ($\sim 9\%$) on its 16-180 keV polarization (Chauvin et al., 2018, Nature Astronomy); the result has an important implication, that the emission is not strongly influenced by general relativistic effects.

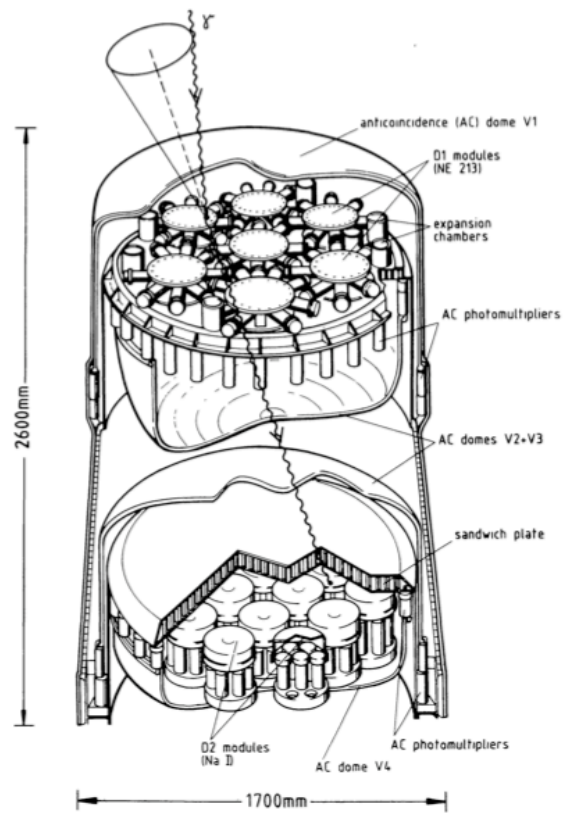


Figure 2.12: The COMPTEL onboard Compton Gamma-Ray Observatory (adopted from Lei et al., 1997).

Chapter 3

Compton Camera

3.1 Principle of Compton Camera

The Compton camera studied here is a high energy resolution and position-sensitive device that can estimate the direction of individual incoming photons by obtaining information of Compton interactions between the incoming photon and the Compton camera.

Figure 3.1 shows a simple configuration of a Compton camera, in which an incident photon is Compton scattered by a top-layer detector called “the scatterer”, and detected by photo-electric absorption in the bottom layer called “the absorber”. The scatterer and absorber are both capable of detecting the energy deposit as well as detection the photon interaction position.

3.1.1 Compton Kinematics

Figure 3.1 shows an edge-on view of the scatterer (blue) and absorber (green) and the kinematic outcome of an incoming photon. We suppose that an incoming photon has energy of E_0 and is Compton scattered at the scatterer and where it deposits an amount of energy E_1 at which time the scattered photon is photo-electrically absorbed by the absorber where it deposits all of its energy of amount E_2 , such that the energy conservation law can be written as

$$E_0 = E_1 + E_2. \tag{3.1}$$

We can solve for the scattering angle θ using Equation (2.72) such that

$$\cos \theta = 1 - m_e c^2 \left(\frac{1}{E_2} - \frac{1}{E_1 + E_2} \right). \tag{3.2}$$

Thus, we can constrain the direction of the incoming photon on a cone, called as “Compton cone”, around the direction which is determined by connecting the two hit positions. By observing many photons, we can determine the two-dimensional source position as an intersection of their Compton cones.

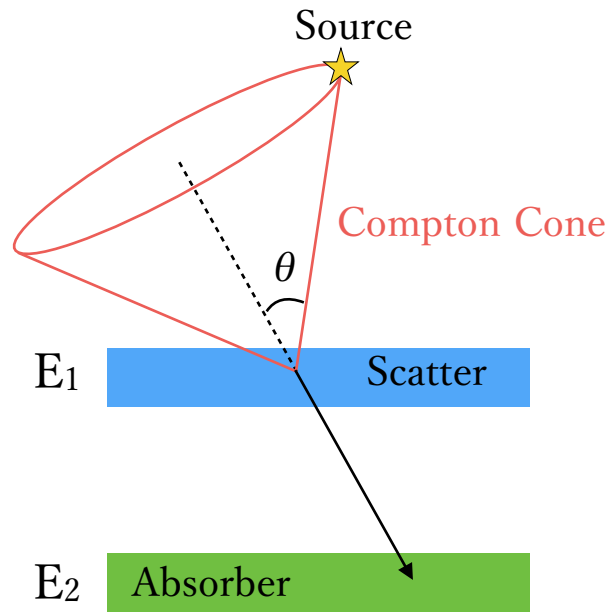


Figure 3.1: An edge-on schematic of a Compton camera showing an incoming photon which has Compton scattered at the scatterer and photo-electrically absorbed at the absorber. The direction of an incident photon is constrained onto the intersection of a Compton cone as defined by Equation (3.2).

3.1.2 Angular resolution of a Compton camera

The results obtained in Equation (3.2) implies that the direction of the incoming photon scattered at an angle of θ_K is constrained to lie somewhere on the cone. Let the true direction of the incoming photon be defined as, \mathbf{r}_0 , then we can also estimate the scattering angle θ_G from the true hit positions located at the scatterer and the absorber such that,

$$\cos \theta_G = \frac{(\mathbf{r}_1 - \mathbf{r}_0) \cdot (\mathbf{r}_2 - \mathbf{r}_1)}{|\mathbf{r}_1 - \mathbf{r}_0| |\mathbf{r}_2 - \mathbf{r}_1|} \quad (3.3)$$

where \mathbf{r}_1 is the first hit position, which is assumed to be at the scatterer, and \mathbf{r}_2 is the second hit, which is assumed to be at the absorber. The difference between the estimated angle θ_K and true angle θ_G is given $\Delta\theta$ such that

$$\Delta\theta = \theta_K - \theta_G, \quad (3.4)$$

is the angular resolution of the Compton camera, and is called as Angular Resolution Measure (ARM). The ARM is distributed around $\Delta\theta = 0$, and the full width half maximum (FWHM) of the distribution is used to estimate the angular resolution.

In an ideal situation, the ARM is always zero. In actuality, however, the ARM usually takes on finite values. In the following three subsections, we describe how the ARM distributions are determined by two instrumental factors, namely, the energy- and position- resolution, and by the intrinsic physics, namely, Doppler broadening (Takeda, 2009).

3.1.3 The effect of energy resolution

The uncertainty in θ_K can be defined by the energy resolution through Equation (3.2) such that

$$\begin{aligned} (\Delta \cos \theta_K)^2 &= \left(\frac{\partial \cos \theta_K}{\partial E_1} \right)^2 \Delta E_1^2 + \left(\frac{\partial \cos \theta_K}{\partial E_2} \right)^2 \Delta E_2^2 \\ &= \left[\frac{m_e c^2}{(E_1 + E_2)^2} \right]^2 \Delta E_1^2 + \left[m_e c^2 \left(\frac{1}{E_2^2} - \frac{1}{(E_1 + E_2)^2} \right) \right]^2 \Delta E_2^2, \end{aligned} \quad (3.5)$$

or,

$$(\Delta \theta_K)^2 = \left[\frac{m_e c^2}{\sin \theta_K (E_1 + E_2)^2} \right]^2 \Delta E_1^2 + \left[\frac{m_e c^2}{\sin \theta_K} \left(\frac{1}{E_2^2} - \frac{1}{(E_1 + E_2)^2} \right) \right]^2 \Delta E_2^2, \quad (3.6)$$

and which shows that the uncertainty in measuring the scattering θ_K is inversely proportion to the square of the total energy, provided that ΔE_1 and ΔE_2 are constants.

In semiconductor detectors, not only does the electronics noise ΔE_{noise} contribute to the value of the energy resolution, which is assumed to be constant, but also does the statistical fluctuations ΔE_{stat} which is a function of the number of created electron-hole pairs. The latter is defined as

$$\Delta E_{\text{stat}} = 2.35 \sqrt{\varepsilon F E}, \quad (3.7)$$

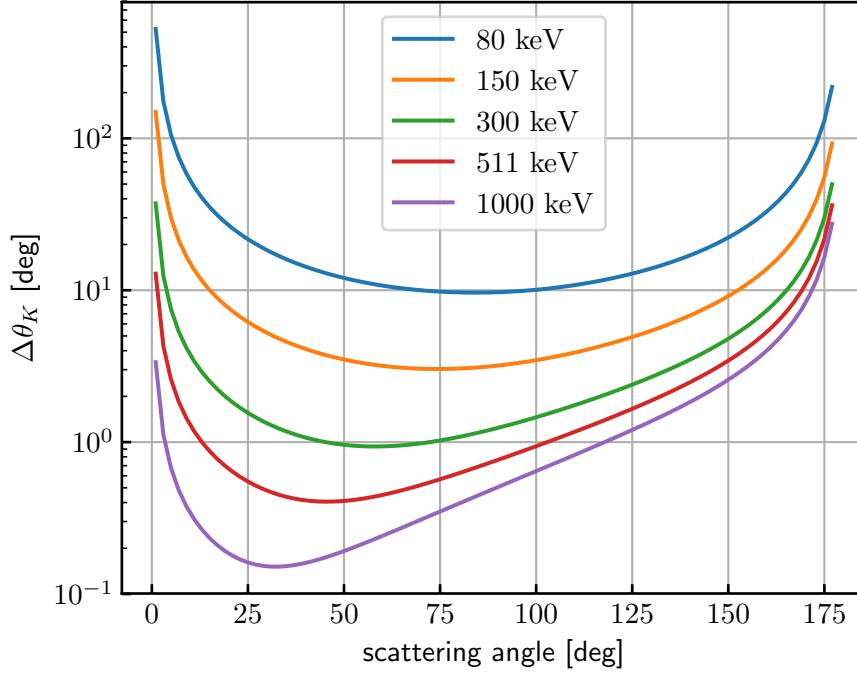


Figure 3.2: A log plot of the energy resolution as a function of the scattering angle when $\Delta E_{\text{noise}} = 2.0$ keV, $F = 0.1$, $\varepsilon = 4.0 \times 10^{-3}$ keV, and $a = 0.001$ in Equation (3.9).

where F is the Fano factor and ε is the average energy for creating a pair of electron and hole. The Fano factor is about 0.1 in semiconductor detectors, and ε is typically 3.6 eV in Si and 4.4 eV in CdTe.

As a result, the energy resolution becomes

$$(\Delta E)^2 = (\Delta E_{\text{noise}})^2 + (\Delta E_{\text{stat}})^2 + (\Delta E_{\text{prop}})^2, \quad (3.8)$$

where ΔE_{prop} is a component proportional to the energy E , which may be expressed as $\Delta E_{\text{prop}} = aE$, where a is a constant. Equation (3.8) can then be expressed as

$$(\Delta E)^2 = (\Delta E_{\text{noise}})^2 + 2.35^2 \varepsilon F E + (aE)^2. \quad (3.9)$$

In Figure 3.2, we show how the value for the energy resolution as a function of the scattering angle when $\Delta E_{\text{noise}} = 2.0$ keV, $F = 0.1$, and $\varepsilon = 4.0 \times 10^{-3}$ keV, and $a = 0.001$.

3.1.4 The effect of position resolution

The detector's pixel size affects both the value in the position resolutions and the ARM, but through θ_G rather than θ_K . Suppose that a photon is traveling along the z -axis, and scatters at $\mathbf{r}_1 = (x_1, y_1, z_1)$ and absorbed at $\mathbf{r}_2 = (x_2, y_2, z_2)$. Then, the scattering angle is expressed as

$$\theta_G = \arctan \left[\frac{z_2 - z_1}{\sqrt{(x_2 - x_1)^2 + (y_2 - y_1)^2}} \right]. \quad (3.10)$$

The uncertainty in the measurement of θ_G is calculated using the usual error propagation method such that,

$$(\Delta\theta_G)^2 = \frac{(z_2 - z_1)^2}{12d^4}(p_1^2 + p_2^2) + \frac{(x_2 - x_1)^2 + (y_2 - y_1)^2}{d^4}(dz_1^2 + dz_2^2), \quad (3.11)$$

where p_1 and p_2 are the pixel size for each detector, dz_1 and dz_2 are the thickness of each detector, and $d = [(x_2 - x_1)^2 + (y_2 - y_1)^2 + (z_2 - z_1)^2]^{1/2}$ is the distance between the two interaction points. Evidently, larger values of d improves the angular resolution.

3.1.5 Doppler broadening

Although we so far assumed that the scattering electron is at rest, in reality electrons are bound to nuclei and have finite momenta. When an incident photon is scattered by a bound electron, the scattering kinematics slightly change due to the electrons' momentum, and equivalently, the interaction cross section is changed. This effect, often called Doppler broadening, is more significant toward lower photon energies, and determines the lower limit of the angular resolution. In other words, this effect cannot be avoided even for an ideal Compton camera which has delta function energy and position resolutions.

According to Ribberfors and Berggren (1982), the Klein-Nishina cross section σ_{KN} is replaced as

$$\left(\frac{d\sigma}{d\Omega}\right)_{\text{incoh},i} = \left(\frac{d\sigma_{KN}}{d\Omega}\right) S_i(E_0, \theta, Z), \quad (3.12)$$

where $S(E_0, \theta, Z)$ is a correction factor called incoherent scattering function, which depends on the scattering angle θ , the energy of incoming photon E_0 and the atomic number Z of scatterer. Here the subscript i indicates the shell number of a bound electron. The incoherent scattering function is expressed in terms of the Compton profile $J_i(p_z)$ where p_z is the initial momentum of the electron in relativistic impulse approximation (Ribberfors and Berggren, 1982). Then, the double differential Compton scattering cross section is give (Namito et al., 1994) as

$$\left(\frac{d^2\sigma}{d\Omega dE}\right)_{\text{incoh},i} = \frac{r_e^2}{2} \left(\frac{E_2 E}{E_0^2}\right) \frac{dp_z}{dE} \left(\frac{E_2}{E_0} + \frac{E_0}{E_2} - \sin^2 \theta\right) J_i(p_z). \quad (3.13)$$

Here p_z is the projection of the initial momentum of the electron along the z -axis. Let $\mathbf{q} \equiv \mathbf{k} - \mathbf{k}'$ where \mathbf{k} and \mathbf{k}' are the momenta of the incident and scattered photons, respectively, Then, p_z is given by

$$p_z \equiv -\frac{\mathbf{p} \cdot \mathbf{q}}{|\mathbf{q}|} = \frac{EE_2(1 - \cos \theta) - m_e c^2(E - E_2)}{c^2 q}, \quad (3.14)$$

where \mathbf{p} is the initial momentum of electron and

$$q = \frac{1}{c} \sqrt{E^2 + E_2^2 - 2EE_2 \cos \theta}. \quad (3.15)$$

If $p_z = 0$, Equation (3.14) reduces to Equation (3.2), and the Doppler broadening vanishes.

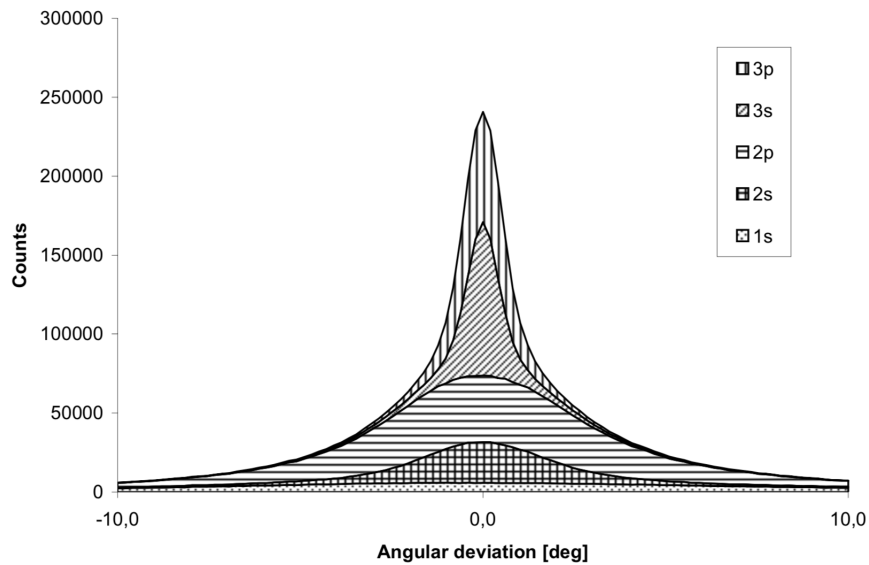


Figure 3.3: ARM distributions for scattering electrons in different atomic shells. The widest distribution is by a K-shell electron because the electron has the largest momentum (adopted from Zoglauer and Kanbach, 2003).

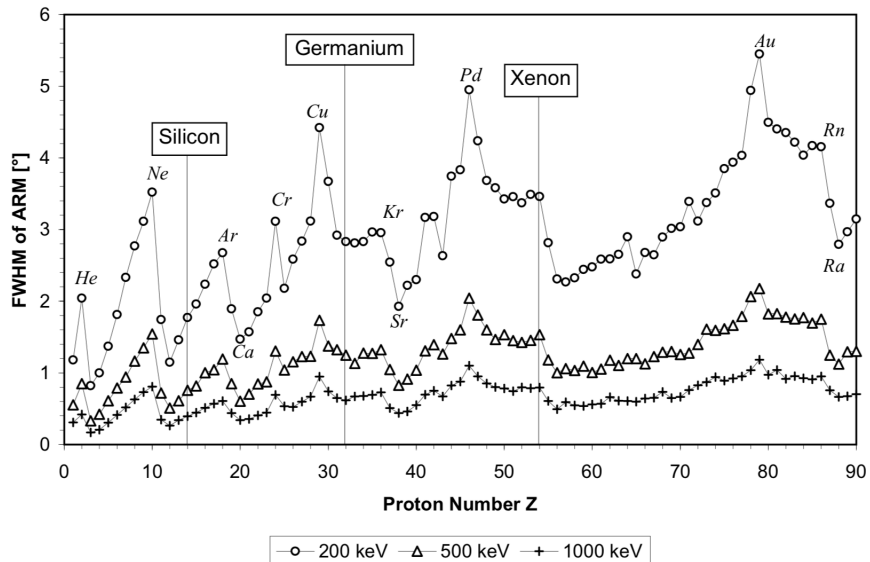


Figure 3.4: The Z dependence of angular resolution. The angular resolution of Si is relatively small (adopted from Zoglauer and Kanbach, 2003).

According to Zoglauer and Kanbach (2003), the Doppler broadening by electrons in various atomic shells affects the ARM profiles as shown in Figure 3.3. Since electron in the inner shells have greater momenta, the ARM distribution gets wider. An average of the angular resolution as a function of atomic number is shown in Figure 3.4. The figure also shows that silicone is a relatively good Compton scattering material since Doppler broadening effects is small compared to heavier atomic elements.

3.2 Si/CdTe Compton camera

In this section, we describe the basic concept of a Compton camera using pixelated (or striped) detectors that utilizes silicon and CdTe for the scatterer and absorber, respectively.

3.2.1 Concept

To realize the manufacturing of a high detection efficiency and angular resolution Compton camera, both the scatterer and the absorber must have both high energy (§3.1.3) and position (§3.1.4) resolutions, and have a low Doppler broadening effect (§3.1.5). To satisfy these requirements, it is suitable to use semiconductor devices. This is because the energy resolution of semiconductor detectors is higher than compared to other types of detectors, such as scintillation detectors, and this is mainly because semiconductor devices can provide good position resolution. Among various semiconductor materials, silicon (Si) is best suited for the scatterer medium, because of its low atomic number, $Z = 14$, the photoelectric effect is suppressed and Compton scattering is dominant above ~ 60 keV, as is shown in Figure 3.6. Another advantage of Si is that effect of Doppler broadening is relatively low as is made clear in Figure 3.4. On the other hand, to realize a high efficiency of photo-absorption, the absorber must be made of high- Z materials. Among several candidate, Cadmium Telluride (CdTe) semiconductor has many advantage (see §3.2.3), including having a high photon stopping power (Figure 3.6). Therefore, we hereafter adopt CdTe devices as the absorber. This combination of the low- Z such as Si and high- Z such as CdTe provides an ideal environment to develop high performance Compton cameras. The basic properties of these two types of semiconductors are shown in Table 3.1.

In the geometry given in Figure 3.1, an incoming photon can either first scatter at the scatterer and then be absorbed at the CdTe or vice versa. Assuming that just these two cases occur, the Compton camera can determine the order in which these hits occurred. According to Equation (2.72) and shown in Figure 3.5, the scattering E_2 is always greater than the absorbed E_1 , regardless of the scattering angles. On the other hand, if an incoming photon's energy is greater than the scattered energy E_1 is greater than the scattered energy E_2 for backscattered photons ($\theta > 90$ degrees), and in the case of forward scattering ($\theta < 90$ degrees) the scattering energy E_2 is greater than the deposit energy E_1 . Both the Klein-Nishina formula (Equation 2.51) and Figure 2.6 show that probability of forward scattering is greater than the probability for backscattering for increasing incoming photon energy. Therefore, forward scattering of the incoming photon is the most likely outcomes when the energy is $> m_e c^2/2$. As a result, it is suitable to assume that the former and the latter hits are more likely to occur in the upper and bottom layer, respectively.

In addition, we developed thin Si and CdTe semiconductor detectors, and the stacked Si

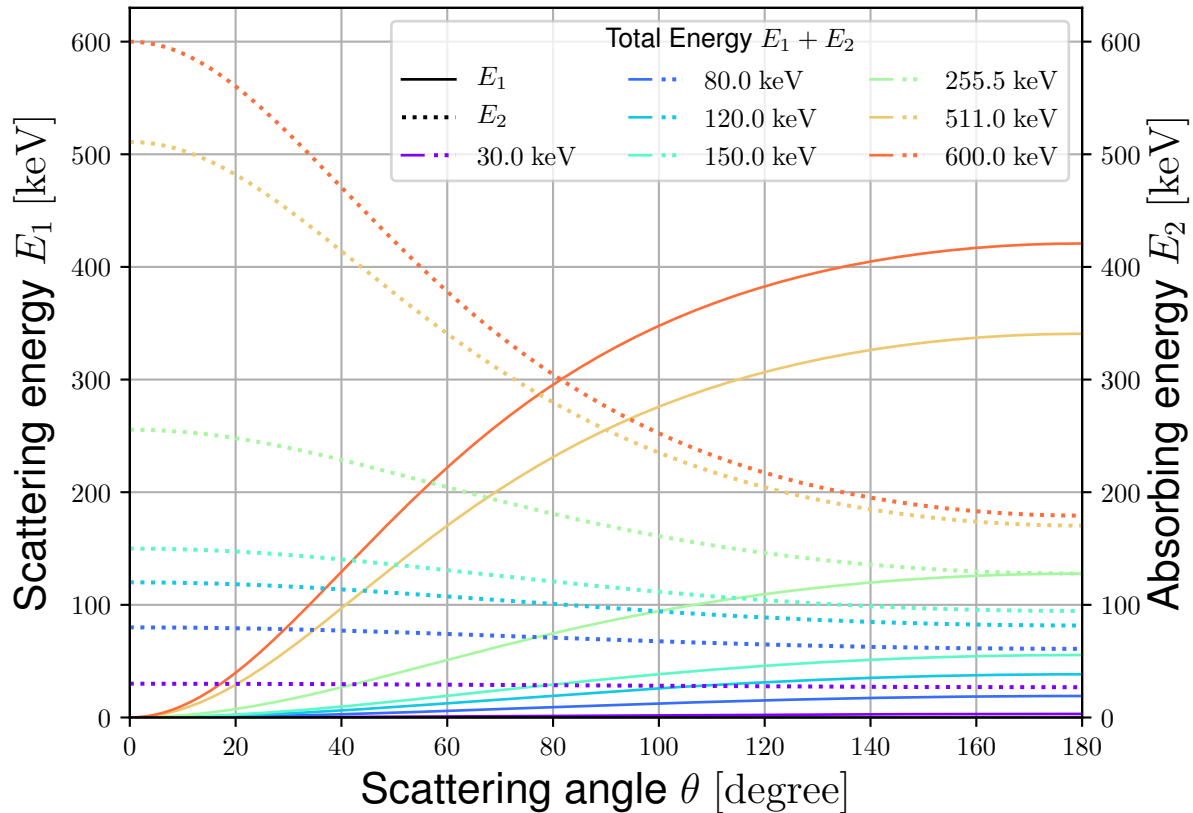


Figure 3.5: The deposit and scattered energy E_1, E_2 against various scattered angle when Compton scattering occur once. Each color shows the energy of the incident photon, and the solid and dashed lines represent deposit E_1 and scattered E_2 energies, respectively. According to Equation (2.72), the energy of incoming photon is lower than a half of electron rest mass, $m_e c^2/2$, then the scattered energy E_2 (dashed) is bigger than the deposit energy E_1 (solid) regardless of scattering angles. In case that the energy of incoming photon is higher than $m_e c^2/2$, in the backscattering ($\theta > 90$ degree) the deposit energy is higher than the scattered energy.

and CdTe Compton camera. The benefit of using Si and CdTe semiconductor detector is that we can improve the angular resolution without reducing the detection efficiency (Takeda, 2009).

Si detectors are suitable as the scatter because Compton scattering in Si is dominant above ~ 60 keV. On the other hand, CdTe detectors are suitable as the absorber since the photoelectric absorption is dominant up to ~ 300 keV. The basic properties of Si and CdTe semiconductors are shown in Table 3.1.

Table 3.1: Basic parameters of Si and CdTe semiconductors

| | Si | CdTe |
|---|------|-------------------------|
| Atomic number Z | 14 | 48, 52 |
| Density (g/cm^3) | 2.33 | 5.85 |
| Band gap E_{gap} (eV) | 1.12 | 1.4 |
| Average ionization energy ε (eV) | 3.61 | 4.43 |
| Mobility of the electron $(\mu\tau)_e$ (cm^2/V) | 0.42 | $\sim 2 \times 10^{-3}$ |
| Mobility of the hole $(\mu\tau)_h$ (cm^2/V) | 0.72 | $\sim 1 \times 10^{-4}$ |

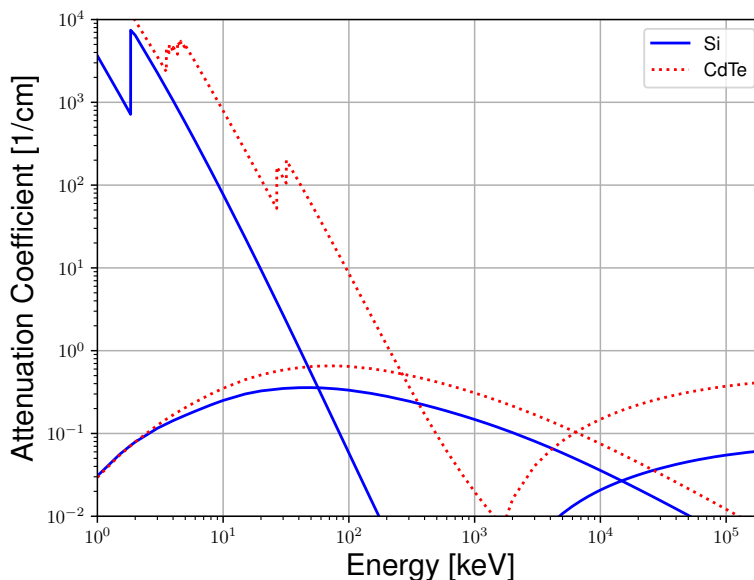


Figure 3.6: The attenuation coefficient of photo absorption, Compton scattering, and pair creation in Si (blue line) and CdTe (red line). The cross section of Si and CdTe is provided by XCOM (Berger et al., 2010).

In order to increase the detection efficiency, it is effective to stack the semiconductor detectors. In the multi-stack configuration, the probability of multiple Compton scattering by an incident photon will increase before it is finally absorbed. A high energy photon in its first interaction is mainly forward scattered, as described in Equation 2.50. However, according to

Figure 2.6, as the photon energy decrease, with increasing Compton collisions, back scattering becomes increasingly more probable. Therefore, to detect these events, it is desirable to surround the stacked semiconductor detector with additional absorbers as shown in an actual configuration in §3.2.4.

3.2.2 Si semiconductor detectors

A semiconductor detector registers a hit of the incident photon by collecting electron-hole pairs generated from the Compton interaction. The charges that reach the electrodes attached to the surface of the semiconductor are readout and used to compute the energy of the interaction. Generally, semiconductors, including Si, have lower ionization potentials (\sim eV) than noble gases (\sim a few tens eV) and scintillators (\sim 100 eV). As a result, semiconductor detectors can produce a larger number of signal carriers, and hence can achieve comparatively higher energy resolution. In addition, various micro fabrication techniques of the electrodes now enable Si detectors to achieve a position resolution down to several hundred μ m.

There are essentially two electrode design; one is a pad type electrode detector and the other is a Double-sided Silicon Strip Detector (DSSD) (Fukazawa et al., 2005, Takeda et al., 2007). As the name suggests, a DSSD has electrode strip on both sides and are orientated strips on one side of the Si or CdTe plates are made of Al and Si n-type structure. By reading out the signals from both sides, we can determine the two-dimensional positions of individual photons. Since a DSSD uses n-type substrate, p-type Si is used to insulate the strips on each side. If the number of strips is N , the total readout channels are only $2N$.

In a Si pad detector, the p-side is divided into two-dimensional pad electrodes, which are mutually insulated by SiO₂ lanes. For each pad, the surface of the p-side is coupled to an Al electrode. For $N \times N$ pixels we need to read out the signals from N^2 chains and the detectors are operated under reverse bias voltage. The leakage current is generated due to thermal excitation of electrons above the band gap energy. Although the energy resolution degrades when the leakage current increases, it can be suppressed by operating the detector at low temperatures, typically -20°C or so.

3.2.3 CdTe semiconductor detectors

Although Ge semiconductor detectors have a high photo-absorption efficiency and a high energy resolution, they must be cooled liquid nitrogen to avoid thermal noise caused by the small band gap energy $E_{\text{gap}} = 0.72$ eV. Since such a cryogenic technique would make a space experiment very difficult, CdTe, has been extensively developed over the past two decades as an alternative compound material, mainly led in Japan (e.g. Takahashi and Watanabe, 2001, Takahashi et al., 1999, Takeda et al., 2012a, Watanabe et al., 2009). Since CdTe has double the band gap energy, $E_{\text{gap}} = 1.4$ eV, it can be operated at room temperature, while still maintaining a reasonably high energy resolution. In addition, thanks to the relatively large values of Z of Cd and Te (Table 3.1), CdTe detectors have a high photo-absorption efficiency up to ~ 300 keV (Figure 3.6), beyond which Compton scattering dominates.

The mean free path of the carriers is an important quantity that affects the energy resolution of semiconductor detectors, which is proportional to the product $\mu\tau$ for a given bias voltage, where μ is the carrier mobility and τ is the charge carrier life time. An intrinsic problem of

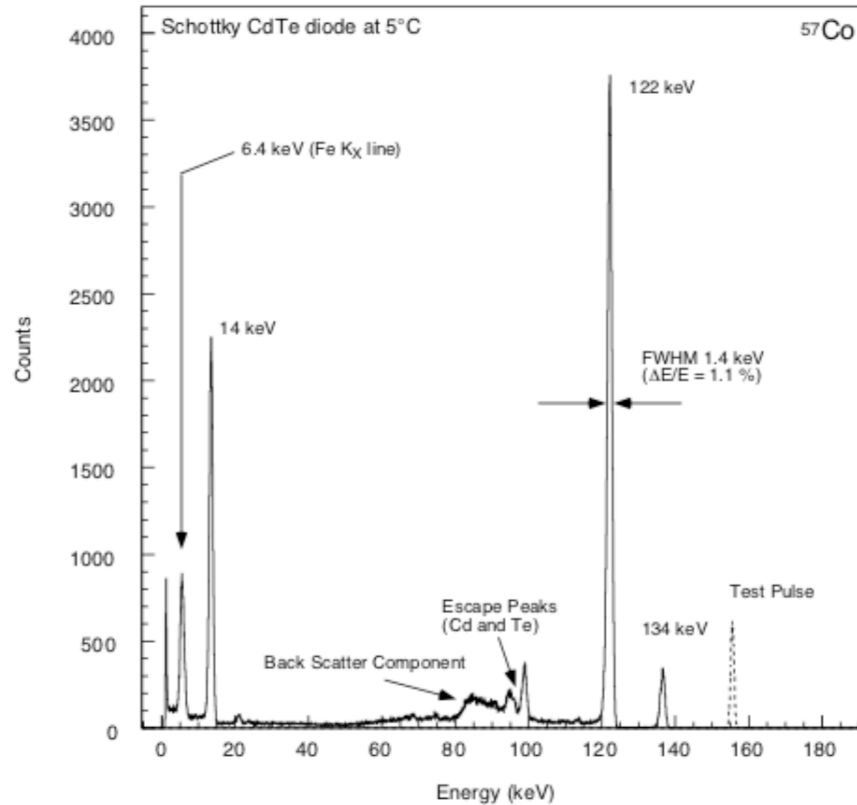


Figure 3.7: ^{57}Co spectrum obtained using Schottky CdTe detector with an area of $2\text{ mm} \times 2\text{ mm}$ and a thickness of 0.5 mm and at operating at $5\text{ }^\circ\text{C}$. The bias voltage of the detector is 800 V . (From Takahashi et al., 2002, .)

CdTe is the product $\mu\tau$ which is considerably shorter than those of Ge and Si. This apparent disadvantage can be avoided by applying a high bias voltage across the detector which increase the mean free path of the charge carriers. However, an increased bias voltage caused the leakage current to also increase which caused the energy resolution to degrade. This dilemma has been solved by Takahashi et al. (2000, 2002); they selected In and Pt, respectively, for the anode and cathode materials on p-type CdTe, to create a Schottky barrier. The Schottky CdTe can obtain the sharp peak such as Figure 3.7.

3.2.4 Prototypes of Si/CdTe Compton camera

The first stacked detector, which is not strictly a Compton camera, used only thin CdTe semiconductor detectors shown in Figure 3.8 (Takahashi et al., 1999). IT is constructed out of 12 Schottky CdTe diodes with surface area of $5 \times 5\text{ mm}^2$ and thickness 0.5 mm . The energy resolution of the summed spectra is 3 keV at 81 keV and 7.5 keV at 356 keV in full width half maximum (FWHM). The aim of this detector was to improve the detector efficiency and the detector obtained a spectrum up to several hundred keV. The same types detector was developed (Watanabe et al., 2002), and it obtained an energy resolution of the summed spectra of 5.3 keV (FWHM) and 7.9 keV at 356 keV and 662 keV in the temperature $-20\text{ }^\circ\text{C}$.

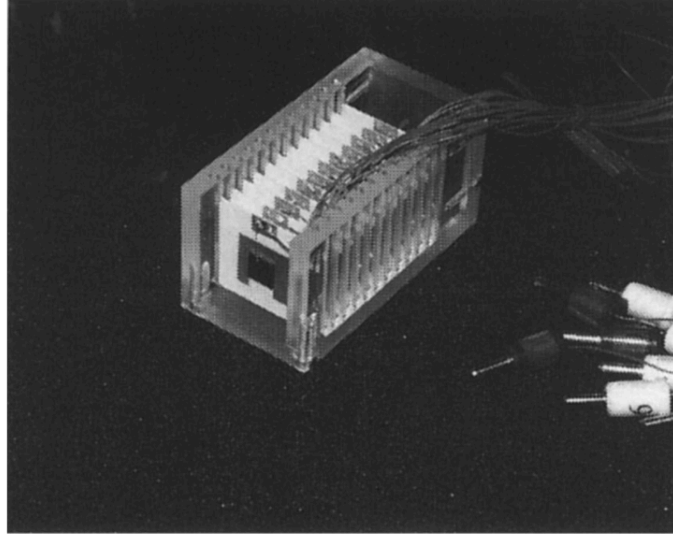


Figure 3.8: The stacked CdTe detector which is constructed from 12 diodes (from Takahashi et al., 1999). The surface area and thickness of the diode are $5 \times 5 \text{ mm}^2$ and 0.5 mm, respectively.

In order to reduce the background with hard X-ray and gamma-ray detectors, Takahashi et al. (2001) introduced the stacked Si and CdTe semiconductor detectors as Compton camera for the first time. In the stacked detector constructed from several tens of thin semiconductor layers, an incident gamma-ray may undergo multiple Compton scattering events. In this case, we determine the order of the hits from the deposited energies and hit positions.

Mitani et al. (2004) developed the Si/CdTe Compton camera constructed of two layers with a DSSD and CdTe pixel detectors as shown in Figure 3.9. The strip pitch of the DSSD is $800 \mu\text{m}$ and the pixel size for the CdTe is 2 mm squared. They irradiate 177 keV monochromatic X-ray beam which is fully linearly polarized to the detector. They obtained a modulation factor of 43 % and they showed that the Si/CdTe stacked detector had the potential to be used as a detector for a Compton telescope and the polarimeter. A stacked Si/CdTe Compton camera was then developed by (Oonuki et al., 2007, Takeda et al., 2009, Takeda, 2009, Watanabe et al., 2006, 2007) while Monte Carlo simulation of the Si and CdTe was performed by (Odaka et al., 2010).

Figure 3.10 is shows one of the prototypes of a Si/CdTe Compton camera constructed from 5 layers with two DSSDs and three CdTe double sided strip detectors (Takahashi et al., 2012, Takeda et al., 2012b). The thickness and the pitch width of the electrodes of DSSDs are 0.5 mm and $250 \mu\text{m}$, respectively. For CdTe double sided strip detectors, the thickness is 0.75 mm, and the pitch width of the electrodes is $250 \mu\text{m}$. The detector demonstrated the visualization of radioactive substances in the Fukushima area, and it obtained the distribution of gamma-rays with energies of 605, 662, 796, and 802 keV from ^{134}Cs and ^{137}Cs and their mapping image shown in right of Figure 3.10.

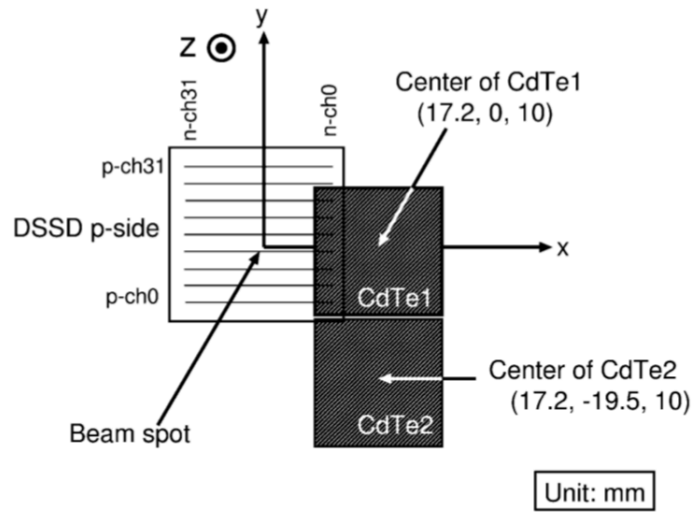


Figure 3.9: A schematic of a Compton camera with two layers using CdTe pixel detectors and DSSD (from Mitani et al., 2004).

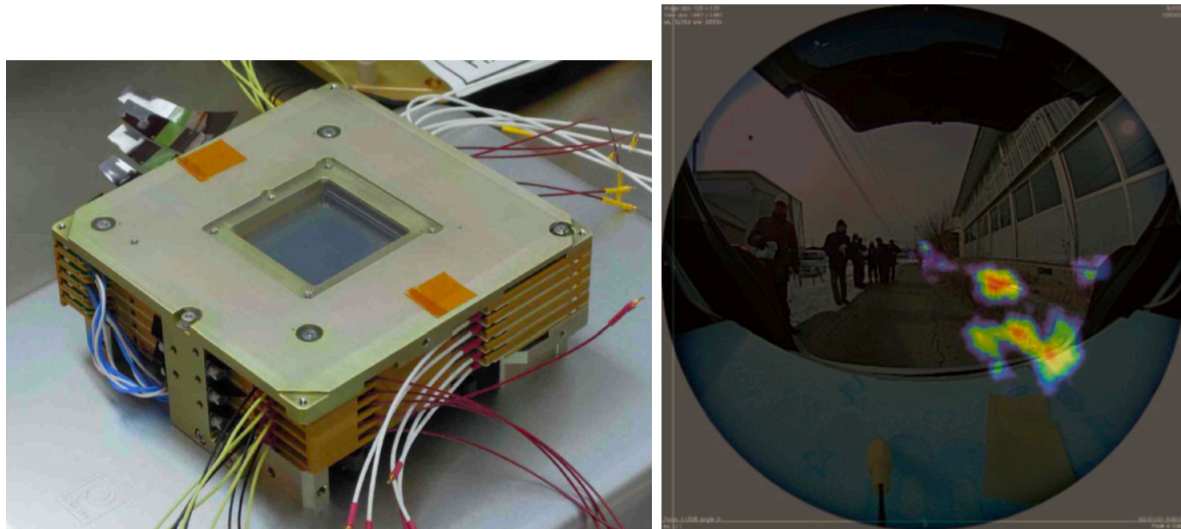


Figure 3.10: (Left) A prototype of a Si/CdTe Compton camera constructed of 5 layers. The top two layers are made from DSSDs and the bottom layers are made from CdTe detectors. (Right) The distribution of the gamma-rays from radioactive substances in the Fukushima area. The energies of the gamma-rays are 605, 662, 796, and 802 keV from ^{134}Cs and ^{137}Cs . The exposure time is 60 min. These figures are from Takahashi et al. (2012).

Chapter 4

The Soft Gamma-ray Detector on board *Hitomi*

4.1 The *Hitomi* Mission

Hitomi, also known as ASTRO-H, is the sixth Japanese X-ray astronomy satellite, shown in Figures 4.1 and 4.2 (Takahashi et al., 2018). The satellite was developed through an international collaboration and was launched by a H-IIA rocket and the 17th of February 2016 from Tanegashima Space Center. At an attitude of 575 km and its inclination angle was 31 degrees, the orbit of *Hitomi* was approximately circular. After the initial start-up operations was nearly completely, *Hitomi* lost communication with ground on March 26. Nevertheless, during its very short mission life, *Hitomi* achieved a number of novel measurements on a handful of cosmic X-ray sources, around 45 referenced papers have been published including both instrumental (about half) and scientific publication.

Hitomi aimed at studying the dynamical Universe, including various astrophysical phenomena which operate under extreme conditions. The distances to these targets spanned to nearby stars to very distant clusters of galaxies and active galactic nuclei. In addition, broadband observations of non-thermal emission from extremely energetic particles (mostly electrons) were a favorite research subject of *Hitomi*. *Hitomi* which planned to conduct these observations using a wide band coverage and high resolution spectroscopy.

Hitomi had an onboard two X-ray focusing optics systems, called the Soft X-ray Telescope (SXT) and the Hard X-ray Telescope (HXT), together with four imaging and/or spectroscopic detectors jointly covering a wide energy range, 0.3 keV to 600 keV. Major parameters of the four detector systems are listed in Table 4.1. The Soft X-ray Spectrometer (SXS) and the Soft X-ray imager (SXI), where placed on the SXT focal planes at a focal length of 5.6 m and measured in the soft X-ray energy band ($E < 12$ keV). The SXS is a micro calorimeter spectrometer and has a very high energy resolution $\Delta E = 7$ eV. In contrast, the SXI is an imaging instrument consisting of two X-ray CCD cameras, and can determine the two-dimensional position and energy (with poorer ΔE than the SXS) of individual X-ray photons. In hard X-ray band ($E \sim 5$ to 80 keV), the Hard X-ray Imager (HXI) performed imaging spectroscopy of each incoming photon, using two identical sensors which were put on a focal plane of the HXT. Each HXI sensor was comprised of a stacked semiconductor detector, consisting of 4 layers of

Table 4.1: Key parameters of the four payload detectors (adopted from Takahashi et al., 2016).

| Parameter | Hard X-ray Imager (HXI) | Soft X-ray Spectrometer (SXS) | Soft X-ray Imager (SXI) | Soft γ -ray Detector (SGD) |
|--------------------------|------------------------------|--|--|--|
| Detector technology | Si/CdTe cross-strips | micro calorimeter | X-ray CCD | Si/CdTe Compton Camera |
| Focal length | 12 m | 5.6 m | 5.6 m | – |
| Effective area | 300 cm ² @ 30 keV | 300 cm ² @6 keV 250 cm ² @1 keV | 350 cm ² @6 keV 370 cm ² @1 keV | >20 cm ² @100 keV Compton Mode |
| Energy range | 5 – 80 keV | 0.3 – 12 keV | 0.4 – 12 keV | 60 – 600 keV |
| Energy resolution (FWHM) | < 2 keV (@60 keV) | < 7 eV (@6 keV) | < 200 eV (@6 keV) | < 4 keV (@60 keV) |
| Angular resolution | 1.7 arcmin (@30 keV) | ~1.2 arcmin | ~1.3 arcmin | – |
| Effective Field of View | ~ 9 × 9 arcmin ² | ~ 3 × 3 arcmin ² | ~ 38 × 38 arcmin ² | <0.6 × 0.6 deg ² (< 150 keV) |
| Time resolution | 25.6 μ s | 5 μ s | 4 s/2 s/0.5 s/0.1 s | 25.6 μ s |
| Operating temperature | –25°C | 50 mK | –120°C | –20°C |

DSSD (§3.2.2) plus another layer of double-side strip CdTe device and was mounted on the end of extensible optical bench (EOB) of length of 6 m. The Soft Gamma-ray Detector (SGD) covered the highest energy band up on soft gamma-ray, $E \sim 600$ keV. The SGD does not use any focusing telescope. Details of the SGD are described in §4.2 and §4.3, since this thesis utilize the data taken in orbit with the SGD.

4.2 Overview of the Soft Gamma-ray Detector

The Soft Gamma-ray Detector (SGD) is a scientific instrument meant to detect the softest gamma-rays in an energy band from 60 to 600 keV. Thus, the SGD enables us to study non-thermal emission from relativistic particles accelerated in various astrophysical objects, including jets from accreting black holes, shocks in expanding supernova remnants, fast-spinning pulsars, and gamma-ray burst. Although the main purpose of the SGD is continuum spectroscopy, its additional objectives including gamma-ray polarimetry, and the study of e^+e^- annihilation lines.

The SGD utilizes two identical sensor units, mounted on the left and right sides of the spacecraft (Figure 4.2). Each unit, in turn, is composed of three nearly identical Compton cameras, all based on the Si/CdTe architecture explained in §3.2. These 6 Compton cameras are aligned along the spacecraft long axis, and measures the direction and energy of each gamma-ray photon arriving from the same direction as observed by the other onboard instruments. The six Compton cameras work simultaneously and independently. Having these 6 cameras

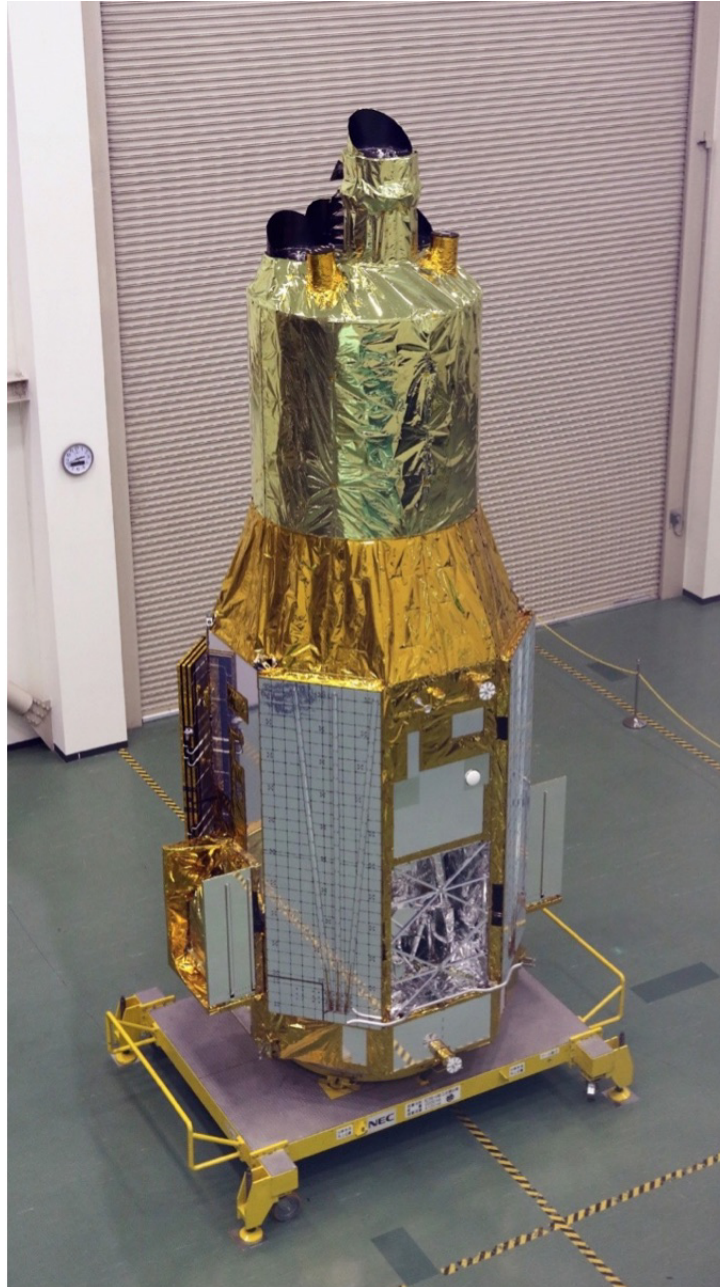


Figure 4.1: A photograph of the *Hitomi* satellite, with the EOB and solar panels removed (from Takahashi et al., 2018).

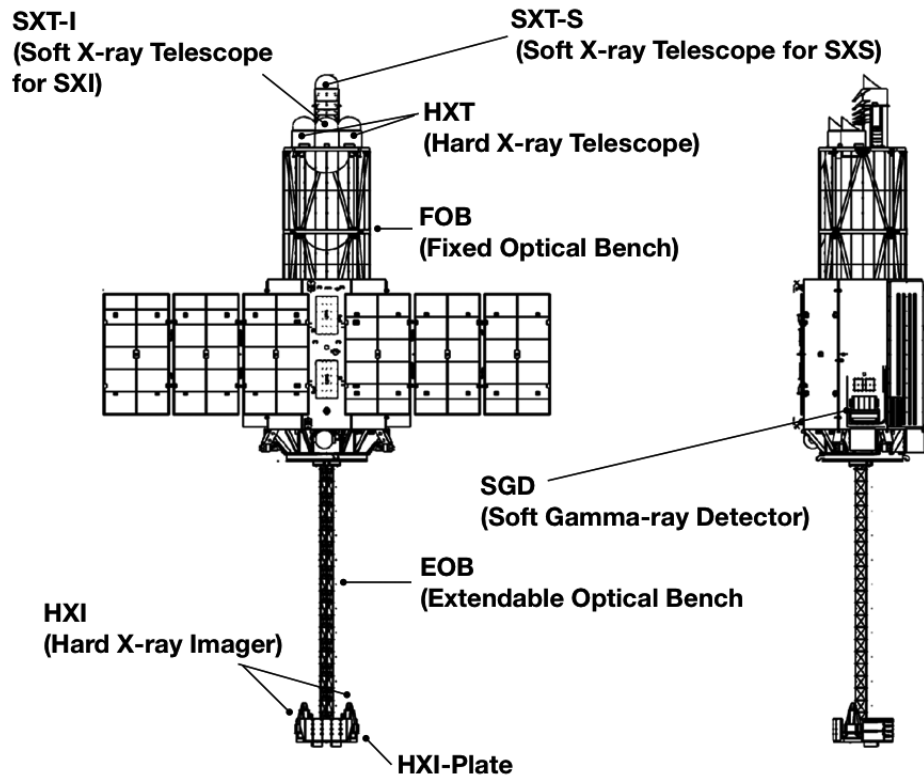


Figure 4.2: A schematic view of *Hitomi*. The EOB and solar panels are extended (from Takahashi et al., 2016).

is simply to obtain enough effective area. The configuration and structures of each Compton camera is described in §4.3.1, and the Si and CdTe devices are explained in §4.3.2. In addition, §4.3.3 gives a description of the front-end electronics installed inside each camera.

The SGD employs another novel concept of “narrow field of view” achieved with a combination of active and passive shields. That is, each Compton camera is installed inside a well-shape active shield made of $\text{Bi}_4\text{Ge}_3\text{O}_{12}$ (BGO) scintillators. This technique adopted from Hard X-ray Detector (HXD) on board *Suzaku*. The BGO shield of the *Hitomi* SGD has two functions. One is simply to reduce backgrounds, such as cosmic X-ray background or high energy charged particle, through anti-coincidence, like in the *Suzaku* HXD. The other is to constrain the camera’s opening angle of its axis to within $\sim 10^\circ$. By doing so, we can discard those sectors of each Compton cone which fall outside the 10° opening. An event can be totally rejected as a background if its Compton cone has no common intersection with the opening solid angle. The configuration of the BGO shield is detailed in §4.3.4. Furthermore, passive fine collimators made of PCuSn metal are placed in front of each camera so to further collimate the field of views in < 100 keV down to $30'$ FWHM. As detailed in §4.3.5, this helps us to reduce the Cosmic hard X-ray background. Figure 4.3 shows the schematics of the SGD.

4.3 Components and Structure

4.3.1 Si/CdTe Compton camera

As shown in Figure 4.4, each Compton camera of the SGD is composed of the scatterer (yellows) and the absorber (gray). The former, in turn, consists of 32 layers of Si pad detectors, whereas the latter 8 layers of CdTe pad absorber (CdTe-Bottom) plus two layers of CdTe pad on each side. In this way, the absorber surrounds the scatterer from 5 sides. A layer of CdTe-Bottom is composed of four CdTe detectors, and a layer of CdTe-Side is composed of six CdTe detectors. Consequently, one camera uses 32 Si detectors and 80 CdTe detectors. As detailed in §4.3.2, one Si detector has 16×16 square pads, and one CdTe detector 8×8 square pads. Therefore, the total number of readout channels becomes $16 \times 16 \times 32 + 8 \times 8 \times 80 = 13312$. The number of channels in one Compton camera is 13312.

The dimensions of a Compton camera including readouts is about $12 \times 12 \times 12\text{cm}^3$. The readout uses application specific ICs (ASICs) with low noise and low power consumption. There are 208 readouts in each Compton camera. A daisy chain connection is carried out eight readouts for Si or CdTe-Bottom and six readouts for CdTe-Side, which results in a total of 28 systems of daisy chain connections. Readouts or parameter settings are carried out on every system. Four systems for Si, one system for CdTe-Bottom and two systems for CdTe-Side are summarized in an ASIC Driver Board (ADB). Four ADBs are connected to an ASIC Control Board (ACB). On board the ACB is a Field Programmable gate array (FPGA) (called CC FPGA hereafter), and it controls the signals of each ASICs. These readout front-end electronics including the ASICs and addition circuits only consume 6 W.

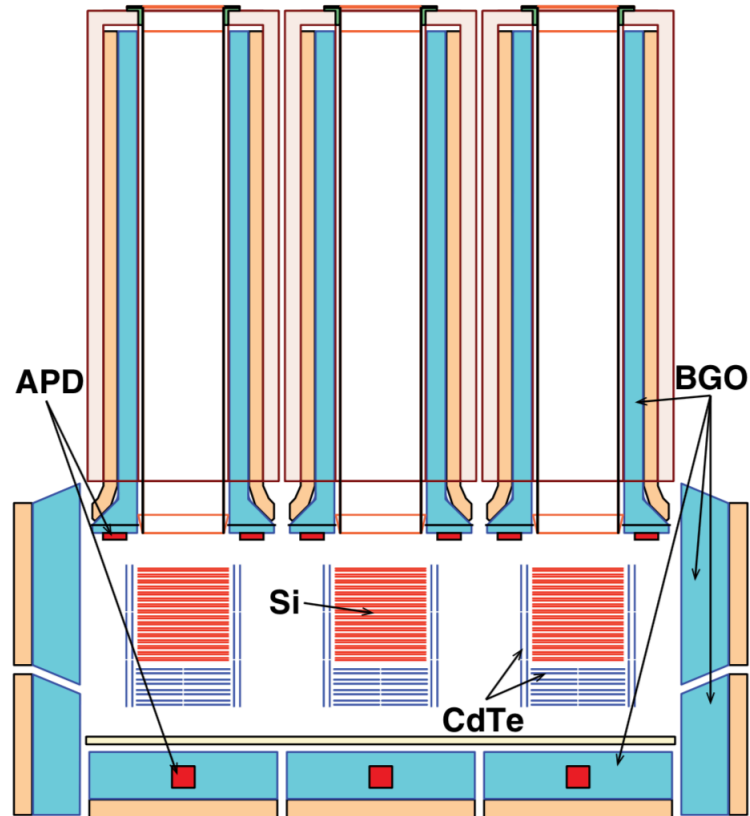


Figure 4.3: Schematics of the SGD. The SGD's Compton camera is constructed by stacking Si (red parts) and CdTe (blue parts) detectors. For anti-coincidence, each Compton camera is surrounded with BGO scintillators (light blue). These signals are readout by APDs (red box). Fine collimators are put on the front of each Compton cameras.

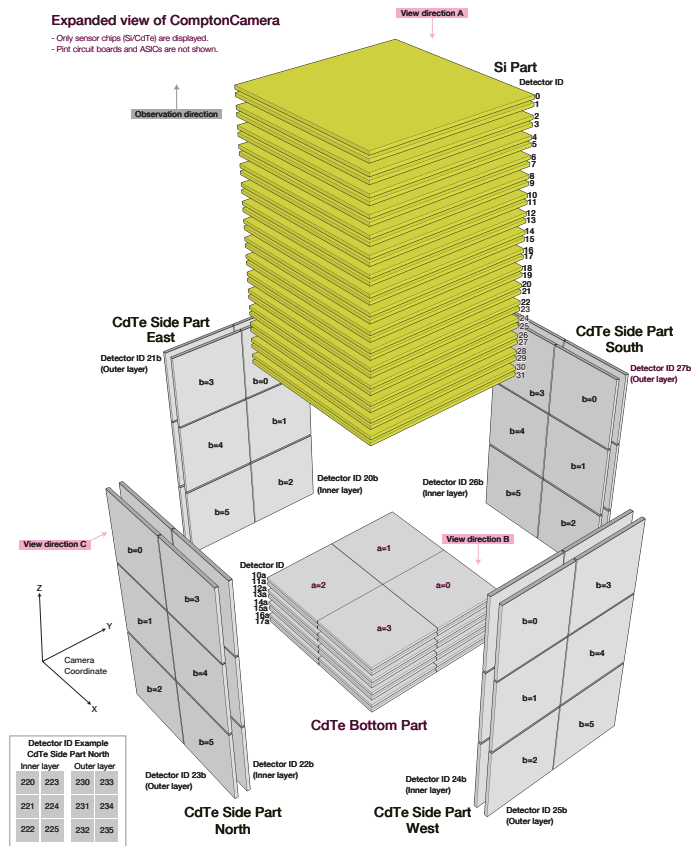


Figure 4.4: A schematic of the Compton camera. The yellow squares are the stacked Si detectors, and the gray squares are CdTe detectors which is separated to two parts, CdTe-Bottom and CdTe-Side.

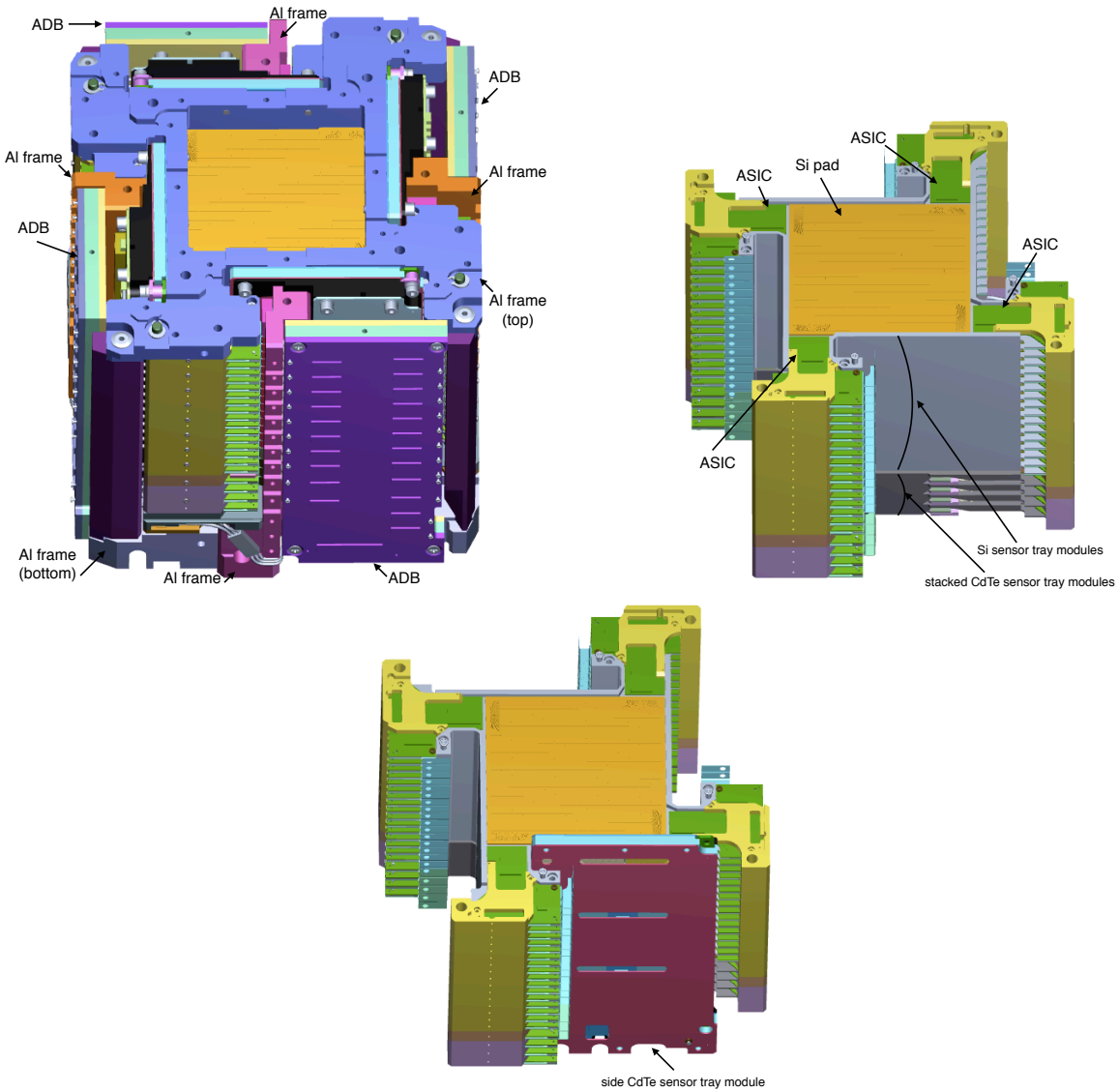


Figure 4.5: (Top left) 3D model of Compton camera. (Top right) Exhibit the Si and CdTe stacked layer. (Bottom) On CdTe-side tray with stacked layer part.

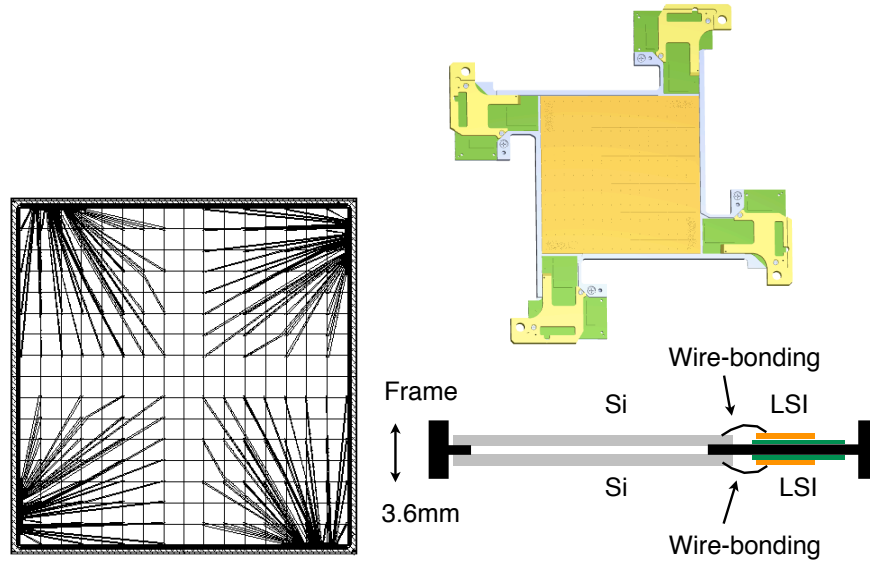


Figure 4.6: (Left) A schematic connection layout of Si and its readout paths. (Right) 3D model of one Si tray.

4.3.2 Si pad and CdTe pad detectors

The Si detector used in the SGD has been developed by ISAS, Nagoya university, Hiroshima university and Hamamatsu Photonics Co. Ltd. The detector has 16×16 pixel electrodes, and a size of $5.12 \times 5.12 \text{ cm}^2$. The operating bias voltage is 230V. The basic parameters are showed in Table 4.2.

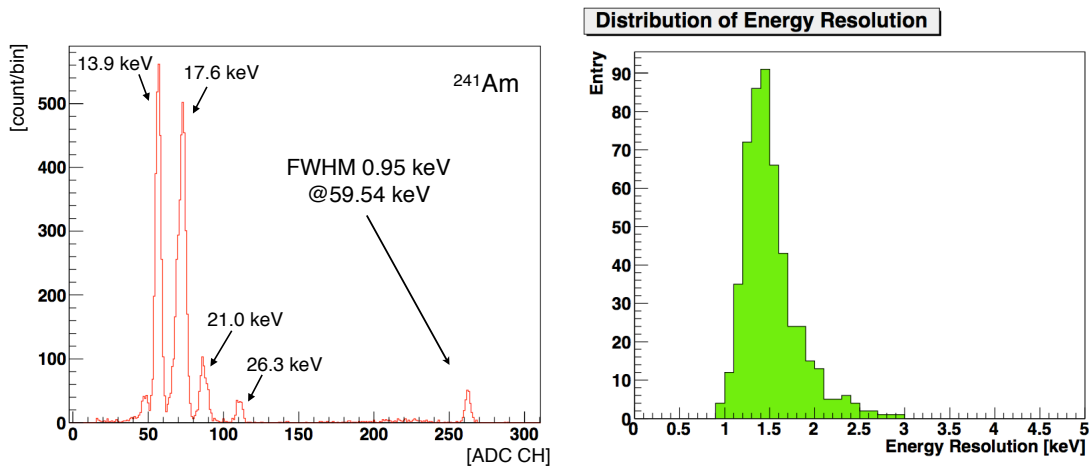


Figure 4.7: (Left) The spectrum of one Si tray irradiated by ^{241}Am . (Right) The energy resolution distribution of one Si tray at 59.45 keV.

The 32 Si pad detectors are arranged in such a way that a pair of them from one tray is shown in Figure 4.6. The two Si pad detectors on one tray are connected by wire bonding to readout ASICs which are placed on the same tray. As described later in §4.3.3, each ASIC has

64 inputs, and hence can read only a quarter of a Si pad. Therefore, one tray has eight readout ASICs.

Figure 4.7 (left) shows a spectrum taken by irradiating ^{241}Am on a Si tray (Watanabe et al., 2014), Figure 4.7 (right) shows the distribution of energy resolution over the 512 pixels on this particular Si tray. Thus, the energy resolution is very high, typically $\Delta E \sim 1.5$ keV at $E = 59.45$ keV, and shows only a scatter among the pixels on the two Si pad detectors.

Table 4.2: Basic parameters of the Si pad detector

| | |
|---------------------------------------|---------------------------------|
| Active area | $5.12 \times 5.12 \text{ cm}^2$ |
| Size of a pixel | $3.2 \times 3.2 \text{ mm}^2$ |
| Number of pixels | 16×16 |
| Thickness of a sensor | 0.62 mm |
| Thickness of active layer in a sensor | 0.60 mm |
| Thickness of inactive layer | 0.02 mm |

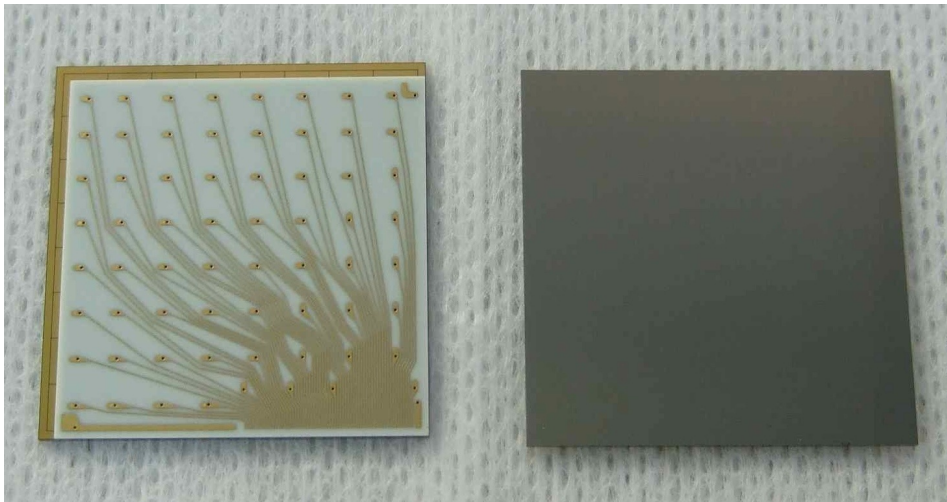


Figure 4.8: Photographs of a CdTe pad detector. The left shows the ceramic fanout board bounded to a CdTe device, and the right shows the plane of common anode electrode (from Watanabe et al., 2014).

The CdTe detectors have been developed by ISAS and ACRORAD Co., Ltd. As shown in Figure 4.8, the detector has 16×16 pixel electrodes and with dimensions of $2.56 \times 2.56 \text{ cm}^2$. The operation bias voltage is 1000 V. Its basic parameters are showed in Table 4.3.

As already described in §4.3.1, each Compton camera uses two absorber parts, CdTe-Bottom and CdTe-Side. In the CdTe-Bottom part, one layer consists of four CdTe detectors, and two layers form one tray as shown in Figure 4.9. In the CdTe-Side part, one layer consists of six CdTe detectors in 2×3 , and two layers are gathered into one tray.

Figure 4.10 shows a spectral performance adopted from Watanabe et al. (2014). The energy resolution of $\Delta E \sim 1.7$ keV, at 122 keV, is achieved thanks to large part of the Schottky-barrier

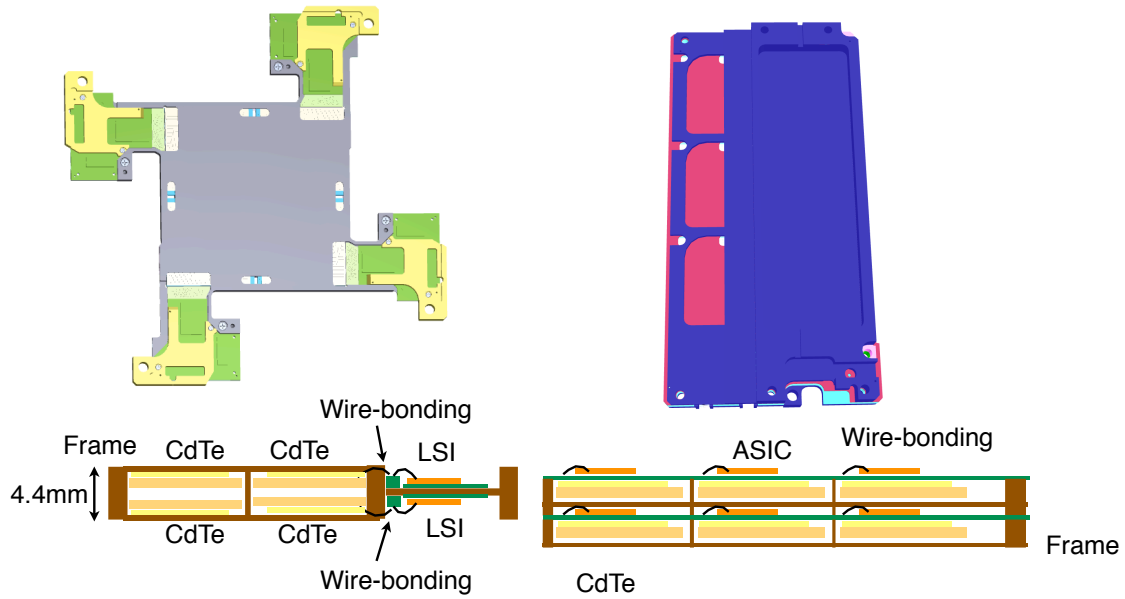


Figure 4.9: 3D modeling of a CdTe-Bottom tray (left) and a CdTe-Side tray (right).

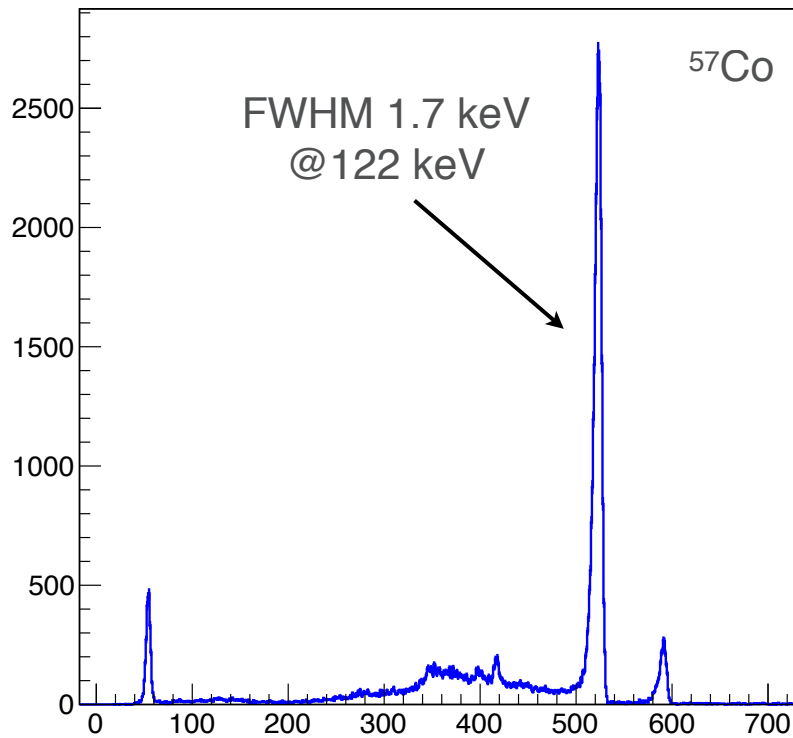


Figure 4.10: A spectrum of one CdTe pad, taken under irradiation with ^{57}Co . The energy resolution is 1.7 keV at 122 keV under a bias voltage of 1000 V and a temperature of -10°C (from Watanabe et al., 2014).

architecture (§3.2.3) and a relatively low ambient temperature ($-10\text{ }^{\circ}\text{C}$), which effectively suppress thermal noise, is for better than those of inorganic scintillators (typically $\Delta E \lesssim 20\text{ keV}$ at $E = 122\text{ keV}$).

It has been known that the energy resolution of the diode type CdTe becomes worse with time. The effect, called “polarization”, is slowly in lower temperature environment and reduce with high bias. In order to suppress the effect, we control the temperature of less than $5\text{ }^{\circ}\text{C}$ and the bias voltage of higher than 1000 V/mm . However, the effect is appeared while a week, we turn on and off the bias voltage to refresh the effect.

Table 4.3: The specification of the CdTe sensor

| | |
|---------------------------------------|--------------------------------|
| Active area | $2.56 \times 2.56\text{ cm}^2$ |
| Size of a pixel | $3.2 \times 3.2\text{ mm}^2$ |
| Number of pixels | 8×8 |
| Thickness of a sensor | 0.75 mm |
| Thickness of active layer in a sensor | 0.75 mm |
| Thickness of inactive layer | N/A |

4.3.3 Front end electronics

As described in Watanabe et al. (2014), the channel readout ASIC, called VATA, for the SGD has low noise and operates at low power. This ASIC is based on the VIKING architecture which has been verified in space experiments with such satellites as Swift, PAMELA and AGILE. As shown in Figure 4.11, this ASIC is divided into two circuit sections; the TA section which is used to generate a trigger and a VA section which outputs a series of digitized pulse heights. One ASIC accepts 64 parallel analog inputs, and each signal is split into the TA and VA sections. The 64 TA signals are independently processed with short-time-constant shapers, and trigger thresholds.

The signal processing commences when an induced charge is processed by charge sensitive amplifier (CSA) which generates a voltage signal. The voltage signal is sent to both the TA section and VA section. The TA section has a shaper whose shaping time is faster than the VA section. The shapers in the TA and VA sections are called as “Fast Shaper” and “Slow Shaper”, respectively. The shaped and amplified signal in the TA section is treated as a trigger signal when the signal is over a threshold, called the “trigger threshold”. After the trigger signal is sent to the CC FPGA in Compton Camera, the CC FPGA sends a sample hold signal to the VA section after a certain time. After the signals of all the channels are converted to digital values by Wilkinson-type analog to digital converters (ADCs). The readout time defines the dead time. To reduce the dead time, we set the digital threshold to each channel.

The ASIC can set a threshold for readout values after analog to digital (AD) converting in every channel, which is called as “digital threshold”. Since the amount of the data is huge if whole ASIC carry out the readout, to suppress the amount of the data and reduce the dead time to read, we set the threshold. The common mode noise of an ASIC is around 1 keV . We take the 32nd ADC value in an ASIC as the common mode noise to subtract the common mode

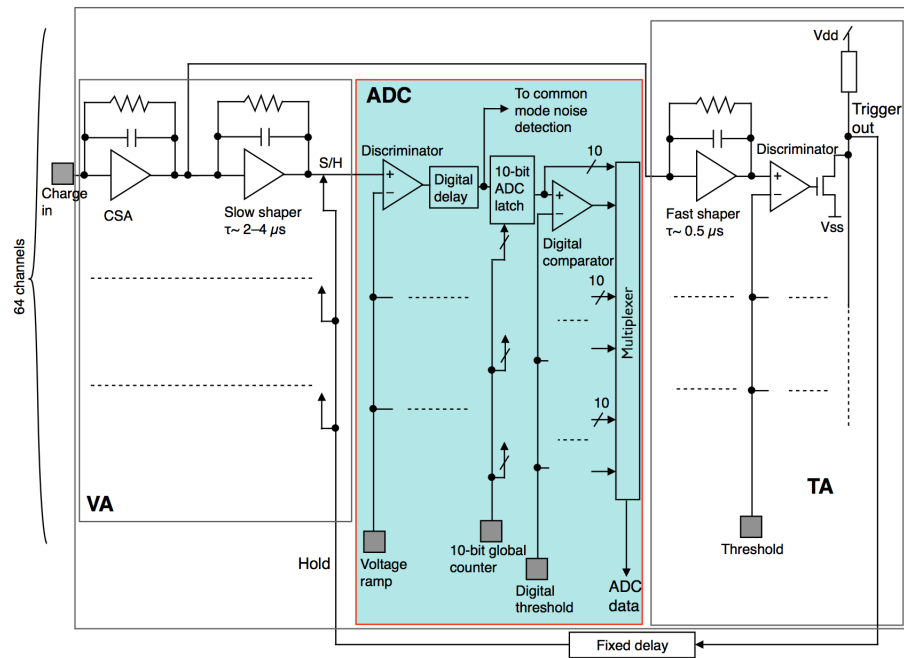


Figure 4.11: The Circuit of one signal channel of one ASIC. After the signal is integrated by a charge sensitive amplifier (CSA), it is split into TA and VA sections. In the former, triggers are generated independently of signals in the other channels. When a trigger is issued, the VA section performs sample-and-hold and analog-to-digital conversion of the same analog signal (but integrated with a longer time).

noise from raw ADC values. The threshold values are set by the ADC value after subtracting the common mode noise.

4.3.4 Active BGO shield

The background is made up of several components which include cosmic rays, radiation from radio activated internal materials and high energy charged particles of South Atlantic Anomaly (SAA). Although the SGD Compton camera can reduce gamma-ray backgrounds by oneself, it is tolerance for the backgrounds by the high energy particles or high energy gamma-rays out of line of sight. Therefore, it is need to prevent from and/or detect the invasion of the SGD Compton camera by the backgrounds.

Compton cameras of the SGD are installed in the well made of 25 Bismuth Germanate ($\text{Bi}_4\text{Ge}_3\text{O}_{12}$; BGO) crystals (see Figure 4.3). The BGO shield has a well-type geometry, which as adopted from the HXD. Each crystal is coupled with avalanche photodiodes (APD) that amplifies the scintillation light in BGO crystal and convert it to digital signals. When the signal in a BGO crystal is detected, the shield system can generate a veto signal. Since the BGO shield reject the background, the field of view of each Compton camera is limited to about 10 degrees square.

BGO is a high Z scintillation material ($Z_{\text{Bi}} = 83$) with a high density of 7.13 g/cm^3 . It also is stable and does not have deliquescence. A BGO crystal can be made larger and is relatively easy to manufacture, and relative to 20 degree temperatures, the amount of luminescence is around 1.5 times higher at the orbital temperature of -20 degrees.

The APD is a compact size $10 \times 10 \text{ cm}^2$ semiconductor photo sensor which operates at high bias voltage levels. The amplification of the BGO scintillation light is proportional to the applied bias voltage, and the APD signal is amplified by a charge sensitive amplifier and converted to a digital signal. The APD is semiconductor photo sensor and need to apply high bias voltage. The APD is compact size rather than a photomultiplier tube which is used to detect BGO scintillation light in HXD.

4.3.5 Fine collimator

The SGD Compton camera detects both target gamma-rays and background gamma-rays in its field of view which is around is about 10 degree \times 10 degree. Additionally, to prevent stray light from entering the detector, fine collimators (FCs) are installed which narrows the field of view to 0.55 degrees and act as a metallic passive shield. The collimator has dimensions of $52 \times 52 \times 300 \text{ mm}^3$ and the thickness of 0.1 mm and is made of phosphor bronze (PCuSn). The interior is divided into 16×16 cells, and each cell has size of 3.2 mm. The opening aperture achieves transmission of about 90 % below 100 keV, as shown in Figure 4.12. Mizuno et al. (2014) demonstrated the performance of the collimator, and confirmed that photons below 100 keV were not transparent out of the field of view.

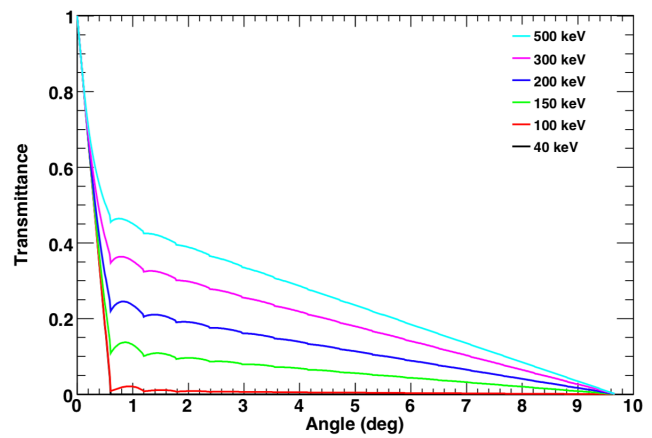
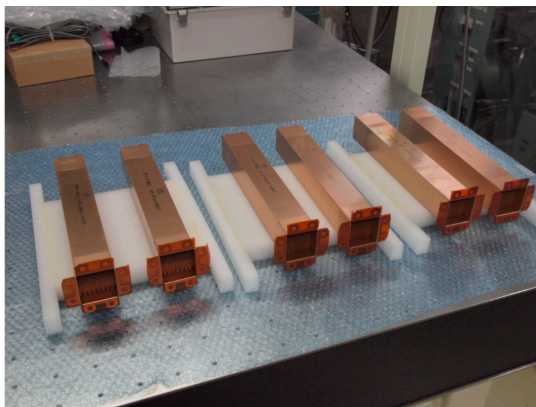


Figure 4.12: (Left) Fine collimator of the SGD. (Right) The transparency of the fine collimator. The higher energy irradiate radiation, the lower transparency fine collimator is as a function of irradiate angle. (The figures are adopted from Mizuno et al., 2014)

Chapter 5

Calibration and Performance Study of the SGD

The hardware for SGD1 and SGD2 was completed by Mitsubishi Heavy Industries (MHI) in November 2014 and January 2015, respectively. To measure the performance of them in extreme environment like space, we carried out experiments on ground for standalone tests and integration tests with the satellite. During implementing these environment tests, we aimed to verify the SGD's energy calibrations and performances to reconstruct a Compton event. After the launch of the satellite, despite a short period of observation time, we can measure background reflected to the orbital environment. In this chapter, we firstly introduce details of these experiments, after that we perform the energy calibration and reconstruction of Compton events, finally we describe the performance in the orbit.

5.1 Experiments on Ground and in Orbit

5.1.1 On ground

The ground tests were carried out as operation test to simulate the space environment. The environment tests, simulating low temperature condition reached ~ -20 °C in-orbit condition which is thermal cycle and in vacuum, implemented step-by-step at Sagamihara campus (Institute of Space and Astronautical Science; ISAS) or Tsukuba space center (TKSC) of Japan Aerospace Exploration Agency (JAXA). After confirming operations of stand-alone in low temperature and thermal vacuum for each SGD, they are assembled to the satellite. We list details of these experiments in Table 5.1.

To confirm performances of the SGD, we irradiated the isotopes during stand-alone experiments. The most important thing of this was to produce energy calibrations for each Compton camera onboard SGD1 and SGD2. We describe the details of it in §5.2.

Operation tests of Compton cameras onboard SGD1

To confirm operations of the Compton camera, it is the test which only uses SGD1 Compton cameras. BGO shields and fine collimator had not been installed into SGD1 then. We put SGD1 into a thermostat chamber with dry air. The experimental environment was assumed to be

Table 5.1: The tests on the ground

| Date | Experiment | Location | assembled components |
|--------------------|------------------------------------|-----------|----------------------|
| 2014/10/12 - 10/19 | Operation tests of Compton cameras | ISAS/JAXA | only SGD1 CC |
| 2014/11/29 - 12/9 | Low temperature test | ISAS/JAXA | whole SGD1 |
| 2014/12/9 - 12/24 | Thermal vacuum test | TKSC/JAXA | whole SGD1 |
| 2015/2 | Thermal vacuum test | TKSC/JAXA | whole SGD2 |
| 2015/2 | Low temperature test | ISAS/JAXA | whole SGD2 |
| 2015/6 | Integrated satellite test | TKSC/JAXA | SGD1 and SGD2 |

orbit conditions and set to -20 °C. Three Compton cameras were operated simultaneously for the first time in this test. There is no shield around the detector to prevent the environmental background counts. Therefore, the background level is higher in all tests.

Low temperature test

This is a full assemble test for the SGD. Operation check of BGO shields was done. The temperature was -20 ± 5 °C. The detector received the blow of the thermostatic chamber which caused noise to the shield system. Therefore, we covered the detector with thermal insulation so that the wind did not hit the detector directly. The chamber prevents the environment background more than the CC BASE2 experiments.

Thermal vacuum test

This test imitated the actual space environment. The vacuum pressure in the chamber was 10^{-4} Pa. There were two temperature mode, low temperature mode ~ -20 °C and high temperature mode ~ 10 °C. In this test, the experiment such as irradiating radio isotopes to the SGD had not carried out.

The chamber is the space chamber $\phi = 8$ m at TKSC. The chamber can simulate the instrument environment in space, such as cryogenic temperature, high vacuum and heat from the Sun. As simulated solar light, Xe lamp irradiate the instruments to be tested.

Integrated satellite test

This is the test of two SGD modules assembled the satellite. We checked the operation with the other instruments on board the satellite simultaneously. It is the first time to operate simultaneously SGD1 and SGD2. The test environment is the same as the thermal vacuum test although the chamber is different.

The chamber is the space chamber $\phi = 13$ m at TKSC. The chamber also can simulate the instrument environment in space, such as cryogenic temperature, high vacuum and heat from the Sun.

5.1.2 In orbit

Hitomi was launched from Tanegashima space center on February 17, 2016. Once in orbit, each

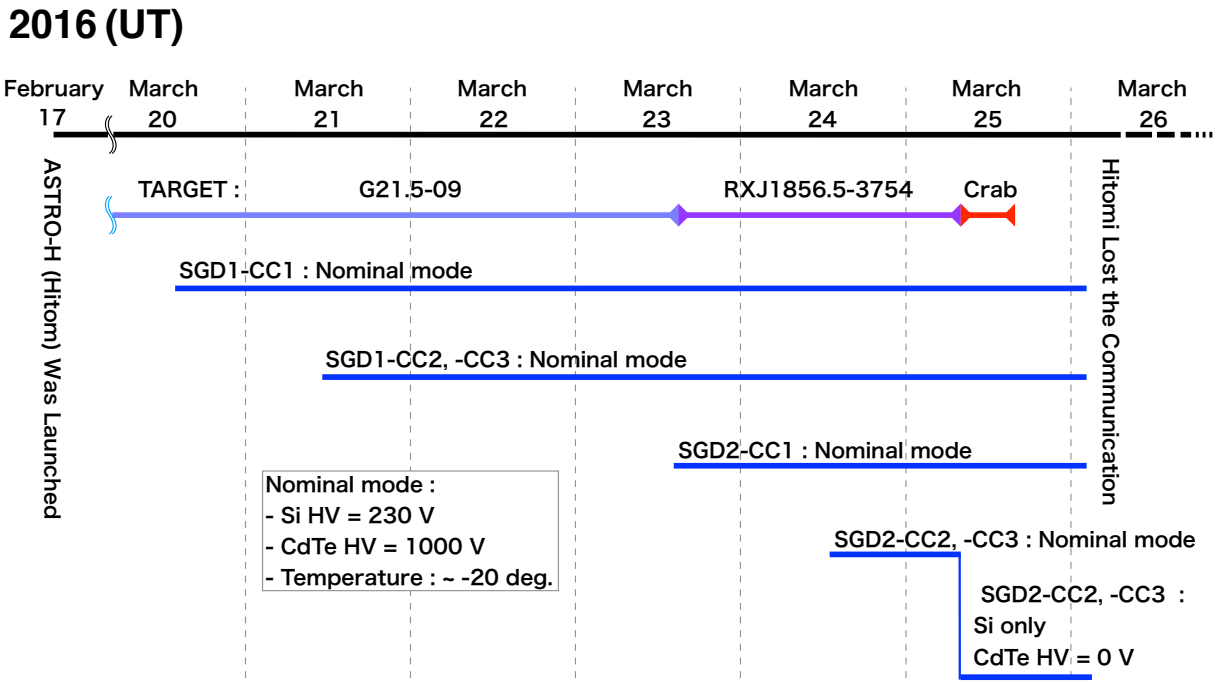


Figure 5.1: Summary of the SGD observation.

detector was started up sequentially and shifted to normal operation. The order of the SGD starting up was the last.

Start-up operation

The operation of the SGD sensors, Compton cameras and the BGO shields, was started on March 15. The instruction of the operation was taken at Uchinoura space center (USC). SGD1-CC1, which was the first operation in preparation for a problem, carefully raised and lowered high voltage of each Si and CdTe sensor. Therefore, the date which SGD1-CC1 shifted to normal operation was on March 20. In the normal operation, the high voltage of each sensors became prescribed states, $V_{\text{Si}} = 230 \text{ V}$, $V_{\text{CdTe}} = 1000 \text{ V}$. We operated to start up remaining Compton cameras of SGD1 and all Compton cameras of SGD2 from March 21 to 24. At that time, the other instruments on board *Hitomi* had already started nominal operation and observed several targets, G21.5-0.9 and RXJ1856.5-3754. Since these objects are dim for the SGD, it is not influence on the confirmation of performance such as background estimation. Before the target had shifted to the Crab nebula, all SGD sensors operated by the nominal mode. We show the operation log in Figure 5.1.

Crab observation

Hitomi observed Crab on March 25, which was the first light for the SGD, and the observation time was about 8.6 ks. The maneuver to Crab was after the first communication with *Hitomi*

at USC. At the second communication, the CdTe high voltage of SGD2-CC2 and -CC3 was set to 0 V, because one channel in CdTe of SGD2-CC2 became noisy. We planned to disturb the trigger of the channel and reapply the high voltage to the CdTe again after the operation of the day. However, *Hitomi* lost the communication with ground after this observation.

5.2 Energy Calibration

The accurate energy determination is important for Compton reconstruction. It also affects the ARM (see §3.1.3). Therefore, we require to establish the energy calibration which can determine the accurate energy.

The readout is ASIC for the SGD with 64 channels (see §4.3.3). Since the each of channels has charge sensitive amplifier (CSA), we need to evaluate the energy calibration for each channel.

An analogue information of the deposit energy in the pixel of the detector is digitalized by ASIC. We must reconvert the digitalized signal into the analogue quantity in energy space. The converter, described in §4.3.3, is not every detector but every pixel. Because there are 64 channels in an ASIC, we need to know functions to reconvert the signal into the energy for 13312 channels in a Compton camera.

An ASIC equip a test pulse generator common to channels. The generator inputs a charge to the converter for each channel. The input charges are generated by a digital-analogue converter (DAC), and it can be expressed by

$$Q = Q_{\max} \frac{1}{127} (b_0 + 2b_1 + 4b_2 + 8b_3 + 16b_4 + 32b_5 + 64b_6), \quad (5.1)$$

where Q_{\max} is maximum value of input charge and b_0 to b_6 are bits. The DAC supplies a charge by the combinations of the bits. Hereafter, the combination is called DAC value.

The ASIC, 64 channels can be aligned against DAC value if it is able to calibrate between ADC and DAC values. Then we obtain a relation $\text{DAC} = F(\text{ADC})$. After that, if the energy is calibrated against DAC, we also obtained the relation between ADC and the energy for each channel, $E = G(\text{DAC})$. Finally, we get a function to convert an ADC value into an energy $E = G \circ F(\text{ADC})$.

5.2.1 Contents of test pulse experiments

The flow of the injection of test pulse (or calibration pulse) is as follows.

1. Set all the modes of the Compton camera to standby, and turn on the calibration function of the Compton camera that inputs the test pulse.
2. Send a command to set the ASIC register for ASIC calibration to DE
3. Set minimum value, maximum value of input charge, DAC value of step interval in ASIC register
4. Select which channel in the ASIC to output test pulses and execute

Table 5.2: Set values related to input charge of Si and CdTe

| | | minimum DAC value | maximum DAC value | step |
|------|------------------------|----------------------|---|---|
| Si | all channels | 2 | 38 (for SGD1-CC1) 37 (for the other CCs) | 9 (for SGD1-CC1) 7 (for the other CCs) |
| | channel number 16 & 40 | 2 | 44 | 1 |
| CdTe | all channels | 5 | 77 | 18 |
| | channel number 16 & 40 | 2 | 80 | 1 |

5. Change the DAC value to change the output charge. The charge amount is increased according to the step interval until the output charge reaches the set maximum value.
6. When the maximum value is reached, select the next channel or turn off the test pulse function.

When inputting the test pulse, it is possible to flag a trigger expressed calibration pulse. Through this test, the trigger was flagged not at the same time as injection but after a fixed time delay. Injection of the test pulse was carried out separately for Si and CdTe. The maximum input charge, different from the maximum value of input charge, was set to 44 fC.

We carried out this test through the all ground test excepted integration satellite test for each CC. Table 5.2 show the set values related to input charge of Si and CdTe.

Experiment contents is roughly,

- For Si and CdTe, input DAC values at certain intervals shown in Table 5.2 for all channels in the ASIC.
- For channels 16 and 40, we set the interval of DAC input as 1.

If we input a charge corresponding to the DAC value at step interval 1 to the test pulse as one channel, it takes 30 minutes to acquire data for one channel. To shorten the time, we injected into channels 16 and 40 in the ASIC, instead of input charge at interval 1 for all channels.

Step 1: Evaluating the ADC value corresponding to injection charge, DAC

The charge injected as test pulse is converted to ADC value and outputted. Figure 5.2 shows the histograms which test pulses were injected by intervals of 7 and 1 at one channel of Si. Each peak was fitted with Gaussian and the ADC value for the DAC value was obtained.

Step 2: Bit shift of DAC values

In order to get the function $DAC = F(ADC)$, we try to fit the relation between ADC and DAC values using third-order polynomial for the channel the injection interval is 1. As shown in Figure 5.3, it seems that the residuals are systematically fluctuated. The cause of variations is

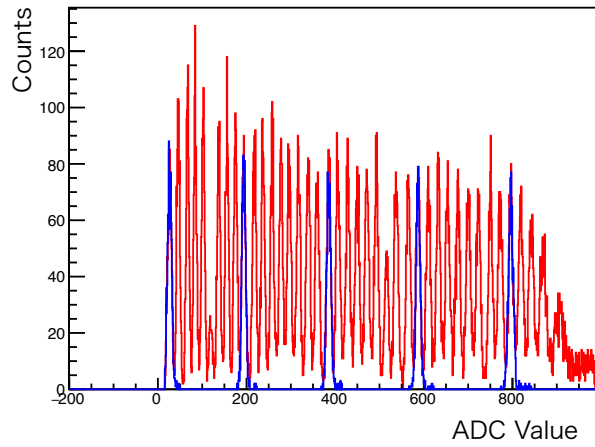


Figure 5.2: One channel spectra of a Si detector. Red histogram shows the spectrum of injecting charge with interval of 1. Blue histogram shows one of injecting charge with interval of 7.

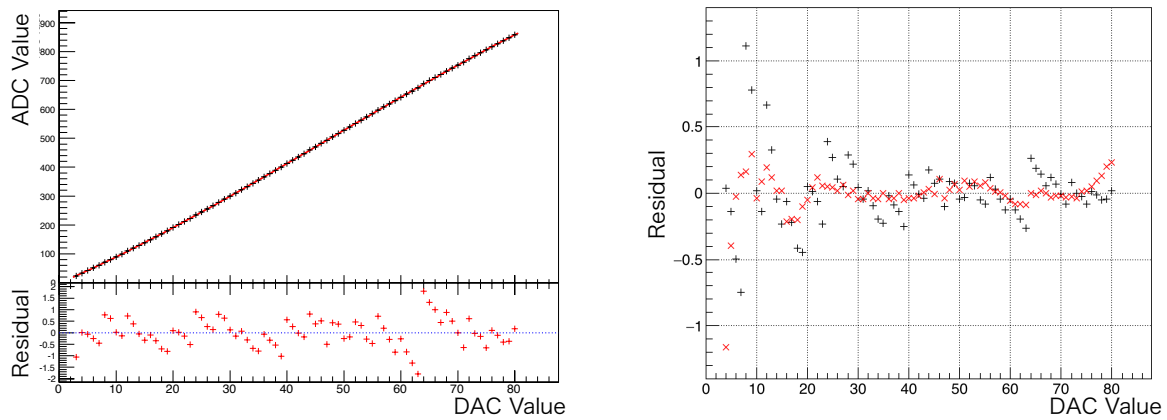


Figure 5.3: (Left) The result to fit the relation between ADC and DAC values with third-order polynomial. (Right) The residuals of the fitting results with and without bit shift correction factor.

because of the digital analog converter is 7 bits. Injected test pulse followed Equation 5.2. To correct the influence, we take the correction factor as

$$Q = Q_{\max} \frac{1}{127} (t_0 b_0 + 2t_1 b_1 + 4t_2 b_2 + 8t_3 b_3 + 16t_4 b_4 + 32t_5 b_5 + 64t_6 b_6), \quad (5.2)$$

where $t_1 \sim t_2$ are correction factors. The correction factors ideally take on the value of 1. We show the residuals with and without bit shift correction factor in Figure 5.3.

Step3: Interpolation

After correcting bit shift, we interpolate the relation of ADC and DAC for the interval is not 1 DAC. The channels 16 and 40 of all ASICs were injected by interval 1 and 7 or 18. We consider the channel which injection interval is 1 to be reference point for the other channel. We interpolate the calibration point with reference to the channel that gets the calibration point at step interval 1 between the calibration points of these 62 channels at each ASIC. As for the interpolation method, first, the differences between the respective ADC values is obtained as a commonly obtained DAC value. Next, consider the line segment connecting the differences, add the increment when the DAC value increases by 1 to the ADC value obtained at step interval 1. This completes the calibration of the ADC value and DAC value of all 13312 channels, and $F(\text{ADC})$ has been completed.

Step4: Evaluation the relation between the injected charge and the energy

We evaluate the energy corresponding to the injection charge. By using the data recorded the radio isotopes irradiation, we calculate the $E = G(\text{DAC})$.

Step5: Connect the relations

We connect the functions $\text{DAC} = F(\text{ADC})$ and $E = G(\text{DAC})$ and obtain the calibration function $E = G \circ F(\text{ADC})$. Figure 5.4 shows one of the results to calibrate the ASIC for energies of Si and CdTe sensors.

5.2.2 Calibration status

We show the calibration status in Figures 5.6 and 5.7 for each detector section, Si, CdTe-Bottom and CdTe-Side. Regarding SGD1, correctness was confirmed by a line of gamma rays not used for calibration less than 1 keV. Since the CdTe detectors are covered with various substances around the SGD assembled, it is difficult for gamma-rays from a direct source to reach. Especially, the influence was remarkable on the low energy side, and there was no way to confirm during the ground test. After launch, when we check the calibration of the CdTe detector using the data on the orbit, it was confirmed that the deviation was on the low energy side. At this time, the line of gamma rays used for confirmation is the gamma ray emitted by the detector and its surrounding substances being activated. We used this gamma ray again to calibrate the CdTe detector. The results are shown in Figure 5.8.

The energy resolution was shown separately for each type of detector in Figure 5.9. Since a deviation of 1 keV is equivalent to a deviation of ARM by 5 degrees, high energy resolution is

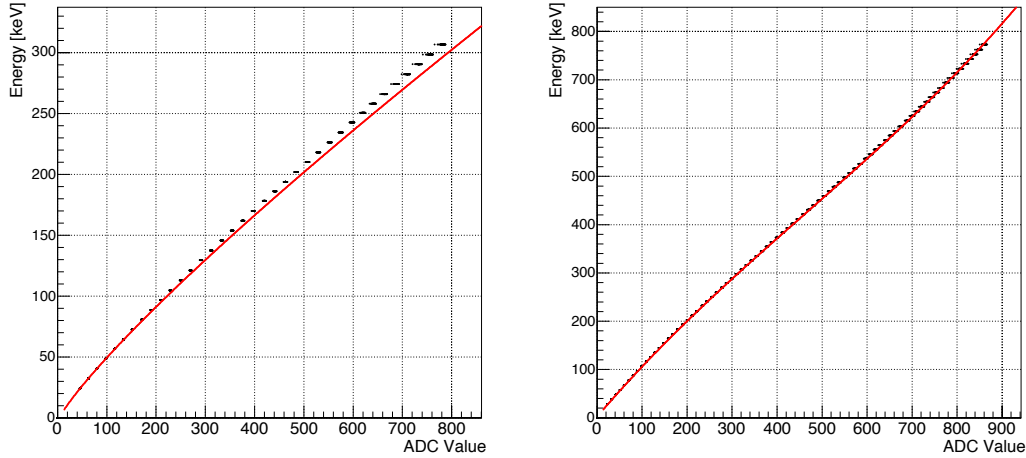


Figure 5.4: Calibration curves for Si (left) and CdTe (right). The black points are obtained calibration relation between ADC and energy for Si and CdTe, and the red curves are obtained by using only the energy peaks of radio isotopes.

required. As the result of energy calibration, the same trend was seen although it has a range depending on the SGD Compton Camera. The resolution for energy of 511 keV was almost 7 keV or less for most detectors. Therefore, the energy resolution achieves less than 2%.

The gain calibrations for each Compton camera are carried out by using data obtained by experiments on ground and in orbit. Corrections for variations of each channel by using DAC is carried out in ground based experiments. Energy definitions are needed to use photoelectric absorption peaks from isotopes. In experiments on ground, we irradiate isotopes. Since one SGD is densely stacked with Si and CdTe semiconductor, the lower energy gamma-ray absorbed by the detector near an irradiation position and the higher energy gamma-ray is scattered by detectors. As a result, the CdTe detector's energy calibration was not satisfied. Therefore, we used the line gamma-ray emitting from radio activated detector.

Table 5.3: Correction coefficients for Si-CdTe event

| SGD CC# | coefficient |
|----------|-------------|
| SGD1-CC1 | 1.33 |
| SGD1-CC2 | 1.32 |
| SGD1-CC3 | 1.33 |
| SGD2-CC1 | 1.33 |
| SGD2-CC2 | 1.4 |
| SGD2-CC3 | 1.4 |

When an incoming gamma-ray is scattered by a Si detector, the ASIC connected to the Si detector does not transmit a trigger. Converting ASICs signal into ADC value, the ADC values is underestimated comparing the signal with trigger in itself (shown in Figure 5.10. Because

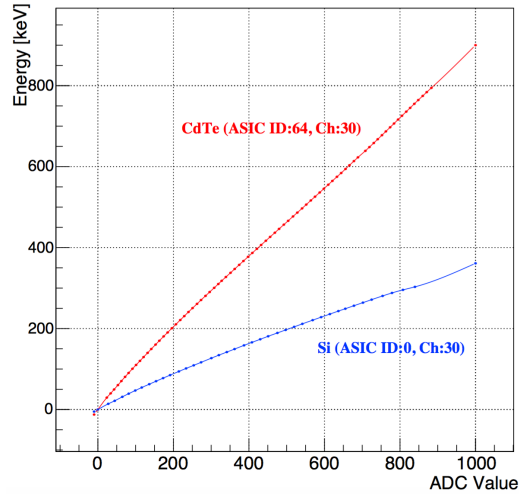


Figure 5.5: Calibration curves of Si and CdTe

the ADC values is decrease linearly, the Si calibration curve is scaled by a coefficient prepared for each Compton camera to deal with the effect. The coefficients are shown in Table 5.3. We call the calibration file applying the coefficient “ALTGAIN” (alternative gain).

The results are released as calibration data base (CALDB) from Goddard Space Flight Center (GSFC) of NASA, which the newest version is 20140101v3. Two types calibration files are included in them, “GAIN” and “ALTGAIN”.

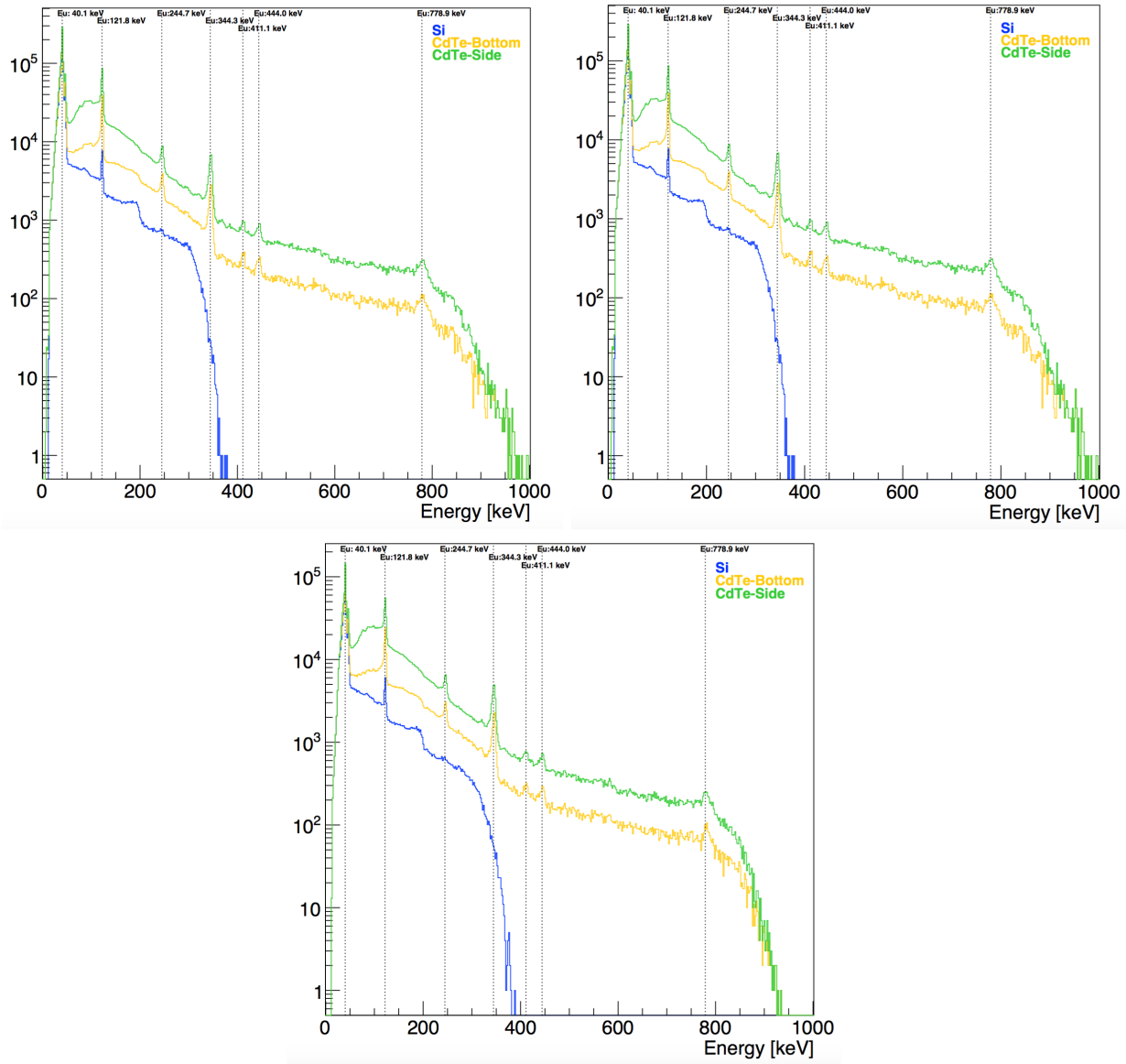


Figure 5.6: Spectra after calibrations for SGD1. Top left shows spectra of Compton camera 1 in SGD1, top right shows ones of Compton camera 2, and bottom shows ones of Compton camera 3. Blue, yellow and green histograms show sum spectra of Si, CdTe Bottom and CdTe Side, respectively. Perpendicular dashed-lines indicate energies of isotopes irradiated for confirming energy determination of Si and CdTe detectors.

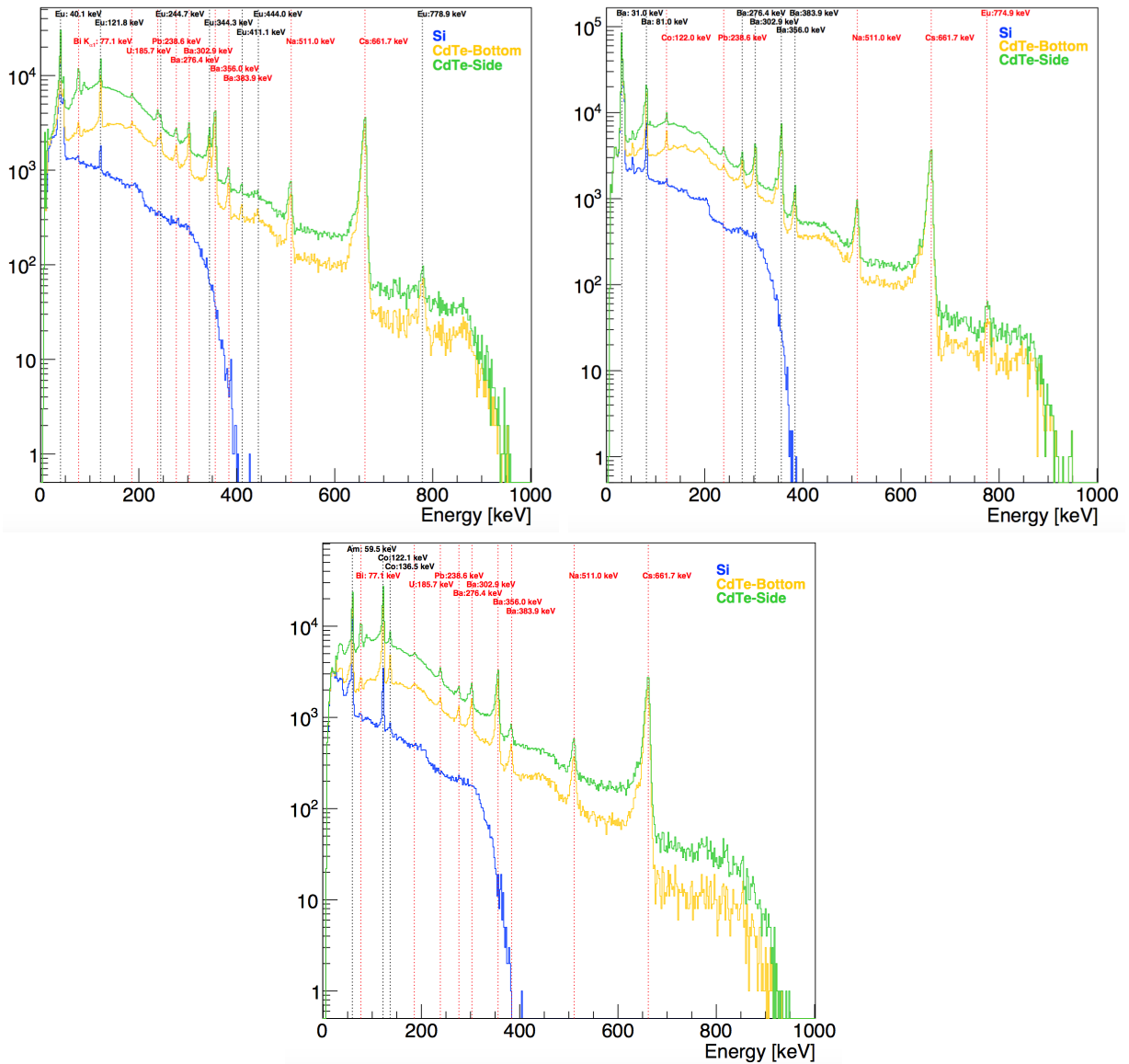


Figure 5.7: Spectra after calibrations for SGD2. Top left shows spectra of Compton camera 1 in SGD2, top right shows ones of Compton camera 2, and bottom shows ones of Compton camera 3. Blue, yellow and green histograms show sum spectra of Si, CdTe Bottom and CdTe Side, respectively. Black perpendicular dashed-lines indicate energies of isotopes irradiated for confirming energy determination of Si and CdTe detectors. Red perpendicular dashed-lines indicate energies of isotopes irradiated for calibration.

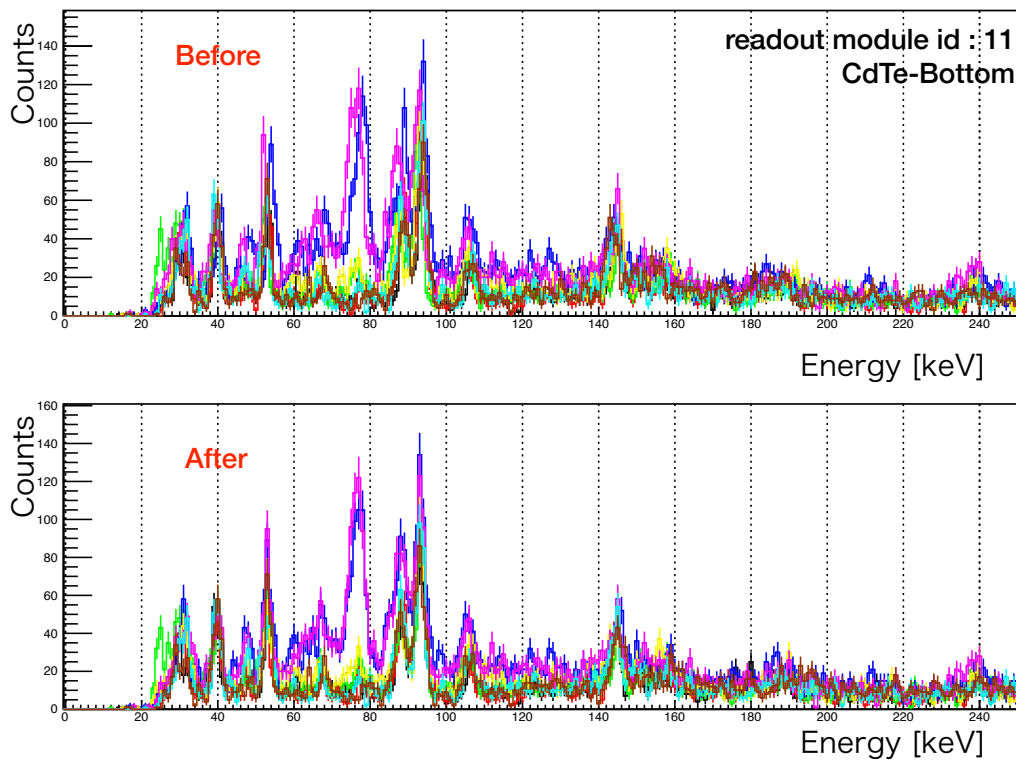


Figure 5.8: Spectrum of CdTe included in a module. Upper panel show spectrum created by calibration obtained by ground test. Bottom panel show spectrum corrected by using data in orbit. The type of gamma ray appearing in the spectrum differs depending on the location of the detector.

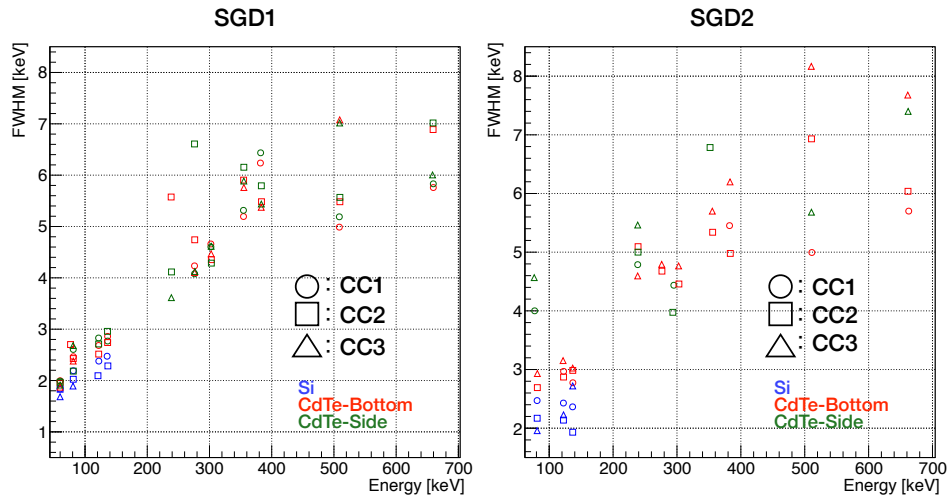


Figure 5.9: Energy resolutions for each detector section, Si, CdTe-Bottom and CdTe-Side, of each SGD Compton camera. The shapes of each point indicate each Compton camera. The colors indicate each detector section Si, CdTe-Bottom and CdTe-Side.

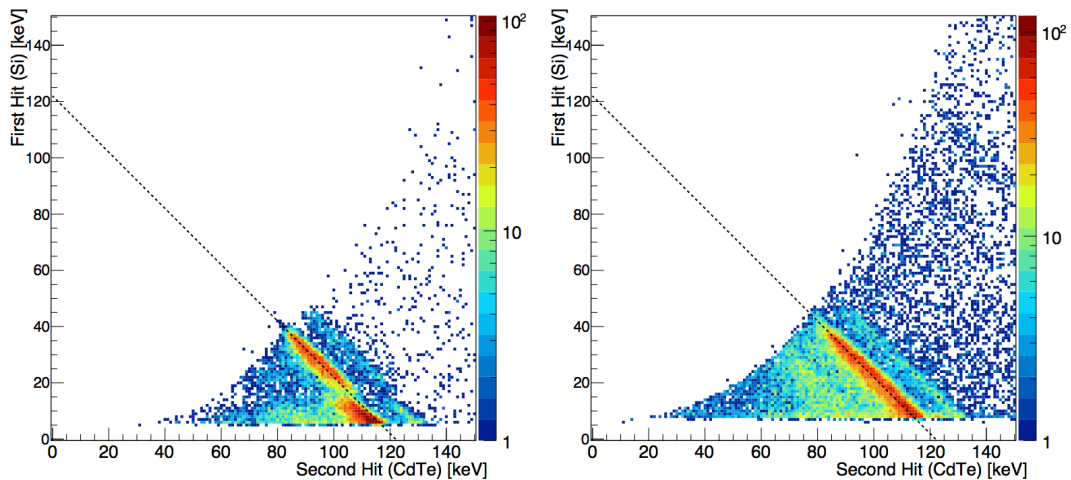


Figure 5.10: Si un-triggered events. Horizontal and perpendicular axes indicate energies of Si as a scatterer and CdTe as an absorber of each of panels. Dashed lines show 122.2 keV. Left and right panel is before and after revising of energy of Si.

5.2.3 Software thresholds

In connection with the gain calibration, we prepared threshold to cut off noise, which is called software threshold. Unlike the trigger threshold, the threshold is used at the time when we analyzed the data off line. We use the threshold to reject the noise signal related to readout of the ASICs. When the signals are obstacle to reconstruction of the event, we set the unnecessary high value to the applied channel. Therefore, we produced the software threshold for each channel in the Compton camera. Figure 5.11 shows the software threshold for each SGD Compton camera. The thresholds are basically around 7 keV and 12 keV for Si and CdTe detectors, respectively, and the noisy channels were set to higher values. For SGD2-CC2 and SGD2-CC3, we are not optimizing the threshold because these detectors were not performed for analysis of Crab.

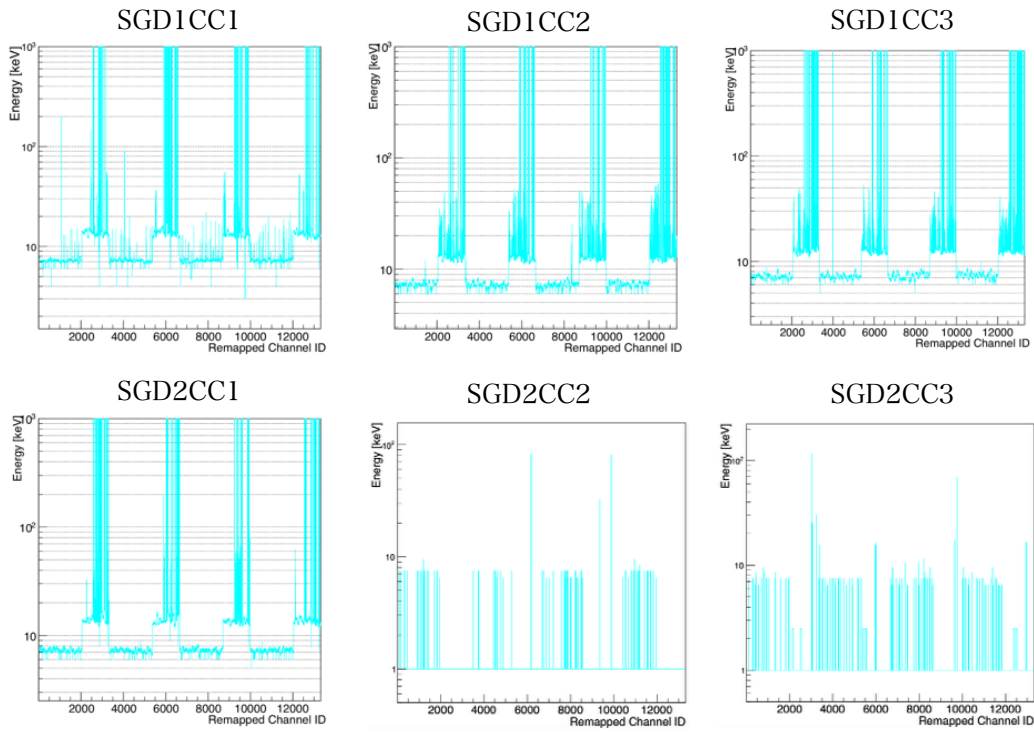


Figure 5.11: Software thresholds of each SGD Compton camera. SGD2-CC2 and SGD2-CC3 was not optimized because they do not use to analysis of Crab.

5.3 Data analysis method

An event is classified into two modes, one is the photoelectric absorption mode and the other is the Compton mode. The former mode is when an incoming gamma-ray is absorbed in a semiconductor detector. The latter mode is when an incoming gamma-ray is scattered by Compton effect and the scattering photon is absorbed or escapes out of a Compton camera. These classifications are determined after event reconstruction (see §5.3.1).

The SGD is available in two types data format. One is ROOT which is a familiar data format for high energy physics. It was developed by CERN, and its newest version is 6.02. We basically use this data format to analyze energy calibration and so on. On the other hand, the other one is Flexible Image Transport System (FITS) which is familiar data format for astronomy. This is formal data format for the observation data in orbit. We have provided some software to analyze the data corresponding to this format. The software is one of FTOOLS which is included in HEASoft provided by GSFC/NASA. For the SGD, there are three tools: (1) `hxisgdsff` which is to reassign position information to each signal in a raw data, (2) `hxisgdpha` which is to carry out gain calibration in data, (3) `sgdevtid` which is to reconstruct events. Although the data format is two types, the analysis procedure is basically carried out same way. We show the methods in the case of the obtained data format is FITS.

The data processing is carried out in the following process. Since the raw data does not include position information for each signal, the information is reassigned by `hxisgdsff`. We call the data style Second FITS File (SFF). When the signals in SFF are calibrated by `hxisgdpha`, the ADC values are converted into energies with randomizing because of the ADC is digital value. Finally, all occurrences are reconstructed by `sgdevtid` after the signals which are not over software threshold are ignored. Then, the signals are reconstructed to hits, and the event is classified by number of hits. If the number of hits is one, it is suggested that the event is photoelectric absorption. If the event includes some hits, the event is the candidate of Compton event. To determine that the event is a Compton event, a Compton reconstruction is carried out in `sgdevtid`. If a Compton reconstruction is success, the event is recoded to output file.

5.3.1 Event reconstruction

The SGD Compton camera has 13312 channels per a unit. The readout is conducted simultaneously by the SGD ASIC (see §4.3.3). Then, the data in an occurrence is only recorded the positions and deposit energies of every signals. Therefore, it is impossible to know the order of hit after readouts. In an occurrence, there are signals such as scattering and absorption of scattered and/or fluorescent photons. To know correctly the order of hits, it is need to reconstruct these signals.

We have examined the reconstruction method (the detail discussion is found in Ichinohe et al., 2016). The method has two procedures, to merge signal and to estimate the order of hits.

Merging the signals

The origins of recorded signals are not only scattering and absorption as the results of Compton scattering and physical processes with scattering, e.g. X-ray fluorescence or recoil electron,

or noise of readout. Although the noise of readout is cut by threshold to prepare for each channel, the signal caused by physical processes is remained. The signal not caused by Compton scattering confuse to reconstruct the order of hits. Therefore, the information of these signals is put back the point occurred these processes. We called these signals, e.g. X-ray fluorescence and recoil electron, “fake” signals. There are mainly following types as fake signal by physical process.

- X-ray fluorescence

Photoelectric absorption lead to an empty electron orbit. When the electron orbit is occupied by the electron from higher energy level orbit, the difference energy between orbit level emits X-ray. In SGD components, energies of X-ray fluorescence of Si are below 2 keV, and them of CdTe are concentrated from 20 to 30 keV (see Table 5.4). The role of Si detectors in SGD Compton camera is scatter. Even if the X-ray fluorescence occur in a Si detector pixel, it is reabsorbed by own pixel. On the other hand, in the case X-ray fluorescence of CdTe, the absorption probability of the X-ray from 20 to 30 keV for detector thickness is about 90%. Therefore, sometimes the X-ray escape from own pixel and reabsorbed in the other pixel or detector. Because the reabsorbed signal is not Compton scattering, Compton reconstruction is failed.

Table 5.4: Energies of Cd and Te X-ray fluorescence. The unit is keV.

| | $K_{\alpha 1}$ | $K_{\alpha 2}$ | $K_{\beta 1}$ | $L_{\alpha 1}$ | $L_{\alpha 2}$ | $L_{\beta 1}$ |
|----|----------------|----------------|---------------|----------------|----------------|---------------|
| Cd | 23.1736 | 22.9841 | 26.0955 | 3.13373 | 3.12691 | 3.31657 |
| Te | 27.4723 | 27.2017 | 30.9957 | 3.76933 | 3.7588 | 4.02958 |

- Recoil electron

The higher the energy of incident is, the higher the energy of the recoil electron by Compton scattering is. The electron is slowdown with losing their energy in the detector. When the electron energy is enough high, the electron run out the pixel and stop in the other pixel or detector. As well as the X-ray fluorescence, the signals detected in other pixel or detector lead to confuse Compton reconstruction.

Si or CdTe detector is semiconductor detector, and sometimes the charge sharing occur in the detector. The incident gamma-ray energy is high, the pair of electron and hole is produced across to some pixels. The fake signals of charge sharing are treated as well as recoil electron.

We judge whether the fake signal in an occurrence with paying attention to the parameters below. If we judge the signals is fake, the signal energy is added to the proper pixel’s energy.

1. the distance between each signals

When the signals crowd around a pixel, the energies of signals is added to the signal of the center of pixels.

2. the energies of the signals

To check signals whether X-ray fluorescence from Cd or Te. If it is true, the energy is added to the nearest CdTe pixel’s one.

3. the total energy in an occurrence
4. the number of signals

After the signals were merged, we obtain some hits in an occurrence. As the next step, we determine the order of hits and judge whether the occurrence is Compton event.

Determination of order

We judge how the incident gamma-ray interact to Si and/or CdTe detectors. When the determination of the order, we reject the order such as the process is physically incorrect or the probability of process is low. Finally, we determine the order of hits.

There are n hits after signal merging. The combination of the order is $n!$. We express for i -th hit the position and energy are \mathbf{r}_i and e_i ($0 \leq i \leq n$), respectively. The steps to reduce inappropriate orders is shown below.

Judge the correctness of physical process

We assume that the relations between each hit in an assumed order are satisfies the Compton formula. Equation (3.2) is rewritten for i -th hit,

$$\cos \theta_{Ki} = 1 - m_e c^2 \left(\frac{1}{E_{i+1}} - \frac{1}{e_i + E_{i+1}} \right) \quad (0 \leq i \leq n-1) \quad (5.3)$$

where $E_i = \sum_{l=i}^{n-1} e_l$ is the sum energy of up to i -th signal, θ_{Ki} is the kinematic scattering angle of i -th hit. Because the $\cos \theta_{Ki}$ is satisfied with $-1 \leq \cos \theta_{Ki} \leq 1$, Equation (5.3) is equal to consider below equation,

$$f_i \equiv 2E_{i+1}^2 + 2E_{i+1}e_i - e_i m_e c^2 \geq 0 \quad (0 \leq i \leq n-1) \quad (5.4)$$

We require all hits to satisfy the condition.

In addition to the kinematic scattering angle, we can determine the scattering angle geometrically from positions of hits. From Equation (3.3), the geometrical scattering angle of i -th hit $\cos \theta_{Gi}$ is given by

$$\cos \theta_G = \frac{(\mathbf{r}_i - \mathbf{r}_{i-1}) \cdot (\mathbf{r}_{i+1} - \mathbf{r}_i)}{|\mathbf{r}_i - \mathbf{r}_{i-1}| |\mathbf{r}_{i+1} - \mathbf{r}_i|}. \quad (0 < i < n) \quad (5.5)$$

The difference of kinematic and geometrical scattering angles is written as

$$g_i \equiv \cos \theta_{Ki} - \cos \theta_{Gi}. \quad (5.6)$$

If the order is physically correct, Equation 5.6 is ideally satisfied with 0.

By using two conditions, Equations (5.4) and (5.6), most of orders are rejected as non-physical. However, realistically some orders remain because the physical values such as energies and positions of each hit have uncertainties. These uncertainties propagate to Equation (5.4) and (5.6). Therefore, it is difficult to judge whether to reject an order candidate by using the equations. We reduce additionally the remained orders by using next steps.

The tendency of hits

In case remaining the several hits sequences, we consider the probability of hits. The cross section of photoelectric absorption of Si is smaller than CdTe. Because there are many other possibilities, we estimated the possibilities to several hit pattern using Monte Carlo simulation.

Due to SGD expects photons from within the field of view, we need to select the event caused by incoming photon. The useful figure of merit is the ARM defined in Equation 3.4. We calculate the value of θ_G as photons come from the direction of the field of view. Only the physically requested value remains for the value of θ_K . Therefore, if the absolute value of ARM, the difference θ_K and θ_G , of one sequence is smaller than the other, the sequence is most probable that the photon come from within the field of view.

5.3.2 Data reductions by using flags

The data include the events likely to incorrect recorded events and/or background events detected by BGO shields. These events are rejected by flags which record every event when the ASICs readout is carried out. There are flags which are shown in Table 5.5.

Table 5.5: Recorded flag in an occurrence. The flag is 64 bits.

| Flag name | number of bits | Descriptions |
|--------------|----------------|--|
| Length Check | 1 | The checksum of ASICs readout in CCFPGA |
| SEU | 1 | If the single upset event is occurred, the flags is high |
| CC BUSY | 3 | The trigger pattern which MIO FPGO received from each Compton camera |
| HITPAT CC | 3 | The signal pattern of HITPAT CC |
| Fast BGO | 4 | The signal pattern of Fast BGO |
| HITPAT BGO | 4 | The signal pattern of HITPAT BGO |
| TRIGPAT | 31 | Trigger patterns of each ASIC in a Compton camera, pseudo trigger, force trigger and calibration trigger |
| TRIGGER | 6 | The omitted trigger information which ASIC generate the fastest. |

To confirm that the event is correctly recorded, we judge the event to see flags which are length check and SEU. The length check flag is recorded whether there is a difference between the length of the data and contents of ASICs readouts. Although we ignore broken data to pay attention to the flags, in SGD2-CC2 the flag is anomaly behavior. The behavior especially occurs when the ASIC recorded the ADC value more than 1020. We used the selection to cut the ADC value in a case recorded it more than 1020 instead of the length check flags for SGD2-CC2. In addition, another thing for checking the recorded data correctness is to see SEU

flags. The SEU is single event upset by such as cosmic ray. We also check the flag with length check flags simultaneously, and the event which is anomaly recorded is ignored.

Next step is to pay attention to actions of the other Compton cameras. In an SGD, three Compton cameras share the same power supply. During the Compton camera readout, the power consumption is large and the current from the power supply fluctuated slightly. The fluctuation affects the readouts of the other cameras. Therefore, there is a facility to stop the event acquisition when the other Compton camera is carried readout, and then the situation is recorded in the flag of the event. The facility and section of the flag is called CC BUSY which is generated in MIO1 FPGA. Since the other Compton camera situations are recorded in CC BUSY flags, we also check the flags in a case of off-line analysis. On the other hand, for the high energy cosmic ray incoming to SGD, there is the case that the Compton cameras trigger simultaneously. The event is also a background. When the Compton cameras trigger simultaneously, the signal which is called HITPAT CC recorded in a flag. As the bit which express a Compton camera's self is only high in generally, we ignore the event in case that the other bit is also high.

To reduce the clear background event, we use the flags which were generated by BGO shields. As described in forward sections, there are two types of signals by the BGO shield. Each Fast BGO and HITPAT BGO are recorded in a flag separately. When the event selection is carried out with BGO anti-coincidence signals, we should check the flags.

Finally, we pay attention to trigger flags. These triggers are recorded in flags, and the sections of the flags is called TRIGPAT. The recorded patterns in TRIGPAT are divided to two types. One type is the pattern which is recorded when each ASIC generate the trigger. To check the section, we can judge which of the ASIC generated the trigger. Several Compton cameras have ASICs which can generate anomaly trigger in CdTe-side modules. We recognized the problem by the structure of the circuit of CdTe-side readout modules. The module id which correspond to daisy chain id is shown in Table 5.6. If the ASICs generate a trigger, sometimes the ADC value is lower than the true value. We assume that the event anomaly trigger includes noise, and we ignore the event. On the other hand, another type of triggers is the pattern which is not the ASIC origin. There are three triggers, trigger for calibration, force trigger and pseudo trigger. The trigger for calibration is generated when the SGD acquisition mode is calibration mode and the calibration pulses are injected to ASICs. The force trigger is generated when the event acquisition carries out by force. The pseudo trigger is generated for dead time correction, which is described in the following section. As these triggers are not physical signals, the event is rejected in analysis.

Table 5.6: The modules which generated anomaly trigger

| SGD CC# | id |
|----------|-----------|
| SGD1-CC1 | 28 |
| SGD1-CC2 | 14 |
| SGD1-CC3 | 14, 28 |
| SGD2-CC1 | None |
| SGD2-CC2 | 7, 14, 28 |
| SGD2-CC3 | None |

5.3.3 Dead time corrections

It is important to know the radiation mechanism of astrophysical objects. To determine the radiation intensity, we need to know the correct exposure times. The exposure times are different from whole observation time. The observation time includes the dead time. The dead time is the time which the detector is recording an event and cannot record another event. Therefore, the exposure time is defined by the time ignoring the dead time.

For each SGD Compton camera, the exposure time corrected for dead time can be derived from “clean” pseudo events. The pseudo event is an event caused by pseudo trigger which is randomly generated in each Compton camera’s FPGA. The generation rate of pseudo trigger is basically set to 2 Hz. The “clean” pseudo event does not include BGO anti-coincidence signals.

5.4 Performance of Ground-based Compton camera

In this section, we show the performances of Compton camera as a spectrometer. The data we show is acquired at the tests of low-temperature and thermal vacuum environment. Then, SGDs were operated at the temperature of around -20°C . During the tests we did not use onboard background cancel function by Fast BGO signal. If we use the channel signals, we operate in off-line analysis.

We have only shown the results of single hit events to measure detector performance so far. For SGD CC to measure its capability as a Compton camera, it is necessary to check whether Compton reconstruction was possible or not. It is also necessary to confirm how the BGO shield functions.

We used the 2-4 hits event which succeeded in Compton reconstruction. We show the performance of Compton reconstruction in Figure 5.12. The spectrum was obtained by irradiating ^{137}Cs which was to set in front of the SGD1-CC1 on ground-based experiments. The black line spectrum is the raw detected events, which we deduce the event from it. First, the rejection by BGO anti-coincidence is done, and mainly continuum component in the spectra is reduced. We show the spectra rejected events in Figure 5.12 bottom left. Although there is a little component seen from ^{137}Cs , most components are background. In addition to this rejection, we perform the rejection by ARM cut. We compare the ARM values obtained by experiment and computed by putting monochromatic gamma-rays in simulator in Figure 5.14. The computed ARM is the function of hits distance and its total energy. Then the spectrum is reduced and ^{137}Cs line is prominent (red line in Figure 5.12). The rejected event shows the same tendency as in the BGO anti-coincidence (brown line in Figure 5.12). We also perform Compton imaging in Figure 5.13. The component derived ^{137}Cs is shown in BGO field of view.

Figure 5.15 shows the various plots such as reconstructed spectra, scattering angle of geometry θ_G and Angular Resolution Measure. We can recognize superiority of scattering pattern for detected energy. The spectra indicate that the (Si, CdTe-Side) scattering occurs better than the (Si, CdTe-Bottom) at 122 keV, but, on the other hand, the (Si, CdTe-Bottom) is good at 662 keV. Because the scattering at high energy is mostly forward scattering by the Klein-Nishina formula. We can confirm the phenomena in the histograms of the scattering angle of geometry θ_G . The histograms also record the perpendicular scattering of (Si, Si). The ARM distribution at the high energy is narrower than the low energy for each scattering pattern.

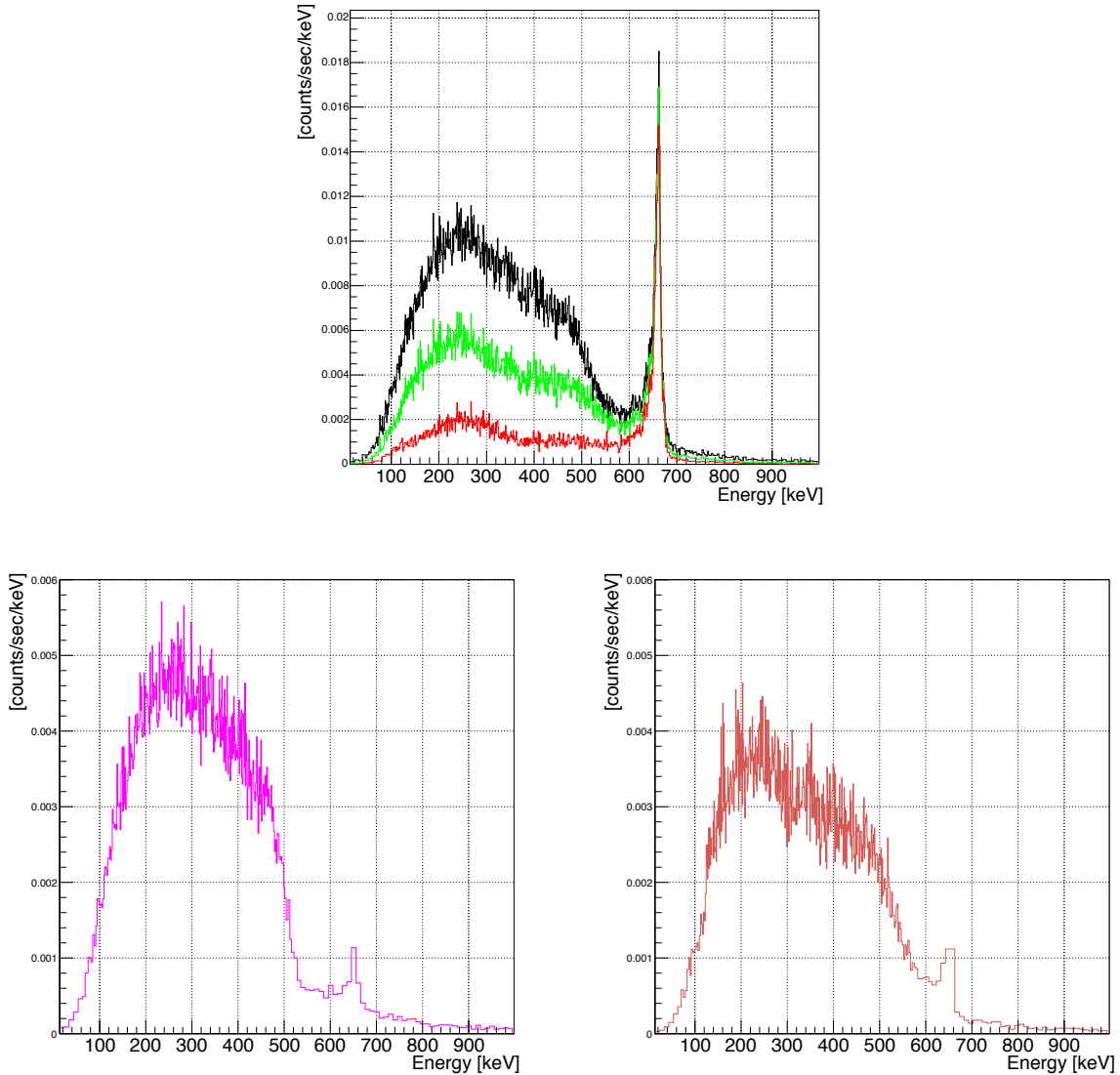


Figure 5.12: Spectra obtained by performing Compton reconstruction. These spectra are of SGD1-CC1 irradiated with ^{137}Cs . Top panel show the spectra, black line is raw spectra, green line is rejected by BGO anti-coincidence, and red line is rejected by ARM cut in addition to BGO anti-coincidence. Bottom left panel show the rejected event spectrum by BGO anti-coincidence. Bottom right panel show the rejected event spectrum by all background rejection.

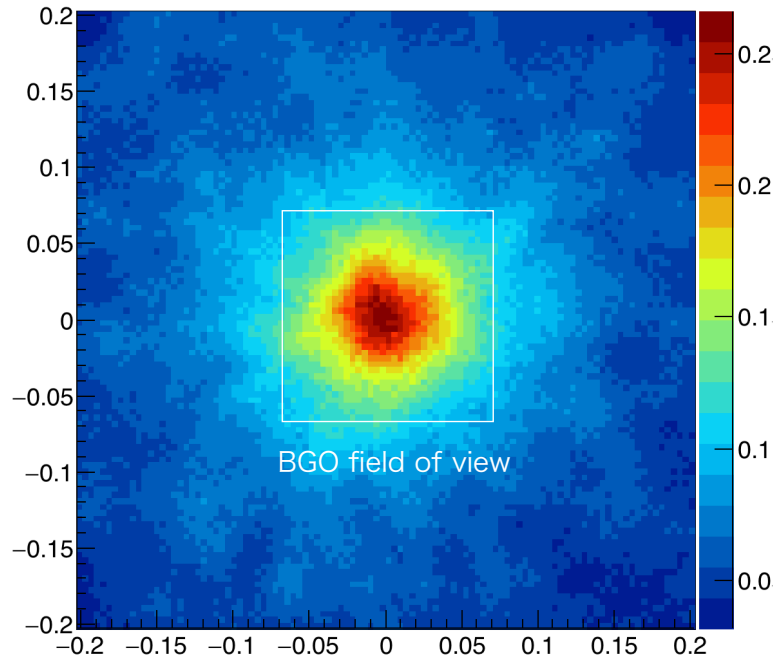


Figure 5.13: Compton imaging of ^{137}Cs to sky. White box in image indicate BGO field of View.

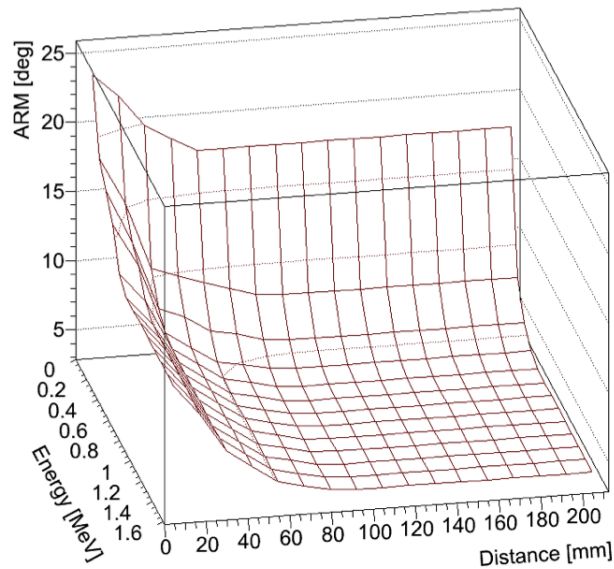


Figure 5.14: Computed ARM value by simulation with monochromatic gamma-rays. The computed ARM is the function of the hits distance and its total energy.

The energy resolutions of total scattering patterns achieved 2.8 keV at 122.2 keV and 4.36 keV at 662 keV.

Table 5.7: The number of events during the satellite integration experiments.

| SGD CC# | Raw events | BGO anti-coincidence | ARM cut | Total rejection ratio |
|----------|------------|----------------------|---------|-----------------------|
| SGD1-CC1 | 323111 | 111946 | 20650 | 0.936 |
| SGD1-CC2 | 447597 | 167446 | 30894 | 0.931 |
| SGD1-CC3 | 404172 | 140918 | 26189 | 0.935 |
| SGD2-CC1 | 322453 | 113550 | 20734 | 0.936 |
| SGD2-CC2 | 382333 | 134043 | 26534 | 0.931 |
| SGD2-CC3 | 420823 | 143043 | 27609 | 0.934 |

The concept of SGD Compton camera is a narrow field of view Compton camera. That is, we capture only the gamma rays we want by narrowing the field of view. For that purpose, it is necessary to evaluate whether background rejection is done correctly. We show the spectrum of environmental radiation measured at the test of integration satellite in Figure 5.16. The environmental radiation means that the potential radiation emitted by substances around the detector. The spectrum also includes the radiation from SGD itself. We show how the event was rejected in the same way as shown in the spectrum of ^{137}Cs . By the rejection BGO anti-coincidence we can see that the number of events is less than half. This event rejection is the same method used in the conventional satellite detector such as *Suzaku* HXD. In the SGD, further voluntary event rejection is done. As a result, the red line in Figure 5.16 indicates it. The ARM cut shows that there were events that could not be rejected by the BGO anti-coincidence. The proportion decreased from all events by event rejection is approximately 93% (show in Table 5.7).

We show also the rejected event spectra in Figure 5.16 The magenta line shows the event by the rejection of BGO anti-coincidence, and the brown line shows the events by the rejection of ARM cut in addition to BGO anti-coincidence. We can show the gamma-ray lines in these spectra, moreover different gamma-ray lines are visible depending on how to reject. According to (Knoll, 2010), the environment radiations are mainly due to daughter of uranium and tritium series. Gamma-rays in Figure 5.17 are also radiation from these sources. The gamma-ray lines rejected by BGO anti-coincidence are derived from ^{208}Tl , ^{106}Ru and ^{214}Bi . These radio isotopes were by β^- decay with more than two gamma-rays. For this reason, it is considered that BGO signals are issued because they are mixed as impurities inside the BGO and respond to electrons released at the time of β^- decay. The gamma-ray lines rejected by ARM cut are derived from ^{214}Pb and ^{212}Pb . These radio isotopes also were collapse by β^- decay with a gamma-ray. Since these gamma rays are not rejected by the BGO shield, it can be thought that this is an event mixed with each component in the detector or reacted by Compton camera slipping through the BGO shield. It is inferred that the component remaining after ARM CUT is the component mixed in the fine collimator in the field of view and the environmental radiation in the field of view.

We show the distribution of ARM value to the energy in Figure 5.18. The distribution is made from the events rejected by BGO anti-coincidence. There are events of line of sight. It

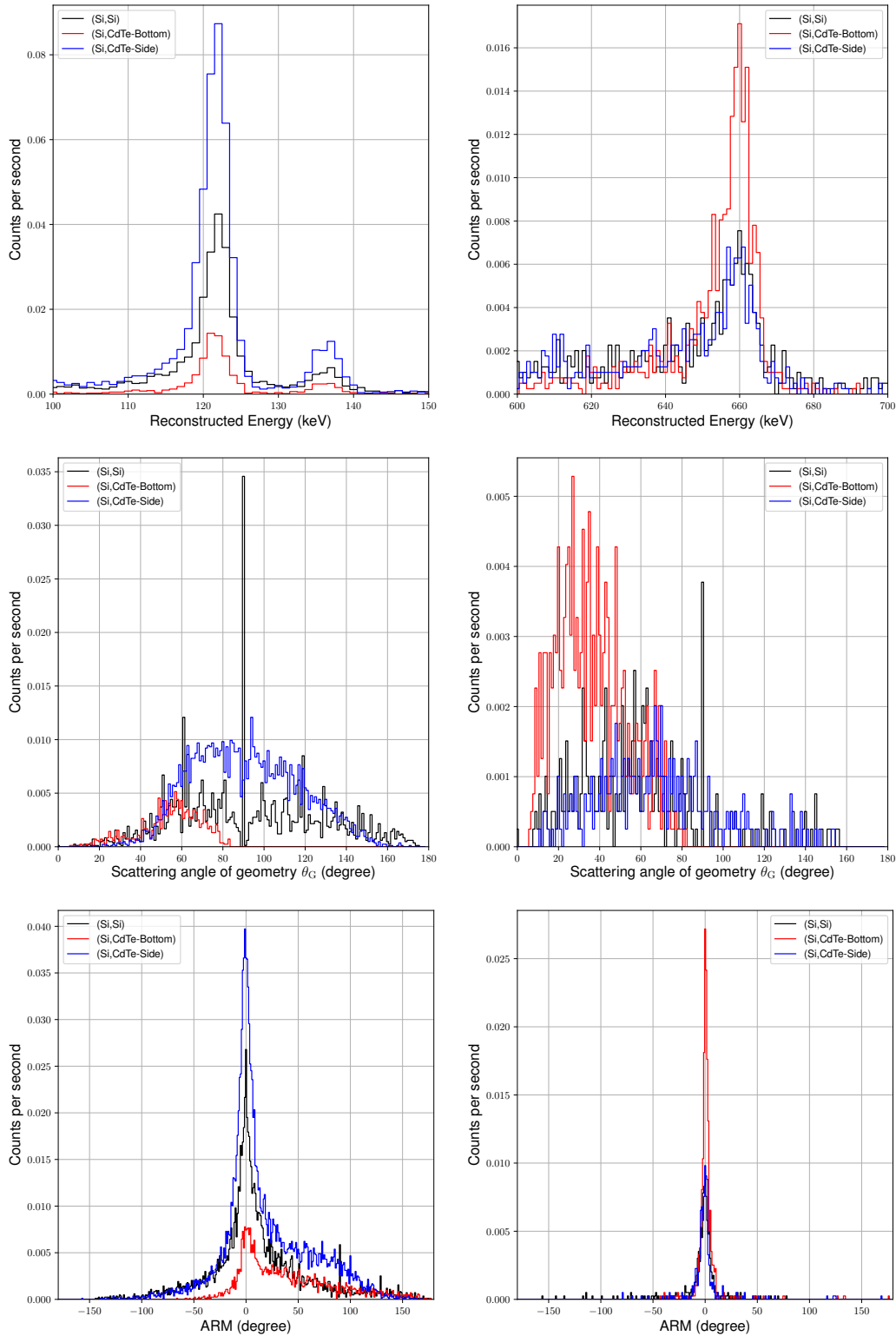


Figure 5.15: Reconstructed spectra (top), scattering angle of geometry θ_G (middle), and Angular Resolution Measure (ARM) (bottom) of SGD1-CC1. The left panels show the histograms at 122 keV when ^{57}Co irradiated, and the right panels at 662 keV when ^{137}Co irradiated. The differences of the histograms are scattering patterns, (Si, Si), (Si, CdTe-Bottom) and (Si, CdTe-Side) where correspond to black, red, and blue line, respectively.

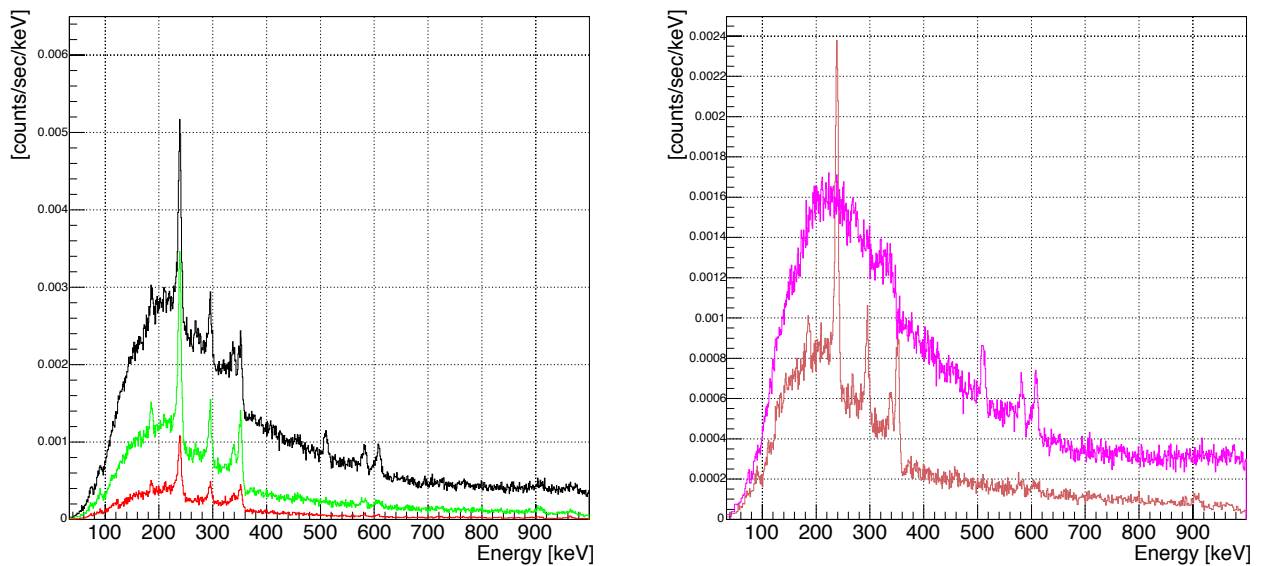


Figure 5.16: Compton reconstructed spectra. The black line is the raw Compton reconstruction spectrum in left panel. After the BGO anti-coincidence rejection, the black line spectrum becomes the green line spectrum. Then the spectrum of rejected event shown in right panel as magenta line spectrum. In addition to operate ARM cut rejection, the green line spectrum becomes the red line. In the right panel, the brown line spectrum indicates the difference of the green line and the red line spectra. We can see several gamma-ray lines.

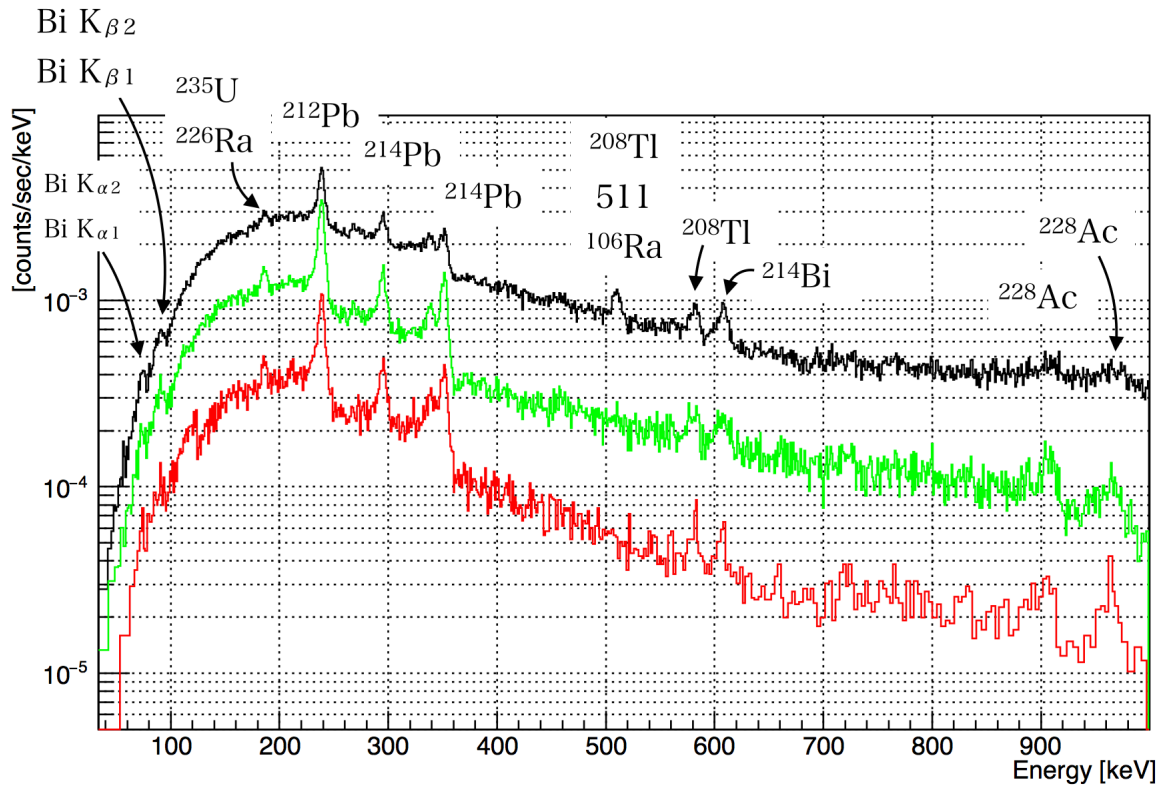


Figure 5.17: Background spectra, black line is raw spectrum, green is the spectrum after rejecting anti-coincidence with BGO shield, and red is the spectrum after ignoring events out of field of view. The peaks of each environment radiation are individualized.

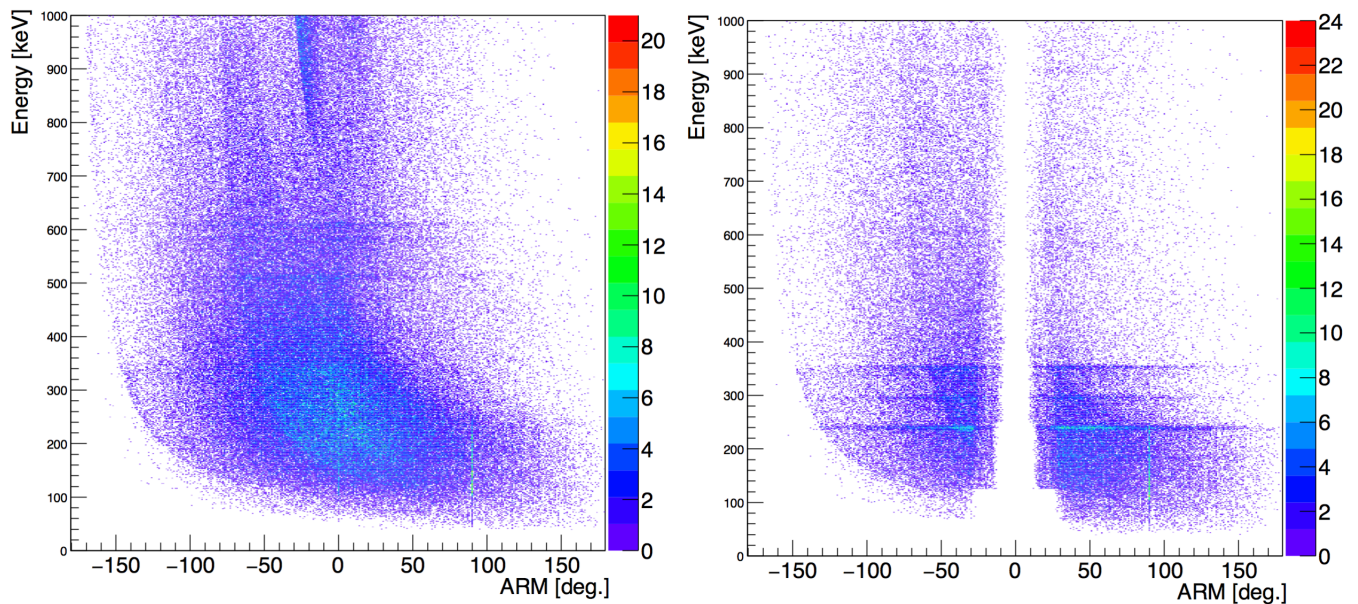


Figure 5.18: Distribution of arm value to the energy. The right panel shows all events, and the left panel shows the rejected events by ARM CUT.

is assumed that incoming photon interact firstly with the BGO shield and secondly with the Compton camera, or the incoming photons are scattered by and escape from the Compton camera and the scattered photon hits the BGO shield. These events are not applied correctly to operate Compton reconstruction because a part of its energy is deposited at BGO shield. As a result, these events become background and are not rejected by the ARM cut. On the other hand, the event rejected by the ARM cut are a lot of events by gamma-ray of ^{214}Pb and ^{212}Pb . As we have already mentioned, these events the gamma-rays come from the inner component of the detector. Therefore, it is difficult to detect by BGO shield. We conclude that the BGO shield can reject the event which are not rejected by the ARM, and the ARM cut can reject the event which are not rejected by the BGO shield. Two different background rejection methods compensate for each other's disadvantages. It can be said that the concept of SGD's "narrow field of view Compton camera" is correctly demonstrated.

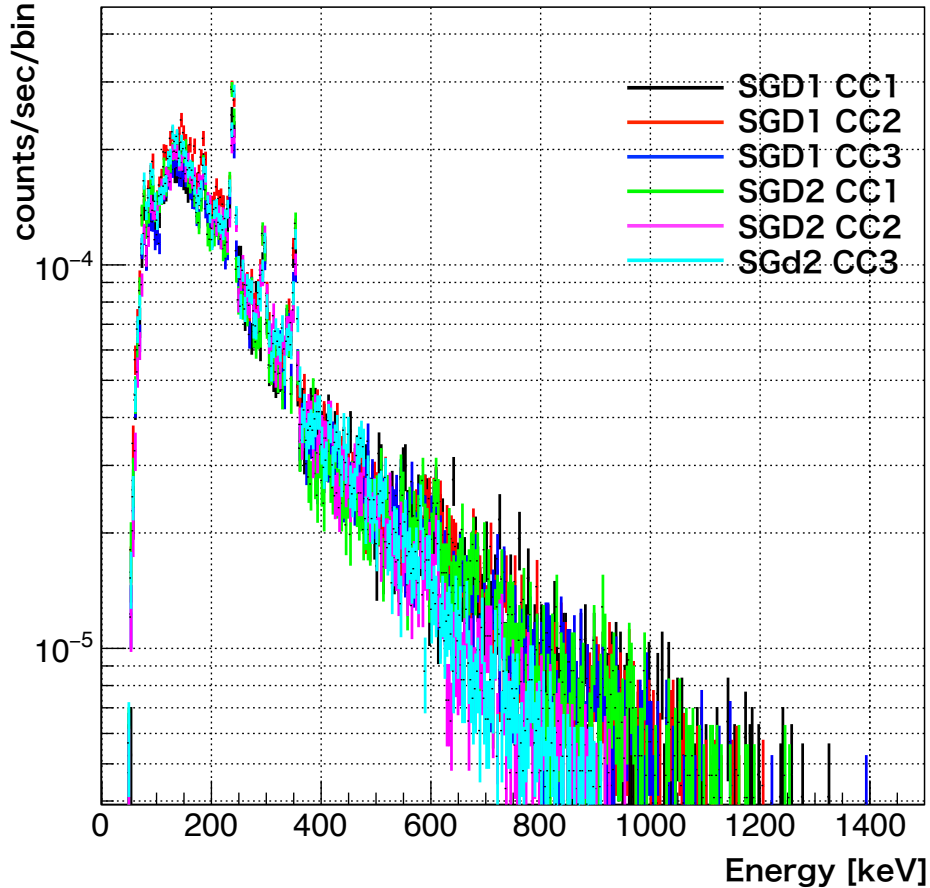


Figure 5.19: Background comparison between each Compton camera.

We show the background comparison between each Compton camera in Figure 5.19. The background was obtained by the satellite integral experiment. The shape and background levels of spectra are same for each Compton camera. Three lines in spectra are gamma-ray of ^{214}Pb

and ^{212}Pb .

5.5 Performance in orbit

After we establish the observation of the SGD, although there are celestial objects, RXJ 1856.5-3754, in the SGD field of view, it is not relevant for the SGD because the object is very dim source for hard X-ray and soft gamma-ray. *Hitomi* orbits are shown in Figure 5.20 during the Crab observation. In Figure 5.20, the meshed regions indicate SAA. Since *Hitomi* surely pass through SAA around the Earth, the background of the SGD is especially increased because some materials in it have been radioactive with short half-life.

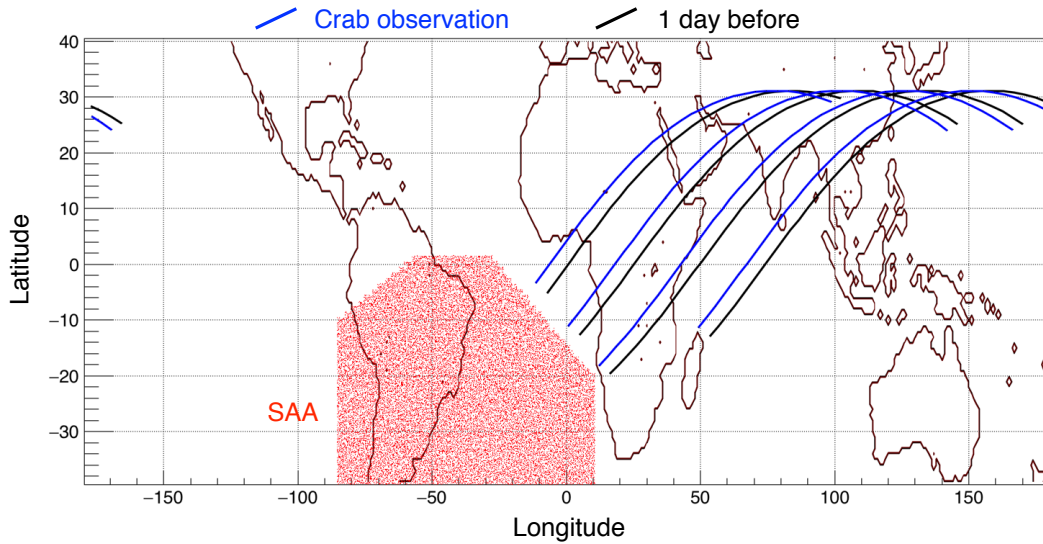


Figure 5.20: The satellite position during observations. The black line shows the satellite position during the Crab GTI, and the blue line shows the position during the epoch one day earlier Crab GTI.

We show the background spectrum of SGD1-CC1 CdTe-Bottom in Figure 5.21. There are some peaks in the spectrum. Since, in orbit, the CdTe detector can be activated by high energy particles, radio activated lines of Cd and Te appear. In addition, the same peak lines, when we compare the spectra obtained in orbit and on ground. These lines indicate that there is a constant inner background in the detector.

In general, the background estimation is carried out by building the background model with a long duration observation data. For example, the background model of the HXD onboard *Suzaku* have been built based on one year observation data (Fukazawa et al., 2009). However, the SGD CCs had been only operating for about a week for long ones. Accordingly, we assumed that the data sets before the observing the Crab treated as background data.

For the SGD CCs, to estimate the background rate during the Crab observation, we used the observation data before the Crab observation. Before Crab observation, *Hitomi* observed RXJ 1856.5 – 3754 which was an isolate neutron star. We neglected the emission because it was dim in the energy range for the SGD CCs. The orbit is almost the same as 24 hours before the

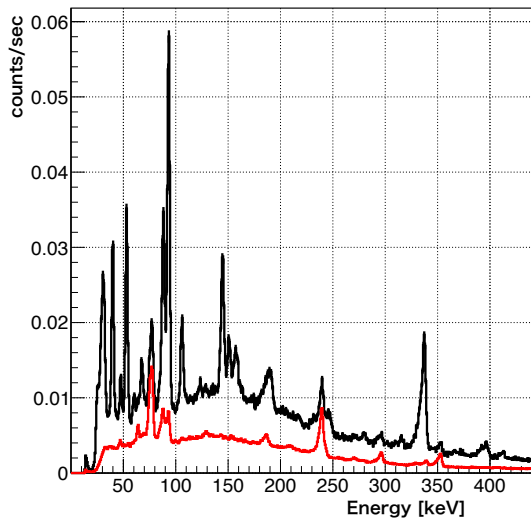


Figure 5.21: SGD1-CC1 CdTe-Bottom spectra obtained at in-orbit (black) and integration experiment (red).

observation (see Figure 5.21). To confirm whether the background was fluctuated, we compared the observation data between 24 hours and 48 hours before Crab observation GTI, hereafter we called these data as BKG24 and BKG48, respectively. In Figure 5.22, there is almost no difference between the single hit spectra of 1 day earlier and 2 day earlier. Figure 5.23 shows various spectra plots, scattering angles θ_G , ARM and azimuthal angles. The scattering angles θ_G were derived from hit positions, and is was useful to confirm the background's reaction distributions in Compton cameras not to rely on energy resolutions. Although the statistical uncertainty was big because the exposure time of BKG48 was short and both of the background rate was low. The count rates integrated azimuthal background distributions for BKG24 and BKG48 hours ago were 2.53 and 2.54, respectively. As a result, we considered that the BKG24 distributions were almost as good as BKG48 with uncertainties. We confirmed that the BKG24 is the background model to analyze spectrum.

Table 5.8: The dead time corrected exposure time for some kinds of background.

| Detectors | 24 hours ago | 48 hours ago | All observation of RXJ 1856.5-3745 |
|-----------|--------------|--------------|------------------------------------|
| SGD1-CC1 | 5299.5 | 3818.5 | 84358.5 |
| SGD1-CC2 | 5273.0 | 3825.0 | 84432.5 |
| SGD1-CC3 | 5268.5 | 3838.0 | 84559.5 |
| SGD2-CC1 | 5265.615 | 3958.5 | 89159.24 |

In order to obtain statistically significant background, we need to get the data with long exposure time. In the previous paragraph, we mentioned that the almost the same orbital data as the background. To obtain more data, we also used the other data which did not get in same orbit of the Crab observation. That is, we used all data during the RXJ 1856.5-3754

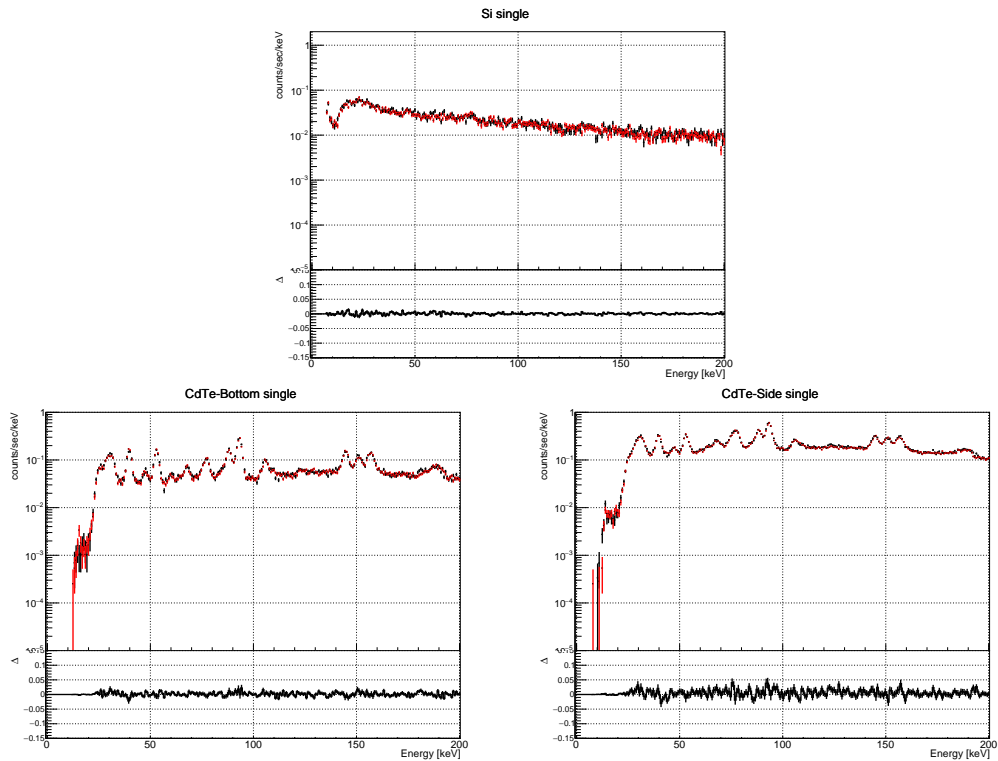


Figure 5.22: Comparison of 1 day earlier (red) and 2 day earlier (black) single hit spectra of Si (top), CdTe-bottom (bottom left) and CdTe-side (bottom right). The difference between 1 day earlier and 2 day earlier single hit spectra is almost nothing at any spectra.

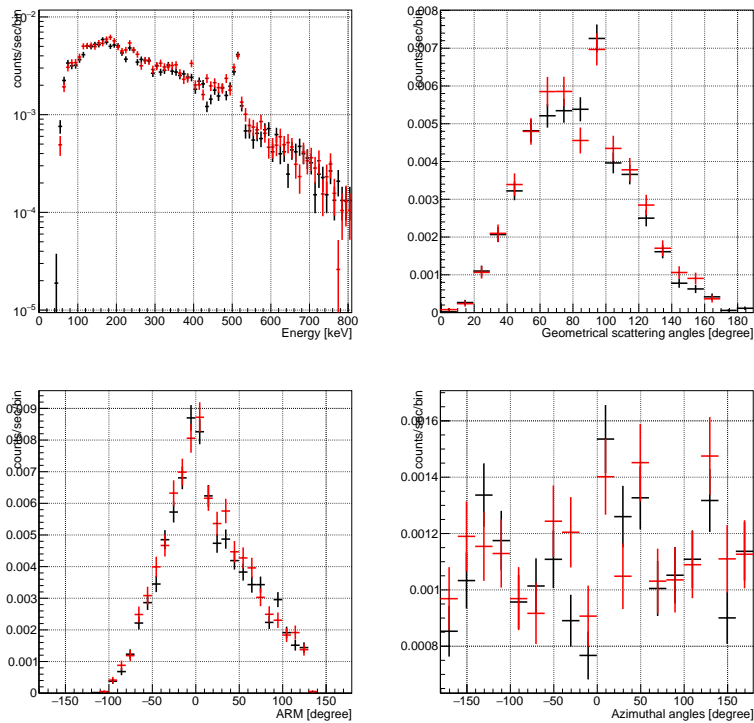


Figure 5.23: Various plot for comparing two kinds of background. The black lines show the background regarded to the observation data 24 hours ago. The red lines show the background regarded to the observation data 48 hours ago.

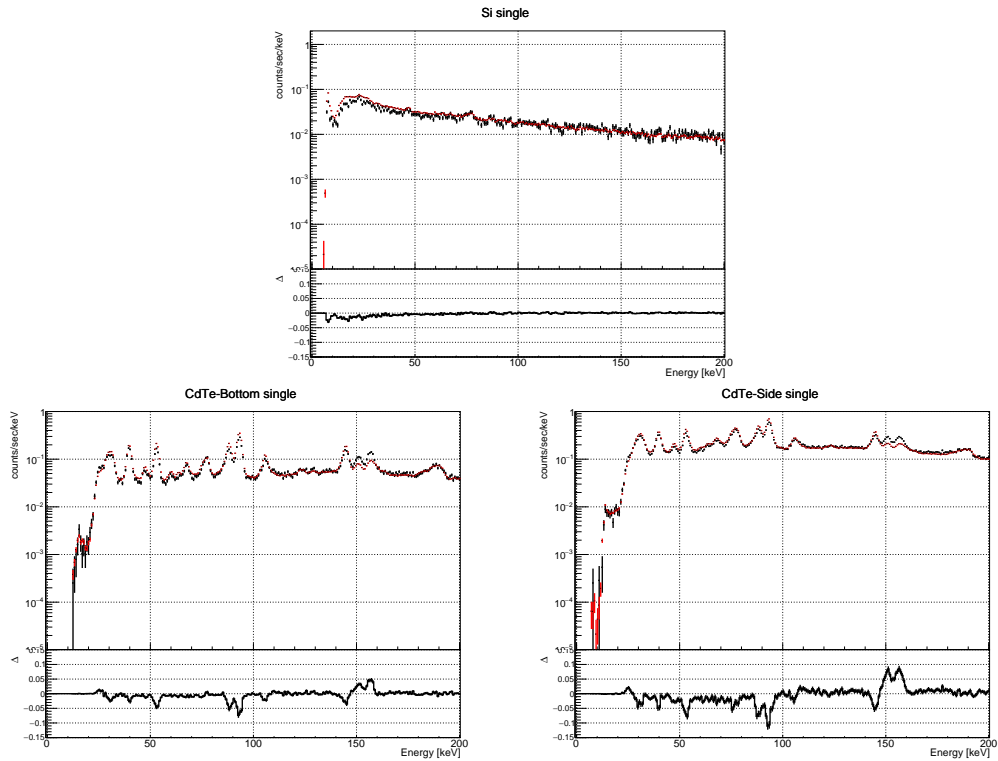


Figure 5.24: Comparison of 1 day earlier (black) and whole RXJ 1856.5-3754 observation (red) single hit spectra of Si (top), CdTe-bottom (bottom left) and CdTe-side (bottom right). The spectra of whole RXJ 1856.5-3754 observation is scaled to make the count rates equal to 1 day earlier. The difference between 1 day earlier and 2 day earlier single hit is almost nothing at Si spectra. Although CdTe detectors have difference at line gamma-rays caused by radio activation of detectors, the difference of continue components are around zero.

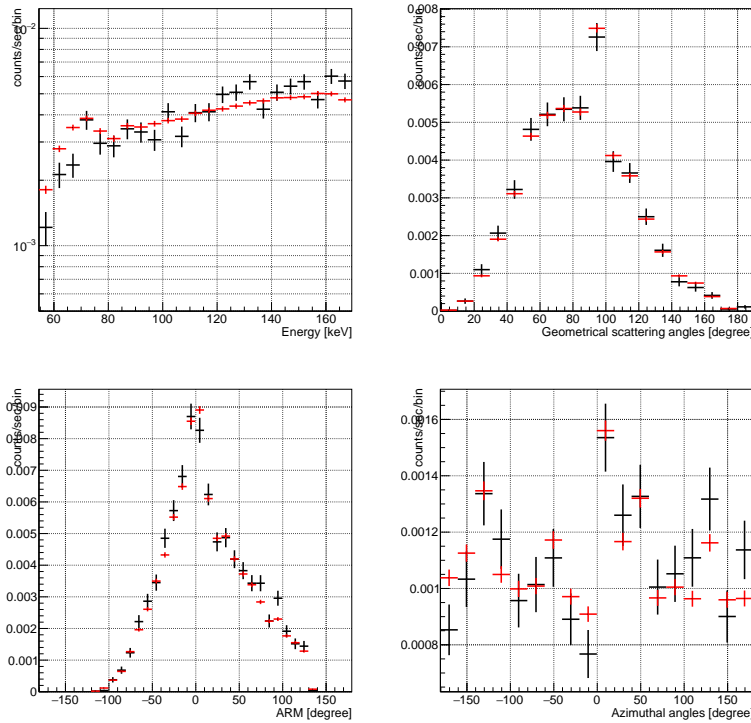


Figure 5.25: Various plot for comparing two kinds of background. The black lines show the background in relation to the observation data 24 hours ago. The red lines show the background in relation to the whole RXJ 1856.5-3754 observation.

observation except passing through the SAA, hereafter we called the background BKGALL. The exposure time for each Compton camera is shown in Table 5.8. We calculate the time based on Figure 5.24 shows comparison of 1 day earlier and whole RXJ 1856.5-3754 observation single hit spectra of Si, CdTe-bottom and CdTe-side detectors. The spectra of whole RXJ 1856.5-3754 observation is scaled to make count rates equal to 1 day earlier. For Si detector, there is almost nothing difference between the single hit spectra. For CdTe detectors, because there are differences in the number of passes through SAA, there are difference between the single hit spectra around line gamma-rays caused by radio activation of detectors. Since the line gamma rays incoming to sensors from out of field of view, this component decreases due to Compton reconstruction. Figure 5.25 shows the various distribution both of BKG24 and BKGALL. The BKGALL included in the data gotten in orbit not to pass through SAA for a long time. Therefore, the gamma-ray backgrounds by radio activation with short half-life were decrease to compare the BKG24. The count rates of BKG24 and BKGALL for azimuthal distributions were 2.53 and 1.77 counts/sec. In order to compare various distributions, we normalized the BKGALL count rate to BKG24 one. As the result, these distributions are almost same forms. We adopted the BKGALL data as background to analyze polarization.

In order to further verify the background subtraction using the data one day earlier, the count rates as a function of the time during the Crab GTI and one day earlier are compared in Figure 5.27. The red and the blue points show the count rates during the Crab GTI and one day earlier. The black points show the count rates of the Crab GTI after subtracting the count

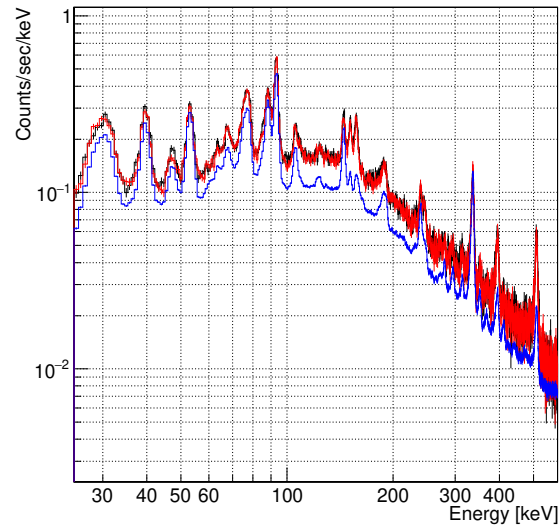


Figure 5.26: Spectra of CdTe side single hit events. The red and the black show the spectra for the one day and two days earlier than the Crab GTI, respectively. The blue spectrum shows the single hit events of CdTe-Side sensors on the orbit that the satellite does not pass the SAA region.

rates one day earlier, which corresponds to the count rates of Crab. Since the black points do not show any visible systematic trend like backgrounds, it implies this background subtraction is appropriate.

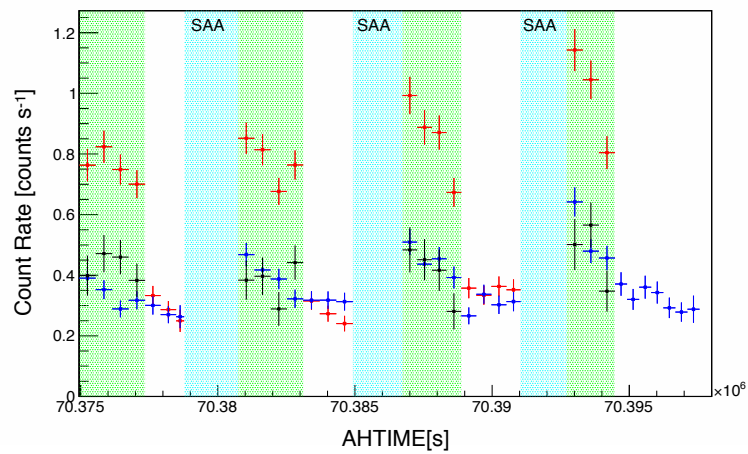


Figure 5.27: Count rate the SGD Compton camera as a function of time. The red and the blue points show the count rates during the Crab observation and one day earlier. The black points show the count rates of the Crab GTI after subtracting the count rates one day earlier. The regions filled in green show the Crab GTI. The regions filled in cyan show time intervals excluded from the GTI due to the SAA passages. In the “white” portions of time intervals, the Crab nebula was not able to be observed because of the Earth occultation.

Chapter 6

Polarized Photon Experiments at Spring-8

In order to fit the data to evaluate the radiation from the astrophysical objects, a detector response has important roll. The response is described by the detection efficiency, and generally us used by convolving with a model of the radiation. To provide the response, we have developed a Monte Carlo (MC) simulator for the SGD. The correctness of the simulator is confirmed by using monochromatic X-ray at SPring-8.

6.1 Monte Carlo Simulator

In order to understand the physics of a target object, we need to compare the observation result with expected models. However, it is impossible to simply compare them because the observation results are dependent on the detector responses. Incoming gamma-rays interact with some materials in a detector. It is necessary to take the response in the expected model.

It is difficult to study appropriately some of the SGD responses by solving analytically physical processes occurring in the complex geometry. Therefore, in general, the detector responses are estimated by using a Monte Carlo simulator. The roll of the simulator is to accurately reproduce interactions in a detector and responses of the semiconductor detectors.

In order to compute the interactions between gamma-rays of various energies with materials, we use the Geant4 Monte Carlo tool kits. It has been developed by CERN, which is usually used for simulating in high energy physics field. The toolkit is possible to determine the detector geometry by the user, and the codes to compute probability physical process between particles and materials are prepared in it. In the energy range of the SGD, the class G4EMLivermorePolarizedPhysics which specializes in computing electromagnetic interactions for low energy photons (< 100 MeV) is useful. The class is possible to compute the effects of atomic shell, fluorescent X-ray, Auger electron, the supplementary for the Klein-Nishina formula by atomic form factor and Doppler broadening. In addition to computing accurate interactions, it is important to define accurately the detector geometry. We have developed the detector geometry with the following considerations: (1) the sensitive detector such as Si, CdTe and BGO are built-in by right formation, (2) the electrical circuits such as ASICs and FECs near the sensitive detector are built-in, (3) the materials among the sensitive detectors are

Table 6.1: Physical parameters of Si and CdTe detectors for simulation.

| | Si | CdTe |
|----------------------------------|---------|-----------------------|
| Bias Voltage (V) | 230 | 1000 |
| $\mu\tau_e$ (cm ² /V) | — | 1.41×10^{-3} |
| $\mu\tau_h$ (cm ² /V) | — | 7.70×10^{-5} |
| Diffusion parameter (cm) | cathode | 8.0×10^{-4} |
| | anode | 8.0×10^{-4} |

built-in, (4) the case of Compton cameras, the foundation of them and supporting structures of the SGD are built-in as heavier materials. Figure 6.1 shows the geometry.

Although Geant4 computes physical processes for interactions, the responses of Si and CdTe semiconductor detector need to simulate behaviors of holes and electrons in the semiconductor detector. Compton Soft, which is a tool kit, can simulate the effect with combining Geant4. The tool kit is possible to simulate $\mu\tau$ effect of CdTe detector, charge sharing between adjacent pixels and trigger signals defined sensitive detectors. These simulations refer to parameter estimated from real detectors. The parameters are shown in Table 6.1.

6.2 Experiment at SPring-8

It is suitable to use high rate and monochromatic X-ray beam to compare with the result obtained by the Monte Carlo simulator. Therefore, we conducted the experiment at the synchrotron radiation factory, SPring-8 in Japan on November 2015. The beam line is BL08W at SPring-8 (Itou et al., 2014). The beam can irradiate monochromatic X-ray between 100 and 300 keV. Since the origin of the X-ray is synchrotron radiation, the emitted photon is almost completely polarized. The beam intensity is 5×10^{12} ph/s at 115 keV. The intensity is higher, the dead times increase. Therefore, we obstruct the incoming photons by using the plates of Pn, Sn and Pb locating the beam upstream. The beam size is 0.5 mm \times 3.0 mm at 115 keV and behind 40 m from the irradiation point. The beam is almost 100% polarized, and the size is 0.8 mm width and 1.4 mm height. We irradiated the beam at 122.2 and 194.5 keV to the detector.

When we conduct the experiment, we use the Compton camera which is similar to the installed in the SGD. There are a few differences in configurations from the one at the SGD, but the readout system is same. We called the Compton camera as “Engineering prototype Compton camera (prototype CC)”. We also evaluate the performance and develop the calibration.

We show the schematic of the setup in Figure 6.2. The prototype CC is installed in a thermostat chamber with four stages, and we defined the coordinate of the experiment. The temperature had been kept about -20 degrees which is operation temperature of the SGD in orbit.

In order to evaluate the performance of the CC as the polarimetry, we irradiate the beam with various angles of polarization. Since the polarized angle of the beam is fixed to the horizontal against the floor, we rotated the Compton camera by using stages. We set the Y-axis of the detector as the rotation angle. In addition, the beam position is controlled by

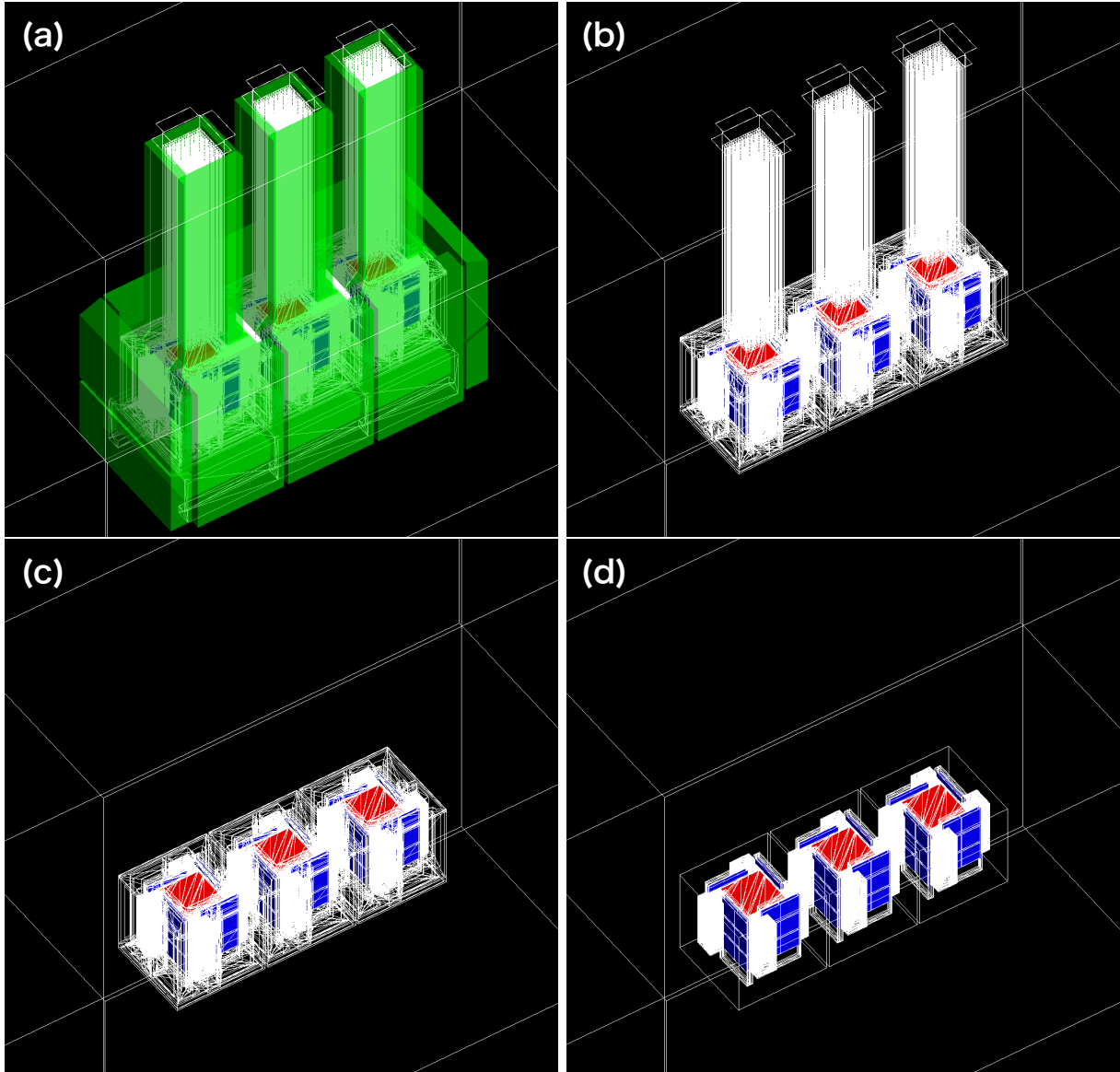


Figure 6.1: Simulation geometry of the SGD. (a) Whole geometry. Green sections are BGO scintillators. (b) Structure without BGO scintillators. White long sections are fine collimators. (c) Structure without fine collimators. Remaining structures are Compton cameras and electric circuits around them. (d) Compton cameras. Red parts are Si detectors and Blue parts are CdTe detectors.

moving along the X and Z directions by stages for translations.

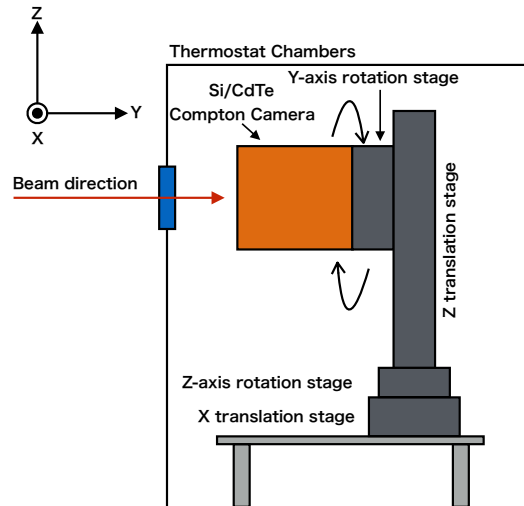


Figure 6.2: The schematic of the experiment setup. The direction of the beam is along Y-axis. There are four different stages, and the irradiation point is changed by controlling these stages.

6.3 Compare to simulation

In order to get some responses of the Compton camera, we need to use the Monte Carlo simulator. We mentioned in §6.1 that we must check the detector performances using the simulator. Although the detector responses can be estimated by using irradiate some isotopes, it is very difficult because we should consider multiple gamma-ray lines from an isotopes and backgrounds. However, the beam at Spring-8 is monochromatic and high intensity and so we do not need to consider background. Therefore, we used the beam to check simulator response.

First of all, we adjust the position of the irradiated beam (see in Figure 6.3). The number of counts is high at the irradiated pixel, and the count map elliptically spread at center of it. The reason why the spread forms an ellipse is because the beam is lineally polarized. That is, the incident photons scattered before any reaction at a detector and the scattered direction was polarized. At the CdTe detector, the irradiation points span two pixels. There are inactive regions whose wide is 0.01 mm between two pixels of the CdTe detector. If the incident photon income at the position, the charge generated in the CdTe detector spreads to the surrounding pixels. Therefore, it is useful to the test of the charge sharing of the CdTe detector in Monte Carlo simulator. This is mentioned in §6.3.2.

6.3.1 Si detector response

We aimed to reproduce the Si detector. There is totally 0.02 mm inactive layer in the Si detector on the P side and the N side. We assume the different two types inactive layers: (1)

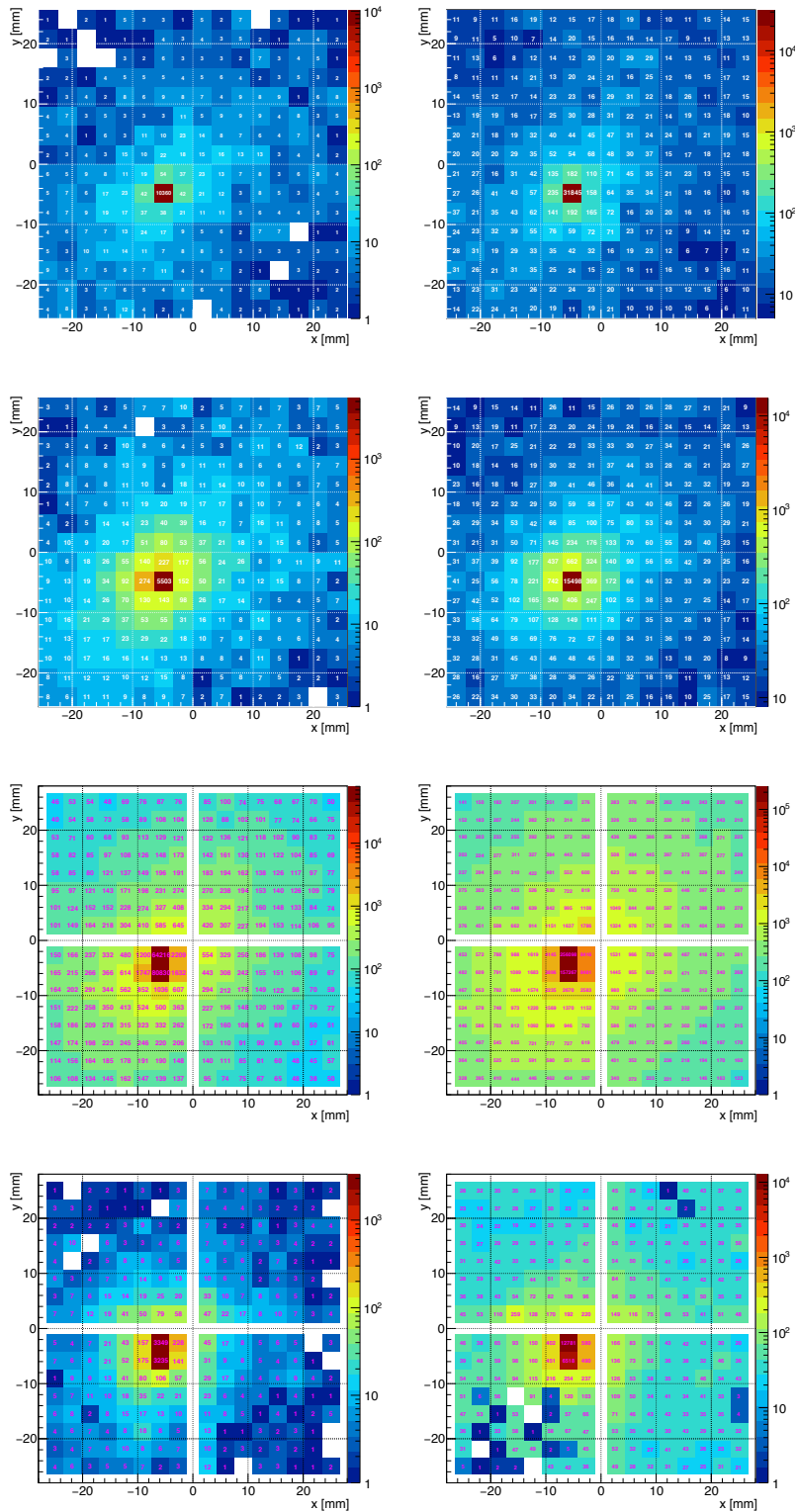


Figure 6.3: Count maps indicate irradiation points of the beam ($E_{\text{beam}} = 122.2$ keV) at Si and CdTe detectors. The count maps of the left side and right side are experimental and simulation results, respectively. The count maps from top to bottom are Si top layer (layer id : 0), Si bottom layer (layer id : 31), CdTe-bottom top layer (layer id : 100) and CdTe-bottom bottom layer (layer id : 170) . The reason of elliptically bright at count maps is that the beam is polarized.



Figure 6.4: Inactive layers in Si detectors.

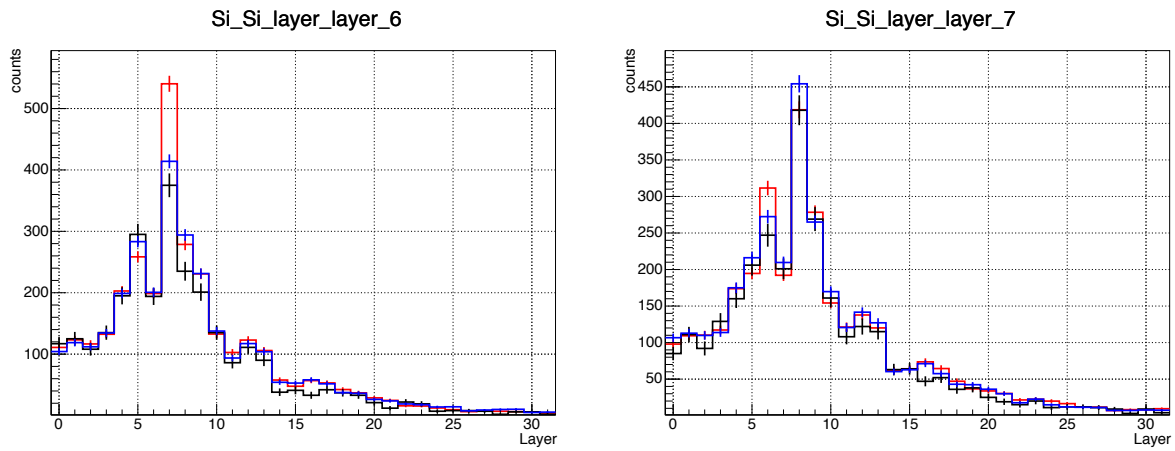


Figure 6.5: Influence of inactive layers in Si detectors.

inactive layer of 0.005 mm on P side and 0.0015 mm at N side shown in Figure 6.4, and (2) inactive layer of same thickness on P side and N side. In Figure 6.5, we show the comparison of the number of counts in each layer. This figure shows which layer 2nd hit was after 1st hit when selecting Si-Si event. The left panel in the figure shows the case of 1st hit in the 6th layer and the right panel shows the case of 1st hit in the 7th layer. The Si detector of the SGD is installed so that the P side or N side of adjacent layers face each other. Therefore, in the case of (1), the inactive layer of the portion where the P sides face each other gets thicker than the S side faces each other. We can get reasonable results when the situation of inactive layer is (1).

6.3.2 CdTe detector response

For semiconductor detector, an incoming photon to the detector create electron-hole pairs. These electrons and holes are called as carriers. The carriers move along the electric field applied to the detector. As a result, the charges are induced at the surface of electrode. These charges are called induced charge and read out as signal.

The recombination of the carriers reduces exponentially because the moving velocity is finite. The moving velocity is expressed as μE where μ is mobility and E is the electric field. Then the mean free path is expressed as $\lambda = (\mu\tau)E$ where τ is life time. The $\mu\tau$ product is the quantity related to induced charge.

The $\mu\tau$ product of CdTe semiconductors is smaller than other semiconductor detector. Since the decrease of the carriers are not negligible, the spectrum peak has a tail which has a low energy side. According to Hecht (1932), the charge induction efficiency is given by

$$\eta(Z) = \frac{\lambda_e}{D} \left[1 - \exp\left(-\frac{D-Z}{\lambda_e}\right) \right] + \frac{\lambda_h}{D} \left[1 - \exp\left(-\frac{Z}{\lambda_h}\right) \right], \quad (6.1)$$

where D is a detector thickness, Z is the depth occurred the carriers. Here, the first term indicates electron and the second term indicate hole.

In order to describe to the charge collection efficiency, we prepare the charge collection efficiency map shown in Figure 6.6. We assume the electric field in CdTe semiconductor to gradually increase and decrease. Thus, the shape of it is trapezoid as shown in left panel of Figure 6.6. We set the electric field to 0.001 V at 30 μm in the vicinity of the surface. In addition, we set the $\mu\tau$ values as $(\mu\tau)_e = 0.00141 \text{ cm}^2\text{V}^{-1}$ and $(\mu\tau)_h = 0.000077 \text{ cm}^2\text{V}^{-1}$. We show the CdTe-bottom spectra to compare the obtained spectra from experiment and simulation in Figure 6.7. The energies of irradiated X-ray are 122.2 keV and 194.5 keV. Focusing on the vicinity of the peak, the structure shows almost the same state with any energy.

6.3.3 Implementation of triggering efficiency

Ideal detector detects all X-ray or gamma-ray events. However, the SGD Compton camera only read out the triggered events. Therefore, it is necessary to reproduce the trigger of the detector in the simulator.

Triggers are generated by an ASIC shaper called ‘‘fast shaper’’. In an ideal ASIC, the trigger threshold is a step function with energy as a variable. However, due to the noise of electrons in

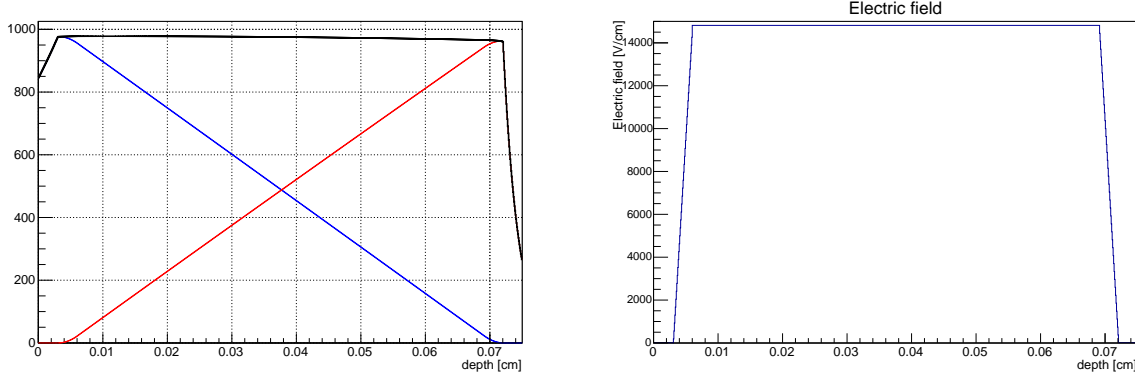


Figure 6.6: The charge collection efficiency map and the electric field in CdTe detector. (Left) The red line indicates the efficiency of holes, the blue line indicates the efficiency of electrons and the black line indicate the total efficiency. (Right) The electric field in CdTe detector is set to 0.001 V at 30 μm in the vicinity of the surface. The electric field gradually increases or decreases, and the shape is trapezoid.

the ASIC, the distribution becomes an error function. It is desirable to obtain the parameters of this error function for each ASIC and reproduce them with a simulator.

In order to obtain parameters related to trigger of ASIC, we created a ratio of triggered events to all events and fitted an error function,

$$f(x) = \frac{1}{2} \left[1 + \operatorname{erf} \left(\frac{x - \mu}{\sqrt{2}\sigma} \right) \right], \quad (6.2)$$

where μ is the threshold mean energy and σ is the variance. Figure 6.8 shows the result of fitting error function to an ASIC for Si. The mean energy of error function is 19.22 ± 2.5 keV and the variance σ is 3.15 ± 1.85 keV. In Figure 6.8, we show the scatter plot of the mean energy and variance for all ASIC of prototype Compton camera. For ASICs of CdTe detectors, since the threshold energy of analysis is higher than trigger threshold, we set the threshold of trigger at the same value for all ASICs of CdTe detector.

6.4 Comparison of Compton reconstruction data

We adjusted the parameters of Si and CdTe detectors. Before operating Compton reconstruction, we check the two hit events of Si and CdTe-bottom hits. We show the energy relations between Si and CdTe-bottom in Figure 6.9 at $E_{\text{beam}} = 122.2$ keV. Then we can see the double peak at 122.2 keV. Since the synchrotron radiation by the accelerator incoming at the detector as a bunch, the detector sometimes detects two photons. Therefore, the event sometimes in several cases for example, both photons are absorbed or scattering by other detectors, or one photon is scattered and another is absorbed. The simulator can only simulate one photon at a time. Thus, the experimental data and simulator detector are difference in type of several event. However, these events rejected by Compton reconstruction because these events are physically impossible compared to one photon event. These events influence the count rate of the experimental data.

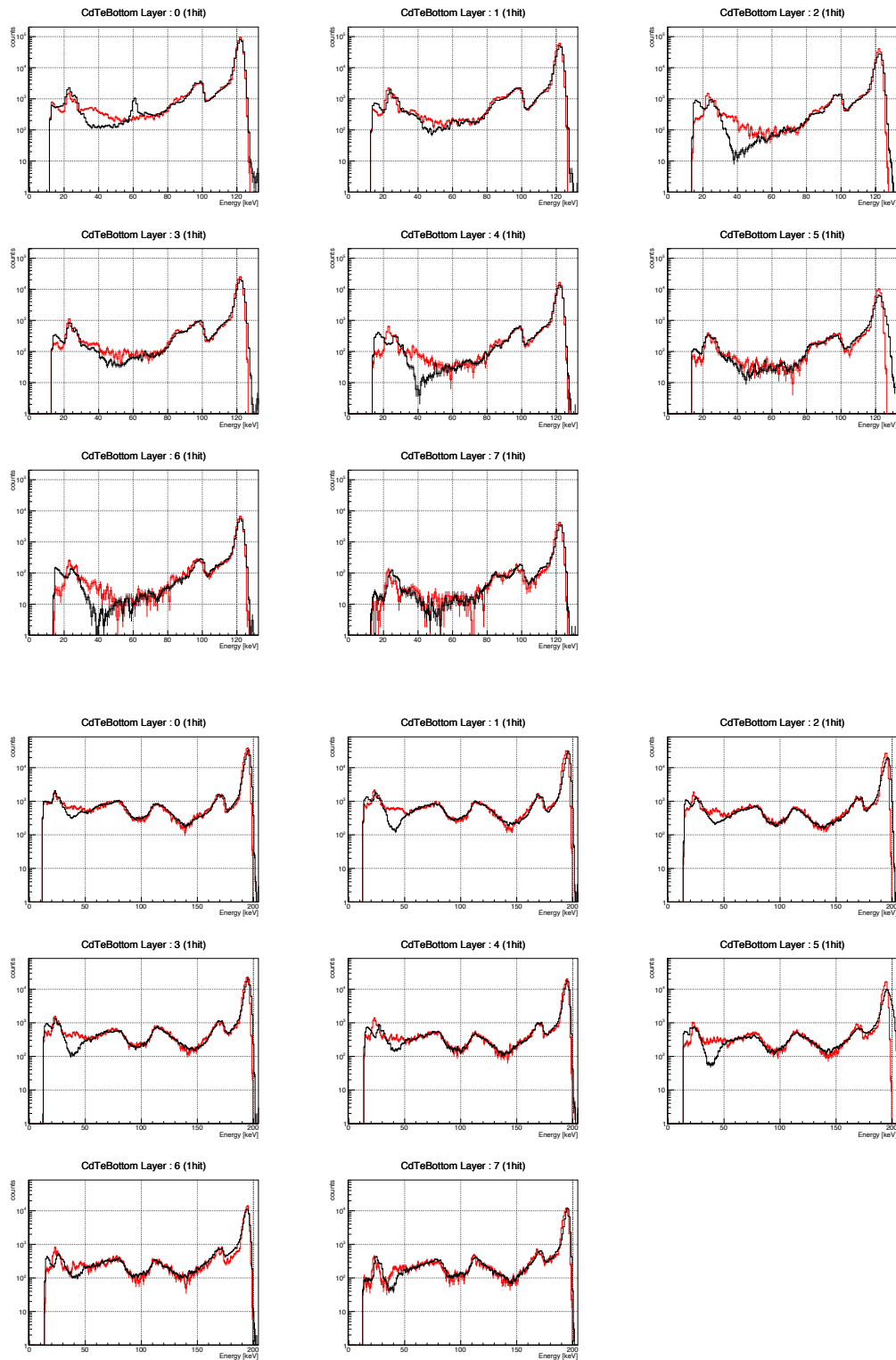


Figure 6.7: The spectra of CdTe in each layer. The black line indicates experiment data, and the red line indicates simulation data. The energies of irradiated X-ray are 122.2 keV (top panel) and 194.5 keV (bottom panel).

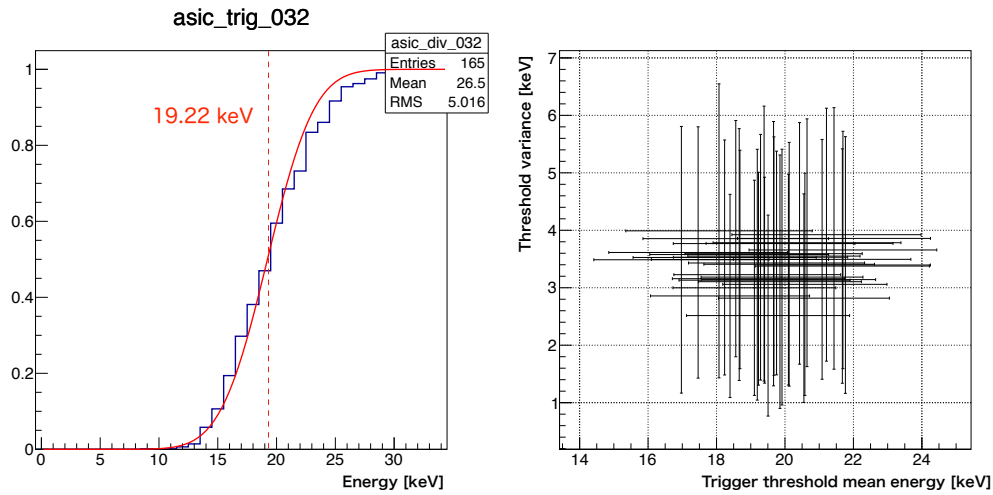


Figure 6.8: (Left) Trigger threshold of an ASIC. The blue line is experimental data, and the red line is the fitted error function. The mean energy of the error function is 19.22 ± 2.5 keV and the variance σ is 3.15 ± 1.85 keV. (Right) Scatter plot of the mean energy and variance for all ASICs of Si detectors for the prototype Compton camera.

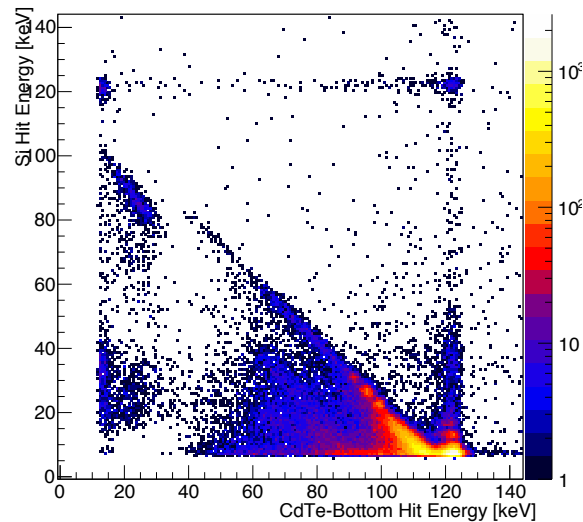


Figure 6.9: The energy distribution of the events hit Si and CdTe-bottom which do not operate the Compton reconstruction. The irradiate X-ray energy is 122.2 keV. We can see the double peak of 122.2 keV.

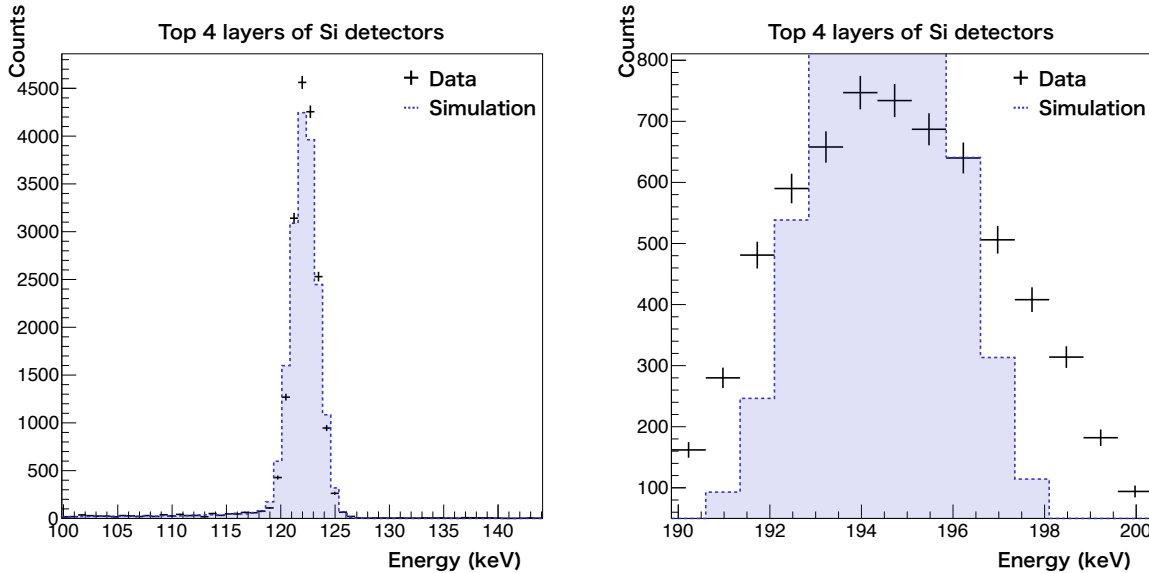


Figure 6.10: The comparison between experimental and simulation at $E_{\text{beam}} = 122.2$ keV (left) and $E_{\text{beam}} = 194.5$ keV (right). The black points indicate the experimental data and the blue shaded histogram indicate the simulation data.

In order to compare the experimental data and simulation data, we scale the events. The way to scale is to compare the count of Si single hit events in the top 4 layers. In Figure 6.10, we show the comparison between experimental and simulation scaled by number of counts at $E_{\text{beam}} = 122.2$ keV and $E_{\text{beam}} = 194.5$ keV. When we compare the count rate, we set the energy range width as ± 5 keV. At $E_{\text{beam}} = 194.5$ keV, since the energy calibration of Si only used radio isotopes up to 122 keV (^{57}Co), the experimental data is wider than simulation data.

We show the Figures to compare various parameters of Compton scattering. The first, in Figure 6.11 we show the spectra of Si-Si and Si-CdTe Side scatterings spectra at $E_{\text{beam}} = 122.2$ keV and $E_{\text{beam}} = 194.5$ keV. The widths of the spectra are all similar. For the geometry plots in Figure 6.4 and 6.13, there are peaks at 90 degrees in all of them. There is a high probability to detect scattered photons at the perpendicular directions to incoming direction. Focusing Si-CdTe-Side events, the forward scattering components are difference between experiment and simulation. For the ARM plots in Figure 6.4 and 6.13, Si-CdTe Side events are difference. As the cause of the differences, we think the CdTe-side energy calibration is still worse. The SGD Compton camera can use the in-orbit data to correct the CdTe detectors on the lower side of the energy calibration. However, for the prototype Compton camera it is not easy to calibrate the lower energy side. We can see the center ARM degree is below 5 degrees. Since the energy mistake is below 1 keV, the difference is marginal.

6.5 Performance as Polarimetry

We show the polarization analysis results. The beam size is smaller than the pixel size of Si and CdTe. Therefore, we show the irradiate point as pixel position of top layer Si.

The polarization of beam is ordinary parallel to the floor. In order to measure the polar-

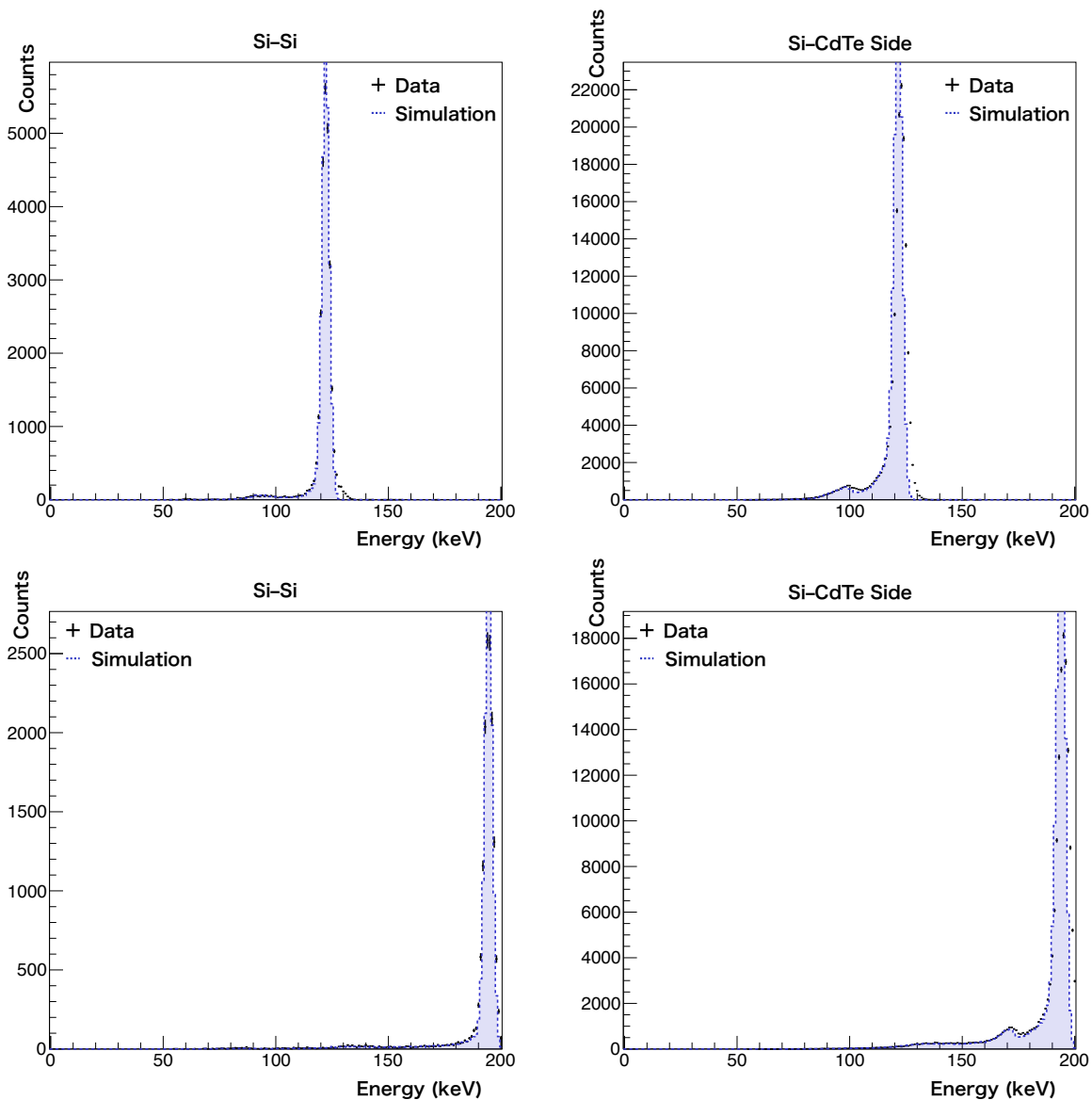


Figure 6.11: Spectra for events of Si-Si and Si-CdTe Side scatterings. Top panels show the spectra at $E_{\text{beam}} = 122.2$ keV, and bottom panels show the spectra $E_{\text{beam}} = 194.5$ keV.

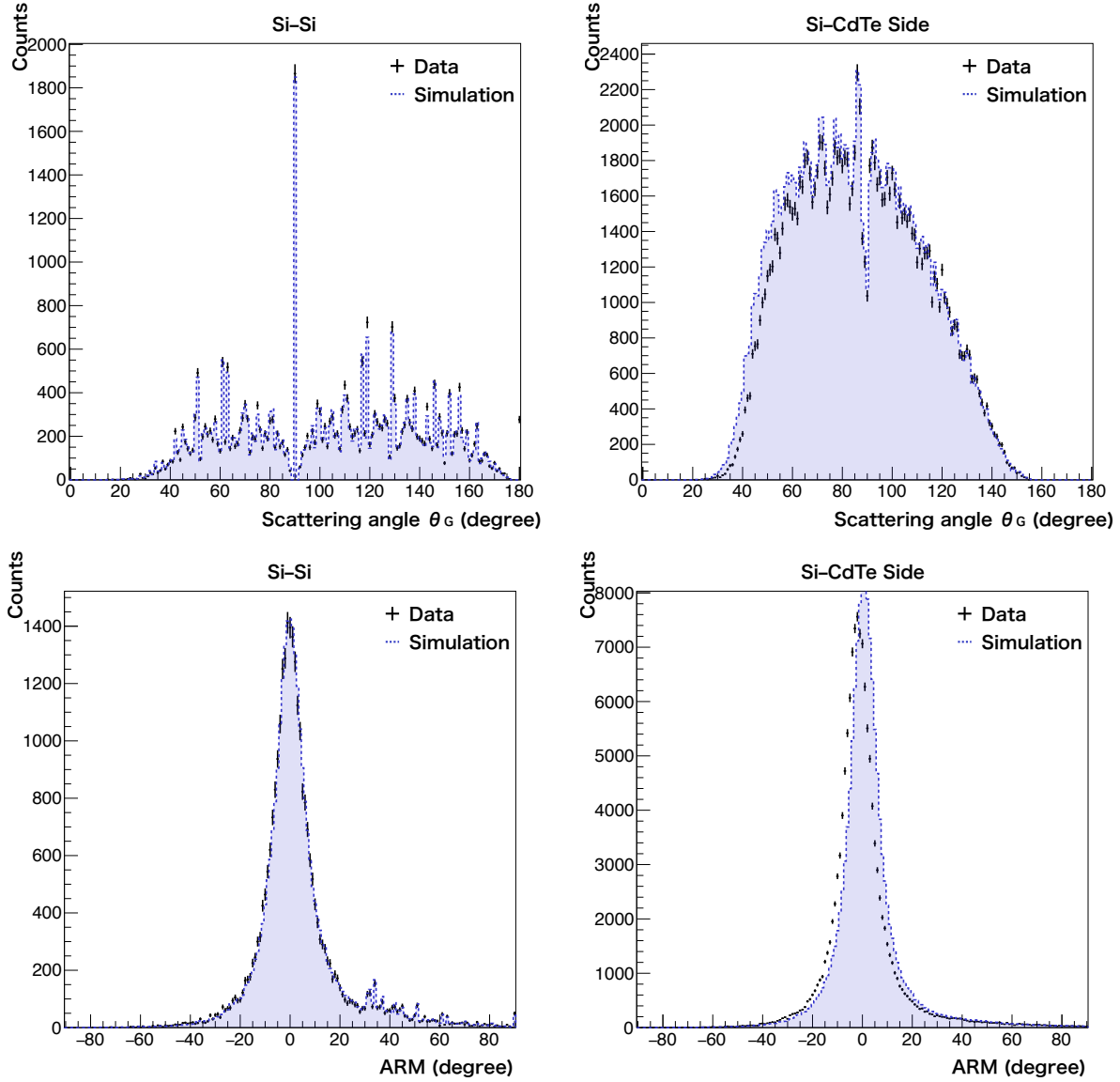


Figure 6.12: Distributions of scattering angles from geometrical calculations (top panels) and angular resolution measure (bottom panels) at $E_{\text{beam}} = 122.2$ keV. Black points are obtained data, and blue dashed lines are simulated data. Left and right panels show the events of Si-S and Si-CdTe Side scatterings, respectively. For scattering angles distributions, 0 degree indicates the forward scattering.

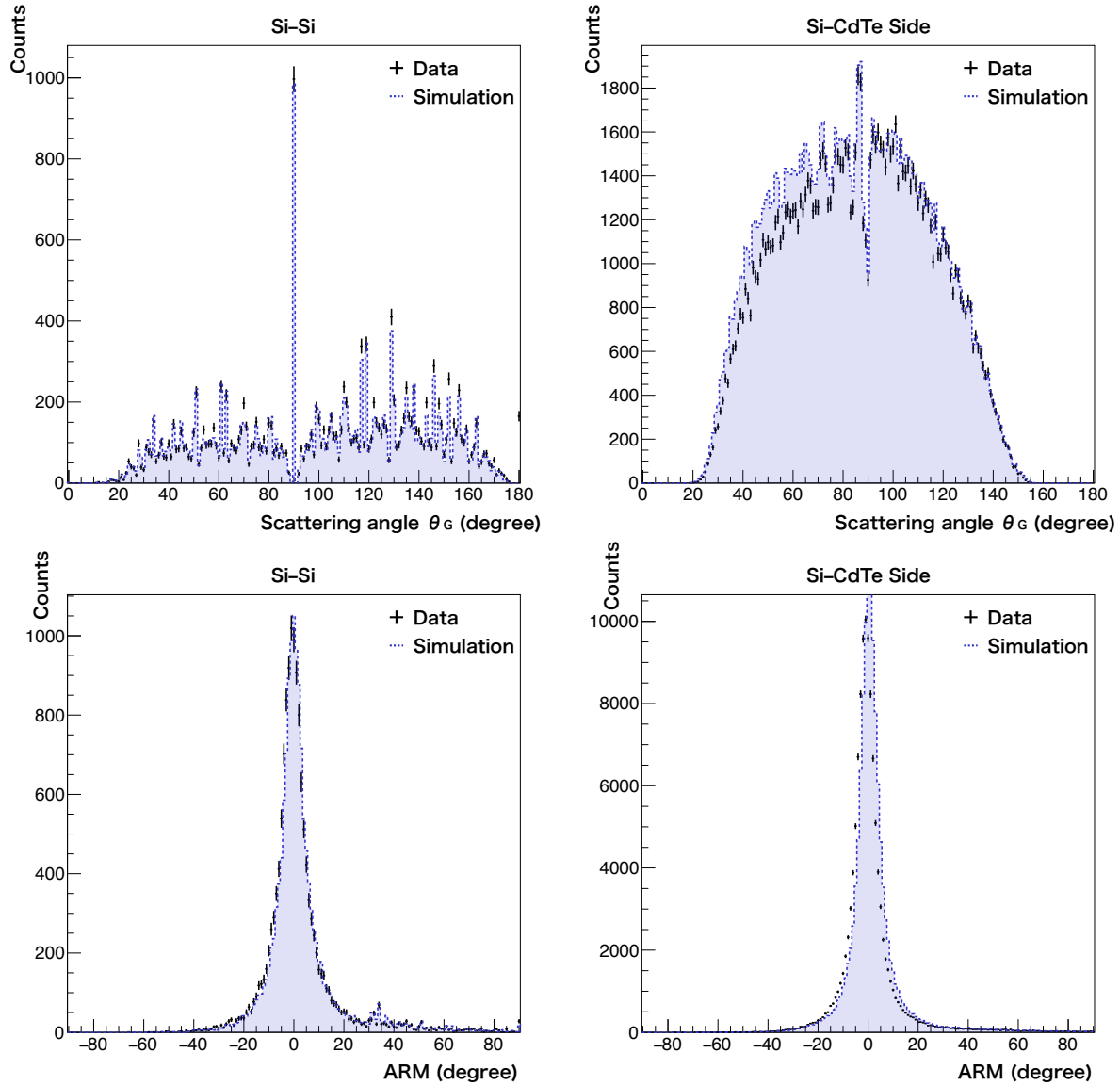


Figure 6.13: Distributions of scattering angles from geometrical calculations (top panels) and angular resolution measure (bottom panels) at $E_{\text{beam}} = 194.5$ keV. Black points are obtained data, and blue dashed lines are simulated data. Left and right panels show the events of Si-S and Si-CdTe Side scatterings, respectively. For scattering angles distributions, 0 degree indicates the forward scattering.

ization in various directions, we rotate the Compton camera. Therefore, the polarization angle corresponds to a rotation angle.

In analysis, we use the `sgdevtid`. We select the event which first hits the detector is Si after performing the Compton reconstruction. We made the azimuthal distribution without care of the irradiate point. The selected energy range was $E_{\text{beam}} \pm 5$ keV, and we did not use the geometry angle cut. Several of these points of view are different from Katsuta et al. (2016).

In order to make response of polarization, we simulate the non-polarization. The irradiate position is set to the same position as the experiment. According to Katsuta et al. (2016), since the irradiation beam is leaned to horizontal plane, we treated carefully in simulator. The number of seed photons is 10,000,000. The irradiate photon's energy is monochromatic, thus $E_{\text{beam}} = 122.2$ keV or 194.5 keV. We analyze the same process as experiment.

We use the following equation as the fitting function (see §2.4.1),

$$f(\phi) = A(1 - Q \cos(2(\phi - \phi_0))). \quad (6.3)$$

When we get the azimuthal distribution, we divide the experimental distribution by the simulation distribution. Therefore, the base line is shift to coefficient A in Equation (6.3). The fitting tool is a fitter prepared in ROOT which is an analysis tool provided by CERN. The fitting method is chi-square fitting, and the option of fitting are to use the integrated value of bin instead of bin center of histograms and to use Minos technique for error estimation (see the details in <https://root.cern.ch/>).

6.5.1 The polarization by various rotation angles of the detector

The irradiation point of the beam is the point (2, 2) in Si detector position. The rotation angles are 0.0, -45.0, -67.5, -90.0 and 90.0 degrees. We show the fitting results at 122.2 keV and 194.5 keV in Table 6.2 and Table 6.14, and Table 6.3. Regardless of the angle of polarization, the degree of polarization is about $Q \sim 0.55$ – 0.58 at 122.2 keV and $Q \sim 0.47$ – 0.49 at 194.5 keV.

Table 6.2: Polarization parameters at same position (2, 2). $E_{\text{beam}} = 122.2$ keV

| rotation angle [deg] | coefficient A | Q | ϕ_0 [deg] |
|----------------------|-------------------|-------------------|---------------------|
| 0.0 | 0.284 ± 0.001 | 0.561 ± 0.002 | -0.511 ± 0.148 |
| 90.0 | 0.264 ± 0.001 | 0.585 ± 0.003 | -91.356 ± 0.147 |
| -45.0 | 0.255 ± 0.001 | 0.553 ± 0.003 | -47.688 ± 0.151 |
| -67.5 | 0.259 ± 0.001 | 0.581 ± 0.002 | -69.691 ± 0.151 |
| -90.0 | 0.326 ± 0.001 | 0.585 ± 0.002 | -90.729 ± 0.135 |

6.6 Response of the spectrum

In order to get polarization information from the astrophysical object, the unpolarized azimuthal distribution is needed as a response when we obtained it. We used the Monte Carlo simulator described in section 6.1. In previous sections, although we described results of some

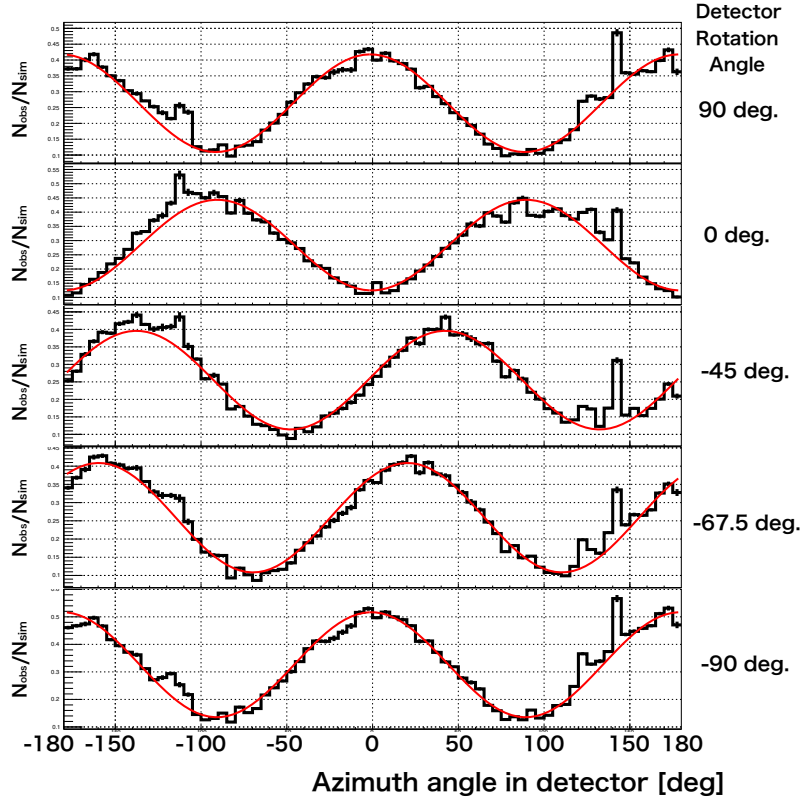


Figure 6.14: Azimuth angle distributions at $E_{\text{beam}} = 122.2$ keV. From top to bottom, the detector rotation angles are 90, 0, -45 , -67.5 and -90 degrees. Note that the coordinate of the azimuthal distribution is in detector.

Table 6.3: Polarization parameters at same position (2, 2). $E_{\text{beam}} = 194.5$ keV

| rotation angle [deg] | coefficient A | Q | ϕ_0 [deg] |
|----------------------|-------------------|-------------------|---------------------|
| 0.0 | 0.369 ± 0.001 | 0.472 ± 0.003 | -0.768 ± 0.180 |
| 90.0 | 0.387 ± 0.001 | 0.491 ± 0.003 | 89.567 ± 0.171 |
| -45.0 | 0.393 ± 0.001 | 0.476 ± 0.003 | -47.269 ± 0.174 |
| -67.5 | 0.382 ± 0.001 | 0.494 ± 0.002 | -69.064 ± 0.174 |
| -90.0 | 0.387 ± 0.001 | 0.492 ± 0.002 | -90.333 ± 0.171 |

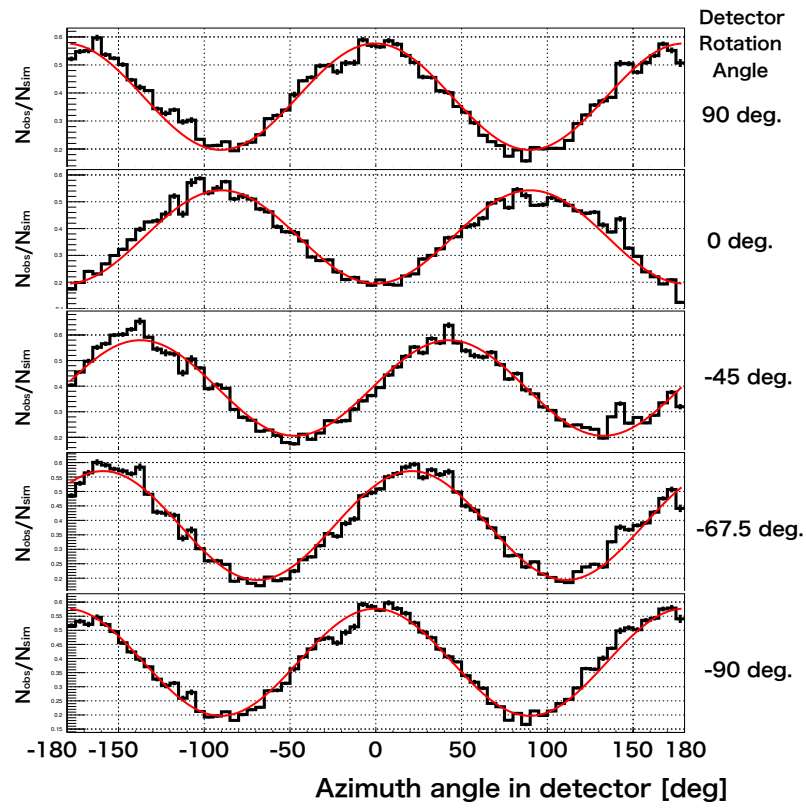


Figure 6.15: Azimuth angle distributions at $E_{\text{beam}} = 194.5$ keV.

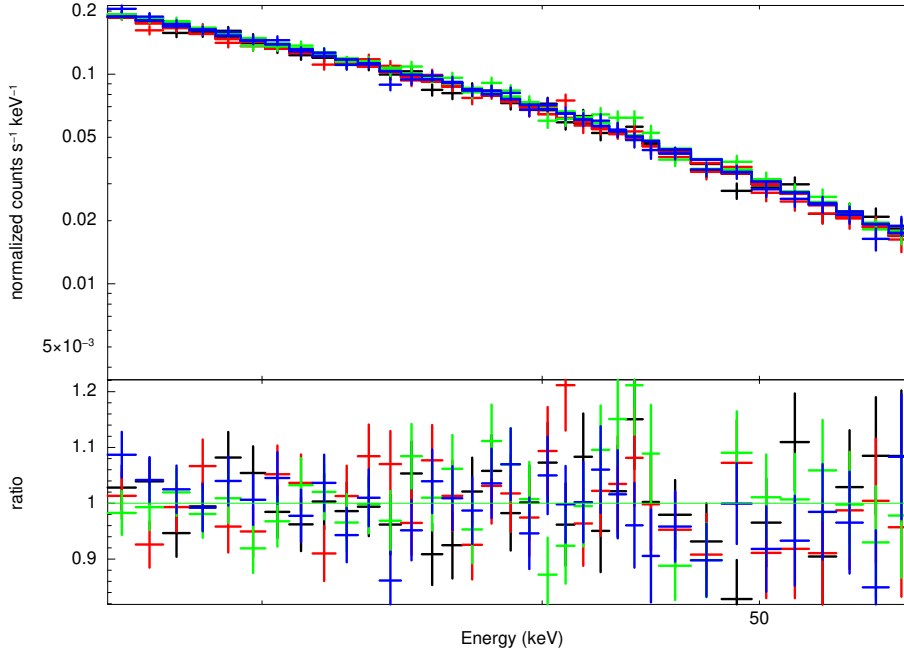


Figure 6.16: The Si spectrum of the Crab. The fit statistic is $\chi = 136.53$ with degree of freedom 136. The fit result is shown in Table 6.4.

ground test, we have not had a direct opportunity to compare the data obtained by the SGD and Monte Carlo simulator. For that reason, we only knew the detector assembled responses which were obtained by simulations. The things that we were concerned about the structure distortions in the detectors, especially for the Fine Collimator. With this in mind, we simulated the Crab observation within any backgrounds.

The Crab model is described by a power-law spectrum, $KE^{-\Gamma}$, and generally in some papers e.g. Yamada et al. (2011) and Madsen et al. (2017). The K is normalization at 1 keV, and Γ is called photon index. The Crab spectrum fluctuates in long duration. We adopted the photon index 2.1, and the normalization K is derived by Si single spectrum of the Crab observation. The parameter estimation was carried out by using Xspec, which was a tool specific spectral analysis in high energy astrophysics provided by NASA GSFC and the version was 12.9.0n. We show the fitting result in Table 6.4 and in Figure 6.4. The averaged flux in the energy range 2–10 keV corresponds to 1.89^{-8} erg/sec/cm². According to Madsen et al. (2017), the normalization K is 9.71 with photon index 2.106, which is bigger than our estimated value. We assume the reason why was caused by Fine Collimator’s distortions.

When we compare the ARM (or OFFAXIS) of the Crab observation and the simulation, the difference is shown in Figure 6.17. The ARM of the simulation result is narrower than that of the observation. In case we choose an event from the field of view, we limit the ARM as $-30^\circ < \text{ARM} < +30^\circ$. Then, the total number of events in the selection becomes 8.6% smaller than the simulation count rate. We think that the difference is due to Doppler broadening

Table 6.4: The obtained values by fitting the Crab with 1σ confidence level. The photon index is fixed as $\Gamma = 2.1$. The fit statistic is $\chi = 136.53$ with degree of freedom 136.

| Detector | Normalization | Flux ergs/cm ² /s (2–10 keV) |
|----------|------------------------|---|
| SGD1-CC1 | $8.17^{+0.13}_{-0.13}$ | 1.88×10^{-8} |
| SGD1-CC2 | $8.03^{+0.14}_{-0.14}$ | 1.85×10^{-8} |
| SGD1-CC3 | $8.43^{+0.14}_{-0.14}$ | 1.94×10^{-8} |
| SGD2-CC1 | $8.25^{+0.13}_{-0.13}$ | 1.90×10^{-8} |

effect in the Si layer. Therefore, we adjust the ARM value to the same count rate between the observation and simulation of the Crab. Figure 6.18 shows that the relation between their count rates. As the observation count rate is 0.40 counts per second, we obtain the ARM value for the event selection of the field of view is 22.13 degree for simulation.

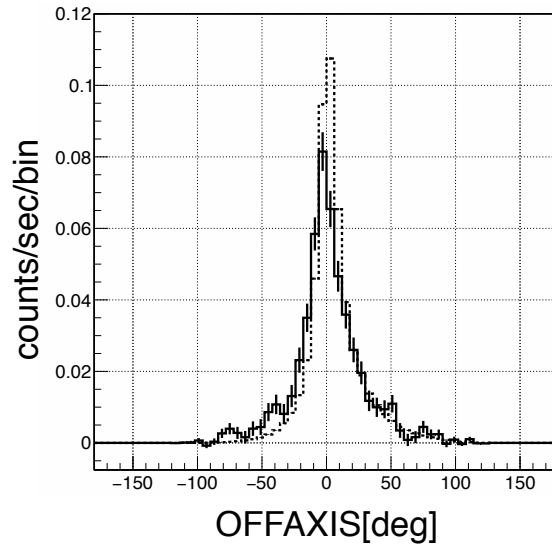


Figure 6.17: The ARM (OFFAXIS) distribution of the observation and the simulation. The solid line and the dotted line show the observation data and the simulation data, respectively.

Figure 6.19 shows the spectrum and the scattering angle distribution of geometry, θ_G , of the observation, the background, and the simulation data. The distribution is well reproduced between the observation (plotted in red) and sum of the background and the simulation (plotted in blue).

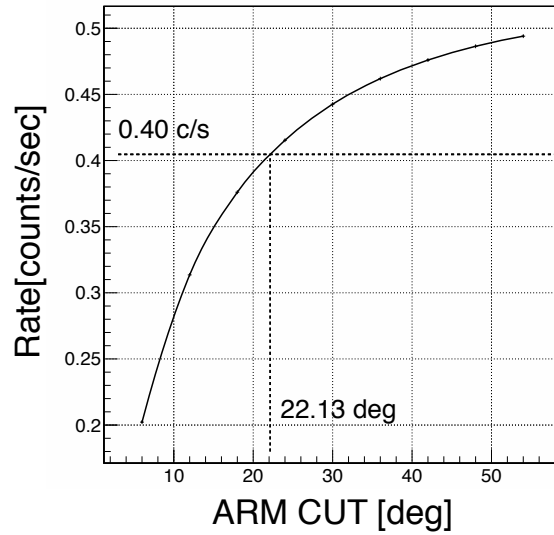


Figure 6.18: The relation between the count rate and the OFFAXIS selection for the simulation events. The count rate of $0.40 \text{ count s}^{-1}$ derived from the observation data corresponds to the OFFAXIS selection of 22.13° .

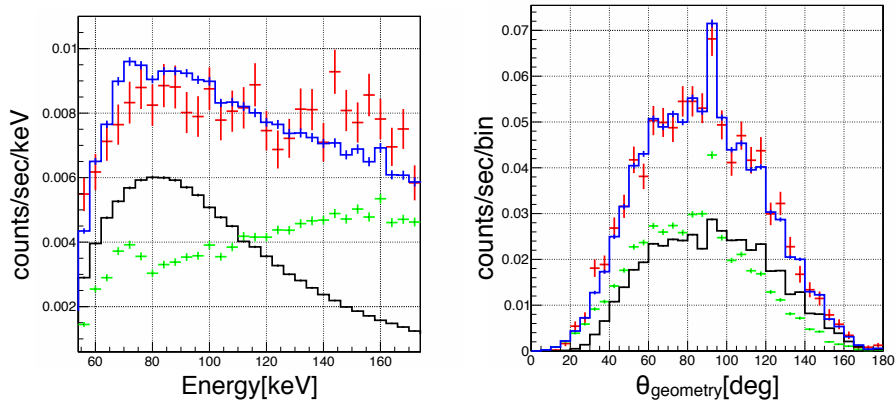


Figure 6.19: The spectrum and the scattering angle distribution of geometry, θ_G , of the observation, the background, and the simulation data. The observation data are plotted in red. The simulation data with the selection of $-22.13^\circ < \text{OFFAXIS} < +22.13^\circ$ are shown in black, and, the background data derived from the all RXJ 1856.5–3754 observation are shown in green. Sum of the simulation data and the background data are plotted in blue.

Chapter 7

Crab Observation

7.1 Crab pulsar wind nebula

At the center of the Crab Nebula lies a neutron star that rotates with a high angular velocity. The Crab Pulsar is the result of a super nova explosion which was reported by ancient astronomers in 1054. The neutron star in the Crab Nebula is classified as a pulsar, and its pulsation is observed in multi wavelengths. The accuracy of these measurements is so high that one can measure not only the rotation period, but also its time derivatives. Observations shows that the Crab pulsar, as any other isolated pulsar, slows down. Since one does not expect any notable change of the neutron star shape, this slowing down requires a release of rotational energy and angular momentum, which are believed to be carried away by an ultra-relativistic outflow, the so-called pulsar wind.

Energy loss rate relates to the rotation period P and its time derivative \dot{P} of the pulsar. We can derive the spin-down luminosity from $L_s = 4\pi^2 I \dot{P} / P^3$, where I is the moment of the pulsar. In case of the Crab pulsar, the spin-down luminosity is $L_s \sim 5 \times 10^{38}$ ergs s⁻¹, where $P = 33.6$ ms, $\dot{P} = 4.21 \times 10^{13}$ s/s and $I = 1.1 \times 10^{45}$ g cm² (as obtain for a sphere with the radius of 10 km and the mass of $1.4M_\odot$). The pulsar wind is believed to be formed in the pulsar magnetosphere, a region where the magnetic field can co-rotate with the pulsar. The distance at which the co-rotation breaks is known as the light cylinder, $R_{LC} = cP/(2\pi)$. In case of the Crab Pulsar, the radius is $R_{LC} \sim 10^8$ cm.

Because of the very large spin-down losses and fast rotation of the pulsar, the matter gets ejected away from the pulsar, forming the ultra-relativistic pulsar wind. The wind appears to be so over pressed, as compared to the interstellar medium, that once ejected from the magnetosphere, it keeps expanding in the super-sonic regime up to distances exceeding the size of the magnetosphere by approximately nine orders of magnitude. All the internal energy of particles in the wind is spent on the wind expansion, thus the pulsar wind is not expected to generate any detectable non-thermal signal. At 0.13 parsec from the pulsar, the pulsar wind is heated up by passing through a so-called termination shock. Beyond this point, most of the electrons in the shocked wind have energies of 100-300 GeV, with the maximum energy beyond 1 PeV. For a black body, such average thermal particle energies would be reached at extreme temperatures of 10^{15} K, clearly demonstrating that this system is a non-thermal particle accelerator. The shocked wind keeps on propagating away from the pulsar, reaching at

the present epoch out to distances of ~ 2 pc. In this part of the wind behind the termination shock, relativistic electrons strongly interact with the ambient magnetic and photon fields thereby producing electromagnetic radiation across the entire spectrum. Radio to soft gamma-ray emission is synchrotron radiation, whereas higher-energy gamma rays are produced via Inverse Compton (IC) scattering of photons by the relativistic electrons. This region filled with radiating electrons is known as the Crab pulsar wind nebula (PWN).

The spectrum and morphology of the PWN depend on the structure of the post-shock magnetohydrodynamic (MHD) flow. Observations in the X-ray energy band with Chandra revealed a complex structure consisting of a bright torus and a narrow jet emerging in the direction perpendicular to the torus plane. The X-ray structure suggests that the underlying MHD flow is nearly axisymmetric. The apparent deviation from this symmetry in the X-ray image is mostly due to Doppler boosting, which enhances the X-ray emission of fluid elements moving towards us. MHD instabilities developing in the post-shock region also alter the symmetry, but at a less important level.

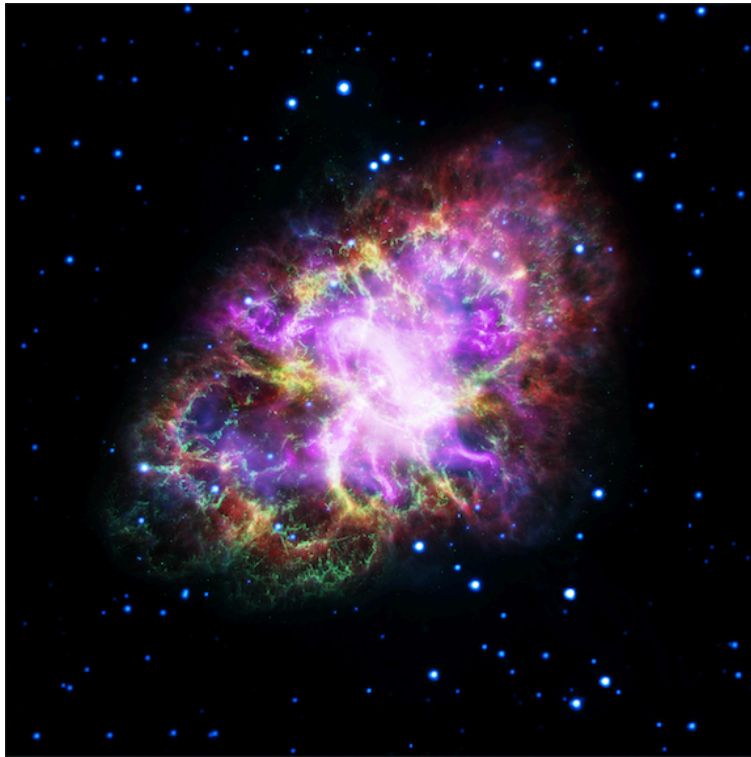


Figure 7.1: The image of the Crab Nebula composited different telescopes. The telescopes used to create this image are the Very Large Array (radio) in red, the Spitzer Space Telescope (infrared) in yellow, the Hubble Space Telescope (optical) in green, the XMM-Newton Observatory (ultraviolet) in blue, and the Chandra X-ray Observatory (X-ray) in purple. Credits: NASA, ESA, NRAO/AUI/NSF and G. Dubner (University of Buenos Aires).

Table 7.1: The good time intervals of the Crab observation. (Hitomi Collaboration et al., 2018)

| TSTART [s] ¹ | TSTART [UTC] | TSTOP [s] ¹ | TSTOP [UTC] | duration [s] |
|-------------------------|---------------------|------------------------|----------------------------|--------------|
| 70374949.000000 | 2016/03/25 12:35:48 | 70374979.000000 | 2016/03/25 12:36:18 | 30 |
| 70375027.000000 | 2016/03/25 12:37:06 | 70377352.000000 | 2016/03/25 13:15:51 | 2325 |
| 70380742.000000 | 2016/03/25 14:12:21 | 70383114.000000 | 2016/03/25 14:51:53 | 2372 |
| 70386733.000000 | 2016/03/25 15:52:12 | 70388875.000000 | 2016/03/25 16:27:54 | 2142 |
| 70392719.000000 | 2016/03/25 17:31:58 | 70394479.234375 | 2016/03/25 18:01:18.234375 | 1760 |

Table 7.2: Exposures of the Crab observation.

| | No. of all pseudo | No. of “clean” pseudo | Live Time from clean pseudo | dead time fraction due to BGO accidental hits | Live Time for SGD2 CC1 |
|----------|-------------------|-----------------------|--------------------------------|--|---------------------------|
| SGD1 CC1 | 11084 | 9879 | 4939.5 s | | |
| SGD1 CC2 | 10624 | 9478 | 4739.0 s | | |
| SGD1 CC3 | 11036 | 9879 | 4939.5 s | | |
| SGD2 CC1 | 11826 | | | 0.1161 | 5226.29 s |
| SGD2 CC2 | 11788 | 10419 | 5209.5 s | 0.1161 ² | |

7.2 Observations

7.2.1 Crab observation

Hitomi observed the Crab Nebula from 12:35 to 18:01 UT on March 25, 2016. For the SGD, this observation was the first light, and the SGD had been started up as nominal mode before the observation. However, because a channel of CdTe in SGD2-CC2 was noisy, we set the voltage to 0 V for CdTe sensors of SGD2-CC2 and SGD2-CC3. Therefore, only four Compton cameras, SGD1-CC1, -CC2, -CC3, and SGD2-CC1, were operating at the nominal mode to enable the Compton reconstruction.

We determine the Good time intervals (GTIs) of the SGD during the Crab observation shown in Table 7.1. The GTI are excluded in the Earth occultation and South Atlantic Anomaly (SAA) passages, and the total observation times was about 8.6 ks. In order to obtain the exposure time, the dead-time correction for each Compton camera is needed (see §5.3.3). The dead time correction is conducted by counting the pseudo flags, and the “clean” pseudo-events do not include the BGO anti-coincidence signals, and there is no FBGO flag and no HITPATBGO flag. However, it was found that an error exists in the on-board readout logic of adding the HITPAT BGO flags to pseudo-events for the parameter setting of SGD2-CC1. Therefore, we cannot obtain the true “clean” pseudo count for SGD2-CC1. The BGO signals are common among all SGD2 Compton cameras, and the dead-time fraction by accidental hits in the BGO must be same among them. We derive the pseudo count by using the fraction to the “clean” pseudo-events of SGD2-CC2. We summarize the exposure time in Table 7.2.

The attitude of the Hitomi satellite was stable throughout the Crab GTI. The nominal

¹TSTART and TSTOP is expressed in AHTIME, defined as the time elapsed since 2014/01/01 00:00:00 in seconds.

²It is derived from the comparison of a number of all pseudo events and a number of “clean” pseudo events. [(11788 – 10419)/11788]

pointing position is (R.A., DEC.) = (83.6334°, 22.0132°) and the nominal roll angle is 267.72° that is measured from the north to the satellite Y axis counter-clockwise. The distance from the nominal pointing position is within 0.3 arcmin for 98.7% of the observation time. The difference from the nominal roll angle is within 0.05° for the 99.6% of the observation time. Therefore, these offsets from the true direction of Crab are negligible and we have not considered them in the analysis.

7.3 Polarization Analysis

After the data reduction in the previous section, we obtained the azimuthal angle distributions in Figure 7.2 with bin width of 18 degrees. We did not randomize positions of hits for pixel size whenever an event was filled in each bin. The SGD2 is attached in point symmetry with respect to the SGD1, hence the azimuthal angle distribution of the SGD2 shifted by 180 degree.

7.3.1 parameter search method

In order to derive the polarization angle ϕ_0 and amplitude Q of the Crab, we adopted a binned likelihood fitting. We scaled the background data and unpolarized simulation with exposure times of the Crab observation for each CC. Expected counts $n_{\text{exp}}(\phi_i)$ in each bin are explained by the following equation using the background $b_{\text{bkg}}(\phi_i)$ and unpolarized simulation data $n_{\text{sim}}(\phi_i)$ in count space:

$$n_{\text{exp}}(\phi_i) = n_{\text{sim}}(\phi_i; \Pi = 0) (1 - Q \cos(2(\phi_i - \phi_0))) + b_{\text{bkg}}(\phi_i), \quad (7.1)$$

where Q is modulation factor, ϕ_0 is polarization angle in the coordinate of CC, i is bin number ($i > 1$) and ϕ_i is azimuthal angle of i -th bin. The azimuthal distributions of binned n_{obs} , b_{bkg} , n_{sim} are shown in Figure 7.2. When we evaluate the polarization components, realistically the azimuthal distributions are not binned. We assume that the Crab observation counts n_{obs} is given by Poisson distributions which can be written by

$$\text{Poisson}(n_{\text{obs}}(\phi_i) | n_{\text{exp}}(\phi_i)) = \frac{n_{\text{exp}}^{n_{\text{obs}}} e^{-n_{\text{exp}}}}{n_{\text{obs}}!}. \quad (7.2)$$

Likelihood function is sum of the Poisson distributions:

$$L(\phi_0, Q) = \prod_i \text{Poisson}(n_{\text{obs}}(\phi_i) | n_{\text{exp}}(\phi_i)). \quad (7.3)$$

Best fit parameters of Q and ϕ_0 , can be obtained by searching the minimum of

$$\mathcal{L} = -2 \log L. \quad (7.4)$$

The errors of estimated valued are evaluated from the confidence level. In case of the large sample limit, the difference between minimum of the log likelihood \mathcal{L} corresponding to the coverage provability. $\Delta\mathcal{L}$ is 2.30, 6.18, 11.83 for 68%, 95.45% and 99.73 %, respectively. In addition, the errors of the estimated values are applied when $\Delta\mathcal{L}$ is 2.30.

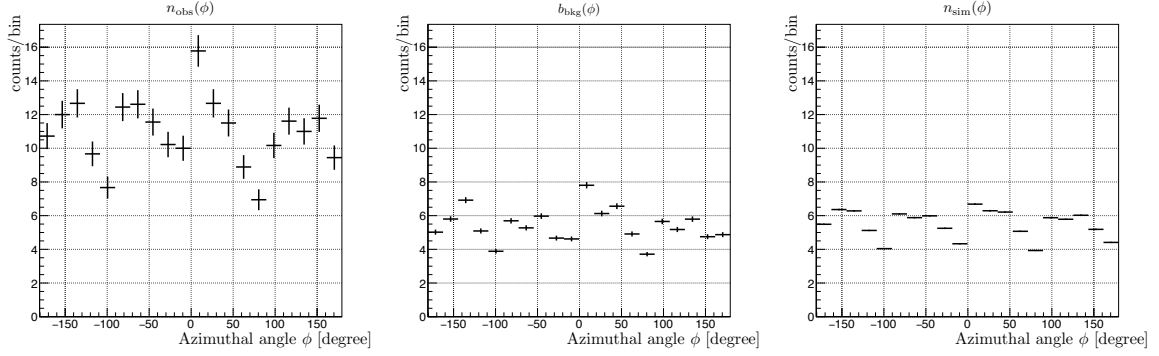


Figure 7.2: Binned azimuth angle distributions of n_{obs} , b_{bkg} , n_{sim} from the left. From these histograms, the polarization degree and the polarization angle are determined by likelihood using Equations (7.1) and (7.2).

7.3.2 Fitting Results

We show the results in Fig. 7.4. The polarization amplitude of the Crab is $Q = 0.1425$ ($-0.0682/+0.0681$) in 60 - 160 keV. The polarization angle is $\phi_0 = 67.10$ ($-13.21/+13.00$) degree. For the 100 % polarized photons, the polarization amplitude is estimated to be $Q_{100} = 0.6419$ given by simulations to set the polarization angle $\phi_0 = 65$ degree. As a result, the polarization degree of the Crab is $\Pi = 0.2222$ ($-0.1062/+0.1062$) %.

We also checked the polarization of the backgrounds (Figure 7.5), the RXJ 1856.5-3754 observations (BKGRXJ) and 24 hours before the Crab observation (BGK24). The estimated values of the background are showed in Figure 7.5.

In order to confirm the validation of the statistical confidence, we simulated the Crab observation 1000 times, and we derived the degree and the angle of polarization for each simulation using the binned likelihood fitting. The exposure time of each simulation was set to 5 ksec because one of the observations is about 5 ksec. The parameters of the simulation for the degree and angle of polarization were set to $\Pi = 0.22$ and $\phi_0 = 67^\circ$, respectively, which were obtained from observation. Moreover, we reproduced the background from the background data shown in Figure 7.3, and we obtained the 1000 sets of 5 ksec the background.

Figure 7.6 shows the result of the fitting to the 1000 times simulations for Q and ϕ_0 . The numbers of the data sets inside the contours of $\Delta\mathcal{L}$ s of 2.30, 5.99, and 9.21 are 668, 945 and 984, respectively. These numbers correspond to the coverage of probabilities in the case for two parameters.

In order to validate the confidence level for the detection of the polarized gamma-rays, we prepared 1000 sets of unpolarized simulation data. The results of the binned likelihood fits for the data sets are shown in the blue points of Figure 7.6. The distribution of the difference between the minimum of the log likelihood \mathcal{L} and the log likelihood of $Q = 0$ is shown in Figure 7.7. It is confirmed that the value of the difference corresponds to the coverage probabilities in the case of two parameters. Therefore, the $\Delta\mathcal{L}$ against the case of $Q = 0$ of 10.03 derived from the Crab observation corresponds to the confidence level of 99.3%.

Figure 7.8 shows the azimuthal distribution of the gamma-rays emitted by the Crab Nebula

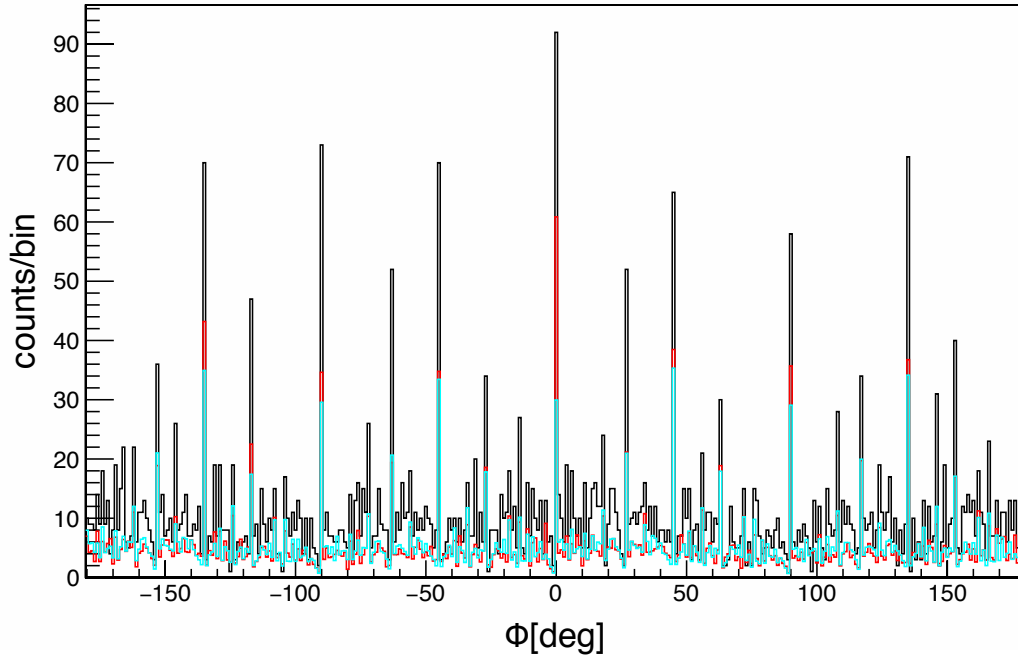


Figure 7.3: The binned azimuthal distribution of the Crab observation (black), the background (red) and the simulation (cyan).

with the parameters determined in this analysis. Figure 7.9 shows the relationship between the satellite coordinate and the sky coordinate. The roll angle during the Crab observation was 267.72° , and then, $\phi_0 = 67.02^\circ$, which corresponds the polarization angle of 110.70° .

7.4 Discussions

The detection of polarization and the measurement of its angle indicates the direction of an electric vector of radiation. In our analysis, the polarization angle is derived to be $PA = 110.7^\circ \pm_{-13.0^\circ}^{+13.2^\circ}$. The energy ranges of gamma-rays contributing most significantly to this measurement is $\sim 60\text{--}160$ keV. The spin axis of the Crab pulsar is estimated at $124^\circ \pm 0.1^\circ$ from X-ray imaging (Ng and Romani, 2004). Therefore, the direction of the electric vector of radiation as measured by the SGD is about one standard deviation with the spin axis. The Crab polarization observation resulting from other instruments are listed in Table 7.3. These instruments can be divided into three types based on the material of the scatterer. The PoGO+ and the SGD employ carbon and silicon for as scatterer, respectively, while the remaining instruments employ CZT or germanium. Since the cross section of the Compton scattering exceeds that of the photo absorption at above 20 keV for carbon, below 60 keV for silicon and above 200 keV for CZT and germanium, which constrain the minimum energy range for each instrument. Since the flux decreases with E^{-2} , the effective maximum energy for polarization measurements will be less than four times of the minimum energy. Therefore, the PoGO+, the SGD and the other instruments have more or less non-overlapping energy range and are

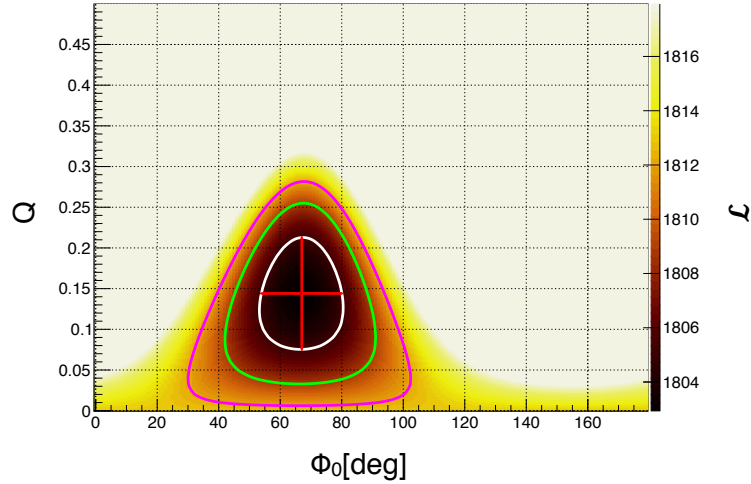


Figure 7.4: A result of the maximum log likelihood estimation. The contours indicate the confidence level. The green, orange and brown lines are the coverage provability of 68%, 95.45% and 99.73%, respectively.

complimentary. The PoGO+ team has reported the polarization angle $PA = 131.3^\circ \pm 6.8^\circ$ and the polarization fraction $PF = 20.9\% \pm 5.0\%$ for the pulse-integrated, and $PA = 137^\circ \pm 1.5^\circ$ and $PF = 17.4\%_{-9.3\%}^{+8.6\%}$ for off-pulse period (Chauvin et al., 2017). The results from the PoGO+ were consistent with our results. On the other hand, for the higher energy range, the INTEGRAL IBIS, SPI and the AstroSat CZTI have performed the polarization observation of the Crab Nebula in recent years, and, reported the slightly different polarization fractions and the polarization angles from our results. Furthermore, the AstroSat CZTI reported varying polarization fraction during the off-peak period (Vadawale et al., 2018). However, we have not been able to verify those results because of extremely short observation time, which was less than 1/18th of the PoGO+, and less than 1/100th of the higher energy instrument. Despite such short observation time, the errors of our measurements are within a factor of two of other instruments. This result demonstrates the effectiveness of the SGD design such as high modulation factor of the azimuthal angle dependence, highly efficient instrument design and low backgrounds. Extrapolating from this result, we expect that the 20 ks SGD observation can achieve statistical error equivalent with the PoGO+ and the AstroSAT CZTI, and the 80 ks SGD observation can perform phase resolved polarization measurements with similar errors.

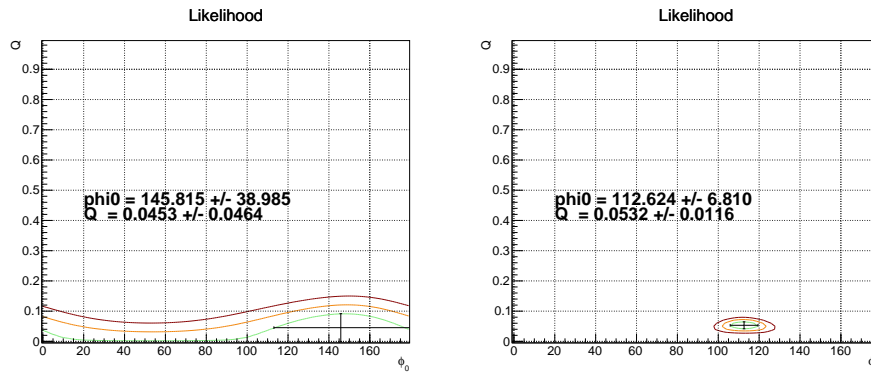


Figure 7.5: Results of backgrounds. The left panel is bkg24, and the right panel is bkgRXJ

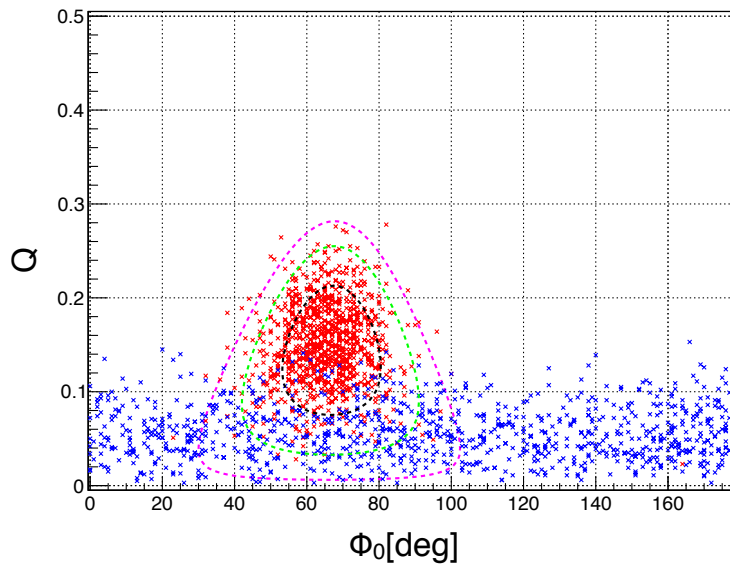


Figure 7.6: The results of Likelihood estimations for 1000 sets of simulation data. The red points show the best-fit parameters for the Crab simulation data with the polarization parameters derived from the observation data, and, the blue points show the best-fit parameters for the unpolarized simulation data. The contours are same as in Figure 7.4.

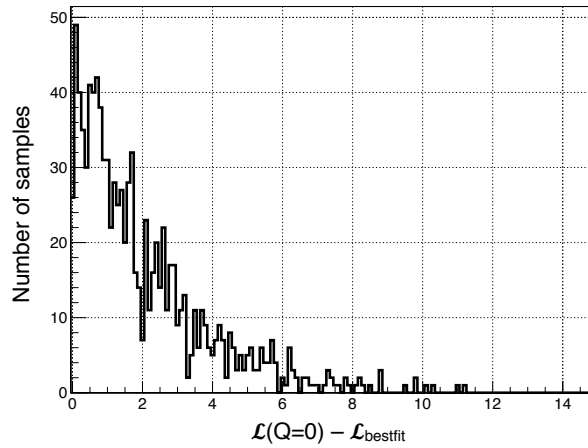


Figure 7.7: The histogram of the difference between the minimum of the log likelihood \mathcal{L} and the log likelihood of $Q = 0$ for the 1000 sets of unpolarized simulation data. The numbers of the data set within the differences of 2.30, 5.99 and 9.21 are 668, 955, and 993, respectively. The difference between the minimum of the log likelihood \mathcal{L} and the log likelihood of $Q = 0$ also corresponds to the coverage probability for two parameters.

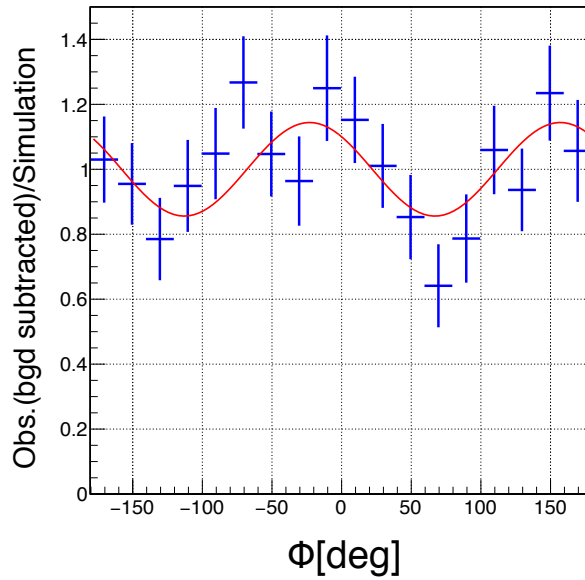


Figure 7.8: Modulation curve of the Crab Nebula observed with the SGD. The data points show the ratio of the observation data subtracted the background to the unpolarized simulation data. The error bar size indicates their statistics errors. The red curve shows the sine curve function substituted the estimated parameters by the log-likelihood fitting.

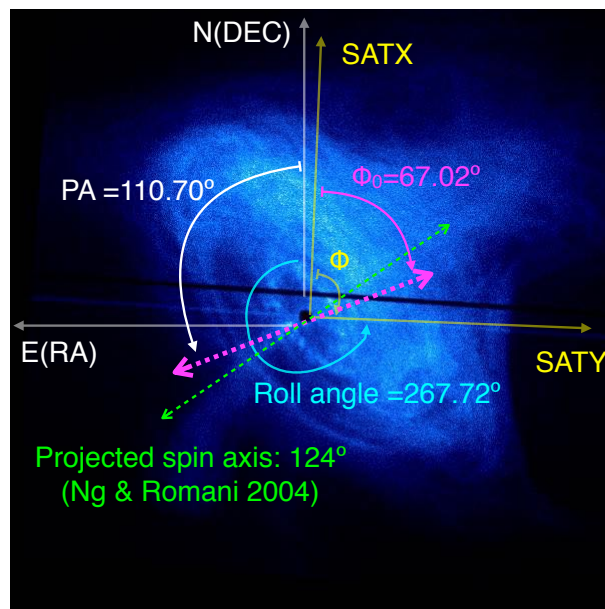


Figure 7.9: The polarization angle of the gamma-rays from the Crab Nebula determined by the SGD. The direction of the polarization angle is drawn on the X-ray image of Crab with Chandra.

Table 7.3: Results of polarization observations for Crab

| Satellite/Instruments | Energy band (keV) | Polarization angle (degree) | Degree of polarization (%) | Exposure time (ks) | phase | supplement |
|-----------------------|----------------------|--------------------------------|-------------------------------|-----------------------|-------|------------------------|
| PoGO+(Balloon Exp.) | 20-160 | 131.3 ± 6.8 | 20.9 ± 5.0 | 92 | All | Chauvin et al. (2017) |
| Hitomi/SGD | 60-160 | $110.7^{+13.2}_{-13.0}$ | 22.1 ± 10.6 | 5 | All | this work |
| AstroSat/CZTI | 100-380 | 143.5 ± 2.8 | 32.7 ± 5.8 | 800 | All | Vadawale et al. (2018) |
| INTEGRAL/SPI | 130-440 | 117 ± 9 | 28 ± 6 | 600 | All | Chauvin et al. (2013) |
| INTEGRAL/IBIS | 200-800 | 110 ± 11 | 47^{+19}_{-13} | 1200 | All | Forot et al. (2008) |

Chapter 8

Polarization degree of torus modeled on Crab Wind Nebula

8.1 Model of the electron flow and magnetic field of the Crab Nebula

In order to reproduce the measurements of polarization in X-ray and gamma-ray band, we simulate synchrotron radiation of the Crab Nebula. The emission intensity depends on the magnetic field and the electron energy distribution, and the degree of polarization depends additionally on the geometry of the magnetic field and spacial distribution of high-energy electrons. We start with a standard one-zone model, which can reproduce the broadband emission from the source (see §8.1.1). To study the polarimetric properties of this model we introduce a realistic geometry of the magnetic field. There are some observational (e.g., the morphology of the nebula seen in the X-ray) and theoretical (e.g., rapid decrease of the poloidal magnetic field in the wind) arguments for a toroidal geometry of the magnetic field in the nebula. For this geometry, we homogeneously distributed emitting electrons along the field line, i.e., assuming that electrons form a ring-like configuration in the nebula. We analytically computed the polarization degree and concluded that the prediction of the one-zone model seems to be inconsistent with polarimetric measurement in the X-ray energy band (see §8.1.2). Therefore, we proceed to develop a more detailed model for the synchrotron radiation. We use a magnetohydrodynamic (MHD) model to describe the structure of the nebula (which defines the magnetic field strength, flow bulk velocity, and particle density, see §8.1.5), and a particle transport module based on Fokker-Planck equation to compute particle energy distribution (see §8.1.6). Finally, we obtained the emission intensity and polarization (see §8.1.7) of synchrotron radiation using obtained distributions of magnetic field and non-thermal particles and accounting for relativistic transformation of the emission and its polarization (see §8.1.8).

The used approach is based on a seminal paper by Kennel and Coroniti (1984) and was gradually developed in the past years. Kennel and Coroniti (1984) suggested their model to provide a qualitative verification for the scenario that involves ejection of ultra-relativistic pulsar wind (Rees and Gunn, 1974). They suggested that the pulsar wind should influence the emission by defining the conditions at the inner boundary of the synchrotron nebula. This boundary coincides with a shock wave at which the pulsar wind gets heated up (so-called pul-

sar wind termination shock). The boundary conditions determine the MHD flow in the nebula, and Kennel and Coroniti (1984) suggested an analytic solution for 1D relativistic MHD equations. Based on that solution, they solved the transport equation for non-thermal particles and obtained the volume synchrotron emissivity in the nebula. The spectra predicted by the model agreed well with the observations provided that the pulsar wind is weakly magnetized and ultra-relativistic. Atoyan and Aharonian (1996) extended the approach suggested by Kennel and Coroniti (1984) and computed self-consistently the inverse Compton emission for the distribution of the non-thermal particles obtained in frameworks of the Kennel and Coroniti (1984) model. Later on, Bogovalov and Khangoulyan (2002) suggested that the energy flux in the pulsar wind should be highly anisotropic with the largest fraction of energy released in a limited range of solid angles close to the equatorial plane. It was suggested that a simple MHD model that utilizes the analytical solution by Kennel and Coroniti (1984) limited to a region close to the equatorial plane can qualitatively reproduce the bright torus seen in the X-ray energy band with Chandra (Weisskopf et al., 2000b). The formation of jet-like plumes in the nebula is likely caused by magnetic collimation (Khangoulian and Bogovalov, 2003), but the jet emission gives a quite small contribution to the overall X-ray emission. Thus, even being highly polarized, the jet emission can give only a modest contribution to the polarization of the total emission from the nebula. The model suggested by Bogovalov and Khangoulyan (2002) was numerically verified by a number of groups (see, e.g., Bucciantini, N. et al., 2004, Komissarov and Lyubarsky, 2004), and one found that a numerical treatment of 2D MHD equations confirms the model by Bogovalov and Khangoulyan (2002) and additionally allows us to reproduce many fine structures seen in the nebula. In particular, X-ray wisps are robustly associated with MHD waves propagating in the nebula.

To study the polarization properties of the Crab Nebula we extend the model suggested by Bogovalov and Khangoulyan (2002) (which is a simple 2D generalization of the original Kennel and Coroniti (1984) model) for calculation of polarization. We found that this model, in contrast to the one-zone model, predicts a quite different polarization degree in the X-ray band.

8.1.1 Broadband spectrum

Observations in the range from radio frequencies to gamma rays have revealed the broadband emission from the Crab Nebula. The emission below several GeV is interpreted as synchrotron radiation of relativistic electrons. Meanwhile, gamma rays from GeV to TeV are produced through the inverse Compton scattering. A synthetic spectral energy distribution (SED) of synchrotron and inverse Compton emission in the Crab Nebula is shown in Figure 8.1 together with available observational data.

The SED of the nebula in Figure 8.1 is produced in framework of a one-zone model. This implies that the strength of the magnetic field and intensities of target photons were assumed to be the same for all emitting electrons. As dictated by the observations, there are two general trends in the spectrum: from radio to optical band the spectrum is hard, and from optical to soft gamma rays the spectrum is soft. Above soft gamma rays, the SED rapidly decreases due to a cutoff. In the very high energy regime the SED features a second hump, that is conventionally interpreted as the inverse Compton (IC) emission. Therefore, in the one-zone model we adopted a broken power-law with exponential cutoff distribution for non-thermal

electrons:

$$n(E) = \exp(-E/E_{\text{cut}}) \times \begin{cases} AE^{-\alpha_1} & (E < E_b) \\ AE_b^{\alpha_2 - \alpha_1} E^{-\alpha_2} & (E > E_b) \end{cases}, \quad (8.1)$$

where E_b is break energy, E_{cut} is cut-off energy, and A is a normalization coefficient. To match the measured radio and X-ray spectra we adopted the following indexes $\alpha_1 = 1.5$ and $\alpha_2 = 3.2$. The break and cutoff energies were assumed to be $E_b = 265$ GeV and $E_{\text{cut}} = 1.8$ PeV, respectively. For the magnetic field of $B = 125$ μ G the synchrotron component reproduces the observations correctly. Above several GeV, the inverse Compton (IC) scattering starts to dominate the synchrotron radiation. Following Atoyan and Aharonian (1996), we considered seed photons of three different types: (i) the 2.7 K cosmic microwave background, (ii) the far-infrared radiation from ambient dust with temperature $T \simeq (70-100)$ K and the energy density of $w_{\text{ir}} = 0.5$ eV/cm³, (iii) the synchrotron radiation produced in the nebula (we note that the near-infrared background affects the IC component weakly).

The SED shown in Figure 8.1 is obtained with python package *naima* (Zabalza, 2015), the emission was computed with the standard methods in *naima*, i.e., one computed the synchrotron emission with the parameterization by Aharonian et al. (2010), IC emission on CMBR and FIR with method suggested by Khangulyan et al. (2014), and SSC component with the cross-section obtained by Aharonian and Atoyan (1981).

8.1.2 Simple calculation of the degree of polarization

Here we proceed with calculations of the degree of polarization by using the one-zone model which we introduced above. In order to derive polarization, one needs to assume a geometry of the magnetic field, which was adopted as toroidal, which is consistent with the theoretical expectations and also observations in the X-ray energy band. The schematic view is shown in Figure 8.2. In this figure, the rotation axis of the Crab Pulsar is along z -axis. We set the observer direction as $\mathbf{n} = (\sin \theta_{\text{obs}}, 0, \cos \theta_{\text{obs}})$, where θ_{obs} is inclination angle, i.e., the angle between the line of sight and the rotation axis. The vector of the toroidal magnetic field can be represented as $\mathbf{B} = B(-\sin \phi, \cos \phi, 0)$, where ϕ is azimuth angle. There are two effects that influence the emission intensity and polarization in framework of this simplified model. First, depending on the location on the magnetic loop, the pitch angle, which is the angle between the magnetic field and line-of-sight, is changing. Second, emission from each segment of the magnetic loop is partially linearly polarized, but the direction of the polarization varies with angle ϕ .

The pitch angle is given by $\sin \alpha = \sqrt{1 - \sin^2 \theta_{\text{obs}} \sin^2 \phi}$. To compute the polarization, we need to define a direction in the plane of sky: $\mathbf{l}_1 = \mathbf{l}_2 \times \mathbf{n} = (\cos \theta_{\text{obs}}, 0, -\sin \theta_{\text{obs}})$, where $\mathbf{l}_2 = (0, 1, 0)$ is an auxiliary vector. The electric field of the electromagnetic wave is $\mathbf{e} \propto \mathbf{B} \times \mathbf{n}$, which makes an angle $\cos \chi = \mathbf{e} \cdot \mathbf{l}_1 / |\mathbf{e}| = \cos \phi (1 - \sin^2 \theta_{\text{obs}} \sin^2 \phi)^{-1/2}$ to the selected direction \mathbf{l}_1 .

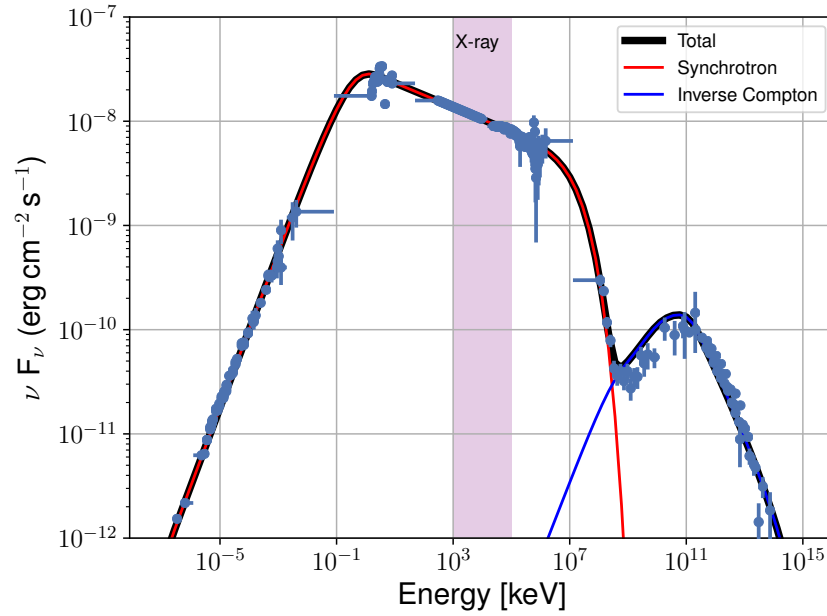


Figure 8.1: The broadband spectrum of the Crab Nebula. The data points are obtained by various observations from radio to gamma-rays (the detail is described in Meyer et al., 2010, and Table 1 therein). The red line is the synchrotron radiation, the blue line is the inverse Compton radiation, and the black line is the total emission. The filled region in purple indicate the X-ray energy range, 1-100 keV. The figure is created by using the python package, naima (Zabalza, 2015).

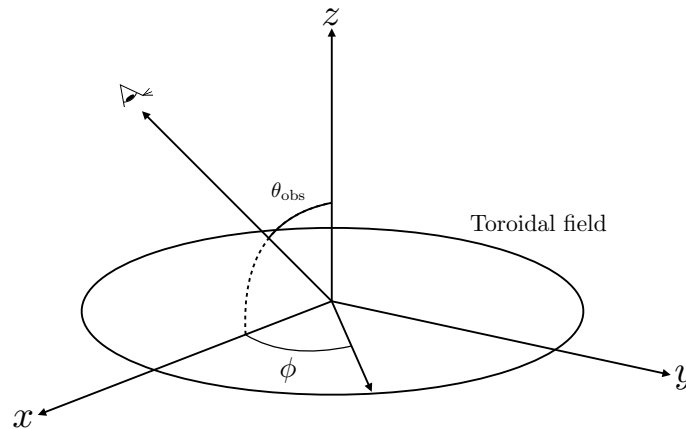


Figure 8.2: A schematic of the toroidal electric field in the Crab Nebula and the relation between the observer and it. The rotation angle of the Crab Pulsar is along z -axis.

The Stokes parameters of the synchrotron radiation can be expressed as

$$I(\phi, \theta_{\text{obs}}) = A \times (B \sin \alpha)^{(p+1)/2} \int_0^\infty x^{\frac{p-3}{2}} F(x) dx, \quad (8.2)$$

$$Q(\phi, \theta_{\text{obs}}) = A \times (B \sin \alpha)^{(p+1)/2} \int_0^\infty x^{\frac{p-3}{2}} G(x) dx \times \cos 2\chi, \quad (8.3)$$

$$U(\phi, \theta_{\text{obs}}) = A \times (B \sin \alpha)^{(p+1)/2} \int_0^\infty x^{\frac{p-3}{2}} G(x) dx \times \sin 2\chi, \quad (8.4)$$

where A does not depend on $(\phi, \theta_{\text{obs}})$ (see Section 2.2.1). When we calculate the degree of polarization, we integrate these equations over the azimuth angle ϕ . Then, the degree of polarization is given by

$$\begin{aligned} \Pi &= \frac{\sqrt{\left(\int Q(\phi, \theta_{\text{obs}}) d\phi\right)^2 + \left(\int U(\phi, \theta_{\text{obs}}) d\phi\right)^2}}{\int I(\phi, \theta_{\text{obs}}) d\phi} \\ &= \frac{p+1}{p+\frac{7}{3}} \frac{\int_0^{2\pi} \left(\sqrt{1 - \sin^2 \phi \sin^2 \theta_{\text{obs}}}\right)^{(p+1)/2} \frac{\cos^2 \phi - \sin^2 \phi \cos \theta_{\text{obs}}}{1 - \sin^2 \phi \sin^2 \theta_{\text{obs}}} d\phi}{\int_0^{2\pi} \left(\sqrt{1 - \sin^2 \phi \sin^2 \theta_{\text{obs}}}\right)^{(p+1)/2} d\phi}. \end{aligned} \quad (8.5)$$

It indicates that the degree of polarization is function of the power-law index p of the electron energy distribution, for a fixed observer direction. In the case of the Crab Nebula, the above equation yields in degree of polarization of 46%, where we assumed that the inclination angle is $\theta_{\text{obs}} = 60^\circ$ and the index is $p = 3.2$. The derived polarization degree is higher than all measurements in the X-ray band, except the highest energy point measured with INTEGRAL/IBIS, see Figure 8.3. We note that the slight increase of the polarization seen in this figure is caused by the influence of the high-energy cutoff in the electron spectrum, which makes the effective power-law index for 1 MeV-emitting particles to be a bit higher than for electrons that radiate at 1 keV.

Thus, in framework of the one-zone radiation model for Crab Nebula, one should expect a very weak dependence of polarization degree on photon energy in the X-ray energy band. This prediction seems to be inconsistent with the polarization measurements show in Figure 8.3. Thus, in what follows we develop a more detailed radiation model that accounts for (i) MHD flows in the nebula (ii) electron cooling and advection (iii) Lorentz transformation of the electromagnetic waves.

From the observational point of view, PWNe correspond to the region of shocked pulsar wind. The MHD flow in this region is expected to be sub-sonic, thus the entire nebula should be nearly isobaric. However, there could be a non-trivial dependence of the magnetic field. Moreover, the non-thermal particles are injected to the nebula at the pulsar wind termination shock and should have a very non-homogeneous energy distribution through the nebula. The electron cooling time due to the synchrotron radiation in the Crab Nebula can be estimated as

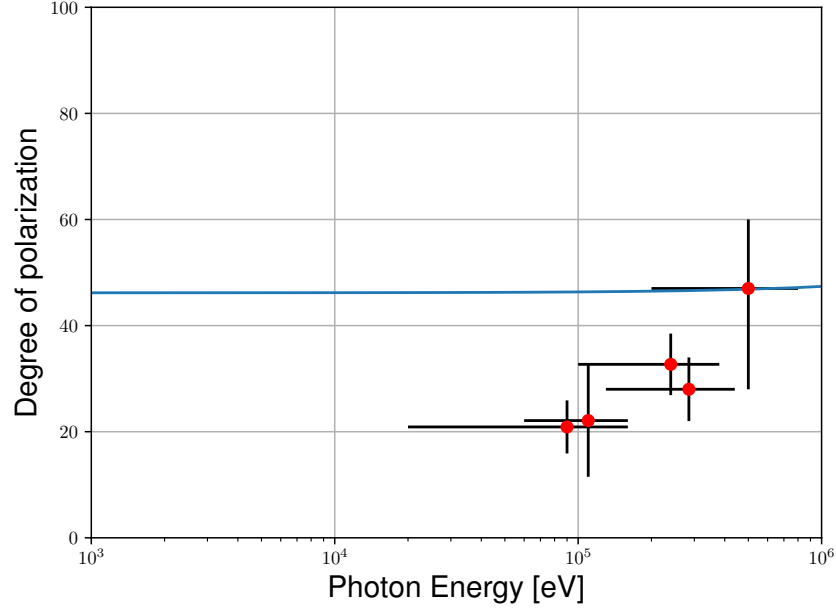


Figure 8.3: The degree of polarization in X-ray of the Crab Nebula. The solid line indicates Equation (8.5). The index of the electron distribution is calculated from the model in Figure 8.1. Points indicate the observation results from Table 7.3.

(Atoyan and Aharonian, 1996)

$$t_{\text{syn}} \approx 2.8 \times 10^8 \left(\frac{B}{3 \times 10^{-4} \text{ G}} \right)^{-2} \gamma^{-1} \text{ yr}, \quad (8.6)$$

where $\gamma = E/m_e c^2$. This implies that the high energy electrons are localized nearby the termination shock. Therefore, it is expected that the inner region of the nebula is bright in high energy X-ray or gamma-ray. This expectation is consistent of results of imaging analyses in soft and hard X-ray bands (Madsen et al., 2015, Mori et al., 2004, Weisskopf et al., 2000b).

The motion of non-thermal particles is determined by the particle energy and the properties of the magnetic field, and can be extremely complex. Conventionally, the particle transport is considered as superposition of two processes: advection and diffusion. Advection is related to the (average) energy-independent displacement of the high-energy particles as they are dragged by the background plasma, in particular by its irregular magnetic field, and is determined by the background flow MHD. Diffusion is the result of microscopic chaotic scatterings of the particles in the plasma irregular field. In the parameter range in which the diffusion approximation is valid, the particle effective velocity in the flow co-moving frame is small as compared to the light velocity, and thus in relativistic outflows advection typically dominates over diffusion. Therefore, at the basic approximation one typically assumes that the diffusion contribution to the particle transport is small. If advection is the dominant particle transport mechanism, then non-thermal particles are effectively confined within their fluid elements, thus their displacement is entirely determined by the structure of the MHD flow.

8.1.3 MHD model by Kennel & Coroniti

Kennel and Coroniti (1984) suggested a hybrid MHD-kinetic model that on one hand includes a 1D relativistic MHD flow that correctly reproduces the radius of the pulsar termination shock (which is constrained with the X-ray observations), size of the nebula, and its expansion velocity. On top of this MHD description, the kinetic part of the model describes the particle cooling and advection consistently with the used MHD solution.

We extend the approach of Atoyan and Aharonian (1996), Kennel and Coroniti (1984) and Bogovalov and Khangoulyan (2002) to compute the degree of polarization of synchrotron radiation in Crab Nebula. In order to calculate the intensity of the synchrotron radiation, we obtain the magnetic field strength and the flow velocity along the radial direction by using the MHD models of Kennel and Coroniti (1984) in the geometry suggested by Bogovalov and Khangoulyan (2002). We enhance the one-dimension MHD description to three-dimension radiation model under the assumption of axial symmetry. We divide the three-dimension volumes into fluid elements. The properties of the particles in these fluid elements is determined by a single parameter: fluid element's distance to the termination shock. Emission of each fluid element is, however, anisotropic and it is necessary to account for 3D structure of the magnetic field, relativistic Doppler boosting, relativistic swinging of electric field (also known as relativistic de-polarization). All these effects are accounted in frameworks of used 3D radiative model.

8.1.4 Condition at the inner boundary of the nebula

Upstream the termination shock the pulsar wind is assumed to be an ultrarelativistic cold magnetized outflow. Given that the total wind luminosity is determined by the pulsar spin-down losses, the wind can be fully described with two phenomenological parameters: its bulk Lorentz factor, γ_1 , and its magnetization, σ . The magnetization of the wind is defined as the ratio of the Poynting flux to the kinetic energy;

$$\sigma = \frac{[\text{the magnetic energy flux}]}{[\text{the kinetic energy}]} = \frac{B_1^2}{4\pi n_1 u_1 \gamma_1 m_e c^2}, \quad (8.7)$$

where B_1 is the magnetic field, n_1 is the proper density, u_1 is the radial four speed of the flow, $\gamma_1^2 = 1 + u_1^2$, m_e is the electron mass and c is the speed of light. The spin-down luminosity L_s is written by it as follows;

$$L_s = 4\pi n_1 \gamma_1 u_1 r_s^2 m_e c^3 (1 + \sigma), \quad (8.8)$$

where r_s is the radius of the termination shock. The subscripts “1” and “2” indicate the upstream and downstream, respectively.

The properties of the cold pulsar wind determine the boundary condition for the flow through the Rankine-Hugoniot conditions (8.1.4). This allows a completely analytical description of the flow in the nebula under the approximation of 1D MHD (8.1.5).

The downstream conditions are determined through the Rankine-Hugoniot relation. Assuming that the flow is ultrarelativistic and perpendicular to the shock, the following MHD

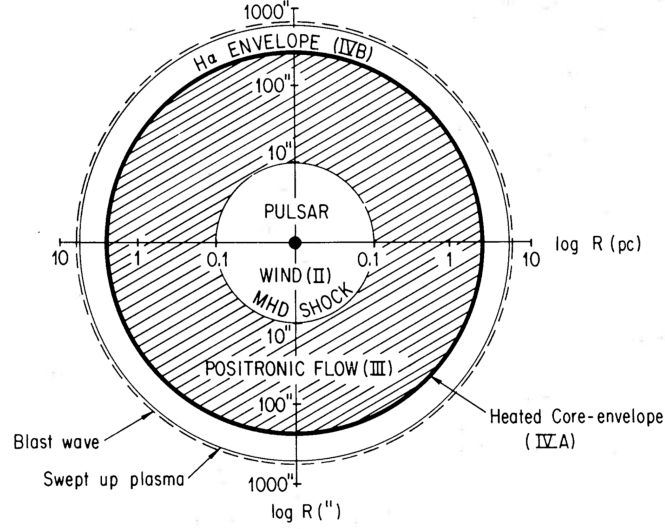


Figure 8.4: A schematic of view of the Crab Pulsar Wind Nebula (adopted from Kennel and Coroniti, 1984).

conservation laws should be fulfilled:

$$n_1 u_1 = n_2 u_2, \quad (8.9)$$

$$E = \frac{u_1 B_1}{\gamma_1} = \frac{u_2 B_2}{\gamma_2}, \quad (8.10)$$

$$\gamma_1 \mu_1 + \frac{EB_1}{4\pi n_1 u_1} = \gamma_2 \mu_2 + \frac{EB_2}{4\pi n_1 u_1}, \quad (8.11)$$

$$\gamma_1 u_1 + \frac{P_1}{n_1 u_1} + \frac{B_1^2}{8\pi n_1 u_1} = \gamma_2 u_2 + \frac{P_2}{n_1 u_1} + \frac{B_2^2}{8\pi n_1 u_1}, \quad (8.12)$$

where E is the electric field, μ is the specific enthalpy, and P is the pressure. The number density in the laboratory frame is $N = \gamma n$. The equation (8.9) has been applied to the equations (8.11) and (8.12). The specific enthalpy is defined with adiabatic index Γ ,

$$\mu = m_e c^2 + \frac{\Gamma}{\Gamma - 1} \left(\frac{P}{n} \right). \quad (8.13)$$

It is generally difficult to solve the Rankine-Hugoniot relation for the downstream conditions. However, under the strong shock approximation the equations can be resolved analytically. The assumptions are the following: $P_2/n_2 m_e c^2 \gg 1$, P_1 and u_2/u_1 are small, and $u_1/\gamma_1 \sim 1$. This approximation reduces the Rankine-Hugoniot relations to

$$u_2^2 = \frac{8\sigma^2 + 10\sigma + 1}{16(\sigma + 1)} + \frac{1}{16(\sigma + 1)} [64\sigma^2(\sigma + 1)^2 + 20\sigma(\sigma + 1) + 1]^{1/2}, \quad (8.14a)$$

$$\frac{B_2}{B_1} = \frac{N_2}{N_1} = \frac{\gamma_2}{u_2}, \quad (8.14b)$$

$$\frac{P_2}{n_1 m_e c^2 u_1^2} = \frac{1}{4u_2 \gamma_2} \left[1 + \sigma \left(1 - \frac{\gamma_2}{u_2} \right) \right]. \quad (8.14c)$$

Under this approximation, the flow speed, the magnetic field and density ratio, and the pressure and the temperature of the downstream depend only upon σ .

The behaviors of these parameters are different between large and small σ limits. In case of the large- σ limits, one obtains

$$u_2^2 = \sigma + \frac{1}{8} + \frac{1}{64\sigma} + \dots, \quad (8.15a)$$

$$\gamma_2^2 = \sigma + \frac{9}{8} + \frac{1}{64\sigma} + \dots, \quad (8.15b)$$

$$\frac{B_2}{B_1} = \frac{N_2}{N_1} = 1 + \frac{1}{2\sigma} + \dots, \quad (8.15c)$$

$$\frac{P_2}{n_1 m c^2 u_1^2} = \frac{1}{8\sigma} \left(1 - \frac{1}{16\sigma} + \dots \right). \quad (8.15d)$$

These equations indicate that the shock becomes weak. Since the flow speed in downstream approach the speed of light, the jumps of the density and magnetic field at the shock are small, and the magnetic pressure is still large in downstream region.

On the other hands, in the case of the small- σ , the Rankine-Hugoniot relation yields to

$$u_2^2 = \frac{1 + 9\sigma}{8}, \quad (8.16a)$$

$$\gamma_2^2 = \frac{9 + 9\sigma}{8}, \quad (8.16b)$$

$$\frac{B_2}{B_1} = \frac{N_2}{N_1} = 3(1 - 4\sigma), \quad (8.16c)$$

$$\frac{P_2}{n_1 m c^2 u_1^2} = \frac{2}{3}(1 - 7\sigma). \quad (8.16d)$$

In the limit $\sigma \rightarrow 0$, the speed of the downstream flow approaches $c/3$, the compression ratio B_2/B_1 and N_2/N_1 approach 3, and the particle pressure approaches $2/3$. It indicates that the shock is strong and the upstream total energy is converted into the downstream thermal energy, which can be emitted as synchrotron radiation in the volume of the nebula. By fitting the broadband SED of the Crab Nebula, Kennel and Coroniti (1984) revealed that the σ parameter seems to be small, $\sigma = 0.003$.

8.1.5 Propagation of the flow in the downstream

In the downstream, the flow is described by the following equations under the toroidal field approximation;

$$\frac{d}{dt} (c n u r^2) = 0, \quad (8.17)$$

$$\frac{d}{dr} \left(\frac{r u B}{\gamma} \right) = 0, \quad (8.18)$$

$$\frac{d}{dr} (n u r^2 e) + P \frac{d}{dr} (r^2 u) = 0, \quad (8.19)$$

$$u \frac{d}{dr} (\gamma \epsilon) = \frac{d}{dr} \left[n u r^2 \left(\gamma \mu + \frac{B^2}{4\pi n \gamma} \right) \right] = 0, \quad (8.20)$$

where e is the relativistic internal energy per particle, μ is the specific enthalpy ($\mu = \epsilon + p$), and ϵ is the sum of the electromagnetic and particle energy per particle in the proper frame. The four equations describe conservation laws and a propagation; the conservation of number flux (8.17), the conservation of magnetic flux in the magnetohydrodynamic approximation (8.18), the propagation of internal energy (8.19), and the conservation of total energy (8.20).

We define the flow speed downstream of the shock and the radius as $u(z) = u_2 v$ and $z = r/r_s$, respectively. Then the combination of four equations (8.17) – (8.20) leads to the following algebraic equation:

$$(1 + u_2^2 v^2)^{1/2} \left[\delta + \Delta (vz^2)^{-1/3} + \frac{1}{v} \right] = \gamma_2 (1 + \delta + \Delta), \quad (8.21)$$

where the parameters δ and Δ are

$$\delta = \frac{4\pi n_2 \gamma_2^2 m c^2}{B_2^2} \approx \frac{u_2}{u_1 \sigma}, \quad (8.22)$$

$$\Delta \equiv \frac{16\pi P_2 \gamma_2^2}{B_2^2} = \left(\frac{1 + \sigma}{\sigma} \right) \frac{u_2}{\gamma_2} - 1. \quad (8.23)$$

Since the δ and Δ depend only upon σ , we can solve the equation (8.21) for the normalized flow speed v with arbitrary z . In the small- σ limits, $\Delta \approx \sigma/3$. The Alfvén four speed downstream of shock can be expressed as following equation in the assumption of relativistically adiabatic hot plasma,

$$U_{A2}^2 \equiv \frac{B^2}{4\pi n_2 \gamma_2 \mu_2} \approx \frac{1}{\Delta}. \quad (8.24)$$

The four equations Eq. (8.17) – (8.20) reduce to the four speed $u(z)$ and the magnetic field $B(z)$;

$$u(z) = u_2 v(z) = \frac{u_2}{z^2} \left(\frac{\Delta}{1 + \Delta} \frac{G}{3} \right)^3, \quad (8.25)$$

$$B(z) = \frac{u_2 B_2}{z u(z)} = B_2 \left(\frac{\Delta}{1 + \Delta} \frac{G}{3} \right)^{-3} z, \quad (8.26)$$

where

$$G = 1 + \left[1 + x^2 + \sqrt{(1 + x^2)^2 - 1} \right]^{1/3} + \left[1 + x^2 - \sqrt{(1 + x^2)^2 - 1} \right]^{1/3}, \quad (8.27)$$

$$x = z \left[\frac{2}{27} \frac{\Delta^3}{(1 + \Delta)^2} \right]^{-1/2}, \quad (8.28)$$

The G depend upon z and σ . We show the downstream four velocity and the magnetic field against z in Figure 8.1.5.

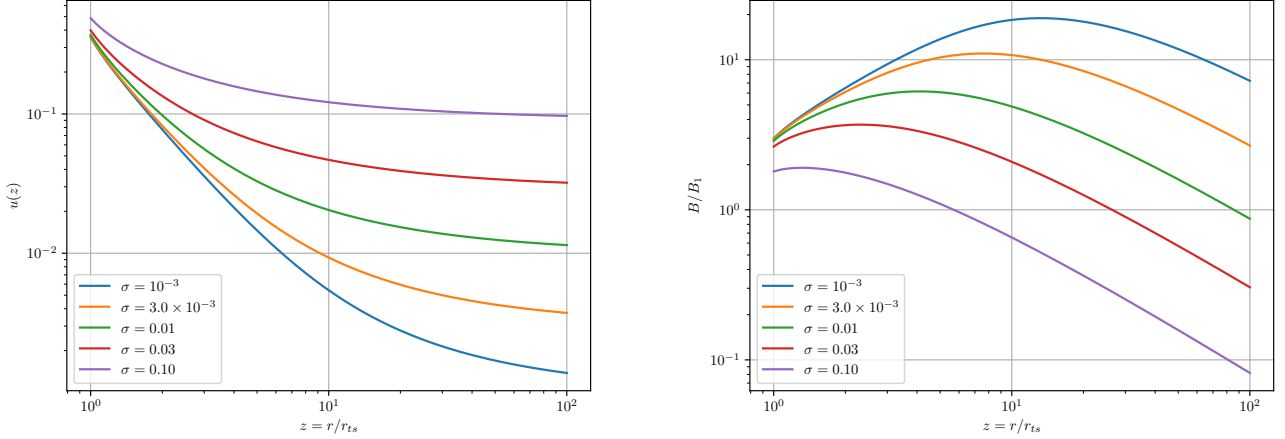


Figure 8.5: The downstream four velocity (left panel) and the downstream magnetic field normalized upstream magnetic field (right panel) against $z = r/r_s$ in the small- σ limits. The σ is smaller, the downstream four velocity is smaller and the magnetic field is higher. The magnetic field is increase in small z and decrease in large z .

8.1.6 Particle cooling

The electron energy distribution in the flow changes with distance from the termination shock due to particle energy losses. We consider a differential volume element dV at the time t in the flow. The electron energy distribution $n(t, E)$ is changed with time. Since we assume the number of electrons N is conserved, the transformation of the electron energy distribution is described by

$$dN = n(t, E)dEdV = n(t = 0, E_0)dE_0dV_0, \quad (8.29)$$

where subscription 0 indicates the particles at $t = 0$, which corresponds to the moment when the fluid element passed the termination shock and non-thermal particles were accelerated to a predefined initial distribution. The electron energy distribution n in Equation (8.29) at arbitrary time t is given by

$$n(t, E) = n(t = 0, E_0) \frac{dE_0}{dE} \frac{dV_0}{dV} = n_0 \varphi \frac{dE_0}{dE}, \quad (8.30)$$

where n_0 is an initial electron energy distribution, and $\varphi = \rho/\rho_0$ is the plasma compression (i.e., a parameter revealed with MHD simulations).

The time variation of the energy E in the element is described by the particle cooling equation

$$\frac{dE}{dt} = \dot{E}(t, E), \quad (8.31)$$

where \dot{E} is energy loss rate. For the nebula, the energy loss rate is typically accounted for synchrotron, inverse Compton and adiabatic losses of electrons, as

$$\dot{E}(t, E) = \dot{E}_{\text{syn}}(t, E) + \dot{E}_{\text{IC}}(t, E) + \dot{E}_{\text{AD}}(t, E). \quad (8.32)$$

The term of synchrotron and inverse Compton is

$$\dot{E}_{\text{syn}} + \dot{E}_{\text{IC}} = -aE^2, \quad (8.33)$$

$$a = \frac{4}{3} \frac{\sigma_{\text{T}} c}{(m_e c^2)^2} (w_{\text{ph}} + w_B), \quad (8.34)$$

where σ_{T} is Thomson cross section, and w_{ph} and w_B are the energy density of the target photons and the magnetic field, respectively. The adiabatic loss rate is

$$\dot{E}_{\text{AD}} = \frac{1}{3} \frac{d \ln \rho}{dt} E, \quad (8.35)$$

where ρ is plasma density in the fluid element. Then, Equation (8.32) is rewritten by using Equations (8.34) and (8.35), as

$$\frac{d}{dt} \left(\frac{\rho^{1/3}}{E} \right) = \rho^{1/3}(t) a(t). \quad (8.36)$$

Solving this equation, we obtain the relation between the particle energy at the injection point and the emission point as

$$\left(\frac{\rho^{1/3}}{E} \right) - \left(\frac{\rho_0^{1/3}}{E_0} \right) = \int_0^t \rho^{1/3}(t') a(t') dt' = \lambda, \quad (8.37)$$

where ρ_0 and E_0 are injection electron density and energy, respectively. This equation defines the initial energy E_0 of the electron as

$$E_0 = E \frac{\varphi^{1/3}}{1 - E \lambda \rho^{-1/3}}. \quad (8.38)$$

Substituting this equation to Equation (8.30), the electron energy distribution is

$$n(t, E) = \varphi^{4/3} \left(\frac{E_0}{E} \right)^2 n_0. \quad (8.39)$$

For example, if the electron injection distribution is described by power-law distribution with index p_{inj}

$$n_0 \propto E_0^{-p_{\text{inj}}}, \quad (8.40)$$

then at an arbitrary position the electron energy distribution can be expressed by Equation (8.39) as

$$n(t, E) \propto E^{-p_{\text{inj}}} \varphi^{\frac{p_{\text{inj}}-2}{3}} (1 - E \lambda \rho^{-1/3})^{p_{\text{inj}}-2}. \quad (8.41)$$

According to Atoyan and Aharonian (1996), SED of Crab Nebula is well reproduced if the injection electron distribution is a broken power-law. However, since we are interested in

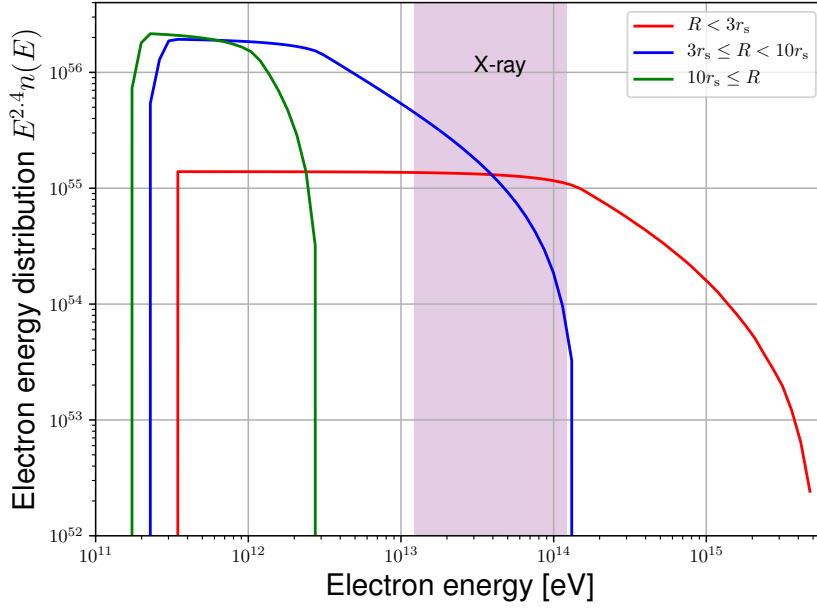


Figure 8.6: Electron energy distributions by differences of distances from the termination shock r_s . The red solid line is $R < 3r_s$, the blue line is $3r_s \leq R < 10r_s$, and the green line is $R \geq 10r_s$. Multi TeV energy electrons, responsible for the X-ray emission, resides close to the termination shock. The shade region in purple indicates that the synchrotron radiation energy is in X-ray.

the X-ray energy band, which is produced by TeV electrons, we consider a power-law with exponential cutoff injection spectrum:

$$n_0 = AE_0^{-p_{\text{inj}}} \exp\left(-\frac{E_0}{E_{\text{cut}}}\right), \quad (8.42)$$

where $E_0 = \gamma_0 m_e c^2$, A is a constant, and E_{cut} is the cut-off energy of the broken power-law. Following Atoyan and Aharonian (1996), we adopted the following values $E_{\text{cut}} = 2.5 \times 10^{15}$ eV and $p_{\text{inj}} = 2.4$.

To illustrate the effect of particle cooling we show the electron energy distributions in spherical shells located at different distances from the termination shock

$$N_{i,j} = \int_{i \times r_s}^{j \times r_s} dV \frac{dn}{dE dV}. \quad (8.43)$$

We show differences between three distributions, $N_{1,3}$, $N_{3,10}$, and $N_{10,\text{max}}$ in Figure 8.6. As it is highlighted in the figure, the electron energy range relevant for the X-ray emission undergoes strong spectral transformations on the scale similar to the size of the nebula, $\sim 20r_s$.

8.1.7 Synchrotron radiation

We consider the synchrotron radiation in the flow which moves relativistically. The electron energy distribution being a power-law, $n(E)dE \propto E^{-p}dE$, the emissivity is given by Equation

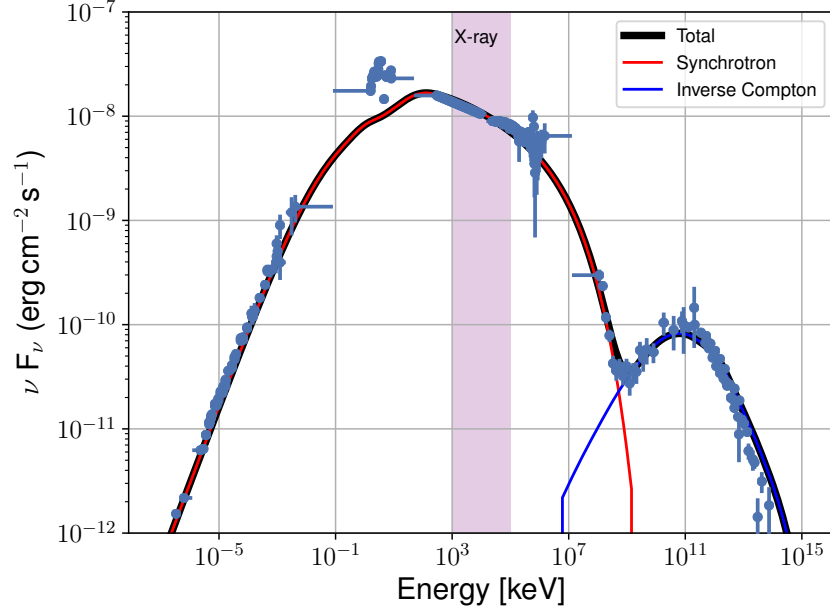


Figure 8.7: Spectral energy distribution of the Crab Nebula computed in the frameworks of multi zone model (for detail see Atoyan and Aharonian, 1996). The solid lines are the model considering the magnetic field distribution and the electron cooling in the flow. The data points are same as in Figure 8.1.

(2.30) as

$$I' = \int P(\nu')n(E)dE \propto \nu'^{-(p-1)/2}, \quad (8.44)$$

where ν' is the radiation frequency, $\nu' = \omega'/2\pi$ in Equation (2.35), and primed quantities refer to the reference frame co-moving with the flow. If we set the spectral index as $s = (p-1)/2$, the intensity is $I' \propto \nu'^{-s}$. The flow moves relativistically with the Lorentz factor $\Gamma = (1 - \beta^2)^{-1/2}$, where β is the flow speed. Therefore, in the observer frame, the emissivity is enhanced by Doppler boosting. The emissivity and the frequency are transformed by the Doppler boosting as $\nu = \mathcal{D}\nu'$ and $I = \mathcal{D}^2 I'$, respectively. As the result, the emissivity in the observer frame is written as

$$I \propto \mathcal{D}^{s+2} \nu'^{-s}. \quad (8.45)$$

The Doppler factor is

$$\mathcal{D} = \frac{1}{\Gamma(1 - \beta \cdot \mathbf{n})}, \quad (8.46)$$

where \mathbf{n} is the line of sight.

In order to obtain the surface brightness in our computer simulations, we need to integrate the emissivity over the line of sight. If the observer direction is along z -axis, the surface

brightness is obtained as

$$I(x, y) = \int I(x, y, z) dz = \int (I_{\perp}(x, y, z) + I_{\parallel}(x, y, z)) dz \quad (8.47)$$

Then, considering the polarization, the Stokes parameters are expressed as

$$I(x, y) = \int (I_{\perp}(x, y, z) + I_{\parallel}(x, y, z)) dz, \quad (8.48)$$

$$Q(x, y) = \int (I_{\perp}(x, y, z) - I_{\parallel}(x, y, z)) \cos 2\chi dz, \quad (8.49)$$

$$U(x, y) = \int (I_{\perp}(x, y, z) - I_{\parallel}(x, y, z)) \sin 2\chi dz. \quad (8.50)$$

To derive the degree of polarization from Stokes parameters, we integrate over whole region for each Stokes parameter over the entire source and then use Equation (2.20).

8.1.8 Lorentz transformation of electromagnetic fields

The electric wave polarization changes depending on the reference frame. Thus, we need to consider the Lorentz transformation of the polarization from each fluid element. Lyutikov et al. (2003) derived the Lorentz transformation for the case of emission produced at blast wave of Gamma-ray bursts, and we follow their approach to obtain the transformation relevant for the case considered here.

We define the K' -frame as the fluid element co-moving frame, which moves with velocity $\boldsymbol{\beta}$ in the laboratory system K , $\Gamma = 1/\sqrt{1 - \boldsymbol{\beta}^2}$. Then, the magnetic fields in the K' system is

$$\mathbf{B}' = \frac{1}{\Gamma} \left(\mathbf{B} + \frac{\Gamma^2}{\Gamma + 1} (\mathbf{B} \cdot \boldsymbol{\beta}) \boldsymbol{\beta} \right) = \frac{1}{\Gamma} \left(\Gamma \mathbf{B} + \frac{\Gamma^2}{\Gamma + 1} \boldsymbol{\beta} \times (\boldsymbol{\beta} \times \mathbf{B}) \right) \quad (8.51)$$

and electric macroscopic field vanishes. If the direction to the observer is expressed as \mathbf{n} , its transformation is given by

$$\mathbf{n}' = \mathcal{D} \left(\mathbf{n} + (\Gamma - 1) \frac{(\mathbf{n} \cdot \boldsymbol{\beta}) \boldsymbol{\beta}}{\boldsymbol{\beta}^2} - \Gamma \boldsymbol{\beta} \right) = \mathcal{D} \left(\mathbf{n} + \Gamma \boldsymbol{\beta} \left(\frac{\Gamma}{1 + \Gamma} (\mathbf{n} \cdot \boldsymbol{\beta}) - 1 \right) \right), \quad (8.52)$$

where $\mathcal{D} = (\Gamma(1 - \boldsymbol{\beta} \cdot \mathbf{n}))^{-1}$ is the Doppler factor (Komissarov and Lyubarsky, 2004).

In the fluid element co-moving frame, the microscopic electromagnetic field associated with synchrotron radiation is directed along

$$\mathbf{e}' = \mathbf{n}' \times \mathbf{B}', \quad (8.53)$$

$$\mathbf{b}' = \mathbf{n}' \times \mathbf{e}'. \quad (8.54)$$

These vectors' lengths are equal if \mathbf{n}' is normalized to unit length. In the laboratory reference frame, the electric field component is transformed as

$$\mathbf{e} = \Gamma \mathcal{D}^2 \mathbf{n} \times \left(\mathbf{B}' + \mathbf{n} \times (\boldsymbol{\beta} \times \mathbf{B}') - \frac{\Gamma}{\Gamma + 1} (\mathbf{B}' \cdot \boldsymbol{\beta}) \boldsymbol{\beta} \right). \quad (8.55)$$

Using Equation (8.51), we can rewrite the above equation to

$$\mathbf{e} = \Gamma \mathcal{D}^2 \mathbf{n} \times (\mathbf{B} + \mathbf{n} \times (\boldsymbol{\beta} \times \mathbf{B})), \quad (8.56)$$

which contains only physical parameters measured in the laboratory frame. The vector normalized to unit length is then

$$\hat{\mathbf{e}} = \frac{\mathbf{n} \times \mathbf{q}}{\sqrt{q^2 - (\mathbf{q} \cdot \mathbf{n})^2}}, \quad (8.57)$$

where $\mathbf{q} = \mathbf{B} + \mathbf{n} \times (\boldsymbol{\beta} \times \mathbf{B})$ is an auxiliary vector. One can also consider the component of the vector that lays in the plane of the sky:

$$\mathbf{q}_\perp = \mathbf{q} - (\mathbf{q} \cdot \mathbf{n})\mathbf{n}. \quad (8.58)$$

For the case of partially linear polarized light the Stokes parameters are determined by the angle χ that makes the wave electric field with some direction, \mathbf{l}_1 , in the plane of the sky. More specifically, $Q \propto \cos 2\chi$ and $U \propto \sin 2\chi$. It is easy to see that $\cos \chi = -\mathbf{q}_\perp \cdot (\mathbf{n} \times \mathbf{l}_1)/q_\perp$ and $\sin \chi = \mathbf{q}_\perp \cdot \mathbf{l}_1/q_\perp$, thus one obtains

$$\cos 2\chi = \frac{(\mathbf{q}_\perp \cdot (\mathbf{n} \times \mathbf{l}_1))^2 - (\mathbf{q}_\perp \cdot \mathbf{l}_1)^2}{q_\perp^2}, \quad (8.59)$$

$$\sin 2\chi = -\frac{2(\mathbf{q}_\perp \cdot (\mathbf{n} \times \mathbf{l}_1))(\mathbf{q}_\perp \cdot \mathbf{l}_1)}{q_\perp^2}. \quad (8.60)$$

8.2 Torus geometry

Observations with Chandra revealed that the dominant fraction of X-ray emission radiated in Crab Nebula is produced in an extended torus region. Another clearly seen feature is a jet-like plume which emerges in the direction presumably perpendicular to the torus plane. Although the plume is clearly seen in high-resolution X-ray images, its contribution to the total emission is very small. Currently available polarimetric observations allow registering only the polarization of the total nebula emission. Thus, for interpretation of these observation is sufficient to consider the polarization of the emission produced in the torus region. This can be achieved with using of the model explained above. For the sake of clearness, in Figure 8.8 we sketch the relation of the model to the structure of the nebula seen in the X-rays.

The 1D MHD solution by Kennel and Coroniti (1984) provides us with the velocity of the shocked flow and the magnetic field strength as function of the distance to the termination shock. If we consider an arbitrary position in Cartesian coordinate $\mathbf{r} = (x, y, z)$ (the unit vector of \mathbf{r} is $\mathbf{n}_r = \mathbf{r}/r$), then the magnetic field vector direction is expressed by $\mathbf{B} \propto \mathbf{n}_r \times \mathbf{n}_{\text{axis}}$ in the nebula. The angle between the arbitrary fluid element at \mathbf{r} and the pulsar rotation axis is given by $\sin \theta = |\mathbf{n}_r \times \mathbf{n}_{\text{axis}}|$. We assume that the flow propagates in a limited range of solid angle defined by the following condition $\theta_0 < \theta < \pi - \theta_0$ on the polar angle θ . Here θ_0 is a model parameter.

We adopt a geometry where the observer direction is z -axis, thus the pulsar rotation axis is $\mathbf{n}_{\text{axis}} = (\sin \theta_i, 0, \cos \theta_i)$ where θ_i is the inclination angle. The pitch angle for synchrotron radiation, α , is determined by $\cos \alpha = \mathbf{B} \cdot \hat{\mathbf{e}}_z$ where $\hat{\mathbf{e}}_z$ is the unit vector along z -axis.

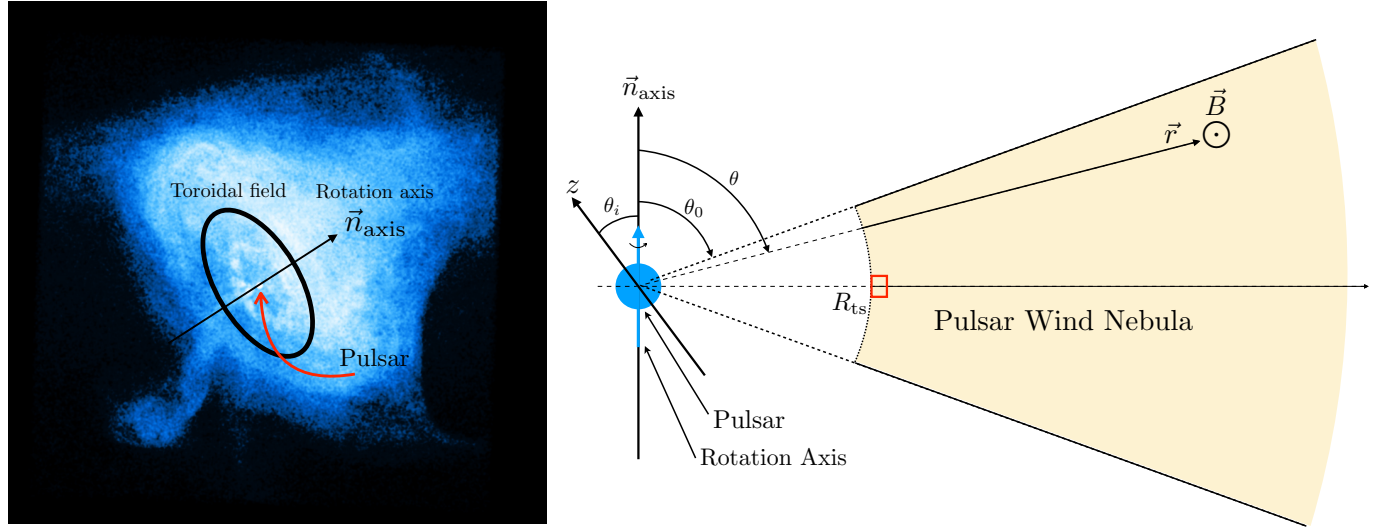


Figure 8.8: Left panel: The Crab Nebula image obtained with Chandra X-ray Observatory. We show the rotation axis and the toroidal field as solid lines in the figure. Right panel: schematic picture for the assumed toroidal geometry. The inclination angle θ_i is defined as the angle between the rotation axis \mathbf{n}_{axis} and the line of sight. The thick arrows indicate the direction of the pulsar wind. The red box indicates the region used to verify the code for calculation of the polarization. The region is limited by $r/r_{ts} < 1.05$ and $\sin \theta > \sin(0.95 \times \pi/2)$.

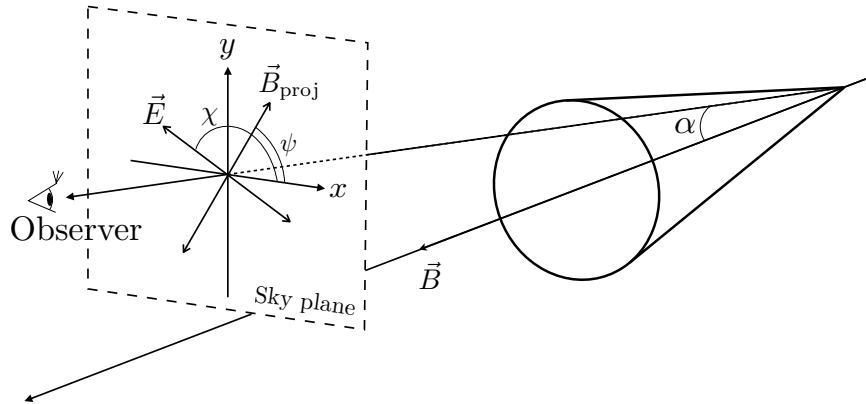


Figure 8.9: The schematic of the electromagnetic wave vector on the sky plane. Electrons whose pitch angle is α radiate the synchrotron radiation towards the observer. If the relativistic effects are ignored, the projected magnetic field direction is same as the photon's magnetic field.

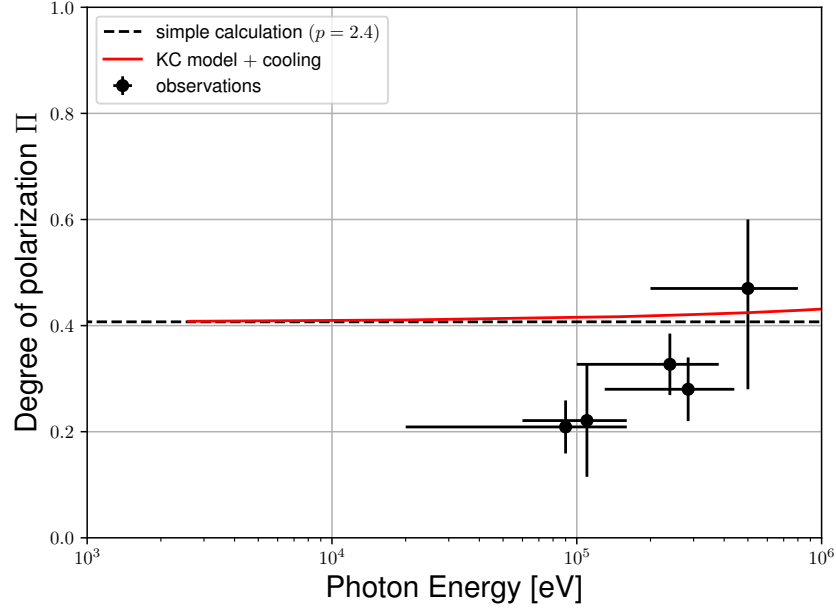


Figure 8.10: Dependence of the polarization degree with the energy. Red line shows the polarization expected from the test region (red box in Figure 8.8) without Doppler boosting. Dash line shows the calculation result of one-zone model with the electron energy distribution $p = 2.4$ which is same as injection electron energy distribution described in §8.1.6. The data points are the same as in Figure 8.3.

Finally, for illustrative purposed in Figure 8.9 we show the basic geometry that illustrates the polarization of synchrotron radiation for the case when the fluid element, where the emission was generated, does not move relativistically. In order to define the polarization, it is needed to obtain magnetic field projection on the sky plane (x - y plane in the adopted notations). If the projected magnetic field direction is defined by \mathbf{B}_{proj} , then the polarization angle ψ is determined by the angle between \mathbf{B}_{proj} and x -axis. If one selects x -axis as the reference direction for polarization measurements, then the polarization angle χ is simply $\chi = \psi + \pi/2$. We note however, that it is necessary to account for the Lorentz transformation of polarization, as obtained above.

8.3 Calculation of polarization

To verify the developed code, we performed a number of model simulations for a limited region of the nebula, which corresponds to the one-zone emitter introduced in §8.1.2. This region is shown in Figure 8.8 with a red box (in the 3D space the region has a ring shape).

First we computed the polarization degree disabling the Doppler boosting and swinging effects in the code. The results are shown in Figure 8.10 and in Figure 8.11. The polarization degree and the value agree with Equation (8.5) where $p = 2.4$ (the injection index of the electron energy distribution). The slight increase of the red line is due to particles cooling that appears non-negligible even for the test region. The brightening in Figure 8.11 is due to the

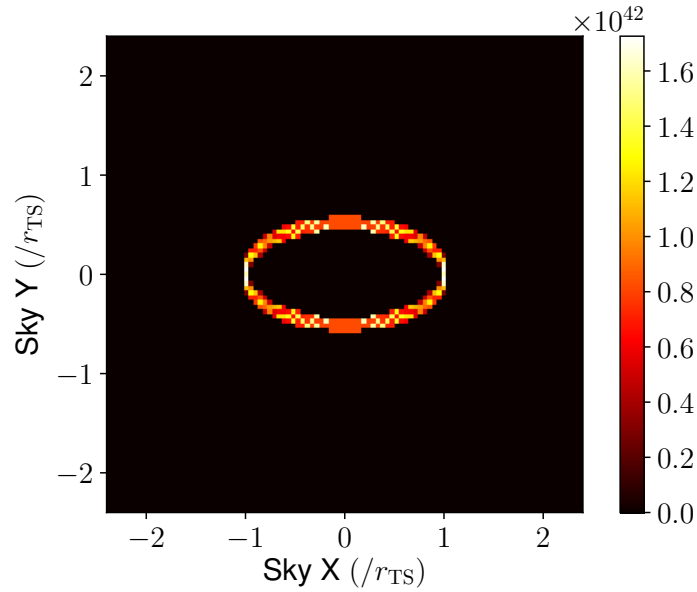


Figure 8.11: The intensity map of Synchrotron radiation. The calculation region is shown in Figure 8.8 with a red box.

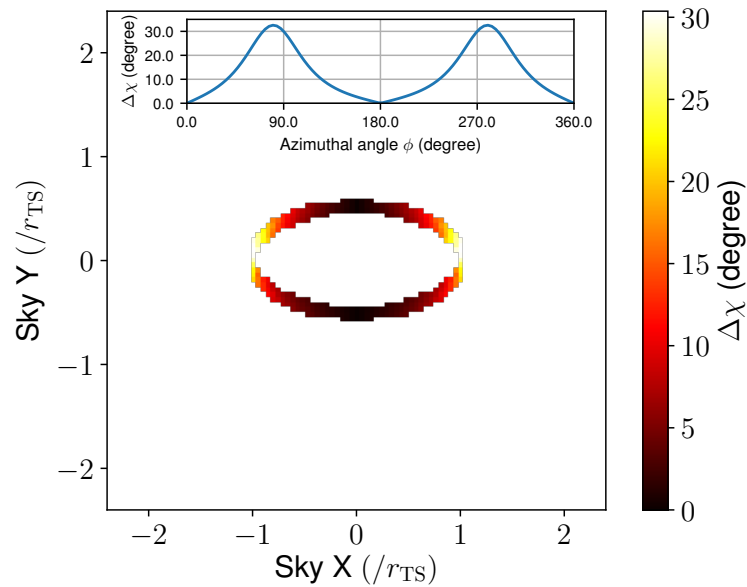


Figure 8.12: Angle $\Delta\chi$ between \mathbf{B}_\perp and \mathbf{q}_\perp (see § 8.1.8). Sub-plot shows the calculation result based on Equation (8.67).

projection effect.

In Figure 8.12, we present the impact of the swinging effect: rotation of the emission electric field depending on the production site location. For illustrative purposes we limit the figure to the test region. Thus, it is easy to obtain the corresponding angle analytically. Namely, the magnetic field and flow velocity in the equatorial region close to the termination shock have the following form (considering coordinates similar to ones in § 8.1.2)

$$\mathbf{B} = B(-\sin \phi, \cos \phi, 0). \quad (8.61)$$

$$\mathbf{n} = (\sin \theta_i, 0, \cos \theta_i). \quad (8.62)$$

$$\boldsymbol{\beta} = \frac{1}{3}(\cos \phi, \sin \phi, 0). \quad (8.63)$$

Thus, one obtains

$$\mathbf{q} = \mathbf{B} - \frac{1}{3}(0, \sin \theta_i, 0). \quad (8.64)$$

The vectors in the plane are

$$\mathbf{q}_\perp = \mathbf{B}_\perp - \frac{1}{3}(0, \sin \theta_i, 0), \quad (8.65)$$

where

$$\mathbf{B}_\perp = B(-\sin \phi \cos^2 \theta_i, \cos \phi, \cos \theta_i \sin \theta_i \sin \phi). \quad (8.66)$$

The corresponding change of the field direction is given by

$$\Delta\chi = \arccos\left(\frac{\mathbf{B}_\perp \cdot \mathbf{q}_\perp}{|\mathbf{B}_\perp||\mathbf{q}_\perp|}\right). \quad (8.67)$$

Figure 8.12 shows that the comparison of $\Delta\chi$ of computing in the test region and calculation based on Equation 8.67 is almost same. In case of checking in the test region, the flow speed is relatively faster than the outer region. In fact, since we compute the entire region, the swinging effect become weak. We also compute with the effect Doppler boosting in the test region. The degree of polarization with swinging effect is 0.48 and one without swinging effect is 0.51 at 100 keV. This indicates a mild effect of the de-boosting in the test region, where the fluid velocity is about $c/3$.

Finally, in Figure 8.13 we show the expected polarization from the entire computational box. The blue line corresponds to simulations that ignores the effect of electric field swinging (but accounts for relativistic boosting). The red line includes all the considered effects. It can be seen that the Doppler boosting enhances the polarization degree. This is explained by effective weakening of the emission from the regions that produce less polarized emission. For the mildly relativistic flow velocity, the relativistic de-boosting appears to be very weak.

In the model explained above, the key elements of the Crab Nebula are reproduced by approximating the pulsar wind by a one-dimensional axisymmetric MHD flow propagating into a limited solid angle close to the equatorial plane, which corresponds to the bright torus seen in X-rays with Chandra. We combine this simplified MHD description with three-dimensional

Table 8.1: Parameters for the simulation of the degree of polarization

| | |
|---|--------------------------|
| Spin-down Luminosity L_s | 5×10^{38} erg/s |
| Radius of the termination shock r_{ts} | 4.5×10^{17} cm |
| Magnetization parameter σ | 0.003 |
| Opening angle of the pulsar $d\Omega$ | 8 sr |
| Index of injection electrons' energy distribution p | 2.4 |
| Cut off energy of the injection electrons E_{cut} | 2.5×10^{15} eV |

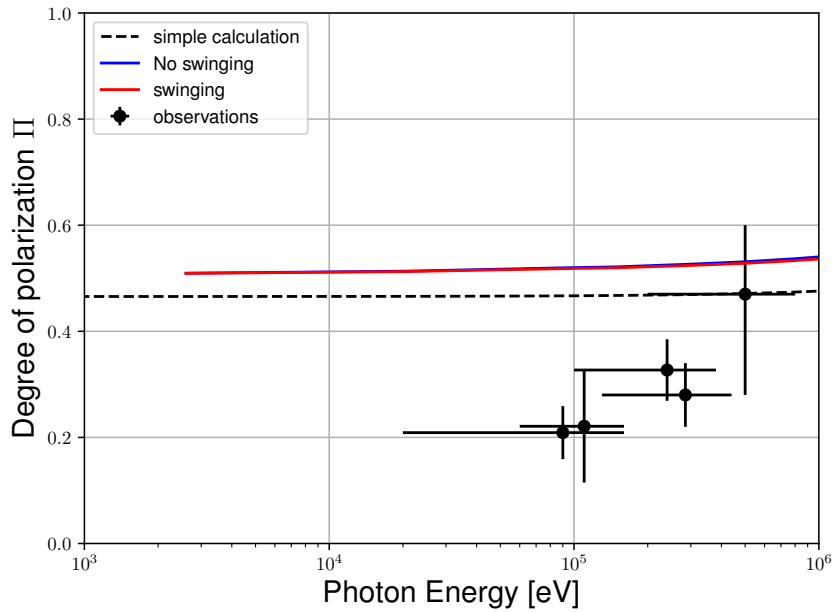


Figure 8.13: Degree of polarization with energy. Black dashed line and points are the same as in Figure 8.3. Model predictions without accounting for the effect of relativistic de-polarization are shown with blue line. Red line shows the result corrected for the relativistic de-polarization.

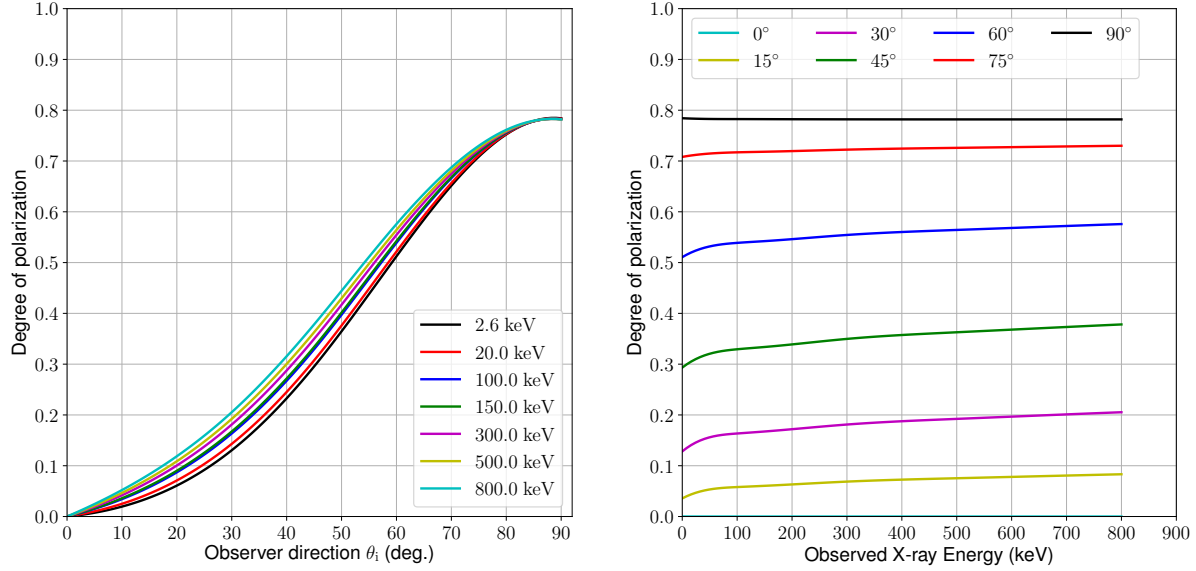


Figure 8.14: The change of the polarization degree to vary the observer direction θ_i and the observed X-ray energy. The radius of the termination shock $r_{\text{ts}} = 4.5 \times 10^{17}$ cm, $\sigma = 0.003$, the spin-down luminosity $L_s = 5 \times 10^{38}$ erg/s, and the opening angle of the pulsar is $d\Omega = 8$ rad.

treatment of the radiation throughout the nebula to account for the Doppler boosting and orientation of the magnetic field. The distribution of high-energy particles is obtained assuming that advection by the MHD flow is the dominant transport mechanism. The non-thermal particles are injected at the pulsar wind termination shock following a power-law with exponential cut-off energy distribution. These particles, being confined in fluid elements, are advected through the nebula by the MHD flow. Accounting for the evolution of the magnetic field, various target photon fields, and the changing rate of adiabatic cooling, the energy distribution of high-energy particles in each point of the nebula is computed. Taking into account the local magnetic and photon fields as well as the Doppler boosting, this allows us to derive the surface brightness and polarization, which can then be directly compared to observations at different X-ray energies.

In the considered model, the radiative properties of the nebula depend on three parameters: the radius of the termination shock r_s , the magnetization of the cold pulsar wind σ , and the wind opening angle Ω defined as the solid angle into which the bulk of the energy is ejected. Other physical parameters of the system are also needed as input for the model, however either observations constraint their values (e.g., the pulsar spin-down luminosity) or they have a small impact on the radiative properties of the nebula (e.g., bulk Lorentz factor of the cold pulsar wind). For a suitable choice of parameters, the model reproduces the broadband SED well, as shown in Figure 8.7. We show the parameters of the simulation in Table 8.1. We set the radius of the termination shock to $r_{\text{ts}} = 4.5 \times 10^{17}$ cm, $\sigma = 0.003$ and the spin-down luminosity $L_{\text{sd}} = 5 \times 10^{38}$ erg/s.

The model predicts that polarization in the X-ray band depends on the energy. There are two main physical effects that provide this dependence. Because of the cooling of the non-thermal particles, the hard X-ray emission is produced in the immediate vicinity of the

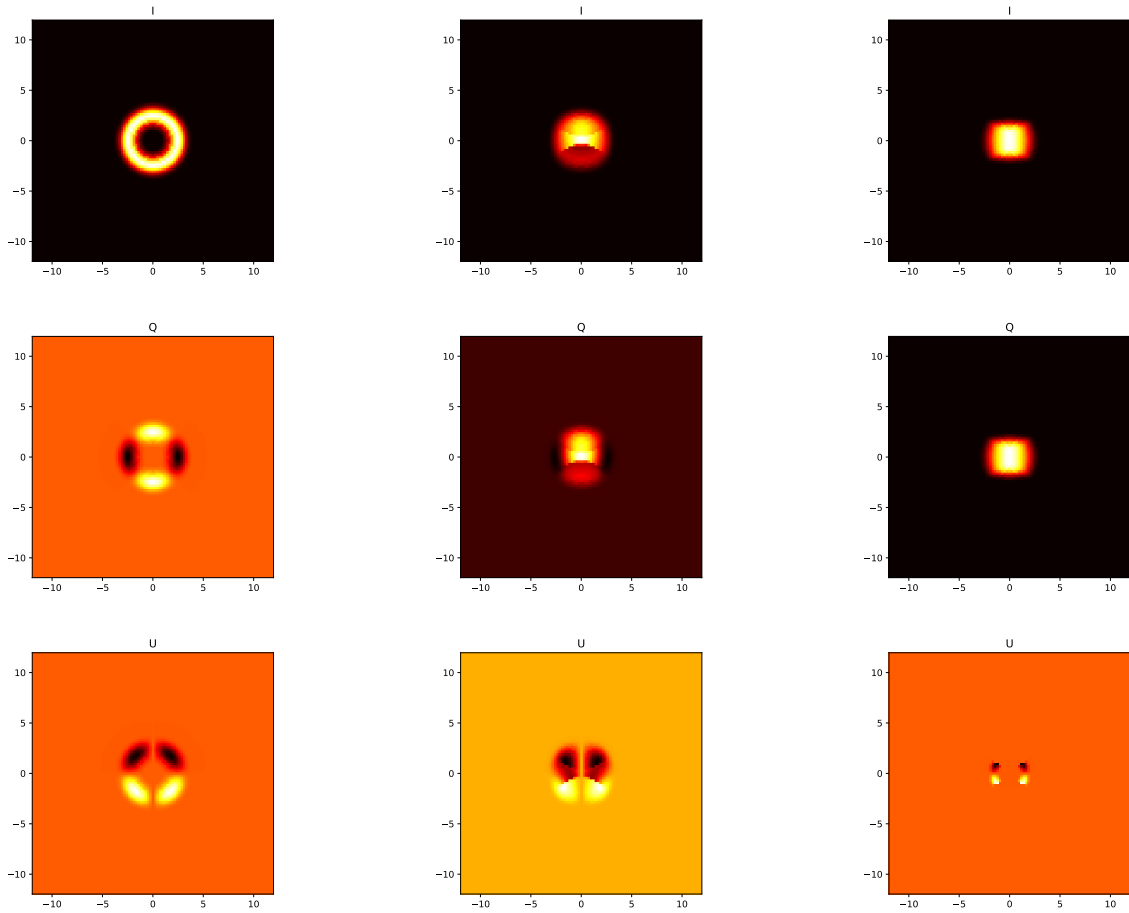


Figure 8.15: The color maps of Stokes parameters: I , Q and U (from top to bottom). The observed X-ray energy is 150 keV. From left to right, the observer direction is $\theta_i = 0^\circ$, 60° and 90° and then the polarization degree is $\Pi = 0.0$, 0.55 , 0.79 , respectively. The brighter region is strong intensity, and dark region is weak intensity. Note that the intensities do not scale to each other.

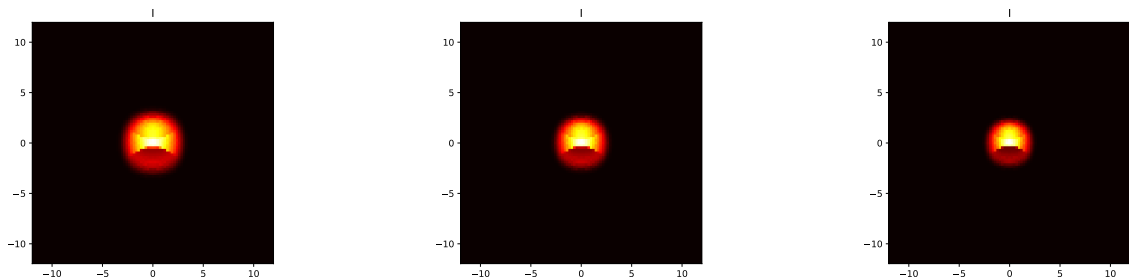


Figure 8.16: The color maps of intensity, I . The observed X-ray energies are 100, 300, 800 keV from left to right. The pulsar inclination was set to $\theta_i = 60^\circ$.

termination shock. In this region, the spectrum is the hardest and the flow velocity is the highest. Since the flow velocity rapidly decreases away from the termination shock, the relative influence of the Doppler boosting enhancement appears to be the most important in the hard X-ray band. Thus, a larger fraction of the hard X-ray emission is produced by a harder distribution of electrons (which decreases the maximum polarization degree) and in a region with homogeneous magnetic field (which increases the maximum polarization degree). Another effect that influences the polarization is increasing magnetic field: in the nebula the strength of the magnetic field linearly increasing close to the termination shock, this allows a more efficient production of the hard X-ray emission in the regions further away from the termination shock. Since these three effects impact the polarization degree in different ways, the overall change is complex, but still relatively modest, as shown in Figure 8.13.

The prediction of the developed radiative mode also depends strongly on the geometrical parameters, such as inclination of the pulsar rotation axis and opening angle of the equatorial outflow. Figure 8.14 shows the change of the polarization degree as a function of the inclination angle, θ_i , and the observed X-ray energy. The polarization degree is evaluated to sum up the intensity image each Stokes parameter I, Q, U . When the θ_i approach to 90 degree, in other words the rotation axis become parallel to sky plane, the polarization degree is stable at about $\sim 77\%$. Since the magnetic field is almost uniform, the polarization degree approaches the theoretical value described in Rybicki and Lightman (1979). On the other hand, the rotation axis is parallel to line of sight, then the polarization degree is 0. Since the components of Stokes parameters Q and U are symmetrical to positive and negative, the components cancel each other out. The appearance is shown in Figure 8.15. We also show the intensity images in Figure 8.16 at $\theta_i = 60^\circ$. In particular, these simulations allow us to see the impact of electron cooling: the extension of emitting region shrinks with the photon energy increasing. This tendency was confirm with various observations, in particular with analysis of hard X-ray images obtained with NuSTAR (Madsen et al., 2015).

8.4 Conclusion

Calculation of polarization degree performed in framework of a simple one-zone model gives a result significantly exceeding the majority of measurements obtained in the X-ray range (Hitomi Collaboration et al., 2018). To evaluated the implications of this discrepancy properly we developed a model that allows us to account for a number of effects, which are expected to be important in PWNe. This includes a realistic distribution of the magnetic field strength; particle transport and cooling; relativistic transformation of emission; and relativistic de-polarization. Our analysis shows that such a radiative model predicts even a higher polarization degree, implying a significant development of turbulence in the nebula.

A more detailed 2D or 3D numerical MHD of the equatorial outflow in the Crab Nebula should allow a more accurate calculation of the polarization. In particular it is likely that such simulations reveal a smaller degree of polarization in soft X-ray band. Turbulence, which develops in 2D or 3D simulation, should reduce the coherency of the magnetic field (see, e.g., Porth et al., 2014) resulting in a smaller polarization degree. Such a detailed consideration is, however, beyond the scope of this study.

Chapter 9

Conclusion

We studied the performance of Si/CdTe semiconductor Compton Telescope (Soft Gamma-ray Detector; SGD) which was onboard 6-th Japanese X-ray Satellite, *Hitomi* (ASTRO-H).

SGD was aimed at detecting one digit high sensitivity and energy resolution approaching 2%, and was developed with a concept of “narrow field of view semiconductor Compton camera”. In order to demonstrate the concept, we evaluated the performance of the detector through test observations on ground and in orbit.

The energy resolution for SGD1 and SGD2 was less than 2% at 511 keV, and after Compton reconstruction we observed the 662 keV peak from the isotope ^{137}Cs . It is possible to determine the direction of incoming photon through its scattering angle. We confirmed that SGD can choose the incoming photon only coming from the field of view by oneself, and that the concept of “narrow field of view semiconductor Compton camera” was established. We investigated the performance for the Compton telescope and the background in orbit. It shows that the data is useful for future gamma-ray missions.

The SGD was successful at detecting polarized gamma-ray emission from the Crab Nebula with only about 5000 seconds, which the confidence level was 99.3%. It indicates that the SGD can detect the polarization several 10 to 100 times shorter time scale compared to other satellites or balloon missions, and the SGD was demonstrated as a high sensitive polarimetry. We obtained the degree of polarization as $22.1\% \pm 10.6\%$ and the angle of polarization as $110.7^\circ + 13.2^\circ / - 13.0^\circ$ for phase integrated with energy range from 60 keV to 160 keV.

The obtained degree of polarization from the radiation emitted by the Crab Nebula is lower than what previous theoretical models predicted. Based on the analytical magnetohydrodynamics (MHD) calculation for the propagation of pulsar wind flows with transport of the magnetic field strength and the particles, we evaluate the emissivity of the synchrotron radiation with particle cooling and the Lorentz transformation of the magnetic waves. Our analysis shows that the effect of relativistic de-boosting is relatively weak. Therefore, it shows that the more physical effects such as turbulence in the pulsar wind nebular is needed.

Acknowledgements

First of all, I would like to express my gratitude to my supervisor Prof. Tadayuki Takahashi who gave me the opportunity to continue this interesting study. I am also deeply grateful to Dr. S. Watanabe who always gave me invaluable comments to analysis of the SGD. I deep gratitude to Dr D. Khangulyan for significant contribution in my science study. Without discussion with him, chapter 8 did not complete. I sincerely thank to Prof. K. Makishima who gave me various technical helps, including English proofreading. I sincerely thank to Dr. P. Caradonna who contributes to correct my English in this dissertation.

I would like to deeply thank to Dr. S. Takeda, Dr. Y. Ichinohe, and Dr. A. Simionescu for their encouragements and practical advice for writing this dissertation. Through the SGD experiments and analysis, I thank to Dr. K. Hayashi, Dr. A. Harayama, Dr. H. Odaka, Dr. M. Ohno, Dr. H. Takahashi and Mr. M. Ohta who advised and encouraged me for frequently. Finally, I really thank my family for their sincerity encouragements and supports for a long time.

Bibliography

- F. A. Aharonian and A. M. Atoyan. Compton scattering of relativistic electrons in compact x-ray sources. *Ap&SS*, 79:321–336, oct 1981. doi: 10.1007/BF00649428.
- F. A. Aharonian, S. R. Kelner, and A. Yu. Prosekin. Angular, spectral, and time distributions of highest energy protons and associated secondary gamma rays and neutrinos propagating through extragalactic magnetic and radiation fields. *Phys. Rev. D*, 82:043002, Aug 2010. doi: 10.1103/PhysRevD.82.043002. URL <https://link.aps.org/doi/10.1103/PhysRevD.82.043002>.
- A. M. Atoyan and F. A. Aharonian. On the mechanisms of gamma radiation in the crab nebula. *Monthly Notices of the Royal Astronomical Society*, 278(2):525–541, 1996. doi: 10.1093/mnras/278.2.525. URL <http://dx.doi.org/10.1093/mnras/278.2.525>.
- M.J. Berger, J.H. Hubbell, S.M. Seltzer, J. Chang, J.S. Coursey, R. Sukumar, D.S. Zucker, and K. Olsen. Nist standard reference database 8 (xgam). Last Update to Data Content: November 2010, 2010. URL <https://dx.doi.org/10.18434/T48G6X>.
- S. V. Bogovalov and D. V. Khangoulyan. The crab nebula: Interpretation of chandra observations. *Astronomy Letters*, 28(6):373–385, Jun 2002. ISSN 1562-6873. doi: 10.1134/1.1484137. URL <https://doi.org/10.1134/1.1484137>.
- W. Brinkmann, B. Aschenbach, and A. Langmeier. X-ray morphology of the crab nebula. *Nature*, 313:662 EP –, 02 1985. URL <https://doi.org/10.1038/313662a0>.
- Bucciantini, N., Amato, E., Bandiera, R., Blondin, J. M., and Del Zanna, L. Magnetic rayleigh-taylor instability for pulsar wind nebulae in expanding supernova remnants. *A&A*, 423(1):253–265, 2004. doi: 10.1051/0004-6361:20040360. URL <https://doi.org/10.1051/0004-6361:20040360>.
- S. Chandrasekhar. *Radiative transfer*. 1960.
- M. Chauvin, J. P. Roques, D. J. Clark, and E. Jourdain. Polarimetry in the hard x-ray domain with integral spi. *The Astrophysical Journal*, 769(2):137, 2013. URL <http://stacks.iop.org/0004-637X/769/i=2/a=137>.
- M. Chauvin, M. Jackson, T. Kawano, M. Kiss, M. Kole, V. Mikhalev, E. Moretti, H. Takahashi, and M. Pearce. Optimising a balloon-borne polarimeter in the hard x-ray domain: From the pogolite pathfinder to pogo+. *Astroparticle Physics*, 82:99 – 107,

2016. ISSN 0927-6505. doi: <https://doi.org/10.1016/j.astropartphys.2016.06.005>. URL <http://www.sciencedirect.com/science/article/pii/S0927650516300846>.
- M. Chauvin, H. G. Florén, M. Friis, M. Jackson, T. Kamae, J. Kataoka, T. Kawano, M. Kiss, V. Mikhalev, T. Mizuno, N. Ohashi, T. Stana, H. Tajima, H. Takahashi, N. Uchida, and M. Pearce. Shedding new light on the crab with polarized x-rays. *Scientific Reports*, 7(1):7816, 2017. doi: 10.1038/s41598-017-07390-7. URL <https://doi.org/10.1038/s41598-017-07390-7>.
- M. Chauvin, H. G. Florén, M. Friis, M. Jackson, T. Kamae, J. Kataoka, T. Kawano, M. Kiss, V. Mikhalev, T. Mizuno, N. Ohashi, T. Stana, H. Tajima, H. Takahashi, N. Uchida, and M. Pearce. Accretion geometry of the black-hole binary cygnus x-1 from x-ray polarimetry. *Nature Astronomy*, 2(8):652–655, 2018. doi: 10.1038/s41550-018-0489-x. URL <https://doi.org/10.1038/s41550-018-0489-x>.
- P. Coppi, L. Stawarz, C. Done, Y. Fukazawa, P. Gandhi, K. Hagino, S. LaMassa, P. Laurent, G. Madejski, T. Mizuno, K. Mukai, H. Odaka, H. Tajima, Y. Tanaka, F. Tombesi, M. Urry, and for the ASTRO-H Science Working Group. ASTRO-H White Paper - Broad-band Spectroscopy and Polarimetry. *arXiv e-prints*, art. arXiv:1412.1190, December 2014.
- Enrico Costa, Paolo Soffitta, Ronaldo Bellazzini, Alessandro Brez, Nicholas Lumb, and Gloria Spandre. An efficient photoelectric x-ray polarimeter for the study of black holes and neutron stars. *Nature*, 411:662 EP –, 06 2001. URL <http://dx.doi.org/10.1038/35079508>.
- A. J. Dean, D. J. Clark, J. B. Stephen, V. A. McBride, L. Bassani, A. Bazzano, A. J. Bird, A. B. Hill, S. E. Shaw, and P. Ubertini. Polarized Gamma-Ray Emission from the Crab. *Science*, 321:1183, August 2008. doi: 10.1126/science.1149056.
- M. Forot, P. Laurent, I. A. Grenier, C. Gouiffès, and F. Lebrun. Polarization of the crab pulsar and nebula as observed by the integral/ibis telescope. *The Astrophysical Journal Letters*, 688(1):L29, 2008. URL <http://stacks.iop.org/1538-4357/688/i=1/a=L29>.
- Y. Fukazawa, T. Nakamoto, N. Sawamoto, S. Uno, T. Ohsugi, H. Tajima, T. Takahashi, T. Mitani, T. Tanaka, and K. Nakazawa. Development of low-noise double-sided silicon strip detector for cosmic soft gamma-ray compton camera. *Nuclear Instruments and Methods in Physics Research Section A: Accelerators, Spectrometers, Detectors and Associated Equipment*, 541(1):342 – 349, 2005. ISSN 0168-9002. doi: <https://doi.org/10.1016/j.nima.2005.01.074>. URL <http://www.sciencedirect.com/science/article/pii/S0168900205001610>. Development and Application of Semiconductor Tracking Detectors.
- Yasushi Fukazawa, Tsunefumi Mizuno, Shin Watanabe, Motohide Kokubun, Hiromitsu Takahashi, Naomi Kawano, Sho Nishino, Mahito Sasada, Hirohisa Shirai, Takuya Takahashi, Tomonori Yamasaki, Tomonori Yasuda, Aya Bamba, Masanori Ohno, Tadayuki Takahashi, Masayoshi Ushio, Teruaki Enoto, Takao Kitaguchi, Kazuo Makishima, Kazuhiro Nakazawa, Yuichi Uehara, Shin'ya Yamada, Takayuki Yuasa, Naoki Isobe, Madoka Kawaharada, Takaaki Tanaka, Makoto Tashiro, Yukikatsu Terada, and Kazutaka Yamaoka. Modeling and Reproducibility of Suzaku HXD PIN/GSO Background. *arXiv e-prints*, art. arXiv:0901.0419, January 2009.

- V. L. Ginzburg and S. I. Syrovatskii. Cosmic Magnetobremstrahlung (synchrotron Radiation). *Annual Review of Astronomy and Astrophysics*, 3:297, January 1965. doi: 10.1146/annurev.aa.03.090165.001501.
- K. Hecht. Zum Mechanismus des lichtelektrischen Primärstromes in isolierenden Kristallen. *Zeitschrift für Physik*, 77:235–245, March 1932. doi: 10.1007/BF01338917.
- W. Heitler. *Quantum theory of radiation*. 1954.
- Hitomi Collaboration, Felix Aharonian, Hiroki Akamatsu, Fumie Akimoto, Steven W Allen, Lorella Angelini, Marc Audard, Hisamitsu Awaki, Magnus Axelsson, Aya Bamba, Marshall W Bautz, Roger Blandford, Laura W Brenneman, Gregory V Brown, Esra Bulbul, Edward M Cackett, Maria Chernyakova, Meng P Chiao, Paolo S Coppi, Elisa Costantini, Jelle de Plaa, Cor P de Vries, Jan-Willem den Herder, Chris Done, Tadayasu Dotani, Ken Ebisawa, Megan E Eckart, Teruaki Enoto, Yuichiro Ezoe, Andrew C Fabian, Carlo Ferrigno, Adam R Foster, Ryuichi Fujimoto, Yasushi Fukazawa, Akihiro Furuzawa, Massimiliano Galeazzi, Luigi C Gallo, Poshak Gandhi, Margherita Giustini, Andrea Goldwurm, Liyi Gu, Matteo Guainazzi, Yoshito Haba, Kouichi Hagino, Kenji Hamaguchi, Ilana M Harrus, Isamu Hatsukade, Katsuhiko Hayashi, Takayuki Hayashi, Kiyoshi Hayashida, Junko S Hiraga, Ann Hornschemeier, Akio Hoshino, John P Hughes, Yuto Ichinohe, Ryo Iizuka, Hajime Inoue, Yoshiyuki Inoue, Manabu Ishida, Kumi Ishikawa, Yoshitaka Ishisaki, Masachika Iwai, Jelle Kaastra, Tim Kallman, Tsuneyoshi Kamae, Jun Kataoka, Satoru Katsuda, Nobuyuki Kawai, Richard L Kelley, Caroline A Kilbourne, Takao Kitaguchi, Shunji Kitamoto, Tetsu Kitayama, Takayoshi Kohmura, Motohide Kokubun, Katsuji Koyama, Shu Koyama, Peter Kretschmar, Hans A Krimm, Aya Kubota, Hideyo Kunieda, Philippe Laurent, Shiu-Hang Lee, Maurice A Leutenegger, Olivier Limousin, Michael Loewenstein, Knox S Long, David Lumb, Greg Madejski, Yoshitomo Maeda, Daniel Maier, Kazuo Makishima, Maxim Markevitch, Hironori Matsumoto, Kyoko Matsushita, Dan McCammon, Brian R McNamara, Missagh Mehdipour, Eric D Miller, Jon M Miller, Shin Mineshige, Kazuhisa Mitsuda, Ikuyuki Mitsuishi, Takuya Miyazawa, Tsunefumi Mizuno, Hideyuki Mori, Koji Mori, Koji Mukai, Hiroshi Murakami, Richard F Mushotzky, Takao Nakagawa, Hiroshi Nakajima, Takeshi Nakamori, Shinya Nakashima, Kazuhiro Nakazawa, Kumiko K Nobukawa, Masayoshi Nobukawa, Hirofumi Noda, Hirokazu Odaka, Takaya Ohashi, Masanori Ohno, Takashi Okajima, Naomi Ota, Masanobu Ozaki, Frits Paerels, Stéphane Paltani, Robert Petre, Ciro Pinto, Frederick S Porter, Katja Pottschmidt, Christopher S Reynolds, Samar Safi-Harb, Shinya Saito, Kazuhiro Sakai, Toru Sasaki, Goro Sato, Kosuke Sato, Rie Sato, Makoto Sawada, Norbert Schartel, Peter J Serlemitsos, Hiromi Seta, Megumi Shidatsu, Aurora Simionescu, Randall K Smith, Yang Soong, Łukasz Stawarz, Yasuharu Sugawara, Satoshi Sugita, Andrew Szymkowiak, Hiroyasu Tajima, Hiromitsu Takahashi, Tadayuki Takahashi, Shin'ichiro Takeda, Yoh Takei, Toru Tamagawa, Takayuki Tamura, Takaaki Tanaka, Yasuo Tanaka, Yasuyuki T Tanaka, Makoto S Tashiro, Yuzuru Tawara, Yukikatsu Terada, Yuichi Terashima, Francesco Tombesi, Hiroshi Tomida, Yohko Tsuboi, Masahiro Tsujimoto, Hiroshi Tsunemi, Takeshi Go Tsuru, Hiroyuki Uchida, Hideki Uchiyama, Yasunobu Uchiyama, Shutaro Ueda, Yoshihiro Ueda, Shin'ichiro Uno, C Megan Urry, Eugenio Ursino, Shin Watanabe, Norbert Werner, Dan R Wilkins, Brian J Williams, Shinya Yamada, Hiroya Yamaguchi, Kazutaka Yamaoka, Noriko Y

- Yamasaki, Makoto Yamauchi, Shigeo Yamauchi, Tahir Yaqoob, Yoichi Yatsu, Daisuke Yonetoku, Irina Zhuravleva, Abderahmen Zoghbi, and Yuusuke Uchida. Detection of polarized gamma-ray emission from the crab nebula with the hitomi soft gamma-ray detector †. *Publications of the Astronomical Society of Japan*, page psy118, 2018. doi: 10.1093/pasj/psy118. URL <http://dx.doi.org/10.1093/pasj/psy118>.
- Yuto Ichinohe, Yuusuke Uchida, Shin Watanabe, Ikumi Edahiro, Katsuhiko Hayashi, Takafumi Kawano, Masanori Ohno, Masayuki Ohta, Shin ichiro Takeda, Yasushi Fukazawa, Miho Katsuragawa, Kazuhiro Nakazawa, Hirokazu Odaka, Hiroyasu Tajima, Hiromitsu Takahashi, Tadayuki Takahashi, and Takayuki Yuasa. The first demonstration of the concept of “narrow-fov si/cdte semiconductor compton camera”. *Nuclear Instruments and Methods in Physics Research Section A: Accelerators, Spectrometers, Detectors and Associated Equipment*, 806:5 – 13, 2016. ISSN 0168-9002. doi: <https://doi.org/10.1016/j.nima.2015.09.081>. URL <http://www.sciencedirect.com/science/article/pii/S0168900215011523>.
- M. Itou, M. Brancewicz, and Y. Sakurai. Present status of bl08w. *SACLA Research Report*, 3 (1):124–129, 2014. doi: 10.18957/rr.3.1.124.
- Tuneyoshi Kamae, Viktor Andersson, Makoto Arimoto, Magnus Axelsson, Cecilia Marini Betolo, Claes-Ingvar Björnsson, Gilles Bogaert, Per Carlson, William Craig, Tomas Ekeberg, Olle Engdegård, Yasushi Fukazawa, Shuichi Gunji, Linnea Hjalmsdotter, Bianca Iwan, Yoshikazu Kanai, Jun Kataoka, Nobuyuki Kawai, Jaroslav Kazejev, Mózsi Kiss, Włodzimierz Klamra, Stefan Larsson, Grzegorz Madejski, Tsunefumi Mizuno, Johnny Ng, Mark Pearce, Felix Ryde, Markus Suhonen, Hiroyasu Tajima, Hiromitsu Takahashi, Tadayuki Takahashi, Takuya Tanaka, Timothy Thurston, Masaru Ueno, Gary Varner, Kazuhide Yamamoto, Yuichiro Yamashita, Tomi Ylinen, and Hiroaki Yoshida. Pogolite – a high sensitivity balloon-borne soft gamma-ray polarimeter. *Astroparticle Physics*, 30(2):72 – 84, 2008. ISSN 0927-6505. doi: <https://doi.org/10.1016/j.astropartphys.2008.07.004>. URL <http://www.sciencedirect.com/science/article/pii/S0927650508000947>.
- Junichiro Katsuta, Ikumi Edahiro, Shin Watanabe, Hirokazu Odaka, Yusuke Uchida, Nagomi Uchida, Tsunefumi Mizuno, Yasushi Fukazawa, Katsuhiko Hayashi, Sho Habata, Yuto Ichinohe, Takao Kitaguchi, Masanori Ohno, Masayuki Ohta, Hiromitsu Takahashi, Tadayuki Takahashi, Shin’ichiro Takeda, Hiroyasu Tajima, Takayuki Yuasa, Masayoshi Itou, and SGD Team. Study of the polarimetric performance of a Si/CdTe semiconductor Compton camera for the Hitomi satellite. *Nuclear Instruments and Methods in Physics Research A*, 840:51–58, December 2016. doi: 10.1016/j.nima.2016.09.057.
- C. F. Kennel and F. V. Coroniti. Confinement of the Crab pulsar’s wind by its supernova remnant. *ApJ*, 283:694–709, August 1984. doi: 10.1086/162356.
- H. L. Kestenbaum, G. G. Cohen, K. S. Long, R. Novick, E. H. Silver, M. C. Weisskopf, and R. S. Wolff. The graphite crystal X-ray spectrometer on OSO-8. *ApJ*, 210:805–809, December 1976. doi: 10.1086/154889.
- D. V. Khangoulia and S. V. Bogovalov. The role of a magnetic field in the formation of jet-like features in the crab nebula. *Astronomy Letters*, 29(8):495–501, Aug 2003. ISSN 1562-6873. doi: 10.1134/1.1598231. URL <https://doi.org/10.1134/1.1598231>.

- D. Khangulyan, F. A. Aharonian, and S. R. Kelner. Simple analytical approximations for treatment of inverse compton scattering of relativistic electrons in the blackbody radiation field. *The Astrophysical Journal*, 783(2):100, 2014. URL <http://stacks.iop.org/0004-637X/783/i=2/a=100>.
- Glenn F Knoll. *Radiation detection and measurement; 4th ed.* Wiley, New York, NY, 2010. URL <https://cds.cern.ch/record/1300754>.
- S. S. Komissarov and Y. E. Lyubarsky. Synchrotron nebulae created by anisotropic magnetized pulsar winds. *Monthly Notices of the Royal Astronomical Society*, 349(3):779–792, 2004. doi: 10.1111/j.1365-2966.2004.07597.x. URL <http://dx.doi.org/10.1111/j.1365-2966.2004.07597.x>.
- L.D. Landau and E.M. Lifshitz. *The Classical Theory of Fields*, volume 2 of *Course of Theoretical Physics*. Pergamon, Amsterdam, fourth edition edition, 1975. ISBN 978-0-08-025072-4. doi: <https://doi.org/10.1016/C2009-0-14608-1>. URL <http://www.sciencedirect.com/science/article/pii/B9780080250724500137>.
- P. Laurent, J. Rodriguez, J. Wilms, M. Cadolle Bel, K. Pottschmidt, and V. Grinberg. Polarized Gamma-Ray Emission from the Galactic Black Hole Cygnus X-1. *Science*, 332:438, April 2011. doi: 10.1126/science.1200848.
- F. Lei, A. J. Dean, and G. L. Hills. Compton Polarimetry in Gamma-Ray Astronomy. *Space Sci. Rev.*, 82:309–388, November 1997. doi: 10.1023/A:1005027107614.
- Malcolm S. Longair. *High Energy Astrophysics*. 2011.
- M. Lyutikov, V. I. Pariev, and R. D. Blandford. Polarization of prompt gamma-ray burst emission: Evidence for electromagnetically dominated outflow. *The Astrophysical Journal*, 597(2):998, 2003. URL <http://stacks.iop.org/0004-637X/597/i=2/a=998>.
- Kristin K. Madsen, Stephen Reynolds, Fiona Harrison, Hongjun An, Steven Boggs, Finn E. Christensen, William W. Craig, Chris L. Fryer, Brian W. Grefenstette, Charles J. Hailey, Craig Markwardt, Melania Nynka, Daniel Stern, Andreas Zoglauer, and William Zhang. Broadband x-ray imaging and spectroscopy of the crab nebula and pulsar with nustar. *The Astrophysical Journal*, 801(1):66, 2015. URL <http://stacks.iop.org/0004-637X/801/i=1/a=66>.
- Kristin K. Madsen, Karl Forster, Brian W. Grefenstette, Fiona A. Harrison, and Daniel Stern. Measurement of the absolute crab flux with nustar. *The Astrophysical Journal*, 841(1):56, 2017. URL <http://stacks.iop.org/0004-637X/841/i=1/a=56>.
- M. Meyer, D. Horns, and H. S. Zechlin. The Crab Nebula as a standard candle in very high-energy astrophysics. *A&A*, 523:A2, November 2010. doi: 10.1051/0004-6361/201014108.
- T. Mitani, T. Tanaka, K. Nakazawa, T. Takahashi, T. Takashima, H. Tajima, H. Nakamura, M. Nomachi, T. Nakamoto, and Y. Fukazawa. A prototype si/cdte compton camera and the polarization measurement. *IEEE Transactions on Nuclear Science*, 51(5):2432–2437, Oct 2004. ISSN 0018-9499. doi: 10.1109/TNS.2004.835653.

- T. Mizuno, D. Kimura, Y. Fukazawa, S. Furui, K. Goto, T. Hayashi, K. S. Kawabata, T. Kawano, Y. Kitamura, H. Shirakawa, T. Tanabe, K. Makishima, K. Nakajima, K. Nakazawa, T. Fukuyama, Y. Ichinohe, K. Ishimura, M. Ohta, T. Sato, T. Takahashi, Y. Uchida, S. Watanabe, K. Ishibashi, K. Sakanobe, H. Matsumoto, T. Miyazawa, H. Mori, M. Sakai, and H. Tajima. Development and calibration of fine collimators for the ASTRO-H Soft Gamma-ray Detector. In *Space Telescopes and Instrumentation 2014: Ultraviolet to Gamma Ray*, volume 9144 of Proc. SPIE, page 91445F, July 2014. doi: 10.1117/12.2054649.
- Koji Mori, David N. Burrows, J. Jeff Hester, George G. Pavlov, Shinpei Shibata, and Hiroshi Tsunemi. Spatial variation of the x-ray spectrum of the crab nebula. *The Astrophysical Journal*, 609(1):186, 2004. URL <http://stacks.iop.org/0004-637X/609/i=1/a=186>.
- Y. Namito, S. Ban, and H. Hirayama. Implementation of the doppler broadening of a compton-scattered photon into the egs4 code. *Nuclear Instruments and Methods in Physics Research Section A: Accelerators, Spectrometers, Detectors and Associated Equipment*, 349(2):489 – 494, 1994. ISSN 0168-9002. doi: [https://doi.org/10.1016/0168-9002\(94\)91215-7](https://doi.org/10.1016/0168-9002(94)91215-7). URL <http://www.sciencedirect.com/science/article/pii/0168900294912157>.
- C. Y. Ng and Roger W. Romani. Fitting Pulsar Wind Tori. *ApJ*, 601:479–484, January 2004. doi: 10.1086/380486.
- Hirokazu Odaka, Soichiro Sugimoto, Shin nosuke Ishikawa, Junichiro Katsuta, Yuu Koseki, Taro Fukuyama, Shinya Saito, Rie Sato, Goro Sato, Shin Watanabe, Motohide Kokubun, Tadayuki Takahashi, Shin'ichiro Takeda, Yasushi Fukazawa, Takaaki Tanaka, and Hiroyasu Tajima. Development of an integrated response generator for si/cdte semiconductor compton cameras. *Nuclear Instruments and Methods in Physics Research Section A: Accelerators, Spectrometers, Detectors and Associated Equipment*, 624(2):303 – 309, 2010. ISSN 0168-9002. doi: <https://doi.org/10.1016/j.nima.2009.11.052>. URL <http://www.sciencedirect.com/science/article/pii/S0168900209022578>. New Developments in Radiation Detectors.
- Kousuke Oonuki, Takaaki Tanaka, Shin Watanabe, Shin'ichiro Takeda, Kazuhiro Nakazawa, Masayoshi Ushio, Takefumi Mitani, Tadayuki Takahashi, and Hiroyasu Tajima. A stacked cdte pixel detector for a compton camera. *Nuclear Instruments and Methods in Physics Research Section A: Accelerators, Spectrometers, Detectors and Associated Equipment*, 573(1):57 – 60, 2007. ISSN 0168-9002. doi: <https://doi.org/10.1016/j.nima.2006.10.251>. URL <http://www.sciencedirect.com/science/article/pii/S0168900206021905>. Proceedings of the 7th International Conference on Position-Sensitive Detectors.
- R. M. Pelling, W. S. Paciesas, L. E. Peterson, K. Makishima, M. Oda, Y. Ogawara, and S. Miyamoto. A Scanning Modulation Collimator Observation of the High Energy X-Ray Source in the Crab Nebula. *ApJ*, 319:416, August 1987. doi: 10.1086/165466.
- Oliver Porth, Serguei S. Komissarov, and Rony Keppens. Three-dimensional magnetohydrodynamic simulations of the crab nebula. *Monthly Notices of the Royal Astronomical Society*, 438(1):278–306, 2014. doi: 10.1093/mnras/stt2176. URL <http://dx.doi.org/10.1093/mnras/stt2176>.

- M. J. Rees and J. E. Gunn. The origin of the magnetic field and relativistic particles in the crab nebula. *MNRAS*, 167:1–12, Apr 1974. doi: 10.1093/mnras/167.1.1.
- R. Ribberfors and K. F. Berggren. Incoherent-x-ray-scattering functions and cross sections $(\frac{d\sigma}{d\Omega})_{\text{incoh}}$ by means of a pocket calculator. *Phys. Rev. A*, 26:3325–3333, Dec 1982. doi: 10.1103/PhysRevA.26.3325. URL <https://link.aps.org/doi/10.1103/PhysRevA.26.3325>.
- George B. Rybicki and Alan P. Lightman. *Radiative processes in astrophysics*. 1979.
- V. Schoenfelder, H. Aarts, K. Bennett, H. de Boer, J. Clear, W. Collmar, A. Connors, A. Deerenberg, R. Diehl, A. von Dordrecht, J. W. den Herder, W. Hermsen, M. Kippen, L. Kuiper, G. Lichti, J. Lockwood, J. Macri, M. McConnell, D. Morris, R. Much, J. Ryan, G. Simpson, M. Snelling, G. Stacy, H. Steinle, A. Strong, B. N. Swanenburg, B. Taylor, C. de Vries, and C. Winkler. Instrument description and performance of the Imaging Gamma-Ray Telescope COMPTEL aboard the Compton Gamma-Ray Observatory. *ApJS*, 86:657–692, June 1993. doi: 10.1086/191794.
- Hiroyasu Tajima, Roger Blandford, Teruaki Enoto, Yasushi Fukazawa, Kirk Gilmore, Tuneyoshi Kamae, Jun Kataoka, Madoka Kawaharada, Motohide Kokubun, Philippe Laurent, Francois Lebrun, Olivier Limousin, Greg Madejski, Kazuo Makishima, Tsunefumi Mizuno, Kazuhiro Nakazawa, Masanori Ohno, Masayuki Ohta, Goro Sato, Rie Sato, Hiromitsu Takahashi, Tadayuki Takahashi, Takaaki Tanaka, Makoto Tashiro, Yukikatsu Terada, Yasunobu Uchiyama, Shin Watanabe, Kazutaka Yamaoka, and Daisuke Yonetoku. Soft gamma-ray detector for the ASTRO-H Mission. In *Space Telescopes and Instrumentation 2010: Ultraviolet to Gamma Ray*, volume 7732 of *Society of Photo-Optical Instrumentation Engineers (SPIE) Conference Series*, page 773216, July 2010. doi: 10.1117/12.857531.
- T. Takahashi and S. Watanabe. Recent progress in CdTe and CdZnTe detectors. *IEEE Transactions on Nuclear Science*, 48:950–959, August 2001. doi: 10.1109/23.958705.
- T. Takahashi, S. Watanabe, G. Sato, Y. Okada, S. Kubo, Y. Kuroda, M. Onishi, and R. Ohno. High resolution cdte detector and applications to imaging devices. In *2000 IEEE Nuclear Science Symposium. Conference Record (Cat. No.00CH37149)*, volume 1, pages 4/31–4/35 vol.1, 2000. doi: 10.1109/NSSMIC.2000.949043.
- T. Takahashi, T. Kamae, and K. Makishima. Future Hard X-ray and Gamma-ray Observations. In H. Inoue and H. Kunieda, editors, *New Century of X-ray Astronomy*, volume 251 of *Astronomical Society of the Pacific Conference Series*, page 210, 2001.
- T. Takahashi, T. Mitani, Y. Kobayashi, M. Kouda, G. Sato, S. Watanabe, K. Nakazawa, Y. Okada, M. Funaki, R. Ohno, and K. Mori. High-resolution schottky cdte diode detector. *IEEE Transactions on Nuclear Science*, 49(3):1297–1303, Jun 2002. ISSN 0018-9499. doi: 10.1109/TNS.2002.1039655.
- T. Takahashi, S. Takeda, S. Watanabe, and H. Tajima. Visualization of radioactive substances with a si/cdte compton camera. In *2012 IEEE Nuclear Science Symposium and Medical*

Imaging Conference Record (NSS/MIC), pages 4199–4204, Oct 2012. doi: 10.1109/NSS-MIC.2012.6551958.

Tadayuki Takahashi, Biswajit Paul, Kazuyuki Hirose, Chiho Matsumoto, Ryouichi Ohno, Tsutomu Ozaki, Kunishiro Mori, and Yoshihiro Tomita. High-resolution schottky cdte diode for hard x-ray and gamma-ray astronomy. *Nuclear Instruments and Methods in Physics Research Section A: Accelerators, Spectrometers, Detectors and Associated Equipment*, 436 (1):111 – 119, 1999. ISSN 0168-9002. doi: [https://doi.org/10.1016/S0168-9002\(99\)00606-3](https://doi.org/10.1016/S0168-9002(99)00606-3). URL <http://www.sciencedirect.com/science/article/pii/S0168900299006063>.

Tadayuki Takahashi, Motohide Kokubun, Kazuhisa Mitsuda, Richard Kelley, Takaya Ohashi, Felix Aharonian, Hiroki Akamatsu, Fumie Akimoto, Steve Allen, Naohisa Anabuki, Lorella Angelini, Keith Arnaud, Makoto Asai, Marc Audard, Hisamitsu Awaki, Magnus Axelsson, Philipp Azzarello, Chris Baluta, Aya Bamba, Nobutaka Bando, Marshall Bautz, Thomas Bialas, Roger Blandford, Kevin Boyce, Laura Brenneman, Greg Brown, Esra Bulbul, Edward Cackett, Edgar Canavan, Maria Chernyakova, Meng Chiao, Paolo Coppi, Elisa Costantini, Jelle de Plaa, Jan-Willem den Herder, Michael DiPirro, Chris Done, Tadayasu Dotani, John Doty, Ken Ebisawa, Megan Eckart, Teruaki Enoto, Yuichiro Ezoe, Andrew Fabian, Carlo Ferrigno, Adam Foster, Ryuichi Fujimoto, Yasushi Fukazawa, Akihiro Furuzawa, Massimiliano Galeazzi, Luigi Gallo, Poshak Gandhi, Kirk Gilmore, Margherita Giustini, Andrea Goldwurm, Liyi Gu, Matteo Guainazzi, Daniel Haas, Yoshito Haba, Kouichi Hagino, Kenji Hamaguchi, Atsushi Harayama, Ilana Harrus, Isamu Hatsukade, Takayuki Hayashi, Katsuhiro Hayashi, Kiyoshi Hayashida, Junko Hiraga, Kazuyuki Hirose, Ann Hornschemeier, Akio Hoshino, John Hughes, Yuto Ichinohe, Ryo Iizuka, Yoshiyuki Inoue, Hajime Inoue, Kazunori Ishibashi, Manabu Ishida, Kumi Ishikawa, Kosei Ishimura, Yoshitaka Ishisaki, Masayuki Itoh, Naoko Iwata, Naoko Iyomoto, Chris Jewell, Jelle Kaastra, Timothy Kallman, Tuneyoshi Kamae, Erin Kara, Jun Kataoka, Satoru Katsuda, Junichiro Katsuta, Madoka Kawaharada, Nobuyuki Kawai, Taro Kawano, Shigeo Kawasaki, Dmitry Khangulyan, Caroline Kilbourne, Mark Kimball, Ashley King, Takao Kitaguchi, Shunji Kitamoto, Tetsu Kitayama, Takayoshi Kohmura, Tatsuro Kosaka, Alex Koujelev, Katsuji Koyama, Shu Koyama, Peter Kretschmar, Hans Krimm, Aya Kubota, Hideyo Kunieda, Philippe Laurent, François Lebrun, Shiu-Huang Lee, Maurice Leutenegger, Olivier Limousin, Michael Loewenstein, Knox Long, David Lumb, Grzegorz Madejski, Yoshitomo Maeda, Daniel Maier, Kazuo Makishima, Maxim Markevitch, Candace Masters, Hironori Matsumoto, Kyoko Matsushita, Dan McCammon, Daniel McGuinness, Brian McNamara, Missagh Mehdipour, Joseph Miko, Jon Miller, Eric Miller, Shin Mineshige, Kenji Minesugi, Ikuyuki Mitsuishi, Takuya Miyazawa, Tsunefumi Mizuno, Koji Mori, Hideyuki Mori, Franco Moroso, Harvey Moseley, Theodore Muench, Koji Mukai, Hiroshi Murakami, Toshio Murakami, Richard Mushotzky, Housei Nagano, Ryo Nagino, Takao Nakagawa, Hiroshi Nakajima, Takeshi Nakamori, Toshio Nakano, Shinya Nakashima, Kazuhiro Nakazawa, Yoshiharu Namba, Chikara Natsukari, Yusuke Nishioka, Masayoshi Nobukawa, Kumiko Nobukawa, Hirofumi Noda, Masaharu Nomachi, Steve O’Dell, Hirokazu Odaka, Hiroyuki Ogawa, Mina Ogawa, Keiji Ogi, Masanori Ohno, Masayuki Ohta, Takashi Okajima, Atsushi Okamoto, Tsuyoshi Okazaki, Naomi Ota, Masanobu Ozaki, Fredrik Paerels, Stéphane Paltani, Arvind Parmar, Robert Petre, Ciro Pinto, Martin Pohl, James Pontius, F. Scott Porter, Katja Pottschmidt, Brian Ramsey, Christopher Reynolds,

- Helen Russell, Samar Safi-Harb, Shinya Saito, Shin ichiro Sakai, Kazuhiro Sakai, Hiroaki Sameshima, Toru Sasaki, Goro Sato, Yoichi Sato, Kosuke Sato, Rie Sato, Makoto Sawada, Norbert Schartel, Peter Serlemitsos, Hiromi Seta, Yasuko Shibano, Maki Shida, Megumi Shidatsu, Takanobu Shimada, Keisuke Shinozaki, Peter Shirron, Aurora Simionescu, Cynthia Simmons, Randall Smith, Gary Sneiderman, Yang Soong, Lukasz Stawarz, Yasuharu Sugawara, Hiroyuki Sugita, Satoshi Sugita, Andrew Szymkowiak, Hiroyasu Tajima, Hiromitsu Takahashi, Shin'ichiro Takeda, Yoh Takei, Toru Tamagawa, Takayuki Tamura, Keisuke Tamura, Takaaki Tanaka, Yasuo Tanaka, Yasuyuki Tanaka, Makoto Tashiro, Yuzuru Tawara, Yukikatsu Terada, Yuichi Terashima, Francesco Tombesi, Hiroshi Tomida, Yohko Tsuboi, Masahiro Tsujimoto, Hiroshi Tsunemi, Takeshi Tsuru, Hiroyuki Uchida, Yasunobu Uchiyama, Hideki Uchiyama, Yoshihiro Ueda, Shutaro Ueda, Shiro Ueno, Shin'ichiro Uno, Meg Urry, Eugenio Ursino, Cor de Vries, Atsushi Wada, Shin Watanabe, Tomomi Watanabe, Norbert Werner, Daniel Wik, Dan Wilkins, Brian Williams, Takahiro Yamada, Shinya Yamada, Hiroya Yamaguchi, Kazutaka Yamaoka, Noriko Yamasaki, Makoto Yamauchi, Shigeo Yamauchi, Tahir Yaqoob, Yoichi Yatsu, Daisuke Yonetoku, Atsumasa Yoshida, Takayuki Yuasa, Irina Zhuravleva, and Abderahmen Zoghbi. The astro-h (hitomi) x-ray astronomy satellite, 2016. URL <https://doi.org/10.1117/12.2232379>.
- Tadayuki Takahashi, Motohide Kokubun, Kazuhisa Mitsuda, Richard L Kelley, Takaya Ohashi, Felix Aharonian, Hiroki Akamatsu, Fumie Akimoto, Steven W Allen, Naohisa Anabuki, et al. Hitomi (astro-h) x-ray astronomy satellite. *Journal of Astronomical Telescopes, Instruments, and Systems*, 4(2):021402, 2018.
- S. Takeda, H. Aono, S. Okuyama, S. n. Ishikawa, H. Odaka, S. Watanabe, M. Kokubun, T. Takahashi, K. Nakazawa, H. Tajima, and N. Kawachi. Experimental results of the gamma-ray imaging capability with a si/cdte semiconductor compton camera. *IEEE Transactions on Nuclear Science*, 56(3):783–790, June 2009. ISSN 0018-9499. doi: 10.1109/TNS.2008.2012059.
- S. Takeda, H. Odaka, S. n. Ishikawa, S. Watanabe, H. Aono, T. Takahashi, Y. Kanayama, M. Hiromura, and S. Enomoto. Demonstration of in-vivo multi-probe tracker based on a si/cdte semiconductor compton camera. *IEEE Transactions on Nuclear Science*, 59(1):70–76, Feb 2012a. ISSN 0018-9499. doi: 10.1109/TNS.2011.2178432.
- Shin'ichiro Takeda. *Experimental study of a Si/CdTe semiconductor Compton camera for the next generation of gamma-ray astronomy*. PhD thesis, The University of Tokyo, 2009. URL <http://id.ndl.go.jp/bib/000010718331>.
- Shin'ichiro Takeda, Shin Watanabe, Takaaki Tanaka, Kazuhiro Nakazawa, Tadayuki Takahashi, Yasushi Fukazawa, Hajimu Yasuda, Hiroyasu Tajima, Yoshikatsu Kuroda, Mitsunobu Onishi, and Kei Genba. Development of double-sided silicon strip detectors (dssd) for a compton telescope. *Nuclear Instruments and Methods in Physics Research Section A: Accelerators, Spectrometers, Detectors and Associated Equipment*, 579(2):859 – 865, 2007. ISSN 0168-9002. doi: <https://doi.org/10.1016/j.nima.2007.05.305>. URL <http://www.sciencedirect.com/science/article/pii/S0168900207011965>. Proceedings of the 6th 'Hiroshima' Symposium on the Development and Application of Semiconductor Detectors.

- Shin'ichiro Takeda, Yuto Ichinohe, Kouichi Hagino, Hirokazu Odaka, Takayuki Yuasa, Shin nosuke Ishikawa, Taro Fukuyama, Shinya Saito, Tamotsu Sato, Goro Sato, Shin Watanabe, Motohide Kokubun, Tadayuki Takahashi, Mitsutaka Yamaguchi, Hiroyasu Tajima, Takaaki Tanaka, Kazuhiro Nakazawa, Yasushi Fukazawa, and Takashi Nakano. Applications and imaging techniques of a si/cdte compton gamma-ray camera. *Physics Procedia*, 37:859 – 866, 2012b. ISSN 1875-3892. doi: <https://doi.org/10.1016/j.phpro.2012.04.096>. URL <http://www.sciencedirect.com/science/article/pii/S1875389212017774>. Proceedings of the 2nd International Conference on Technology and Instrumentation in Particle Physics (TIPP 2011).
- T. Tamagawa, N. Tsunoda, A. Hayato, H. Hamagaki, M. Inuzuka, H. Miyasaka, I. Sakurai, F. Tokanai, and K. Makishima. Development of gas electron multiplier foils with a laser etching technique. *Nuclear Instruments and Methods in Physics Research Section A: Accelerators, Spectrometers, Detectors and Associated Equipment*, 560(2):418 – 424, 2006. ISSN 0168-9002. doi: <https://doi.org/10.1016/j.nima.2006.01.047>. URL <http://www.sciencedirect.com/science/article/pii/S0168900206000672>.
- H. Tsunemi, K. Hayashida, K. Tamura, S. Nomoto, M. Wada, A. Hirano, and E. Miyata. Detection of X-ray polarization with a charge coupled device. *Nuclear Instruments and Methods in Physics Research A*, 321:629–631, October 1992. doi: 10.1016/0168-9002(92)90075-F.
- Yuusuke Uchida. The performance study of soft gamma-ray detector on board astro-h. 1 2015.
- S. V. Vadawale, T. Chattopadhyay, N. P. S. Mithun, A. R. Rao, D. Bhattacharya, A. Vibhute, V. B. Bhalerao, G. C. Dewangan, R. Misra, B. Paul, A. Basu, B. C. Joshi, S. Sreekumar, E. Samuel, P. Priya, P. Vinod, and S. Seetha. Phase-resolved x-ray polarimetry of the crab pulsar with the astrosat czt imager. *Nature Astronomy*, 2(1):50–55, 2018. doi: 10.1038/s41550-017-0293-z. URL <https://doi.org/10.1038/s41550-017-0293-z>.
- S. Watanabe, T. Takahashi, Y. Okada, G. Sato, M. Kouda, T. Mitani, Y. Kobayashi, K. Nakazawa, Y. Kuroda, and M. Onishi. Cdte stacked detectors for gamma-ray detection. *IEEE Transactions on Nuclear Science*, 49(3):1292–1296, June 2002. ISSN 0018-9499.
- Shin Watanabe, Takaaki Tanaka, Kousuke Oonuki, Takefumi Mitani, Shin'ichiro Takeda, Tetsuichi Kishishita, Kazuhiro Nakazawa, Tadayuki Takahashi, Yoshikatsu Kuroda, and Mitsunobu Onishi. Development of cdte pixel detectors for compton cameras. *Nuclear Instruments and Methods in Physics Research Section A: Accelerators, Spectrometers, Detectors and Associated Equipment*, 567(1):150 – 153, 2006. ISSN 0168-9002. doi: <https://doi.org/10.1016/j.nima.2006.05.164>. URL <http://www.sciencedirect.com/science/article/pii/S0168900206008953>. Proceedings of the 4th International Conference on New Developments in Photodetection.
- Shin Watanabe, Shin'ichiro Takeda, Shin nosuke Ishikawa, Hirokazu Odaka, Masayoshi Ushio, Takaaki Tanaka, Kazuhiro Nakazawa, Tadayuki Takahashi, Hiroyasu Tajima, Yasushi Fukazawa, Yoshikatsu Kuroda, and Mitsunobu Onishi. Development of semiconductor imaging detectors for a si/cdte compton camera. *Nuclear Instruments and Methods in Physics Research Section A: Accelerators, Spectrometers, Detectors and Associated Equipment*, 579

- (2):871 – 877, 2007. ISSN 0168-9002. doi: <https://doi.org/10.1016/j.nima.2007.05.306>. URL <http://www.sciencedirect.com/science/article/pii/S0168900207011989>. Proceedings of the 6th 'Hiroshima' Symposium on the Development and Application of Semiconductor Detectors.
- Shin Watanabe, Shin-Nosuke Ishikawa, Hiroyuki Aono, Shin'ichiro Takeda, Hirokazu Odaka, Motohide Kokubun, Tadayuki Takahashi, Kazuhiro Nakazawa, Hiroyasu Tajima, Mitsunobu Onishi, and Yoshikatsu Kuroda. High Energy Resolution Hard X-Ray and Gamma-Ray Imagers Using CdTe Diode Devices. *IEEE Transactions on Nuclear Science*, 56:777–782, June 2009. doi: 10.1109/TNS.2008.2008806.
- Shin Watanabe, Hiroyasu Tajima, Yasushi Fukazawa, Yuto Ichinohe, Shin'ichiro Takeda, Teruaki Enoto, Taro Fukuyama, Shunya Furui, Kei Genba, Kouichi Hagino, Atsushi Harayama, Yoshikatsu Kuroda, Daisuke Matsuura, Ryo Nakamura, Kazuhiro Nakazawa, Hirofumi Noda, Hirokazu Odaka, Masayuki Ohta, Mitsunobu Onishi, Shinya Saito, Goro Sato, Tamotsu Sato, Tadayuki Takahashi, Takaaki Tanaka, Atsushi Togo, and Shinji Tomizuka. The si/cdte semiconductor compton camera of the astro-h soft gamma-ray detector (sgd). *Nuclear Instruments and Methods in Physics Research Section A: Accelerators, Spectrometers, Detectors and Associated Equipment*, 765:192 – 201, 2014. ISSN 0168-9002. doi: <https://doi.org/10.1016/j.nima.2014.05.127>. URL <http://www.sciencedirect.com/science/article/pii/S0168900214008250>. HSTD-9 2013 - Proceedings of the 9th International 'Hiroshima' Symposium on Development and Application of Semiconductor Tracking Detectors.
- M. C. Weisskopf, R. Berthelsdorf, G. Epstein, R. Linke, D. Mitchell, R. Novick, and R. S. Wolff. A graphite crystal polarimeter for stellar X-ray astronomy. *Review of Scientific Instruments*, 43:967–976, January 1972. doi: 10.1063/1.1685840.
- M. C. Weisskopf, G. G. Cohen, H. L. Kestenbaum, K. S. Long, R. Novick, and R. S. Wolff. Measurement of the X-ray polarization of the Crab nebula. *ApJ*, 208:L125–L128, September 1976. doi: 10.1086/182247.
- Martin C. Weisskopf. An overview of x-ray polarimetry of astronomical sources. *Galaxies*, 6(1), 2018. ISSN 2075-4434. doi: 10.3390/galaxies6010033. URL <http://www.mdpi.com/2075-4434/6/1/33>.
- Martin C. Weisskopf, J. Jeff Hester, Allyn F. Tennant, Ronald F. Elsner, Norbert S. Schulz, Herman L. Marshall, Margarita Karovska, Joy S. Nichols, Douglas A. Swartz, Jeffery J. Kolodziejczak, and Stephen L. O'Dell. Discovery of spatial and spectral structure in the x-ray emission from the crab nebula. *The Astrophysical Journal Letters*, 536(2):L81, 2000b. URL <http://stacks.iop.org/1538-4357/536/i=2/a=L81>.
- Martin C. Weisskopf, J. Jeff Hester, Allyn F. Tennant, Ronald F. Elsner, Norbert S. Schulz, Herman L. Marshall, Margarita Karovska, Joy S. Nichols, Douglas A. Swartz, Jeffery J. Kolodziejczak, and Stephen L. O'Dell. Discovery of spatial and spectral structure in the x-ray emission from the crab nebula. *The Astrophysical Journal Letters*, 536(2):L81, 2000a. URL <http://stacks.iop.org/1538-4357/536/i=2/a=L81>.

- Martin C. Weisskopf, Ronald F. Elsner, Victoria M. Kaspi, Stephen L. O'Dell, George G. Pavlov, and Brian D. Ramsey. X-Ray Polarimetry and Its Potential Use for Understanding Neutron Stars. In *Astrophysics and Space Science Library*, volume 357, page 589, January 2009. doi: 10.1007/978-3-540-76965-1_22.
- Martin C. Weisskopf, Brian Ramsey, Stephen O'Dell, Allyn Tennant, Ronald Elsner, Paolo Soffitta, Ronaldo Bellazzini, Enrico Costa, Jeffrey Kolodziejczak, Victoria Kaspi, Fabio Muleri, Herman Marshall, Giorgio Matt, and Roger Romani. The Imaging X-ray Polarimetry Explorer (IXPE). In *Space Telescopes and Instrumentation 2016: Ultraviolet to Gamma Ray*, volume 9905, page 990517, July 2016. doi: 10.1117/12.2235240.
- Shin'ya Yamada, Kazuo Makishima, Kazuhiro Nakazawa, Motohide Kokubun, Madoka Kawaharada, Takao Kitaguchi, Shin Watanabe, Hiromitsu Takahashi, Hirofumi Noda, Hiroyuki Nishioka, Kazuyoshi Hiragi, Katsuhiro Hayashi, Kenta Nakajima, Makoto Tashiro, Makoto Sasano, Sho Nishino, Shunsuke Torii, Soki Sakurai, Tadayuki Takahashi, Tsunefumi Mizuno, Teruaki Enoto, Takayuki Yuasa, Takaaki Tanaka, Tomomi Kouzu, Toshio Nakano, Yasushi Fukazawa, Yukikatsu Terada, Yasunobu Uchiyama, and Wataru Iwakiri. Improvements in calibration of gso scintillators in the suzaku hard x-ray detector. *Publications of the Astronomical Society of Japan*, 63(sp3):S645–S656, 2011. doi: 10.1093/pasj/63.sp3.S645. URL <http://dx.doi.org/10.1093/pasj/63.sp3.S645>.
- V. Zabalza. naima: a python package for inference of relativistic particle energy distributions from observed nonthermal spectra. *Proc. of International Cosmic Ray Conference 2015*, page 922, 2015. URL <http://adsabs.harvard.edu/abs/2015arXiv150903319Z>.
- Roberta Zanin. *Crab Observational Status: Nebulae, Pulsations, and Flares*, pages 101–133. Springer International Publishing, Cham, 2017. ISBN 978-3-319-63031-1. doi: 10.1007/978-3-319-63031-1_6. URL https://doi.org/10.1007/978-3-319-63031-1_6.
- Andrzej A. Zdziarski and Marek Gierliński. Radiative processes, spectral states and variability of black-hole binaries. *Progress of Theoretical Physics Supplement*, 155:99–119, 2004. doi: 10.1143/PTPS.155.99. URL <http://dx.doi.org/10.1143/PTPS.155.99>.
- A. Zoglauer and G. Kanbach. Doppler broadening as a lower limit to the angular resolution of next-generation Compton telescopes. In J. E. Truemper and H. D. Tananbaum, editors, *X-Ray and Gamma-Ray Telescopes and Instruments for Astronomy.*, volume 4851 of Proc. SPIE, pages 1302–1309, March 2003. doi: 10.1117/12.461177.